A Study of Final-State Radiation in Hadronic Z Decays

Thesis by
David P. Kirkby

In Partial Fulfillment of the Requirements
for the Degree of
Doctor of Philosophy

California Institute of Technology
Pasadena, California

1996
(Submitted September 14, 1995)

Acknowledgment

It is a pleasure to acknowledge the support and guidance of my advisor at Caltech, Harvey Newman. I would also like to thank the members of the L3 hadron analysis group — in particular, Thomas Hebbeker, Dominique Duchesneau, and Giorgio Gratta — for providing a stimulating environment for learning about QCD and final-state radiation.

In preparing this manuscript, I have greatly benefited from the careful reading and constructive criticisms of Harvey Newman, Anne Kirkby, and Thomas Hebbeker.

Finally, I would like to thank my parents for the encouragement and nurturing that laid the foundations of this thesis. I am especially grateful to my wife, Annie, who has given me her complete support and understanding at every step. My thesis would not have been possible without her.

Abstract

I have studied hadronic decays of the Z boson that are accompanied by isolated and energetic photon radiation from one of the primary quarks, $\mathrm{Z} \rightarrow \mathrm{q\bar{q}}\gamma$. This study enables me to measure the electroweak couplings and charges separately for up-type and down-type quarks.

I have measured the fraction of hadronic Z decays that contain a photon radiated by a primary quark to be

$$\frac{\mathrm{BR}(\mathrm{Z} \rightarrow \mathrm{q\bar{q}}\gamma)}{\mathrm{BR}(\mathrm{Z} \rightarrow \mathrm{q\bar{q}})} = (2.85 \pm 0.14) \times 10^{-3} ,$$

where I required that the photon have an energy between 8 GeV and 44 GeV and be accompanied by less than 100 MeV of hadronic energy within a 20° cone about its direction. Both the statistical and systematic errors in this result are smaller than those of comparable previous results.

I have calculated the energy distribution of isolated final-state radiation at next-to-lowest order, $\mathcal{O}(\alpha_S\alpha)$, and performed a fit of this prediction to my measured energy distribution to obtain a constraint on the quark couplings. I have combined this constraint with a second constraint that I have derived from the L3 measurements of cross sections and charge asymmetries at the Z peak. By assuming the Standard Model quark charges, I have measured the couplings of up- and down-type quarks to the Z boson, $\overline{c} \equiv 4\,(\overline{g}_V{}^2 + \overline{g}_A{}^2)$, to be

$$\overline{c}_{\mathrm{u}} = 1.11 \pm 0.17 \quad \text{and} \quad \overline{c}_{\mathrm{d}} = 1.52 \pm 0.11 .$$

The experimental errors in this result are smaller than those of comparable previous measurements. By parameterizing $\overline{c}_{\mathrm{u}}$ and $\overline{c}_{\mathrm{d}}$ in terms of the quark charges, I have measured these charges to be

$$3|Q_{\mathrm{u}}| = 1.90\,^{+0.25}_{-0.46} \quad \text{and} \quad 3|Q_{\mathrm{d}}| = 1.06\,^{+0.26}_{-0.11} .$$

This is the first such measurement of the quark charges at LEP. The quark electroweak couplings and charges that I have measured are consistent with the Standard Model.

I have selected a sample of events containing isolated and energetic photons from 2.76 million hadronic Z decays recorded by the L3 detector between 1991 and 1994. I have analyzed this sample to determine the energy distribution of isolated photons radiated by a primary quark by subtracting initial-state bremsstrahlung and hadronic background, and by applying acceptance and detector corrections. The hadronic background, which consists mostly of decays of isolated neutral pions into photons, is underestimated by existing Monte Carlo models. I have used a new technique of analyzing shower shapes in the L3 electromagnetic calorimeter to study this background directly using data. The discrepancies between data and Monte Carlo predictions that I have observed have implications for detecting the Higgs decay, H$\rightarrow \gamma\gamma$, at the next generation of high-energy experiments at the LHC.

Contents

LIST OF TABLES

LIST OF FIGURES

Chapter 1

Introduction and Overview

In this thesis, I study hadronic decays of the Z boson in which a photon is radiated by one of the primary quarks, $Z \to q\bar{q}\gamma$ (see Figure 1.1). My motivation for this study is to measure the couplings of quarks to the Z boson and to the photon.

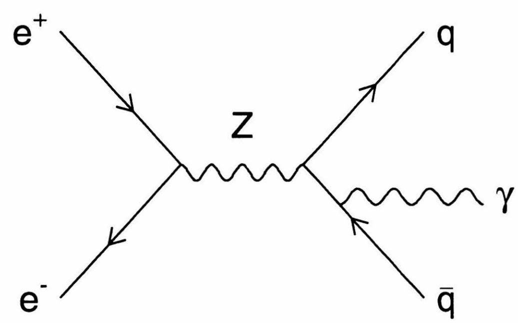

Figure 1.1: Diagram of the reaction $e^+e^- \to q\bar{q}\gamma$ that I study in this thesis.

The data that I will describe were collected between 1991 and 1994 from electron-positron annihilations into Z bosons at 91 GeV. These reactions were produced by the LEP accelerator and recorded by the L3 detector. The Z bosons produced at LEP can decay into leptons or hadrons (which originate from a primary $q\bar{q}$ pair). The specific final state that I study in this thesis consists of hadrons together with an energetic and isolated photon.

In the Standard Model, there are two types of quarks, which I refer to as up-type and down-type, and their interactions with Z bosons and photons can be described using four coupling parameters (see Figure 1.2): $\bar{c}_u$ and $\bar{c}_d$ are the couplings to Z bosons, and ${Q_u}^2$ and ${Q_d}^2$ are the couplings to photons. L3 has measured the inclusive rate of Z decays into quarks, $\Gamma(\mathrm{Z} \longrightarrow \mathrm{q\bar{q}})$; this measurement constrains a linear combination of the quark couplings

$$\Gamma(\mathrm{Z} \longrightarrow \mathrm{q\bar{q}}) \propto 2 \cdot \bar{c}_u + 3 \cdot \bar{c}_d \ ,$$

where the factors 2 and 3 count the numbers of up- and down-type quarks that a Z can decay into. In this thesis, I measure the exclusive rate of hadronic Z decays that are accompanied by final-state radiation, $\Gamma(\mathrm{Z} \longrightarrow \mathrm{q\bar{q}}\gamma)$, and thus constrain a different linear combination

$$\Gamma(\mathrm{Z} \longrightarrow \mathrm{q\bar{q}}\gamma) \propto 2 \cdot \bar{c}_u \cdot {Q_u}^2 + 3 \cdot \bar{c}_d \cdot {Q_d}^2 \ .$$

By combining these constraints, I am able to determine the values of the quark couplings.

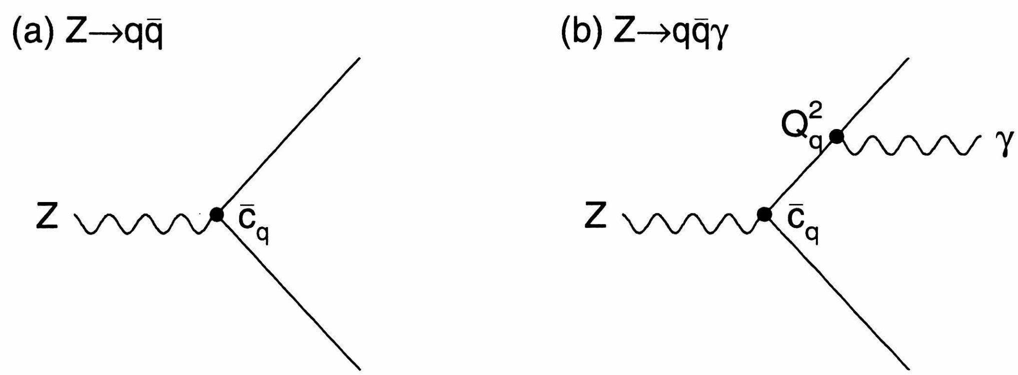

Figure 1.2: Diagrams for two Z decay processes whose rates constrain the quark couplings to the Z boson and the photon: inclusive decays into quarks (a), and exclusive decays that are accompanied by a radiated photon (b).

I have organized this thesis in three parts. In the first part (Chapters 2–4), I give an overview of the theoretical and experimental context of my work. In the second part (Chapters 5–7 and Appendix A), I describe my original contributions to the study of final-state radiation in hadronic Z decays. In the last part (Chapter 8), I describe how I combine my experimental and theoretical results to measure the quark couplings. Below, I give a brief outline of each chapter.

In Chapter 2, I describe the Standard Model of particle physics, concentrating on the electroweak and strong interactions that are relevant to this thesis. Chapter 3 covers the LEP accelerator and the L3 detector in general, and in Chapter 4, I provide a more detailed description of the L3 electromagnetic calorimeter, which is the main component of the detector that I have used.

In Chapter 5, I present the methods that I have used to select a sample of events that is enriched in final-state radiation. As part of this work, I have developed new techniques for discriminating between single and overlapping photons in the detector and I provide details of this approach in Appendix A. Chapter 6 covers the data analysis that I perform on my selected events, which involves estimating and subtracting irreducible background contributions, and correcting for the limited efficiency and acceptance of the detector.

In Chapter 7, I discuss theoretical models of final-state radiation, and in particular, I describe the next-to-lowest order, $\mathcal{O}(\alpha_S\alpha)$, matrix-element calculation that I have performed. I compare theory with data in Chapter 8, in order to measure the couplings of up- and down-type quarks to the Z boson and the photon. Finally, in Chapter 9 I summarize the main results of this thesis and compare them with results from other experiments.

Chapter 2

Standard Model Physics

In this thesis I examine hadronic decays of the Z boson accompanied by hard photon radiation from the final-state quarks. This process involves electromagnetic, weak, and strong interactions. Our present understanding of these interactions and of the fundamental particles of nature is embodied in the *Standard Model* of particle physics. In this chapter I first introduce the key theoretical concepts underlying the Standard Model, and then describe the specific formulation of the electroweak and strong sectors, focusing on aspects relevant to this thesis.

Much of the development of the Standard Model is due to the insight that the laws governing a system can be deduced from its symmetries. A complementary aspect — central to the success of the Standard Model — is that states satisfying the fundamental equations of the theory need not obey the symmetries inherent in the equations. A symmetry of a physical system can be described by generalized coordinate transformations that do not change its equations of motion; the set of these transformations has the mathematical structure of a group. Symmetries can be classified according to whether their corresponding symmetry groups are finite or infinite (discrete/continuous), whether or not group elements commute (abelian/non-abelian), whether the transformations act in Lorentz space or upon internal degrees of freedom (geometrical/internal), and whether the transformations are constant or varying in space-time (global/local). The most convenient method for studying symmetries of a field theory is the Lagrangian formalism, based on a functional $\mathcal{L}(\phi, \partial_\mu \phi)$

of the fields $\phi(x_\nu)$, which is related to the classical action S by

$$S = \int_{t_1}^{t_2} d^4x \mathcal{L}(\phi, \partial_\mu \phi) \ .$$

This Lagrangian density (for convenience referred to simply as the Lagrangian) satisfies a least action principle which leads to the equations of motion

$$\frac{\partial \mathcal{L}}{\partial \phi} = \partial_\mu \frac{\partial \mathcal{L}}{\partial \left(\partial_\mu \phi\right)} \ .$$

For every continuous symmetry of the Lagrangian (or equivalently, the equations of motion) there is a corresponding conservation law[1]; for example, symmetry under space-time translations corresponds to energy-momentum conservation. The program for generating the interactions between the fundamental constituents of the Standard Model consists of generalizing global internal symmetries of the Lagrangian for a free particle as local symmetries (gauge transformations), and identifying the extra terms that must be added to the free-particle Lagrangian to achieve local symmetry as interactions involving a new field (gauge bosons). Interactions are between source fields (fermions) and gauge bosons and, in the case of non-abelian symmetries, also among gauge bosons.

The gauge bosons associated with new gauge fields cannot be massive as this would entail an additional term in the Lagrangian which is not gauge invariant. Massive gauge bosons in a theory are introduced via *spontaneously broken* symmetries that are exact for the Lagrangian, but are not respected by the vacuum state. Symmetry breaking occurs in a system having a degenerate set of possible vacuum states, where the degeneracy reflects the unbroken symmetry, and is a consequence of the fact that nature must pick a unique physical vacuum. The equations of motion expressed in terms of states coupled to the physical vacuum manifest additional massless fields (*Goldstone bosons*) associated with the degrees of freedom of the broken symmetry[2]. However, these Goldstone bosons do not appear in the resulting particle spectrum; the combined effect of the Goldstone and massless gauge boson fields is exactly equivalent to a set of gauge bosons which acquire mass via the interactions of the massless bosons (this is known as the *Higgs mechanism*)[3].

2.1 Electroweak Interactions

In this section, I describe the electroweak sector of the Standard Model, which provides a unified description of the electromagnetic and weak interactions of quarks and leptons. Although weak and electromagnetic phenomena are not obviously related at low energies, their unification is motivated by the observation of charged weak currents which suggests that interactions can occur between the mediators of these forces.

The internal symmetries used to build the electroweak theory are known as weak hypercharge with generator Y and based on the abelian $U(1)$ group, and weak isospin with generators $\mathbf{I} = (I_+, I_-, I_3)$ and based on the non-abelian group $SU(2)$[4–6]. The source fields of the electroweak sector are grouped into families of leptons and quarks and a single family of scalar bosons[1], and form left-handed iso-doublets and right-handed iso-singlets characterized by the quantum numbers $I = |\mathbf{I}|$, I_3 and Y (see table 2.1). The Lagrangian for a non-interacting theory with the source fields described above has an internal global symmetry with the group structure $SU(2) \otimes U(1)$. Requiring that the corresponding local symmetry be spontaneously broken results in a particle spectrum with an additional weak-isospin triplet of vector gauge bosons $W^{\pm}$,Z; a photon; and a scalar Higgs boson H^0. All charged leptons and the $W^{\pm}$,Z,H^0 bosons acquire mass from the spontaneous symmetry breaking through the Higgs mechanism. Although the physical vacuum does not have $SU(2) \otimes U(1)$ symmetry, it does have a manifest $U(1)$ symmetry corresponding to the linear combination of

[1]This is the minimal Higgs content required for spontaneous symmetry breaking and leads to the *Minimal Standard Model*; however, consistent theories with additional Higgs fields are also possible.

generators

$$Q = I_3 + \frac{1}{2}Y ,$$

which results in conservation of electric charge and a massless photon.

Families			I	I_3	Y	Q
$\begin{pmatrix} \mathrm{e} \\ \nu_{\mathrm{e}} \end{pmatrix}_L$	$\begin{pmatrix} \mu \\ \nu_\mu \end{pmatrix}_L$	$\begin{pmatrix} \tau \\ \nu_\tau \end{pmatrix}_L$	1/2 1/2	−1/2 +1/2	−1 −1	−1 0
e_R	μ_R	τ_R	0	0	−2	−1
$\begin{pmatrix} \mathrm{u} \\ \mathrm{d}' \end{pmatrix}_L$	$\begin{pmatrix} \mathrm{c} \\ \mathrm{s}' \end{pmatrix}_L$	$\begin{pmatrix} \mathrm{t} \\ \mathrm{b}' \end{pmatrix}_L$	1/2 1/2	+1/2 −1/2	1/3 1/3	+2/3 −1/3
u_R	c_R	t_R	0	0	4/3	+2/3
d'_R	s'_R	b'_R	0	0	4/3	−1/3
	$\begin{pmatrix} \phi^+ \\ \phi^0 \end{pmatrix}_L$		1/2 1/2	+1/2 −1/2	1 1	+1 0

Table 2.1: Quantum numbers for the source fields of the electroweak sector of the Standard Model.

The phenomenology of hadronic weak interactions dictates that quark mass eigenstates are not electroweak eigenstates. With an appropriate choice of quark state phases, the Cabibbo mixing[7] between eigenstates can be restricted to the down-type ($I_3 = -1/2$) quarks of each family

$$\mathrm{d}'_i = \Sigma_j U_{ij} \mathrm{d}_j ,$$

where U is a unitary matrix[8, 9]. With more than two quark families, U will in general include complex elements, and thus explicitly violate invariance under the combined discrete symmetries of charge conjugation (C) and parity (P)[10, 11].

The best-developed tool for the calculation of electroweak observables is perturbation theory, in which the expansion parameters are the coupling strengths of the gauge bosons. Terms in a perturbative expansion can be represented as Feynman diagrams that depict the topological flow of fermions and bosons through space-time as lines, and interactions as vertices. The set of allowed vertices and the rules for using them are determined by corresponding terms in the Lagrangian (see Figure 2.1); each vertex introduces a gauge coupling so that the perturbative expansion is simply an expansion in the number of vertices in the diagram. The gauge couplings and fermion masses appearing in the Lagrangian are free parameters of the theory, but may be expressed in terms of measurable observables, and thus may by determined experimentally. At a finite order in perturbation theory, this procedure is not exact due to missing higher-order contributions whose size in general decreases as further orders are taken into account.

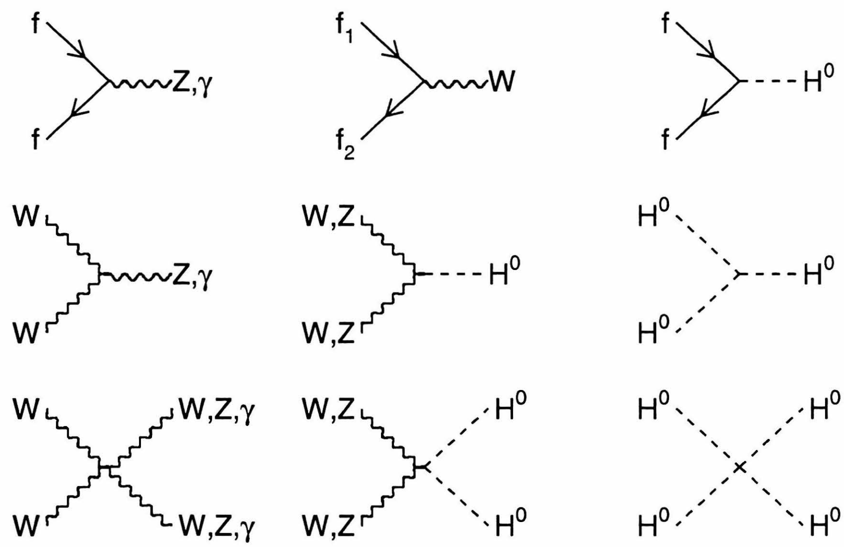

Figure 2.1: Interaction vertices of the electroweak sector of the Standard Model. The diagrams represent topological structure only and any assignment of lines to the initial and final states of the interaction is allowed. f denotes any fermion; f_1, f_2 denote the members of a weak-isospin doublet of fermions.

Beyond lowest order in perturbation theory, it is necessary to consider diagrams including closed loops. Such loops are associated with an unconstrained internal 4-momentum which must be integrated out, and lead to logarithmic *ultraviolet* divergences in the perturbative expansion. It is a general feature of spontaneously broken gauge field theories that such divergences can be consistently handled at each order of perturbation theory by replacing the bare wave-functions, gauge couplings, and propagators of the Lagrangian with *renormalized* quantities, which introduces appropriate canceling singularities[12, 13]. There is some arbitrariness in the choice of renormalization scheme; while all schemes lead to the same results when all orders are included in the perturbation expansion, finite-order calculations have a residual renormalization-scheme dependence. The renormalization program suffers from *anomalies*[14, 15] which are associated with loop contributions that violate classical conservation laws; one of these – the axial anomaly – is conveniently resolved by requiring that the number of quark and lepton families be the same.

2.1.1 Electron-Positron Reactions

I now focus on the initial state consisting of an electron and positron, which is relevant to the subjects covered in this thesis. The lowest-order reaction diagrams are shown in Figure 2.2 and result in final states consisting of a particle anti-particle pair, $\mathrm{x\bar{x}}$, satisfying the kinematic constraint

$$m_{\mathrm{x}} \leq \frac{\sqrt{s}}{2} .$$

The lowest-order diagrams are naturally divided into two classes according to whether the virtual propagator is produced by annihilation of the initial state (*s-channel*, Figure 2.2 (a–f)) or by emission and re-absorption by the initial state (*t-channel*, Figure 2.2 (g–k)).

The relevant center-of-mass energy to the work described here is $m_{\mathrm{Z}} \simeq 91.2$ GeV, where the allowed final states include pairs of all fermions except the t-quark, and the production of pairs of massive bosons ($\mathrm{Z}, \mathrm{W}^{\pm}, \mathrm{H}^0$) is kinematically forbidden. Diagrams involving a virtual H^0 propagator are strongly suppressed due to the smallness of the H^0 coupling to light fermions, and can be neglected.

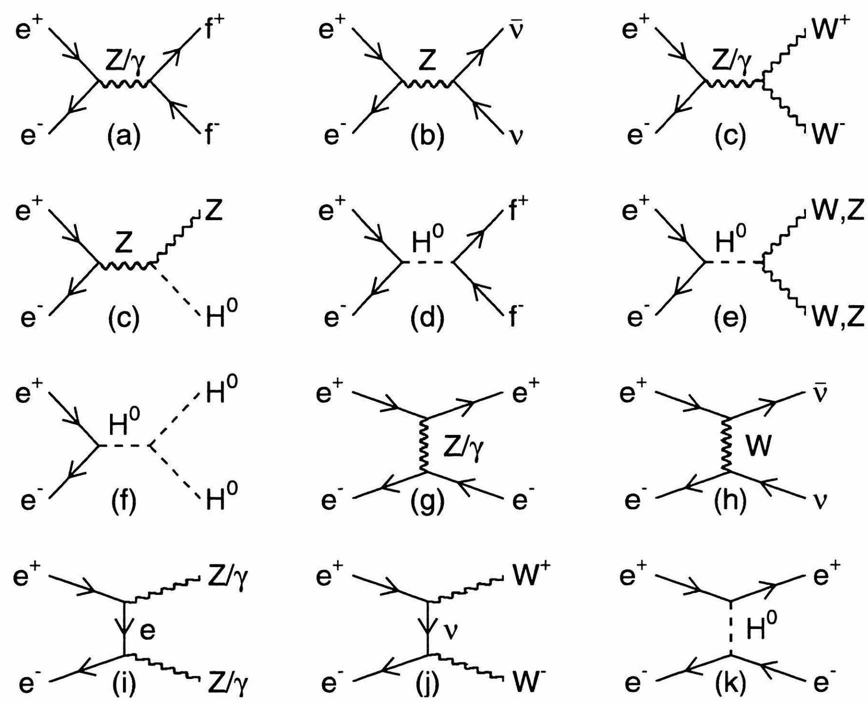

Figure 2.2: Lowest-order Feynman diagrams for electron-positron reactions. The initial state of each diagram is on the left-hand side, and the final state is on the right-hand side. f^+, f^- denote a charged fermion and its anti-particle.

2.1.1.1 The Reaction $e^+e^- \to f\bar{f}$

I now concentrate on the final state consisting of a fermion anti-fermion pair, $f\bar{f}$, produced via s-channel exchange of a photon or Z boson, which is relevant to the work described here. I do not consider the production of e^+e^- or $\nu_e\bar{\nu}_e$ pairs since these can also be produced via t-channel exchange diagrams. The differential cross section for the production of $f\bar{f}$ pairs in collisions of unpolarized e^+, e^- beams corresponding to the lowest-order s-channel diagrams (Figure 2.2 (a,b)) is

$$\frac{d\sigma}{d\Omega}\left(e^+e^- \to f\bar{f}\right) = \frac{\alpha^2}{4s} N_C^f \left\{F_1(s)\left(1+\cos^2\theta\right) + F_2(s)\cdot 2\cos\theta\right\} ,$$

where

$$
\begin{aligned}
F_1(s) &= Q_e^2 Q_f^2 + 2Q_e Q_f g_V^e g_V^f \operatorname{Re}\chi(s) + ({g_V^e}^2 + {g_A^e}^2)({g_V^f}^2 + {g_A^f}^2)\,|\chi(s)|^2 \\
F_2(s) &= 2Q_e Q_f g_A^e g_A^f \operatorname{Re}\chi(s) + 4\, g_V^e g_A^e g_V^f g_A^f\, |\chi(s)|^2 \\
\chi(s) &= \frac{1}{4\sin^2\theta_W \cos^2\theta_W}\,\frac{s}{s - m_Z^2 + i m_Z \Gamma_Z} \\
\Gamma_Z &= \sum_f N_C^f \frac{\alpha}{3} m_Z \left({g_V^f}^2 + {g_A^f}^2\right) .
\end{aligned}
$$

The vector and axial couplings are given by (I_3 refers to the quantum numbers of the left-handed state)

$$
g_V^f = I_3^f - 2Q_f \sin^2\theta_W \qquad , \qquad g_A^f = I_3^f ,
$$

N_C^f is the color factor (with a value of 1 for leptons, and a value of 3 for quarks) and θ is the angle between the incoming e^- and the outgoing fermion in the center-of-mass frame of the reaction. Terms due to the mass of the final-state fermion are $\mathcal{O}(m_f^2/s)$ and can be neglected for the allowed fermions at $\sqrt{s} \simeq m_Z$ (below the threshold for $t\bar{t}$ production). The free parameters in the lowest-order cross section whose values must be determined experimentally are the electromagnetic fine-structure constant[2] $\alpha \simeq 1/128$, the weak mixing angle $\sin^2\theta_W \simeq 0.231$, and the Z boson mass $m_Z \simeq 91.2$ GeV.

The total cross section for the production of $f\bar{f}$ pairs is defined as

$$
\sigma_{f\bar{f}}(s) \equiv \int d\Omega \frac{d\sigma}{d\Omega}\left(e^+e^- \to f\bar{f}\right) ,
$$

and is given to lowest order by

$$
\sigma_{f\bar{f}}(s) = \frac{8}{3}\frac{\alpha^2}{4s} N_C^f F_1(s) ,
$$

which is plotted in Figure 2.3 for $q\bar{q}$ production. The cross section is dominated by resonant Z exchange near $\sqrt{s} = m_Z$, and by non-resonant γ exchange at other energies. The dependence of the differential cross section on the polar angle is shown

[2]This is the value that would be determined by comparing a measurement with the lowest-order calculation. At higher orders, the value $\alpha(m_Z) \simeq 1/128$ arises from the evolution of the running coupling from $\alpha(m_e) \simeq 1/137.04$[16].

at lowest order in Figure 2.4 for $q\bar{q}$ production at $\sqrt{s} = m_Z, m_Z \pm \Gamma_Z$. The energy-dependent asymmetry between forward and backward production is a feature of Z exchange and can be quantified as

$$A_{FB}(s) \equiv \frac{\sigma_F(s) - \sigma_B(s)}{\sigma_F(s) + \sigma_B(s)} ,$$

where

$$\sigma_F(s) = \int_0^{\pi/2} d\Omega \frac{d\sigma}{d\Omega} \quad , \quad \sigma_B(s) = \int_{\pi/2}^{\pi} d\Omega \frac{d\sigma}{d\Omega} .$$

The asymmetry is given to lowest order by

$$A_{FB}(s) = \frac{3}{4} \frac{\alpha^2}{4s} N_C^f \frac{F_2(s)}{F_1(s)} ,$$

which is shown in Figure 2.5 for various final states.

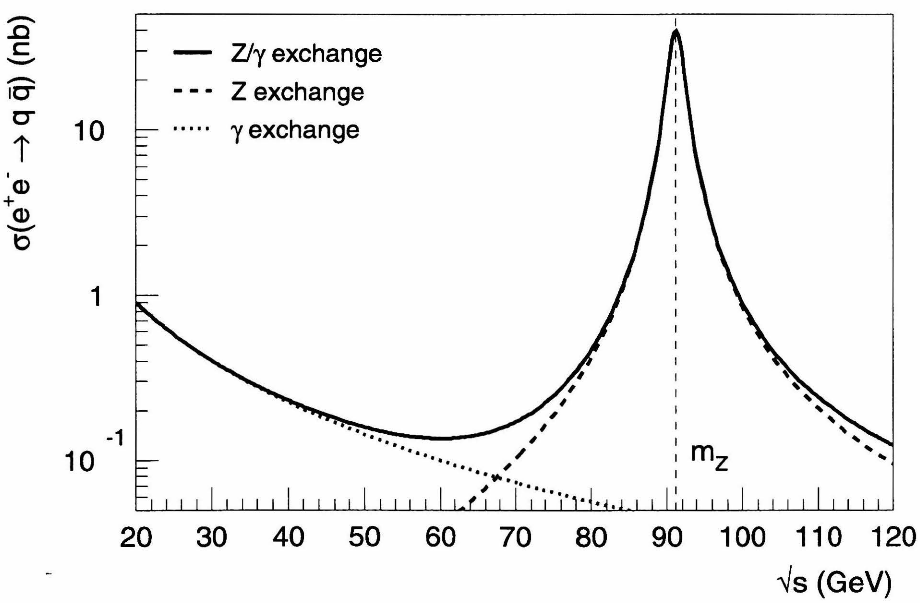

Figure 2.3: Total cross section for $q\bar{q}$ production as a function of collision energy, calculated to lowest order. The individual contributions of Z and γ exchange are shown with dashed and dotted curves.

Calculation of higher-order corrections to the lowest-order results given above requires a choice of renormalization scheme to regulate ultraviolet divergences. A

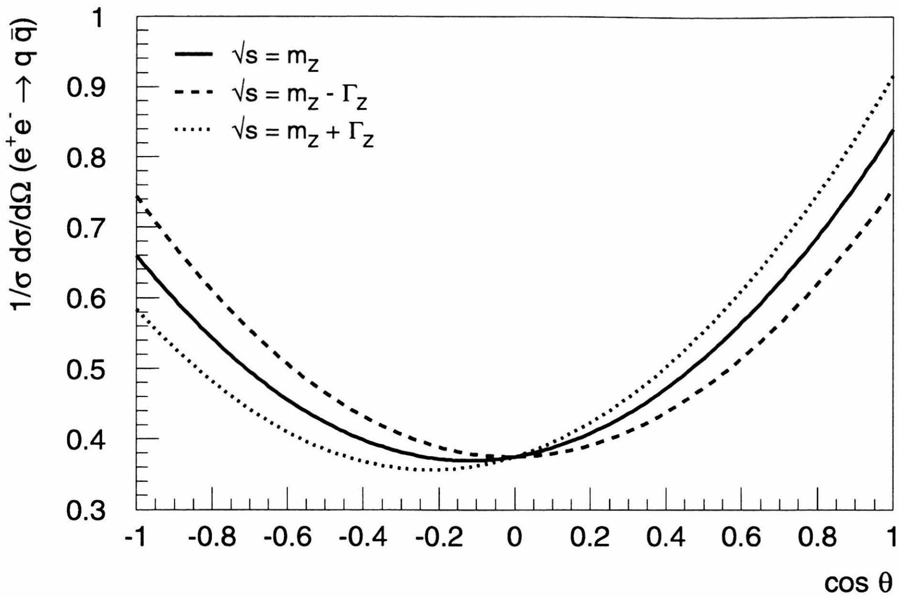

Figure 2.4: Polar angle dependence of the differential cross section for $q\bar{q}$ production, calculated to lowest order, at collision energies near m_Z. The curves for each energy are normalized to the total cross section at that energy.

convenient scheme for electroweak calculations is *on-shell* renormalization in which poles are located at the measured physical particle masses. The free parameters in this scheme are[17]

$$e \ , \ m_f \ , \ m_Z \ , \ m_W \ , \ m_H \ ,$$

which have been directly measured except for m_t, m_H; and the lowest-order expressions for the gauge couplings are promoted to definitions to be used at all orders

$$\alpha \equiv \frac{e^2}{4\pi} \simeq \frac{1}{137.04} \quad , \quad \sin^2\theta_W \equiv 1 - \frac{m_W^2}{m_Z^2} \ .$$

The on-shell renormalized one-loop corrections to $f\bar{f}$ production separate naturally into electromagnetic and non-electromagnetic (*weak*) corrections. The electromagnetic corrections are due to diagrams with additional photons, either radiated or in loops, and are numerically the most important. Near $\sqrt{s} = m_Z$, the largest corrections are due to photon radiation from the initial state, which occurs with a

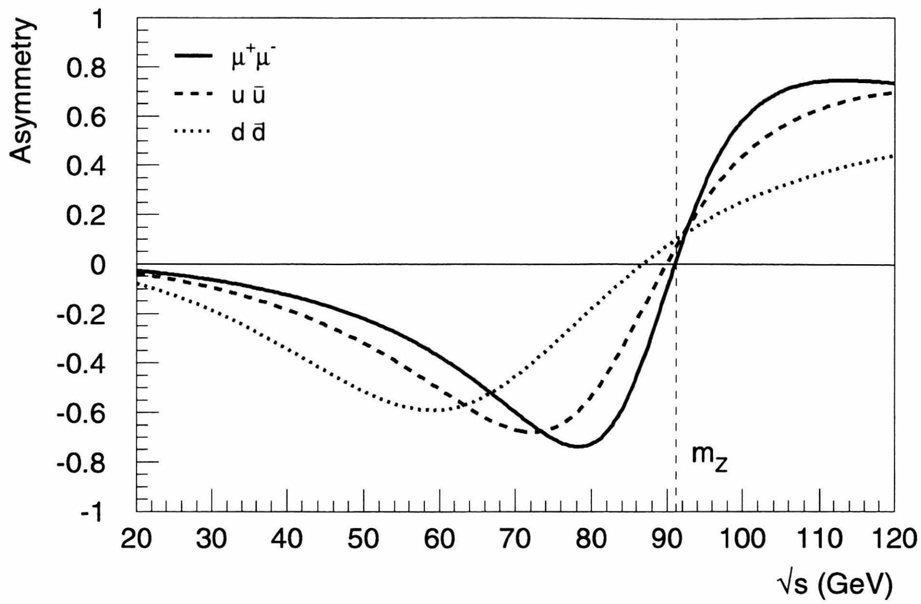

Figure 2.5: Forward-backward asymmetry for different final states in e^+e^- s-channel scattering, calculated to lowest order, as a function of collision energy $\sqrt{s}$.

probability proportional to

$$\frac{\sigma(s - 2E_\gamma\sqrt{s})}{\sigma(s)} ,$$

and is thus sensitive to the rapid variation of $\sigma(s)$ near the Z resonance. The weak one-loop corrections are numerically small and depend on the value of the unknown parameter m_H. The leading weak corrections are conveniently introduced into lowest-order calculations with a set of substitution rules known as the improved Born approximation[18]. These rules parameterize the electromagnetic coupling, α, the Z width, Γ_Z, and the vector and axial couplings, g_V^f and g_A^f, as functions of the center-of-mass energy, $\sqrt{s}$, according to

$$\begin{aligned}
\alpha &\longrightarrow \frac{\alpha}{1 - \Delta\alpha(s)} \\
\Gamma_{\mathrm{Z}} &\longrightarrow \frac{s}{m_{\mathrm{Z}}^2}\Gamma_{\mathrm{Z}} \\
g_V^{\mathrm{f}} &\longrightarrow \sqrt{\rho_{\mathrm{f}}(s)}\,\left(I_3^{\mathrm{f}} - 2\,\kappa_{\mathrm{f}}(s)\,Q_{\mathrm{f}}\sin^2\theta_W\right) \\
g_A^{\mathrm{f}} &\longrightarrow \sqrt{\rho_{\mathrm{f}}(s)}\,I_3^{\mathrm{f}}\,,
\end{aligned}$$

where the functions $\Delta\alpha(s)$, $\rho_{\mathrm{f}}(s)$, and $\kappa_{\mathrm{f}}(s)$ incorporate the weak corrections.

Near $\sqrt{s} = m_{\mathrm{Z}}$, all light fermions can be treated universally, and it is customary to introduce energy-independent effective weak correction factors

$$\begin{aligned}
\rho_{\mathrm{f}}(s) &\longrightarrow \rho_{\mathrm{eff}} \equiv \rho(m_{\mathrm{Z}}) \\
\kappa_{\mathrm{f}}(s) &\longrightarrow \kappa_{\mathrm{eff}} \equiv \kappa(m_{\mathrm{Z}})\,,
\end{aligned}$$

which lead to effective vector and axial coupling constants g_V^{eff}, g_A^{eff}, and an effective weak mixing angle, $\overline{\theta}_W$, via

$$\sin^2\overline{\theta}_W \equiv \kappa_{\mathrm{eff}}\,\sin^2\theta_W\,.$$

Figure 2.6 shows the energy dependence of the total cross section for producing $\mathrm{q\overline{q}}$ pairs near the Z resonance, comparing calculations at lowest order, using the improved Born approximation, and including all calculated corrections.

2.2 Strong Interaction Physics

This section describes the strong sector of the Standard Model, which governs interactions between quarks and gluons (collectively called partons), believed to be the fundamental constituents of hadrons. Although partons and the strong *color* charge[20] are not directly observable, their existence can be inferred from the phenomenology of hadronic interactions, including the partial decay width of neutral pions into photons[21] and the hadronic production cross section in $\mathrm{e^+e^-}$ annihilation[22–24].

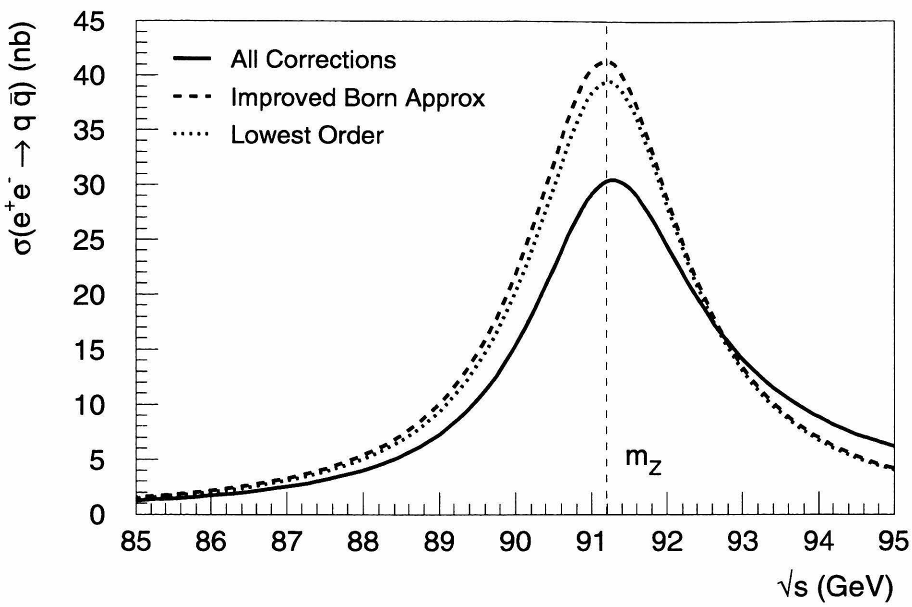

Figure 2.6: Total cross section for $q\bar{q}$ production as a function of collision energy, calculated with different levels of higher-order corrections. The lowest-order curve is calculated with $\alpha \simeq 1/128$. The curve with all corrections was calculated with the program ZFITTER[19].

The gauge theory of quark and gluon interactions is known as Quantum Chromodynamics (QCD)[25–30], and is based on an exact internal symmetry with non-abelian SU(3) group structure. The theory represents quarks as color triplets (labeled as red, green, and blue) and generalization of the global SU(3) symmetry of the free-quark theory to a local symmetry introduces a color octet of massless bosons (*gluons*) that mediate the color force. Gluons carry color charge themselves (each gluon being labeled by two colors) and are thus self-interacting. Figure 2.7 shows the fundamental vertices associated with terms in the QCD Lagrangian.

The usefulness of a finite-order perturbative calculation depends on the size of the expansion parameter. To lowest order, the QCD gauge coupling, α_s, is constant and a free parameter of the theory. When higher-order corrections are included, it is necessary to choose a renormalization scheme for the regularization of ultraviolet

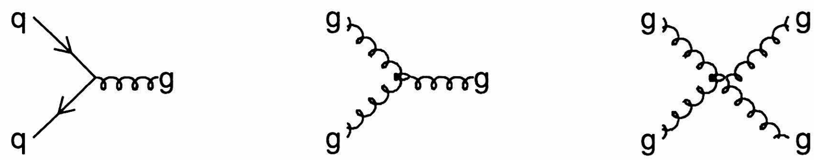

Figure 2.7: Interaction vertices of the strong sector of the Standard Model. The diagrams represent topological structure only and any assignment of lines to the initial and final states of the interaction is allowed.

divergences. The on-shell scheme used in electroweak calculations is not appropriate for QCD where there are no natural physical mass scales. Instead it is convenient to use the *modified minimal subtraction* scheme (denoted $\overline{\mathrm{MS}}$) in which all renormalized quantities are defined at a common arbitrary scale μ. In this scheme the expansion parameter becomes the effective gauge coupling $\alpha_S(\mu)$ whose scale dependence is given implicitly by the renormalization group equation

$$\mu^2 \frac{\partial \alpha_S}{\partial \mu^2} = -\alpha_S^2 \sum_{k=0} \beta_k \alpha_S^k \ .$$

The first three β-coefficients have been calculated[31–33] (β_0, β_1 are renormalization-scheme independent, β_2 is given in the $\overline{\mathrm{MS}}$ scheme)

$$\begin{aligned}
\beta_0 &= \frac{33 - 2n_f}{12\pi} && = 0.610 \\
\beta_1 &= \frac{153 - 19n_f}{24\pi^2} && = 0.245 \\
\beta_2 &= \frac{77139 - 15099n_f + 325n_f^2}{3456\pi^3} && = 0.091 \ ,
\end{aligned}$$

where n_f is the number of active flavors and numerical values are for $n_f = 5$ appropriate for $\mu \simeq m_Z$. Figure 2.8 shows the μ^2-evolution (*running*) of the strong coupling at different orders of perturbation theory, and makes apparent the convergence of the perturbative expansion.

The running of α_S is given explicitly at leading order by

$$\alpha_S(\mu) = \alpha_S(\mu_0) \left[1 - \alpha_S(\mu_0) \log\left(\frac{\mu^2}{\mu_0^2}\right) \left(\frac{33 - 2n_f}{12\pi}\right) + \mathcal{O}(\alpha_S^2) \right] \ ,$$

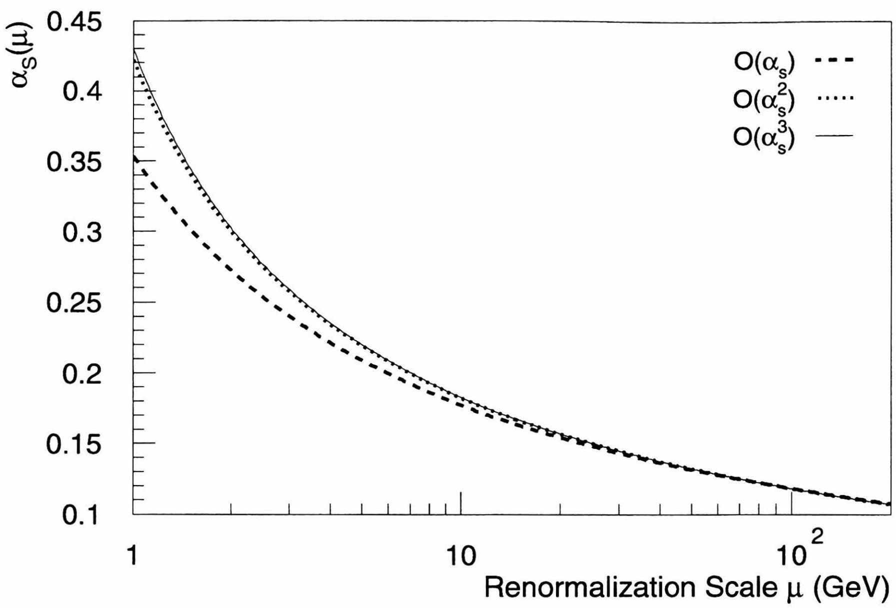

Figure 2.8: Evolution of $\alpha_S(\mu)$ from $\alpha_S(m_Z) = 0.12$ different approximations to the renormalization group equation, with $n_f = 5$.

which decreases with increasing μ for $n_f \leq 16$. This behavior is opposite to the analogous running of the electromagnetic coupling which increases with increasing μ. This trend reflects two important properties of QCD: asymptotic freedom[28–30] and confinement[34, 35]. Asymptotic freedom occurs at large energy scales (short distances), where the strong coupling is small, and partons behave as quasi-free objects whose interactions can be computed perturbatively. Confinement occurs at small energy scales (large distances), where the strong coupling is large and induces confining forces that bind partons into colorless hadrons and forbids the existence of free quarks or gluons. It is customary to denote the scale that characterizes the onset of confinement as

$$\Lambda = \mu_0^2 \exp\left[\frac{-1}{\beta_0 \alpha_S(\mu_0)}\right] .$$

Calculating QCD observables in perturbation theory presents several obstacles that are not present in corresponding electroweak calculations. A fundamental issue is the relationship between the parton production that a calculation describes and the production of hadrons that an experiment can detect. Although the QCD Lagrangian does in principle define this relationship, it is not known how to generate quantitative predictions on this basis, and phenomenological models must be used instead. Another fundamental problem is that a fixed order perturbative calculation depends on the renormalization scale, μ. It is intuitively reasonable that μ should be chosen on the basis of the natural energy scales of a problem, and indeed this effectively includes a class of corrections at all orders. The arbitrariness in the details of this choice, however, can lead to sizable numerical uncertainties. A significant technical obstacle is the rapid proliferation of diagrams at each order due to the gluon self-coupling, which currently limits most calculations to second order. This is further aggravated by the large size of the strong coupling at presently accessible energy scales, which limits the precision of low-order calculations and our ability to test the theory.

2.2.1 Hadronic Z Decays

I now consider the production of hadrons in electron-positron collisions near $\sqrt{s} = m_{\mathrm{Z}}$, for which the dominant process is s-channel Z exchange with subsequent Z decay into a quark-antiquark pair. The calculation of QCD observables in $\mathrm{e}^+\mathrm{e}^-$ collisions is easier than for collisions involving initial-state hadrons since the perturbative hard-scattering sub-system is well-defined. An advantage of large center-of-mass energies, $\sqrt{s} \simeq m_{\mathrm{Z}}$, is that individual events are characterized by narrow *jets* of hadrons that can be identified with the partons of the hard-scattering final state.

Figure 2.9 shows a schematic view of a hadronic Z decay and its conventional decomposition into phases. Although the transitions between these phases are continuous and thus must be chosen arbitrarily, this scheme offers a useful framework for integrating the different methods of calculation available. The first phase, Figure 2.9(a), is the production of a primary quark-antiquark pair, viewed as an essentially electroweak phenomenon; the second phase, Figure 2.9(b), covers the evolution of the primary $q\overline{q}$ pair under perturbative QCD, and is dominated by gluon radiation; the third phase, Figure 2.9(c), represents the transition from partons to hadrons; and the final phase, Figure 2.9(d), consists of the decay chains of unstable hadrons. Although all phases are in principle described by the Standard Model, only phenomenological models are presently able to treat the last two phases.

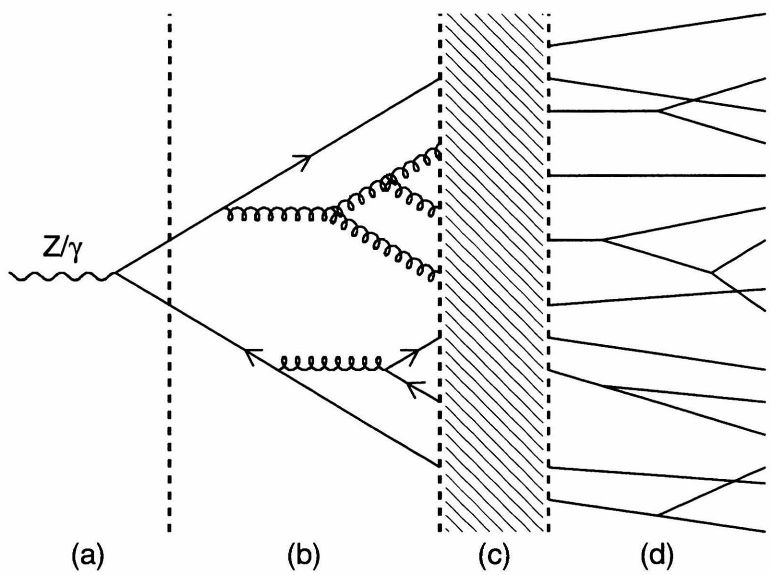

Figure 2.9: Schematic view of a hadronic Z decay, decomposed into phases: (a) represents the electroweak production of a quark-antiquark pair, (b) represents the perturbative QCD evolution, (c) represents the transition from partons to hadrons, and (d) represents the decays of unstable hadrons.

The are several types of observables relevant to hadronic Z decays. The first class contains fully inclusive observables that place no restrictions on the final state, and thus allow an unambiguous interpretation of the partonic calculation since all partons must produce hadrons. Observables in this class are related to the total hadronic cross section, for which QCD corrections can be calculated at the same level of precision as electroweak corrections, but which are not sensitive tests of QCD due to the small size (few percent) of QCD corrections.

Non-inclusive observables describe the distribution of hadrons in the final state, and can be classified as essentially perturbative or non-perturbative. In the first case, a perturbative calculation using partons is used, and the non-perturbative phases (Figure 2.9(c,d)) are expected to introduce only small corrections. This requires that the perturbative observable can be consistently evaluated for both hadrons and partons, and that it reflects features of the hadronic distribution that are present in the underlying parton distribution. Examples of perturbative observables are jet differential cross sections and event-shape variables. In the second case, non-perturbative effects do not represent small corrections and must be explicitly taken into account. Examples of non-perturbative observables are the number of hadrons in the final state and the correlations between identical hadrons.

Diagrams for Z decay into quarks and gluons up to $\mathcal{O}(\alpha_S)$ are shown in Figure 2.10 and correspond to the perturbative expansions

$$\begin{aligned}
\frac{\partial\sigma}{\partial\Phi_2} &\propto \left|\mathcal{M}_0 + \alpha_S\mathcal{M}_2 + \mathcal{O}(\alpha_S^2)\right|^2 \\
&= \left|\mathcal{M}_0\right|^2 + \alpha_S\left(\mathcal{M}_0\overline{\mathcal{M}}_2 + \overline{\mathcal{M}}_0\mathcal{M}_2\right) + \mathcal{O}(\alpha_S^2) \\
\frac{\partial\sigma}{\partial\Phi_3} &\propto \left|\alpha_S^{1/2}\mathcal{M}_1 + \mathcal{O}(\alpha_S^{3/2})\right|^2 \\
&= \alpha_S\left|\mathcal{M}_1\right|^2 + \mathcal{O}(\alpha_S^2) \\
\frac{\partial\sigma}{\partial\Phi_k} &= \mathcal{O}(\alpha_S^2) \qquad k \geq 4 \,,
\end{aligned}$$

where Φ_n parameterizes n-particle phase space, and quarks and gluons are considered to be experimentally indistinguishable. After renormalization of the ultraviolet divergences associated with loops, the total cross sections for different partonic final states

$$\sigma_n \equiv \int d\Phi_n \frac{\partial\sigma}{\partial\Phi_n} = \sum_{k=n-2} \alpha_S^k \sigma_n^{(k)}$$

are still individually divergent. These remaining *infrared* singularities are associated with real or virtual emission of soft and collinear gluons, but cancel at each order k, so that the sum

$$\sum_{n=2}^{k+2} \sigma_n^{(k)}$$

is finite. Infrared divergences are due to the masslessness of the gluon, and also occur for photons in the electroweak sector. A sufficiently inclusive observable that does not upset this cancelation of soft and collinear divergences at each order is known as *infrared safe*. This is equivalent to the condition that the observable does not distinguish between an isolated quark and a quark accompanied by vanishingly soft and collinear gluons.

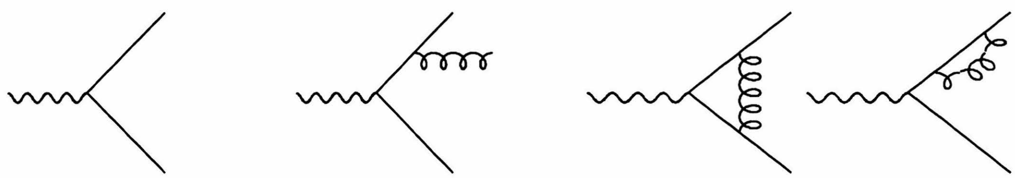

(a) $\mathcal{M}_0$ (b) $\mathcal{M}_1$ (c) $\mathcal{M}_2$

Figure 2.10: Feynman diagrams for hadronic Z decay giving contributions up to $\mathcal{O}(\alpha_S)$. Diagrams (a) and (c) have the final state $q\bar{q}$ and are zeroth and second order respectively. Diagram (b) has the final state $q\bar{q}g$ and is first order.

Chapter 3

The L3 Detector at LEP

The work described in this thesis is based on e^+e^- collisions recorded by the L3 detector at LEP. The L3 detector was designed and constructed by an international collaboration, that presently includes 452 physicists from 43 institutes. In this chapter I describe the LEP collider facility, the components of the L3 detector, the trigger and data-acquisition systems, and the L3 measurement of luminosity.

3.1 The Large Electron-Positron Facility

The Large Electron-Positron facility (LEP) is operated by the European Center for Particle Physics (CERN) located near Geneva, Switzerland (see Figure 3.1). LEP is an e^+e^- accelerator and storage ring with four interaction points, which are instrumented by the ALEPH[36], DELPHI[37], L3[38] and OPAL[39] detectors. Since its commissioning in 1989, LEP has operated with beam energies near 46 GeV, exploiting the large event rate at the Z resonance; by the end of 1996 LEP will enter a new phase, *LEP II*, with beam energies from 83 GeV to about 95 GeV, above the threshold for W^+W^- pair production.

Figure 3.2 shows the stages of the LEP injection system. Electrons from a filament are accelerated to 200 MeV in a linear accelerator (LINAC) and directed at a tungsten target to produce positrons. These positrons together with electrons from a second filament are accelerated to 600 MeV by a second LINAC and then injected into the electron-positron accumulator (EPA), which condenses the beams into compact

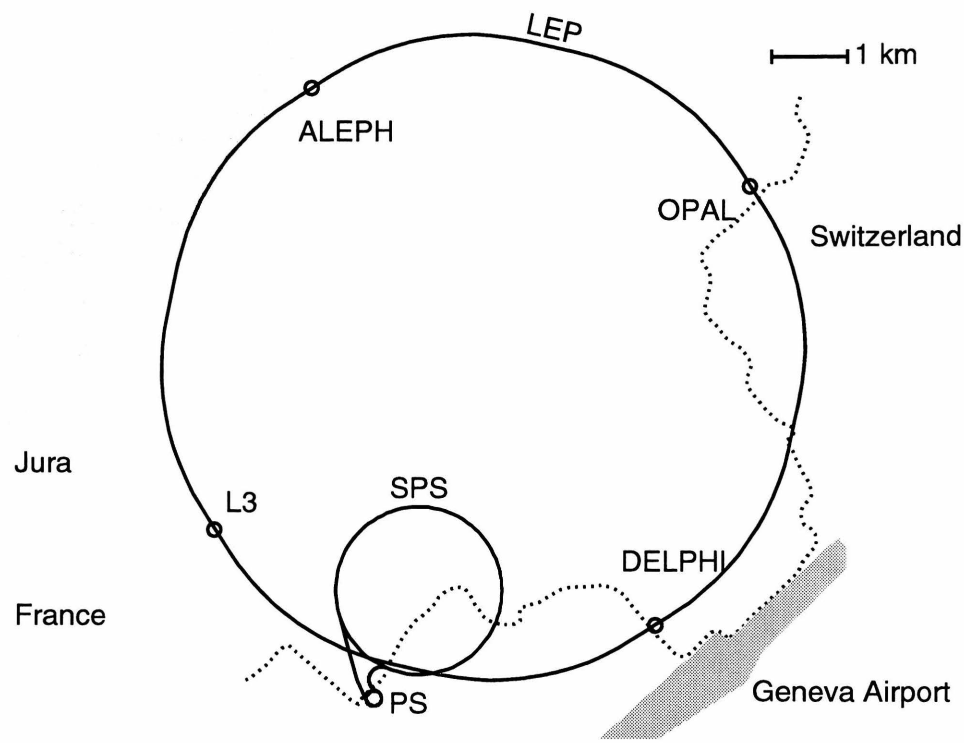

Figure 3.1: Map of the region near Geneva, Switzerland, showing the location of LEP, and the PS and SPS stages of the LEP injection system.

bunches through synchrotron radiation damping. The bunches are accelerated in the converted proton synchrotron (PS) and super proton synchrotron (SPS) to 3.5 and then 20 GeV respectively, after which they are ready for injection into the main LEP ring. The maximum current that can be injected into LEP is presently limited to $\simeq$ 0.8 mA per bunch, by instabilities generated from the coupling between the transverse modes of the two beams[40].

After injection at 20 GeV, LEP accelerates the electron and positron beams to 46 GeV and then operates as a storage ring with collisions at the four interaction points. LEP has a total length of 27 km and is divided into eight curved and eight straight sectors. Each curved sector consists of a lattice of focusing and bending magnets that maintain the bunches in precise orbits during acceleration and storage. Energy for

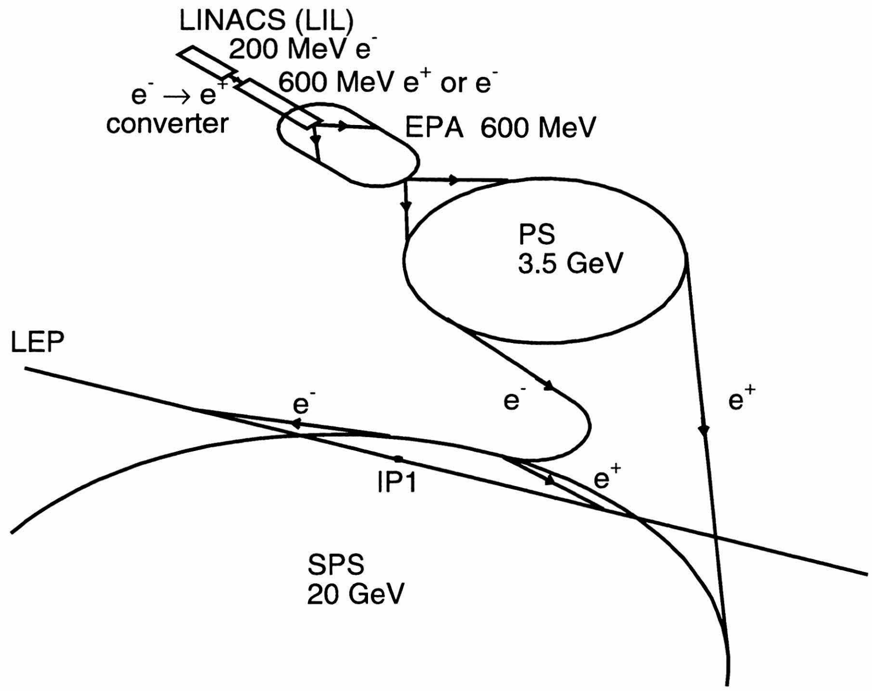

Figure 3.2: Schematic diagram showing the layout of the LEP injection system. The final PS and SPS stages are also used simultaneously for acceleration of protons, anti-protons, and heavy-ions.

acceleration and for compensation of the losses due to synchrotron radiation (about 120 MeV per turn) is provided by 120 copper cavities, excited at radio frequencies and distributed in two of the straight sectors. The higher energies of LEP II will require 176 (240) additional superconducting cavities to reach energies of 90 GeV (95 GeV) per beam. Some of these cavities are already installed and are being used during 1995. The maximum current that can be stored during collisions in LEP is presently limited to $\simeq 0.35$ mA per bunch by beam-beam interactions, which cause the transverse area of the beam to increase in proportion with the bunch current, eventually interfering with the physical aperture[40].

The rate of collisions at the interaction points is proportional to the LEP *lumi-*

nosity

$$L = \frac{kI^2 f}{4\pi e^2 \sigma_x \sigma_y} ,$$

where k is the number of bunches per beam, I is the current per bunch, $f \simeq 11.4$ kHz is the rotation frequency, and σ_x, σ_y are the transverse beam sizes. In practice, the most effective way to increase the luminosity is to increase the number of bunches. Between 1989 and 1991, LEP operated with 4 bunches per beam. Between 1992 and 1994, the optics were upgraded to use a *Pretzel scheme*[41], in which there are 8 bunches per beam, a lower bunch current, and an overall increase of 50% in the average luminosity[40]. During 1995, LEP has been commissioning a further upgrade to *bunch trains*[42] which will eventually provide the higher luminosity required at LEP II. This new scheme is similar to the original four-bunch scheme, but with each bunch now replaced by three *bunchlets* closely spaced over about 750 nanoseconds. The current highest luminosity achieved this year is just over 2.0×10^{31} s^{-1} cm^{-2}.

Figure 3.3 shows the integrated luminosity recorded for physics at the L3 interaction point during each year between 1991 and 1994, as well as during the first part of 1995 (until the end of August). The luminosity recorded by L3 is about 80% of the luminosity delivered by LEP with the remaining 20% being lost due to occasional high-background conditions, data-acquisition dead time, and problems with individual detector and readout components. The improvement in luminosity achieved using bunch trains is not yet reflected in the integrated luminosity for 1995 because of problems with the radio-frequency and injector systems that are currently under investigation.

The most important LEP operating parameter for physics studies is the beam energy. The most precise absolute energy calibration of LEP involves applying a periodic radial perturbation to transversely polarized beams, by sweeping the frequency of the acceleration cavities, and determining the perturbation frequency that causes the largest depolarization[43]. This method fixes the beam energy to better than 1 MeV, but it is time consuming and cannot be done during collisions and thus is

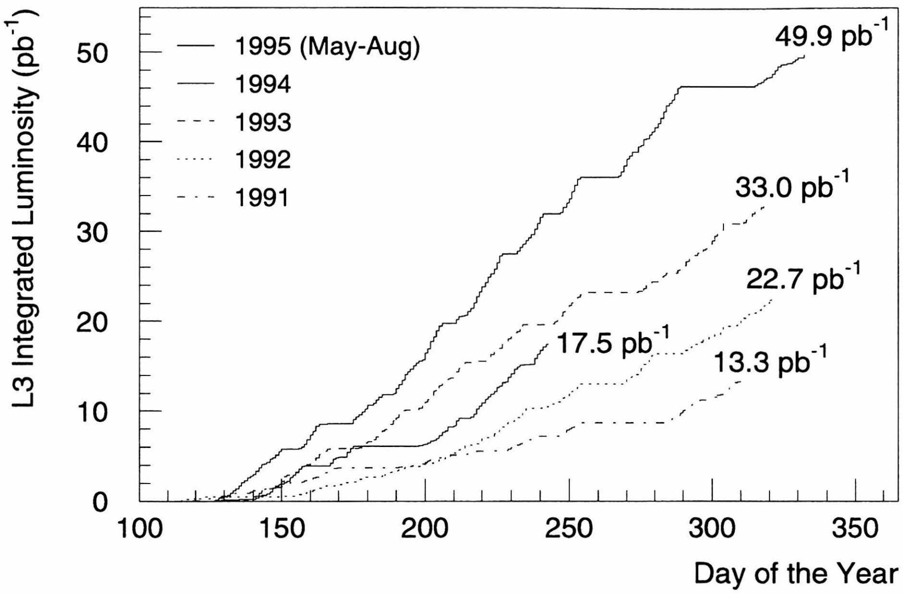

Figure 3.3: Luminosity available for physics at the L3 interaction point, integrated over each of the years 1991–95, as a function of the day of the year (1–365). Note that LEP running during each year typically starts at the beginning of May and continues until the middle of November. The luminosity shown for 1995 is for the first part of the year, between May and August.

only performed every 1–2 weeks. Between these resonant depolarization calibrations, the beam energy drifts by $\simeq$ 1.5 MeV/hour due to tidal deformations of LEP that are predictable and now routinely corrected for[44], and by $\simeq$ 1 MeV/hour by other effects that are not presently understood[1]. Occasional jumps of $\simeq$ 20 MeV have also been observed and are being investigated.

[1]Recently a correlation between these non-tidal drifts and the level of the local water table has been established, which could be corrected for in the future.

3.2 The L3 Detector

L3 is one of four detectors recording data from electron-positron collisions at LEP. The L3 design emphasizes precise measurements of photons, electrons, and muons; and is complementary to the other experiments which have more extensive inner tracking at the expense of less precise calorimetry and muon spectroscopy. Figure 3.4 shows a perspective cut-away view of the detector, which is 14 m long and 16 m wide. Subdetectors are arranged in layers of increasing size surrounding the interaction point; all inner detectors are contained in a long tube (see Figure 3.5), which in turn supports the outer muon detectors and maintains the overall alignment of the detector. The entire detector is surrounded by a 0.5 T solenoidal magnet. In 1994, additional 1.5 T toroidal magnets were added to the main magnet doors.

The L3 coordinate system, which is used throughout this thesis, has its origin at the nominal interaction point; its z axis is aligned with LEP beam in L3, with positive values in the direction of the electron beam; its x axis is in the horizontal plane, with positive values towards the center of LEP; and its y axis is in the vertical plane, with positive values in the upwards direction (see axes in Figure 3.4). Polar angles in the L3 coordinate system are measured from the positive z axis ($\theta = 0°$) and take values in the range $0° \leq \theta \leq 180°$. Azimuthal angles are measured in the $x - y$ plane, from the positive x axis ($\phi = 0°$) towards the positive y axis ($\phi = 90°$), and take values in the range $0° \leq \phi \leq 360°$.

The L3 detector relies primarily on two complementary methods of particle detection: tracking and calorimetry. Tracking detectors locate points along the trajectories of charged particles, which are curved in the L3 magnetic field and thus provide information on particle charge and momentum. Calorimeters measure energy deposits in a segmented absorbing medium, and thus provide information on the energy of both charged and neutral particles and allow identification of different types of particle with characteristic patterns of energy deposits. In this section I briefly describe

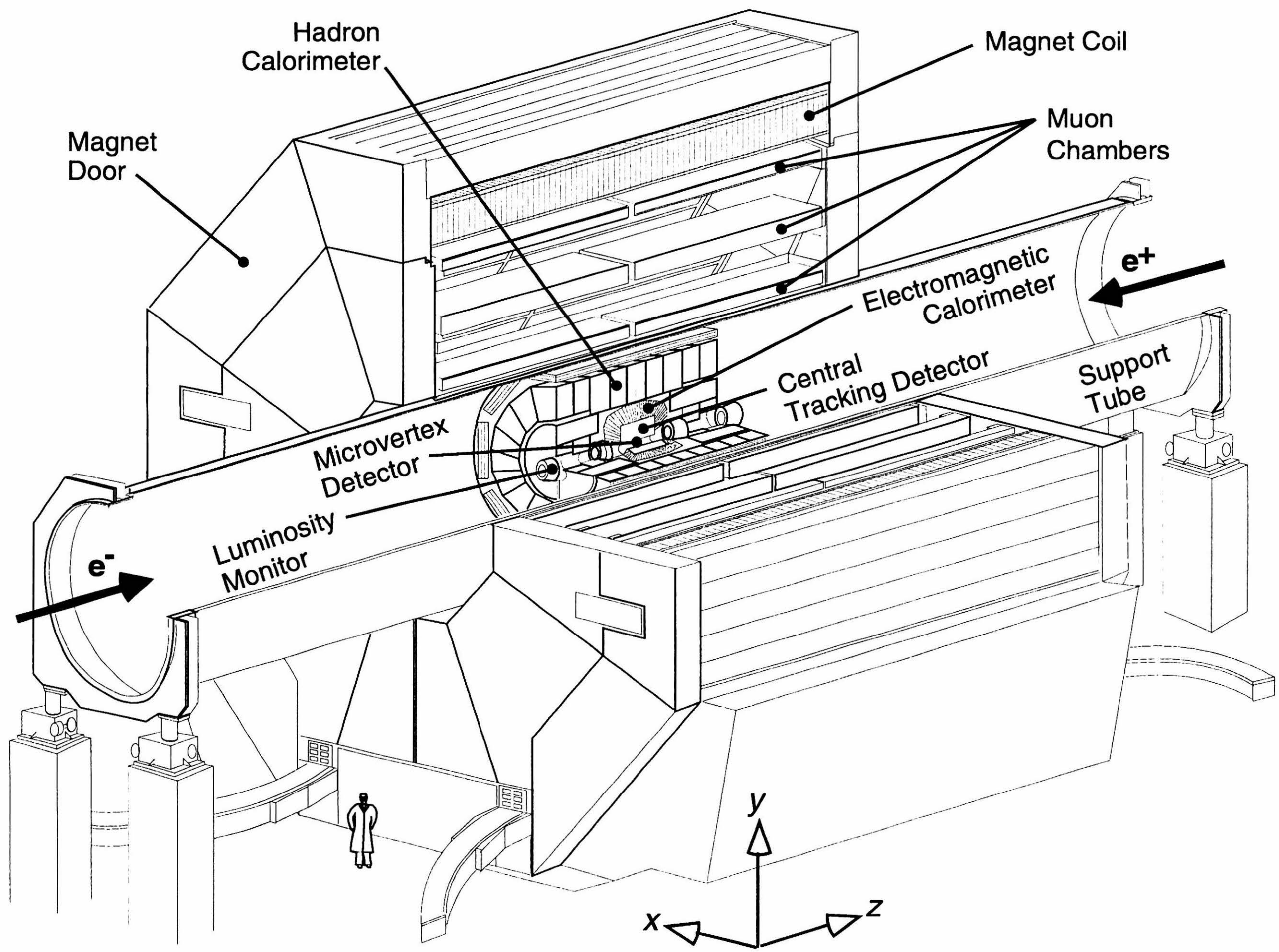

Figure 3.4: Perspective cut-away view of the L3 detector, showing the location of the subdetectors, the support tube, and the magnet. The L3 coordinate system is represented by the axes in the bottom center.

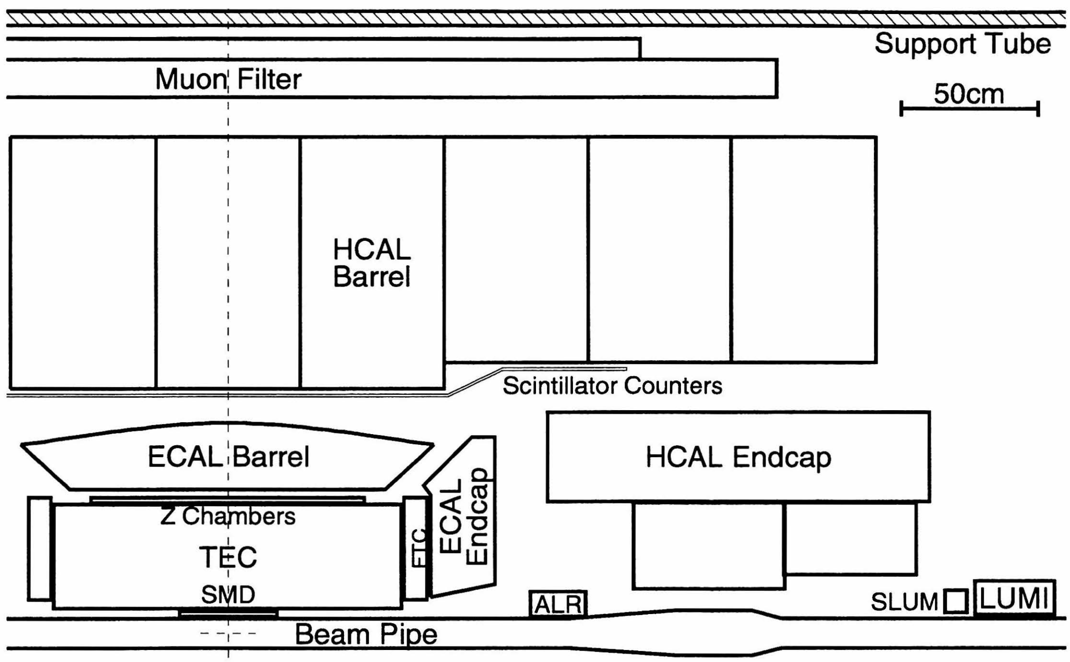

Figure 3.5: Inner detectors of L3 viewed in the y-z plane. The interaction point is near the bottom left corner. Detectors are symmetric with respect to reflection in the x and y axes, and rotation about the z axis. The flare shown in the LEP beampipe exists only on the $+z$ side.

the sensitive components of the L3 detector during 1994, in order of distance from the interaction point. In the next chapter I describe in more detail the electromagnetic calorimeter, which is the subdetector that is used most extensively for the work described in this thesis.

3.2.1 Microvertex Detector

The innermost L3 component is the silicon microvertex detector (SMD), located just outside the LEP beampipe (the original radius of the beampipe in L3 was 9 cm; in 1991, a smaller beampipe of radius 5.3 cm was installed, making room for the SMD). The SMD is 35.5 cm long and consists of two radial layers of double-sided silicon-strip detectors arranged into ladders at 6 cm and 8 cm from the z axis, and covering the polar angles 22°–158° [45] (see Figure 3.6). The outer silicon surface of each ladder is read out at 50 μm intervals for x-y coordinate measurements with a nominal intrinsic resolution of 5 μm, and the inner surface is readout at 150 μm (central region) or 200 μm (forward regions) intervals for z coordinate measurements with a nominal intrinsic resolution of 10 μm. The design resolutions for reconstructed track parameters are 0.3 mrad in ϕ, and 1 mrad in θ. The SMD was installed in L3 at the beginning of 1993, but was not fully exploited for physics analysis during this year due to initial technical problems. The SMD has been fully functional since 1994, but is not used for the work described here.

3.2.2 Central Tracking Detector

Outside the SMD is the central tracking detector, consisting of a time-expansion chamber (TEC) surrounded by z-chambers and forward-tracking chambers (FTCs) (see Figure 3.5). This detector is used to reconstruct charged particle trajectories in the central region of L3, to provide measurements of particle charge and momentum, and to reconstruct secondary vertices from decays in flight.

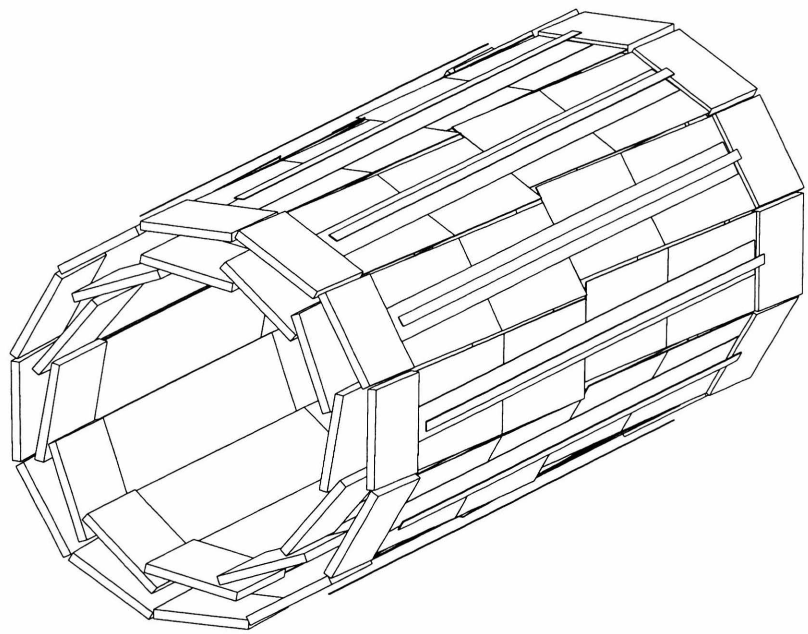

Figure 3.6: Perspective view of the L3 silicon microvertex detector, showing the arrangement of the 11 inner and 13 outer ladders into layers.

3.2.2.1 Time-Expansion Chamber

The time-expansion chamber (TEC) occupies the volume between 8.5 cm $< r <$ 47 cm and $|z| <$ 63 cm, and detects ionization produced by the passage of charged particles through a gas mixture consisting of 80% CO_2 and 20% iso-C_4H_{10} at 1.2 bar. Radial field-shaping cathode wire planes divide the TEC volume into 12 inner and 24 outer sectors, each of which is subdivided by a radial plane of mixed anode sense wires and additional cathode wires (see Figure 3.7). Planes of closely-spaced grid wires on either side of each anode plane establish a homogeneous low electric field in most of the sector, with a small high-field region near the anode plane. Secondary ionization particles produced along a charged track drift slowly ($\simeq 6\mu$m/ns) in the low-field region towards the high-field region, where they produce further ionization particles in an avalanche that amplifies the original ionization signal (this is the *time* *expansion principle*). The timing of the ionization signal measured at each anode determines the distance to the track along a line perpendicular to the anode plane, with an average resolution $\simeq$ 50 μm (the ambiguity between a track that is to the left or the right of the anode plane is resolved by matching between inner and outer sectors, and by pickup wires within the outer sector grid planes).

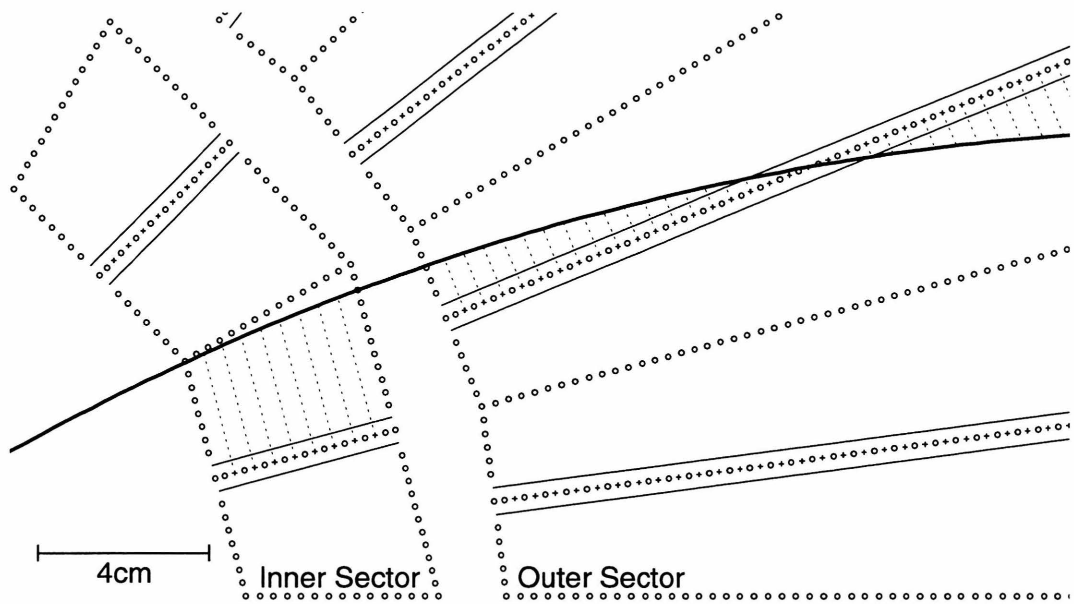

Figure 3.7: Diagram of several TEC drift cells viewed in the x-y plane. Field-shaping cathode wires are shown as hollow circles, anode sense wires are shown as crosses, and grid wire planes are shown as thin solid lines. Dashed lines show the drift of ionization produced along a charged particle trajectory (heavy solid line).

Inner sectors have 8 anodes and outer sectors have 54 anodes, providing a maximum of 62 coordinate measurements in the $x - y$ plane, between 10.5 cm $< r <$ 31.7 cm. Fitting a circular arc to these coordinates measured along a particle's trajectory determines its transverse momentum, p_T, with a resolution of $\sigma(1/p_T) = 0.018/\text{GeV}$. Two anodes in each inner sector and 9 anodes in each outer sector are read out at both ends (*charge division mode*) and provide additional information on the z coordinate of a track with a resolution of $\simeq$ 2 cm.

3.2.2.2 Z Chambers

Two layers of chambers surrounding the cylindrical outer surface of the TEC are used for precise measurements of track z coordinates. The z chambers occupy the volume between 96 cm $< r <$ 98 cm and $|z| <$ 51 cm, and cover the polar angles $45° < \theta < 135°$. Each chamber is filled with a gas mixture of 20% CO_2 and 80% argon and operates in *drift mode*. Ionization signals are read out from cathode strips aligned at 0°, 90°, and ±70.1° with respect to the z axis; which combine to locate the z coordinate of an isolated track with a resolution of 320 μm.

3.2.2.3 Forward Tracking Chambers

Two layers of forward tracking chambers (FTCs) cover the end of the TEC and measure precise track $x - y$ coordinates at fixed $|z|$. The FTCs cover the polar angles $9.5° < \theta(180° - \theta) < 37.5°$. Each chamber is filled with a gas mixture of 38.5% ethane and 61.5% argon and operates in drift mode. Ionization signals are read out from anode wires aligned at 5° and 95° with respect to the x axis, which combine to locate the x and y coordinates of an isolated track with a average resolution of 150 μm. The FTCs were installed at the beginning of 1991.

3.2.3 Electromagnetic Calorimeter

The electromagnetic calorimeter (ECAL) consists of a barrel and two endcaps composed of bismuth germanate crystals, which enclose the outer surfaces of the central tracking detector (see Figure 3.5). The analysis described in this thesis uses primarily this subdetector, and thus it is described in detail in Chapter 4. Here I describe the related subsystems: the active lead rings and the electromagnetic calorimeter gap filler.

3.2.3.1 Active Lead Ring

The active lead ring (ALR) covers the forward angular regions $4.5° < \theta, 180° - \theta < 8.8°$, between the coverage of the ECAL endcaps and the luminosity monitors. The ALR is located at 108.0 cm $< |z| <$ 118.4 cm, just behind the ECAL endcaps (see Figure 3.5). The ALR consists of 3 layers of 18.5 mm thick lead followed by 10 mm thick plastic scintillator. Each layer of scintillator is divided into 16 azimuthal segments which are individually read out by photo-diodes, and successive layers are rotated by one third of a segment. The ALR determines the ϕ coordinate of isolated particles with a resolution of $\simeq 1.3°$. The ALR was installed at the beginning of 1993, replacing a passive lead ring in the same position that was used to protect the central tracking detector from LEP radiation. At the beginning of 1995, the ALR was upgraded to also measure polar angles and thus improve its ability to trigger events due to two-photon processes.

3.2.3.2 Gap Filler

There is presently a gap of 7.4 cm between the ECAL barrel and endcaps, due to the space requirements of the central tracking detector for the end flanges and readout. At the end of 1995, this gap will be instrumented with blocks of lead threaded with plastic scintillating fibers, resulting in improved total energy resolution and hermeticity which will enhance the detector's sensitivity to supersymmetric physics.

3.2.4 Scintillation Counters

The scintillation counters line the narrow gap between the electromagnetic and hadronic calorimeters (see Figure 3.5), and are designed for precise measurement of the relative timing of particles traversing the detector. The primary purpose of the scintillation counters is to discriminate between cosmic ray muons that pass near the L3 origin, causing scintillation signals $\simeq 5.3$ ns apart, and di-muon events originating from the L3 origin, causing nearly coincident scintillation signals.

The scintillation counters are arranged in a cylindrical barrel of 30 strips 290 cm long, and covers 98% of 360° in ϕ. Each strip is a 1 cm thick plastic scintillator, read out at both ends by an adiabatic light guide coupled to a photomultiplier tube. The relative timing resolution of the scintillators is better than 1 ns. At the beginning of 1995, two endcap disks of 16 scintillator sectors were added at $|z| = 103$ cm, to match the new forward-backward muon chambers.

3.2.5 Hadron Calorimeter

The hadron calorimeter (HCAL) surrounds the ECAL, and is designed to measure the energy of hadrons, which typically deposit only a fraction of their energy in the ECAL. Particles traversing the HCAL gradually lose their energy through nuclear interactions with layers of depleted uranium and brass absorber, initiating showers of low energy particles that are detected in layers of proportional wire chambers interspersed with the absorber. The HCAL consists of a barrel covering $35° < \theta < 145°$ and two endcaps that extend the coverage to $5.5° < \theta < 174.5°$ (see Figure 3.5).

The HCAL barrel is divided into 16 modules in ϕ and 9 modules in z (see Figure 3.5). Each module consists of radially stacked alternating layers of 5 mm thick depleted uranium absorber, and 5.6 mm thick brass wire chambers. Wire chambers are filled with a gas mixture of 20% CO_2 and 80% argon and operate in *proportional mode.* Successive chambers are aligned with wires perpendicular to each other; wires are grouped for readout into projective towers with $\Delta\phi \simeq 2.5°$, $\Delta z \simeq 6$ cm, $\Delta r \simeq 8$ cm. A particle originating from the interaction point traverses 3.5–5.5 nuclear interaction lengths in passing through the HCAL barrel.

The HCAL endcaps are each divided into 6 modules making up 3 rings (see Figure 3.5). Each module has a similar construction to a barrel module, except that layers lie in the $x-y$ plane, and successive wire chambers have wires aligned at 22.5°. Endcap wire chambers are grouped for readout into projective towers with $\Delta\phi \simeq 22.5°$ and

$\Delta\theta \simeq 1°$. A particle originating from the interaction point traverses 6–7 nuclear interaction lengths in passing through the HCAL endcaps.

3.2.5.1 Muon Filter

The muon filter surrounds the cylindrical outer surface of the HCAL barrel, and fills the remaining space inside the support tube (see Figure 3.5). The muon filter is designed to ensure that hadrons are completely absorbed inside the support tube, so that only muons and neutrinos pass through to the muon chambers (in addition to a very small rate of hadronic punch through). The muon filter is divided into 8 segments, and operates on a similar principle to the HCAL. Each octant is 139 cm in length, and consists of 6 layers of 1 cm thick brass absorber, interleaved with 5 layers of wire chambers, and followed by 5 layers of 1.5 cm thick brass absorber fitted to the curved contour of the inside of the support tube. All chambers have wires aligned with the z axis, and 3 layers of each octant are read out in charge-division mode with a resulting z coordinate resolution of 3–5 cm. The muon filter thickness corresponds to 1.03 nuclear interaction lengths; the support tube material contributes an additional 0.52 nuclear interaction lengths.

3.2.6 Muon Chambers

The central muon chambers occupy the space between the support tube and the magnet, and are designed for precise tracking of high-momentum muons. The radius of curvature in the $x-y$ plane of a 45 GeV muon trajectory at $\theta = 90°$ is $\simeq 300$ m, so a large lever arm is required for good momentum resolution. The central chambers are arranged in octants of 3 layers each, located just outside the support tube (MI), just inside the magnet (MO), and half-way between these positions (MM) (see Figure 3.4). The remaining volume between the support tube and the magnet is filled with air and is not instrumented.

Each octant layer consists of precisely-located "P" drift chambers (2 each in MO,MM layers; 1 each in MI layers) for measuring track coordinates in the $x - y$ plane, and Z drift chambers (4 each in MO layers, 2 each in MI layers) for measuring track z coordinates. P (Z) chambers are filled with a gas mixture of 38.5% (8.5%) ethane and 61.5% (91.5%) argon and operate in drift mode with an average drift velocity of 50μm/ns (30μm/ns). The MI and MO P-chambers measure coordinates along a track with 16 anode sense wires each; MM P-chambers measure with 24 anode sense wires each. Each P-chamber sense wire measures an $x - y$ coordinate with a resolution of 110–250 μm, depending on the distance to the anode plane. The internal alignment between planes of an octant is maintained to within 30 μm by a sophisticated opto-mechanical system, resulting in a combined octant resolution for track sagitta measurements of better than 30 μm, equivalent to a transverse momentum resolution of $\sigma(p_T)/p_T \simeq 2\%$. Z chambers are arranged in double layers above and below each MO and MI P chamber. Z chambers in each double layer are offset by half a drift cell, and each measure a track z coordinate at a single anode sense wire, with a resolution of $\simeq 500$ μm.

3.2.6.1 Forward-Backward Chambers

The central muon chambers measure track coordinates in all 3 layers over the region $43° < \theta < 137°$. The forward-backward chambers are designed to extend this coverage to $22° < \theta < 158°$, with 3 additional layers mounted on the magnet doors on either side of the interaction point (see Figure 3.8). Each layer consists of 16 non-overlapping chambers filled with a P chamber gas mixture, and instrumented with 4 anode sense wires per cell with an average resolution of 200 μm. Momentum determination in the region $36° < \theta < 43°$ is based on the measurement of curvature in the solenoidal field, using the two inner central chambers and the inner forward-backward chamber, and has a resolution $\sigma(p_T)/p_T$ that degrades with θ from 2–20%. In the region $22° < \theta < 36°$, momentum is determined from the curvature in the toroidal magnet door field, using the 3 layers of forward-backward chambers. The momentum resolution in this region is limited by multiple scattering in the 1 m thick magnet doors to $\sigma(p_T) \simeq 20\%$, for $p < 100$ GeV. In 1994, half of the forward-backward chambers were installed, covering $z < 0$, $x < 0$ and $z > 0$, $x > 0$. The remaining chambers were installed at the end of 1994 and the completed system has been fully operational since the beginning of 1995.

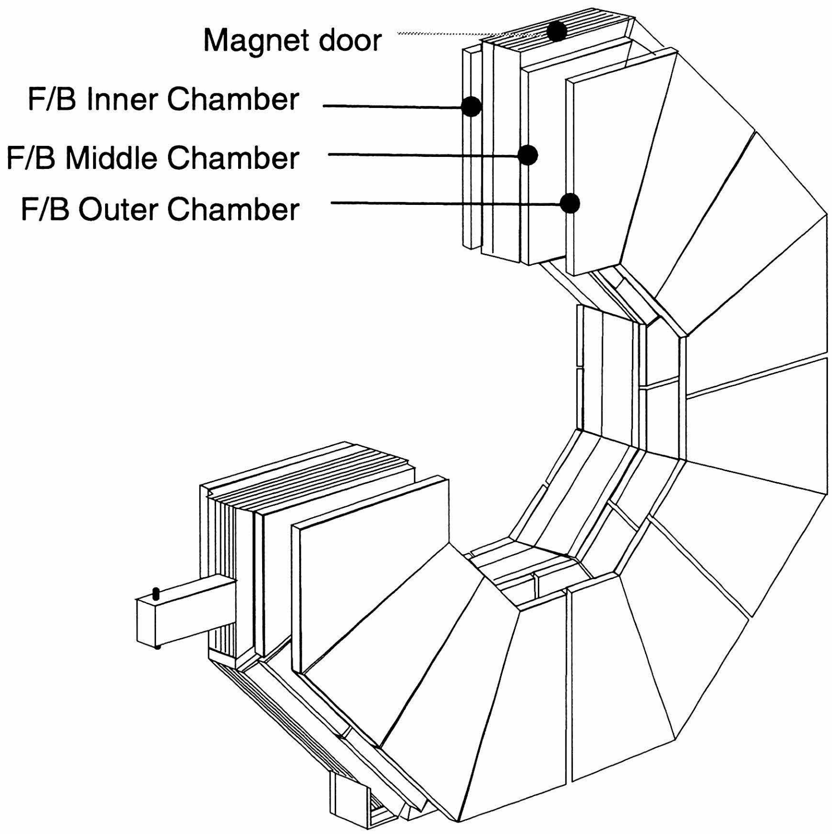

Figure 3.8: Cutaway perspective view of a magnet door, showing the position of the forward-backward muon chambers.

3.2.7 Luminosity Monitors

The luminosity monitors (LUMIs) are located close the the LEP beampipe, 265–280 cm on either side of the interaction point (see Figure 3.5). The LUMIs are designed to detect electrons from small-angle $e^+e^- \rightarrow e^+e^-(\gamma)$ (*Bhabha*) scattering, which is strongly peaked and relatively free of background in the forward and backward regions, and provides the benchmark process for determining the luminosity at L3 (see Section 3.3).

The LUMIs consist of tracking and calorimeter subsystems, covering the regions 31–62 mrad from the z axis on either side of the interaction point. LUMI tracking is presently provided by silicon detectors (SLUM) covering 6.8 cm $< r <$ 15.4 cm which were installed in 1993, replacing the original wire chambers used from 1989–91 (see Figure 3.9). Each SLUM consists of 3 layers of 16 partially overlapping wafers, for a total of 4096 readout strips. Two layers measure r coordinates with strips 0.5–1.875 mm wide, and 1 layer measures ϕ coordinates with strips 0.375° wide. Each LUMI calorimeter consists of 304 BGO crystals grouped into 8 rings aligned with the z axis, and arranged in a cylinder between 6.8 cm $< r <$ 18 cm. The crystals are 26 cm long, 1.5 cm thick in the radial direction, and 1.5–3 cm thick in the azimuthal direction.

Since the electrons and positrons measured by the LUMIs are produced at very small polar angles, they traverse a large amount of material as they leave the LEP beampipe, and can be absorbed or deflected. During the installation of the SLUM in 1993, a modification to the LEP beampipe on the $+z$ side was performed that reduces the amount of material in the central acceptance of the LUMI (see Figure 3.5); the same modification could not be performed on the $-z$ side since it would interfere with access to the SMD.

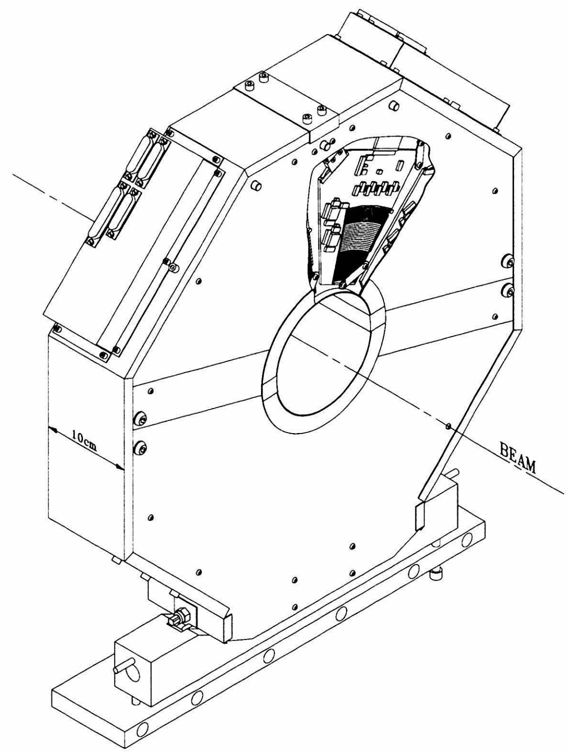

Figure 3.9: Perspective view of the luminosity monitor silicon tracking detector, with a cutout showing a silicon wafer.

3.2.8 Trigger and Data Acquisition

The rate of bunch-bunch crossings at L3 (with 8 bunches in each beam) is 91 kHz, however most crossings do not result in a hard e^+e^- collision. Since the readout and storage technology limits the rate at which the detector can be fully read out to about 10 Hz, a trigger is required to select those bunch-bunch crossings that should be recorded. Backgrounds to genuine hard e^+e^- collisions include scattering of a bunch particle from a molecule of residual gas in the beampipe, cosmic rays, and electronic noise. The data-acquisition system is designed to collect together and store the data from different subdetectors as a single event, when a trigger is generated. The combined trigger and data-acquisition systems (see Figure 3.10) use sufficient parallelism and buffering to ensure that events are only missed during the time required for a full detector digitization of a previously triggered event ($\simeq 500\mu$s), leading to a dead time of a few percent.

3.2.8.1 First-Level Trigger

The trigger is implemented in 3 layers of increasing complexity (see Figure 3.10). The first-level trigger is divided into independent triggers for the TEC[46], calorimeters[47], muon chambers, scintillators, and luminosity monitor, each of which must make a decision to accept or reject an event within the 11 μs before the next bunch-bunch crossing. The combined rate of first-level triggers varies between 5–15 Hz; TEC and luminosity trigger rates are correlated with the instantaneous luminosity, calorimeter and muon chamber trigger rates are dominated by electronic noise levels, and scintillator trigger rates reflect cosmic ray fluxes. Values in parentheses below are typical for the beginning of a LEP fill, when the luminosity is highest.

The TEC trigger ($\simeq$ 5.5 Hz) samples the outer 14 sense wires of each sector, with a coarse 2-bit digitization of drift time resulting in a 96 (ϕ) $\times$ 14 (r) bit pattern which is compared against stored patterns corresponding to realistic track configurations. The calorimetric triggers ($\simeq$ 3.0 Hz) are based on 896 coarse-granularity analog sum signals digitized at 10-bit precision, dividing the ECAL into 32 (ϕ) $\times$ 16 (θ) segments and the HCAL into front and back layers with 16 (ϕ) $\times$ 11/13 (θ) segments. Calorimeter triggers are generated for total energies above preset thresholds, and for localized clusters of large energy deposits. The muon chamber trigger ($\simeq$ 1.0 Hz) records 1-bit hits for adjacent pairs of P and Z chamber sense wires, and identifies drift cells with genuine track segments by comparing the number of hits in each cell with a preset threshold. Triggers are generated for patterns of cells with track segments that correspond to realistic configurations for 1 or 2 muons originating from the interaction point. The scintillator ($\simeq$ 0.5 Hz) trigger records one bit for a signal above a preset threshold within 30 ns of the bunch-bunch crossing time, for each of the 30

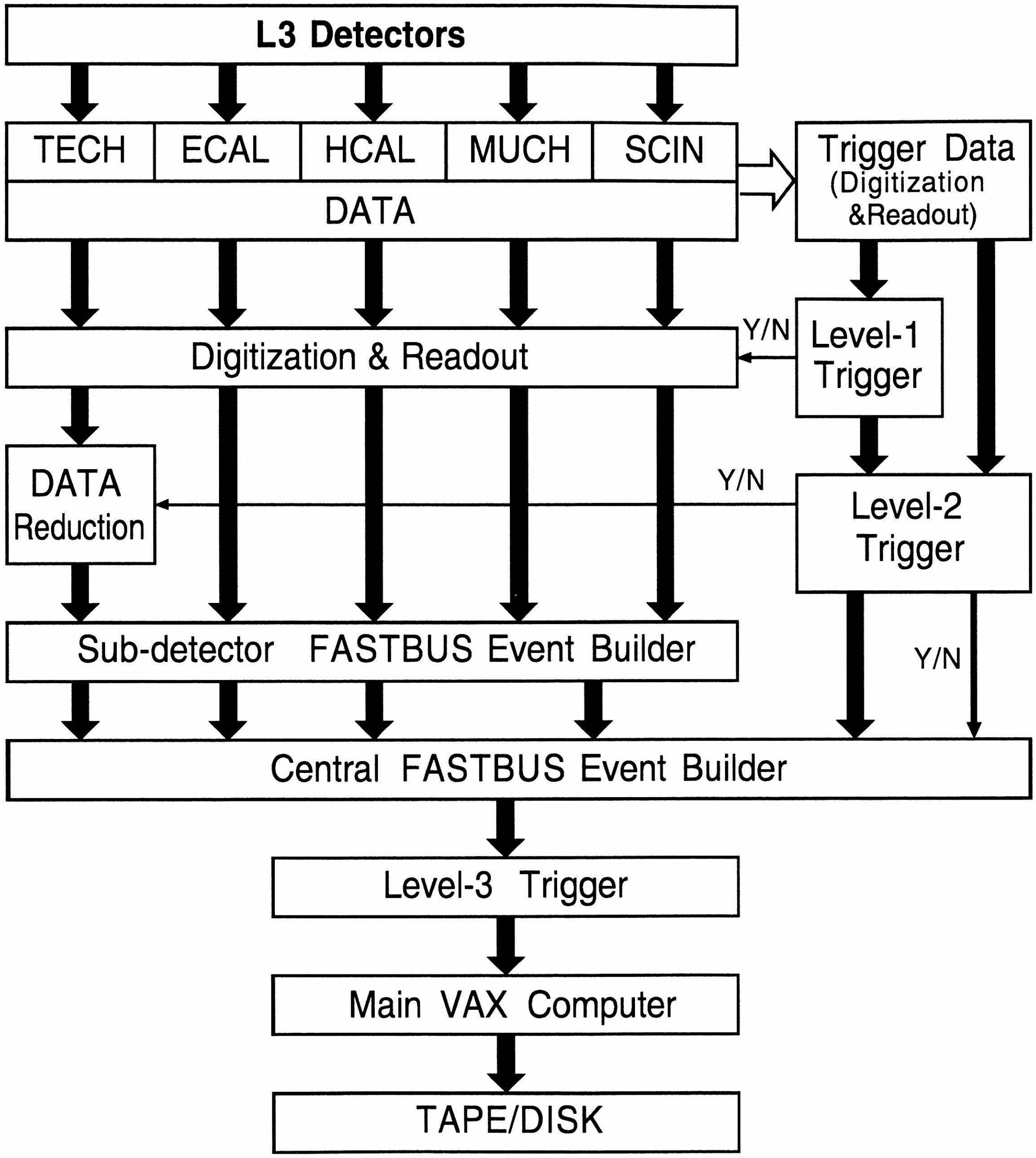

Figure 3.10: Diagram of the L3 trigger and data-acquisition system, showing the relationship between different elements. Arrows denote the flow of data and trigger decisions.

barrel scintillators. Triggers are generated for a high multiplicity and for a back-to-back coincidence. The luminosity trigger ($\simeq$ 4.0 Hz) uses analog sums dividing the luminosity calorimeter into 16 ϕ segments, and selects Bhabha candidate events based on energy thresholds and matching between the detectors at $\pm z$.

3.2.8.2 Second-Level Trigger

The second-level trigger[48, 49] combines the fast digitizations used by the individual first-level triggers together with the first-level decisions, to make a second-level decision within 5 ms. The second-level trigger automatically accepts events with more than one first-level trigger (not including scintillator triggers). Events are rejected by the second-level trigger on the basis of a more detailed calorimetric and track analysis, and the matching between tracks, calorimeters, and scintillators. The second-level trigger is implemented with 3 bit-slice microprocessors handling events in parallel, and achieves an overall rejection of single first-level trigger events of $\simeq$ 50%.

3.2.8.3 Event Builder

The event builder[50] collects together the full digitizations and fast trigger digitizations of an event from each subdetector. It consists of a layer of subdetector event builders that operate in parallel to collect together all data for each subdetector separately, followed by a central event builder that accumulates data from each subdetector's event builder and the level two trigger. The central and subdetector event builders are each implemented as separate FASTBUS crates, communicating via dual ported memories. The typical size of an event after normal online data reduction is $\simeq$ 20 kilobytes.

3.2.8.4 Third-Level Trigger

The third-level trigger[51] performs the last level of filtering in the trigger system, and makes decisions based on the full data present in the event builder. The trigger consists of 4 VAX workstations simultaneously analyzing separate events, and a transputer-based interface to the central event builder. The third-level trigger rejects about 50% of the events accepted by the second-level trigger, resulting in an event storage rate of 1–4 Hz.

3.3 L3 Luminosity Measurement

The measurement of the luminosity in the L3 experiment provides the normalization for the rates of all observed processes. Although each experiment receives approximately one quarter of the LEP luminosity, precise physics analyses require constant monitoring of the instantaneous luminosity at each interaction point. The benchmark process for luminosity monitoring by each experiment is Bhabha scattering, which occurs with a high rate and is relatively free of background at small angles to the z axis.

Bhabha events are selected in L3 with the first-level luminosity trigger, followed by offline reconstruction of the energy (E_i) and direction (θ_i, ϕ_i) of electron candidates in each monitor, which must satisfy

$$\max(E_1, E_2) > 0.8 \cdot E_{beam} \quad , \quad \min(E_1, E_2) > 0.4 \cdot E_{beam}$$
$$|\phi_i - 90°| > 11.25° \quad , \quad |\phi_i - 270°| > 11.25°$$
$$|\phi_1 - \phi_2 - 180°| < 10°$$
$$32 \text{ mrad} < \theta_i < 54 \text{ mrad} .$$

Figure 3.11 shows the good agreement between LUMI data collected in 1993 (with the SLUM installed) and the predictions of the BHLUMI Monte-Carlo program[52–55] for the polar angle distribution of reconstructed Bhabha events.

After selection of N_b Bhabha events, the luminosity is determined as $L = N_b/\sigma_b$, where σ_b is the cross section for Bhabha scattering integrated over the LUMI fiducial volume. The cross section has been determined by detailed Monte-Carlo simulation of the detector, using the BHLUMI and BABAMC[56, 57] event generators, resulting in $\sigma_b \simeq 70.5$ nb. The total error in the luminosity measurement is presently 0.2%, which is dominated by a 0.16% contribution from the theoretical uncertainty in the cross section[58].

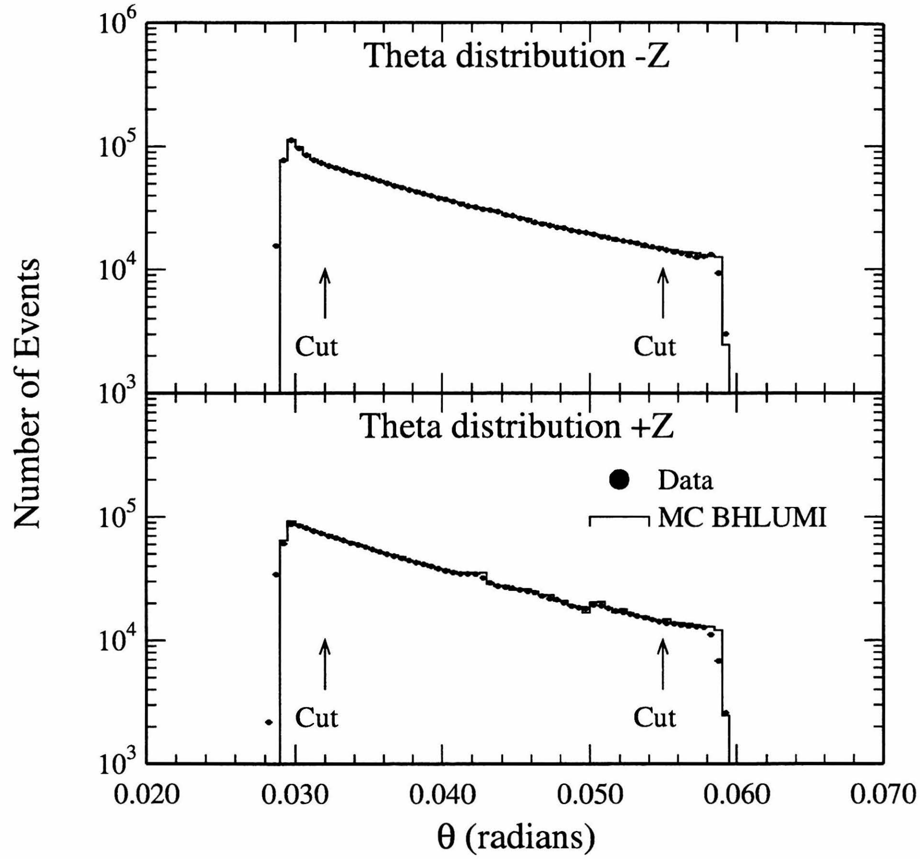

Figure 3.11: Polar angle distribution of Bhabha events in the luminosity monitors. Data are in good agreement with the predictions of the BH-LUMI Monte-Carlo. The difference between $\pm z$ is due to a flare in the LEP beampipe that only exists at $+z$.

Chapter 4

The L3 Electromagnetic Calorimeter

The work that I describe in this thesis relies heavily on the electromagnetic calorimeter (ECAL) of the L3 detector, which is designed to precisely measure the energy and direction of photons and electrons from 100 MeV to 100 GeV. In this chapter, I describe the properties of the scintillating crystals used for the calorimeter, the geometry and construction of the calorimeter, its data-acquisition system, and the methods of physics reconstruction that are applied to calorimeter data.

4.1 Bismuth Germanate

The L3 electromagnetic calorimeter is composed of the dense inorganic crystal scintillator bismuth germanate, $Bi_4Ge_3O_{12}$ (BGO). Photons and electrons traversing BGO undergo electromagnetic interactions, producing secondary photons and electrons that also interact in a chain reaction leading to an *electromagnetic shower* (see Figure 4.1(a)). The dominant processes for electrons and photons with energies much greater than 10 MeV are bremsstrahlung

$$\mathrm{e}^{\pm}(N) \rightarrow \mathrm{e}^{\pm} + \gamma ,$$

and pair creation

$$\gamma(N) \rightarrow \mathrm{e}^{+} + \mathrm{e}^{-} ,$$

where (N) denotes the influence of a nuclear Coulomb field. Since high-energy photons and electrons generate the same chain of reactions with different initial reactions, they produce showers that are practically indistinguishable.

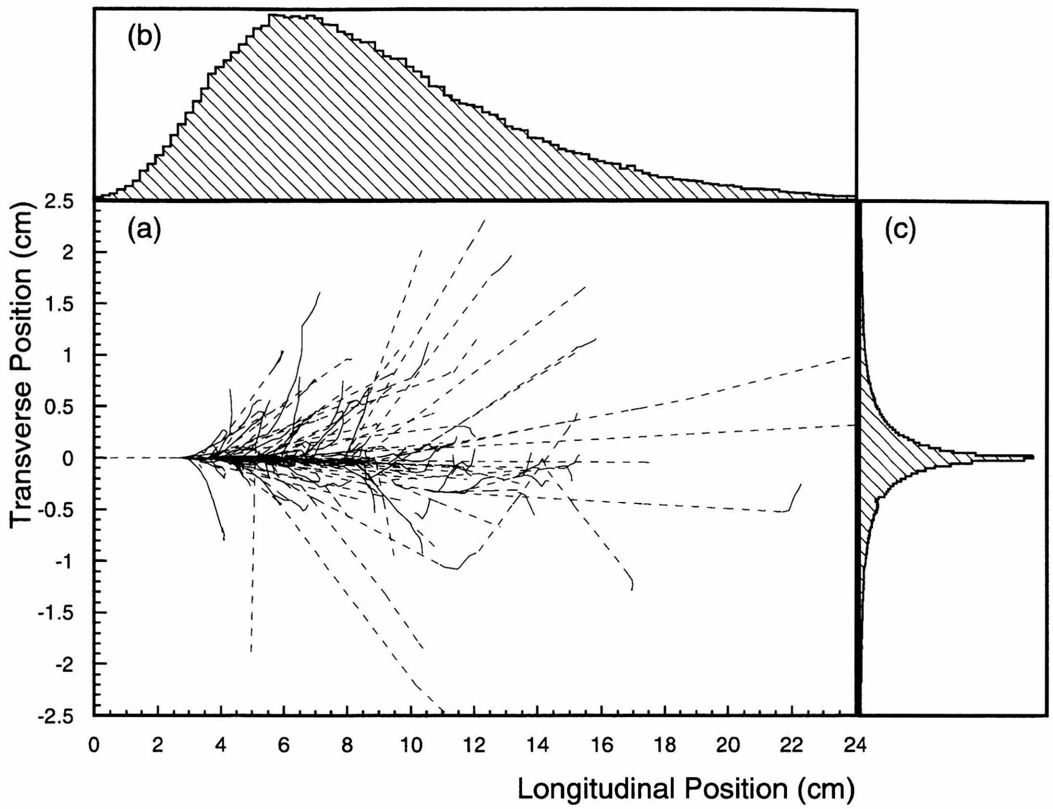

Figure 4.1: Development of electromagnetic showers in BGO. Sub-figure (a) shows a typical shower initiated by a 5 GeV photon incident from the left side; photons are shown as dashed lines, electrons and positrons as solid lines (only particles with $E > 10$ MeV are shown). Sub-figures (b) and (c) show the distribution of average energy deposition from a 5 GeV photon, in longitudinal and transverse projections respectively.

When the energy of an electron in a shower falls below 10 MeV, it loses its remaining energy primarily by ionization of the surrounding BGO. Ionization of the BGO creates excitations in the crystal lattice, with a lifetime of about 0.35 μs, that decay to produce scintillation photons with a wavelength spectrum peaked near 480 nm. The amount of scintillation light produced is proportional to the energy deposited

($\simeq 2.8 \times 10^3$ γ/MeV), making BGO a useful material for calorimetry. For precise energy measurements, variations in the scintillation light yield due to both temperature (-1.55% / °C at 25°) and radiation damage must be monitored and corrected for.

The essentially stochastic development of an electromagnetic shower can be characterized by the *radiation length* and the *Molière radius*, which are intrinsic properties of the showering material. The radiation length, X_0, is the longitudinal distance over which a high-energy electron loses $1/e \simeq 37\%$ of its energy by bremsstrahlung. The Molière radius, R_M, is the radius of the cylinder around the primary particle direction in which 90% of the particle's energy is deposited. Table 4.1 compares the properties of BGO with those of other inorganic scintillators being used in present experiments or planned for future experiments.

	$Bi_4Ge_3O_{12}$	NaI(Tl)	CsI(Tl)	CeF_3	$PbWO_4$
Density (g/cm^3)	7.13	3.67	4.51	6.16	8.28
Radiation length (cm)	1.12	2.59	1.86	1.68	0.85
Molière radius (cm)	2.4	4.5	3.8	2.63	2.19
Peak emission wavelength (nm)	480	410	565	300	420–450
Relative light yield	1	7.7	2.7	0.54	0.05
Temperature coefficient (%/°C)	-1.55	0.22	0.1	0.14	-1.9

Table 4.1: Properties of BGO compared with those of other inorganic scintillators being used in present experiments or planned for future experiments.

4.2 Detector Geometry and Construction

The ECAL consists of 10734 BGO crystals forming a barrel and two endcaps, as shown in Figure 4.2. Crystals are all 24 cm long and have trapezoidal front and back faces with dimensions of approximately 2 cm×2 cm and 3 cm×3 cm respectively (see Figure 4.3). Crystals are tapered and aligned with their long axis pointing towards the interaction point. This arrangement provides many (10–20) samples of the transverse development of an electromagnetic shower, but no longitudinal sampling. Material traversed by particles before entering the ECAL can cause scattering and conversion, which lead to a loss of energy resolution and in the ability to identify particles. The material in front of the ECAL barrel region amounts to 0.3–0.4 radiation lengths and is due mostly to the TEC and the ECAL inner support structure; in the endcap regions, the material in front amounts to 0.7–0.8 radiation lengths and is due mostly to the TEC end flanges (see Figure 4.4). The extra material in front of the endcaps does not lead to a significant deterioration of the energy resolution, since the additional scattering and conversion are concentrated in a region just in front of the endcap crystals.

4.2.1 Electromagnetic Calorimeter Barrel

The barrel is divided into two halves at the x-y plane, to allow any crystal to be exposed to a test beam passing through the geometric center. Each half barrel covers $42.3^\circ < \theta\,(180^\circ - \theta) < 90^\circ$ with 24 crystals, and $0^\circ < \phi < 360^\circ$ with 160 crystals, for a total of 3840 crystals. There are 24 different crystal shapes in the barrel, corresponding to different θ positions, with their front and rear face dimensions determined by the constraints of constant front face area (4.14 cm^2), adjacency, and projective geometry (see Figure 4.3). Each crystal subtends angles with respect to the interaction point of $\Delta\phi = 2.25^\circ$ and $1.5^\circ < \Delta\theta < 2.2^\circ$ with $\Delta\theta \propto \sin\theta$.

Each barrel crystal is contained in a separate cell of a 200–250 μm-thick carbon fiber composite structure, and kept in position with pressure applied from behind by a spring-loaded screw. Cell walls and clearances account for about 2.1% of the solid angle coverage of the barrel. To minimize the loss of efficiency due to this inactive space, each of the 160 ϕ-slices of 24 crystals are rotated by 10 mrad in ϕ, to aim at a position 5 mm away from the interaction point. An analogous tilt in θ is not necessary because of a spread $|\Delta z| \simeq 2$ cm in the position of LEP collisions relative to the nominal interaction point. The overall support of a half barrel is provided by

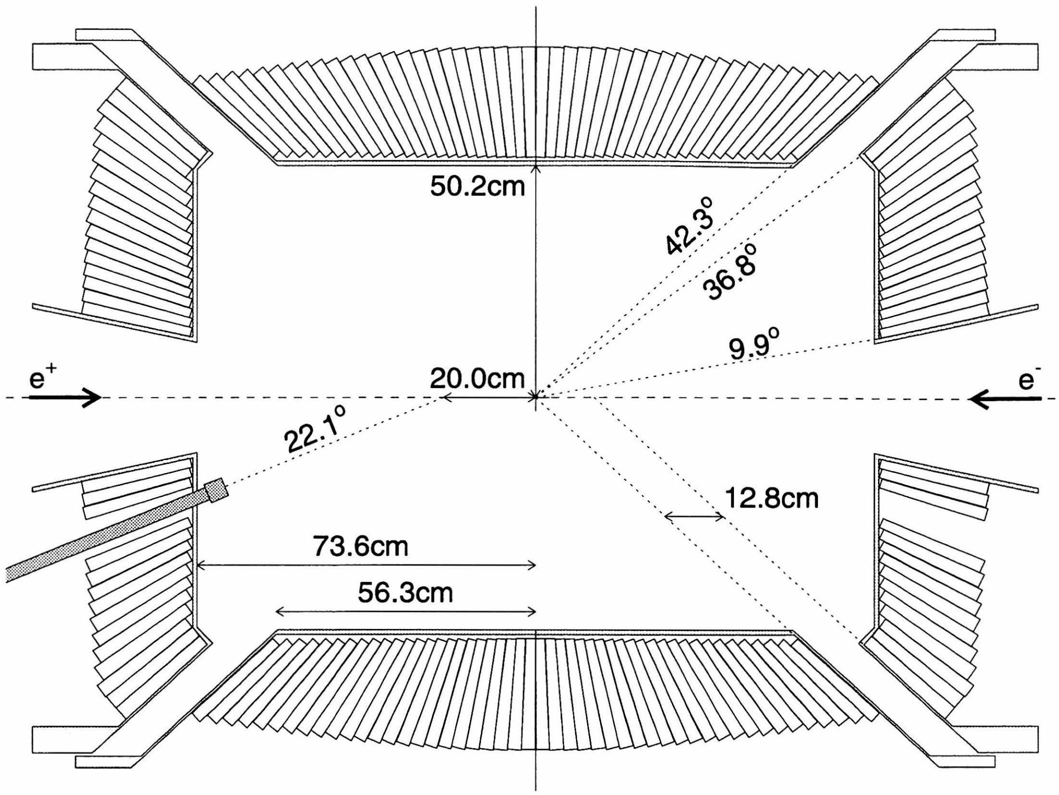

Figure 4.2: View of the ECAL in the y-z plane, showing the geometry of the barrel and endcaps and the arrangement of crystals. The beampipe and target in the bottom left are the final stages of the RFQ accelerator calibration system developed by Caltech. The ECAL is symmetric about the z, axis except for holes on both sides for the RFQ beampipe.

a carbon fiber composite and acrylic foam sandwich structure consisting of a 10 mm thick cylindrical inner tube, with steps on its outer surface matching the front face of each crystal, and a 5 mm thick conical shell supporting the length of the outer crystals (see Figure 4.2). There is a 0.5 mm thick steel membrane reinforcing the surfaces where the two half barrels join.

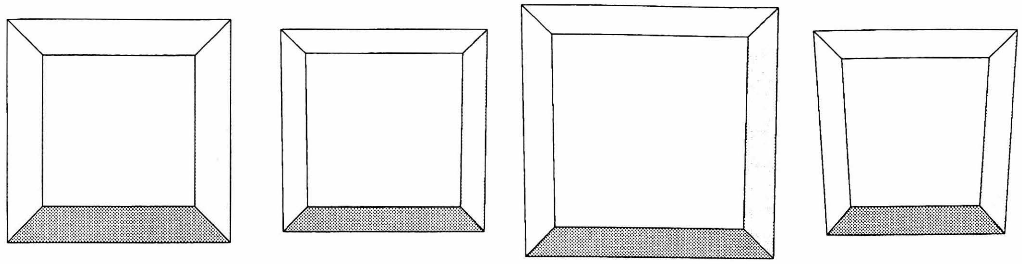

Figure 4.3: Drawing of four crystals, viewed from the interaction point, showing the range of different front and back face shapes. From left to right the shapes correspond to the outer barrel crystals ($\theta = 90°$, $43°$) and the outer endcap crystals ($\theta = 36°$, $10°$). The shapes of the front and back faces are drawn to scale.

4.2.2 Electromagnetic Calorimeter Endcaps

Each endcap is divided into two halves at the y-z plane, to allow easy installation and removal without sacrificing small-angle coverage. The endcaps cover $9.9° < \theta\,(180° - \theta) < 36.8°$ with 17 crystals grouped into 6 crowns; each half endcap is also divided into 16 ϕ sectors (see Figure 4.5). The number of crystals covering $0° < \phi < 360°$ in each crown varies from 128 in the outer crown to 48 in the inner crown, with a reduction of one crystal per ϕ sector between crowns. Each crown consists of 3 rings of crystals in θ, except for the inner crown which has only 2 rings. Nine crystals at $\phi = 270°$ and $\theta\,(360° - \theta) \simeq 16°$ are removed from each endcap to create a hole for the final section of beampipe of an RFQ calibration system, resulting in a total of 1527 crystals per endcap. There are 17 different shapes of endcap crystals, corresponding to the different θ positions, with front and rear face dimensions determined by the constraints of adjacency and projective geometry, and by choosing $\Delta\theta \propto \sin\theta \cdot \Delta\phi$ (see Figure 4.3). Each crystal subtends angles with respect to the interaction point of $2.25° < \Delta\phi < 7.5°$ and $1.68° < \Delta\theta < 1.87°$.

The crystals in each half endcap are supported by a carbon fiber composite cell structure similar to that used in the barrel. This dead material together with clear-

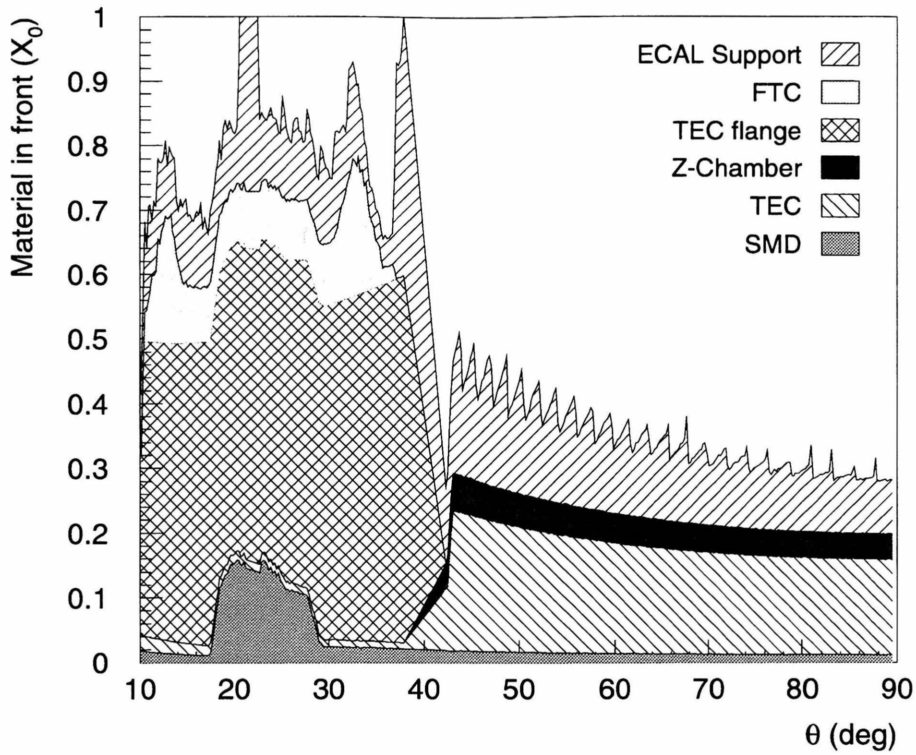

Figure 4.4: Plot of the amount of material in front of the ECAL, measured in radiation lengths, as a function of the polar angle. Different layers show the contributions of various inner detector elements. Periodic variations in the amount of ECAL support material are due to steps used to support the individual crystals.

ances represents about 2.1% of the solid angle coverage of the endcaps. To avoid a corresponding loss of efficiency, all crystals are displaced away from the interaction point by $|\Delta z| = 2.08$ mm, and also tilted in ϕ by 10 mrad as in the barrel. The overall support of a half endcap is provided by a carbon fiber composite structure consisting of a 10 mm thick disk matching the front faces of each crystal, and a 5 mm thick conical shell supporting the length of the outer crystals (see Figure 4.2). The endcaps were installed at the beginning of 1991, and are presently located in a position displaced 12.8 cm along the z axis from their nominal position due to the space requirements of the central tracking detector. In this configuration, particles

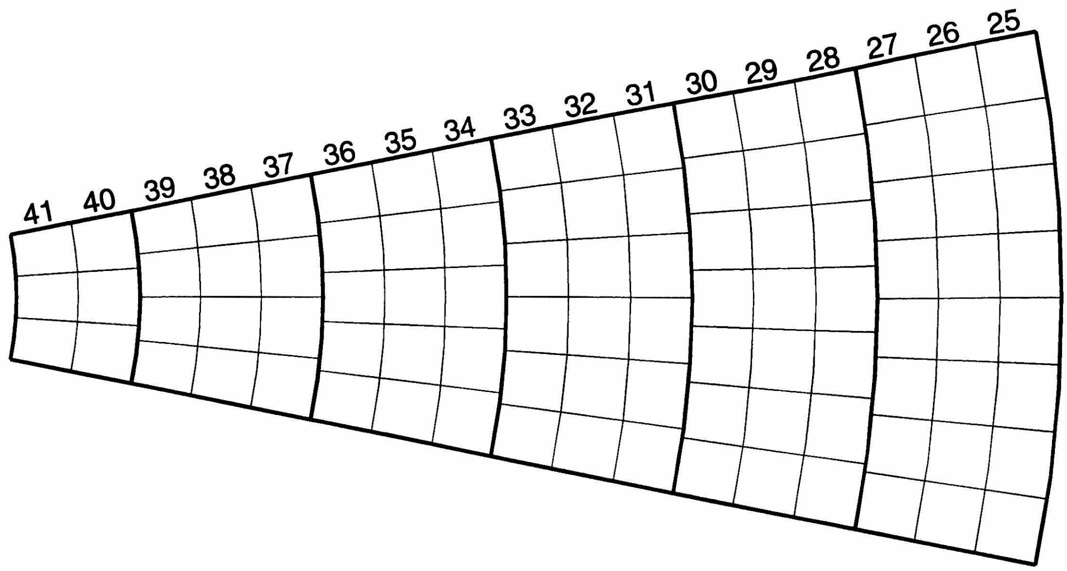

Figure 4.5: Diagram of an endcap ϕ sector viewed in the r-ϕ plane, showing the arrangement of crystals into 6 crowns (heavy outlines). A full endcap consists of 16 such sectors. Numbers along the top of the sector (25–41) correspond to the theta identifiers for each of the 17 theta rings in an endcap.

originating from the interaction point enter endcap crystals at angles offset from the crystal's long axis by 2.1°–5.4°.

4.2.3 BGO Crystals

BGO Crystals for the ECAL and luminosity monitors were produced by the Shanghai Institute of Ceramics in China using a modified Bridgeman method. Each crystal was cut and polished to within -300 – 0 μm of its nominal shape, and was required to meet minimum standards of optical transmission and light output. Good energy resolution and linear energy response requires that the efficiency for collecting scintillation light is nearly independent of where in a crystal it is produced. The factors affecting light collection efficiency are the crystal shape that determines angles of internal reflection, the intrinsic absorption coefficient that reduces the transmission efficiency, and the crystal surface treatment that determines losses and diffuse components of internal reflection. The efficiency for collecting light at the rear face of a polished crystal decreases strongly (up to 50%) with distance from the rear face. After coating crystals with a 40–50 μm thick layer of high reflectivity NE560 paint, the maximum variations were approximately 5%. During production, several batches of crystals were evaluated for radiation hardness. After exposure to a dose of 10^3 rad (the worst case scenario of a LEP beam accident would result in a dose of about 10 rad) the light output immediately dropped by 40%, and then fully recovered spontaneously at room temperature after one month. Some crystals positioned close to the LEP beam were produced with Europium doping, which was found to accelerate the natural recovery process from radiation damage without reducing light output.

4.3 Data-Acquisition System

The ECAL data-acquisition system provides analog and digital signals proportional to the amount of scintillation light collected in each crystal (which is in turn proportional to the energy deposited). The system consists of a front end that converts scintillation light into an analog electronic pulse height, followed by an analog to digital converter (ADC), and a four-level hierarchical readout network that collects together digital signals from the 11000 crystals into a single record for each event.

Each crystal is assigned a unique identifier in the L3 data-acquisition framework of the form **20RTTPPP**, where the initial **20** denotes an ECAL element and is usually dropped when the context is clear, **R** denotes the ECAL region (the half barrel and endcap are labeled 1 and 3 respectively at $z > 0$, and 2 and 4 respectively at $z < 0$), **TT** denotes the theta position of a crystal (01–24 in the barrel and 25–41 in the endcaps), and **PPP** denotes the phi position (001–160 in the barrel, and 001-128 in the endcaps).

4.3.1 Front End Electronics

Both the tapering of crystals and the space constraints favor collection of scintillation light at the crystal's rear face. This is accomplished with a pair of 1.5 cm^2 Hamamatsu S2662 silicon photodiodes glued to the rear face and read out as a single unit. Photodiodes have the advantages over conventional photomultiplier tubes of being insensitive to the L3 magnetic field, and of making efficient use of the available space.

Scintillation photons traversing the depletion region of a photodiode produce an electron-hole pair with a quantum efficiency of about 70%. This pair drifts apart in the electric field of a 15 V reverse bias, resulting in a current of about 0.2 fC (1200 electrons) per MeV of deposited energy. This current is much smaller than the equivalent current from a photomultiplier tube and must be amplified before digitization. The chain of front end electronics shown in Figure 4.6 starts with a charge-sensitive preamplifier that is mounted directly behind each crystal and AC coupled to the pair of photodiodes connected in parallel. The preamplifier output pulse has a 300 ns rise time and an 800 μs exponential decay time, with a peak voltage proportional to the total charge collected in the photodiode. The preamplifier is followed by a pole-zero shaping circuit that differentiates the long preamplifier output pulse to produce a short pulse with a decay time of 1.1 μs.

After shaping, the signal from each crystal is split into three separate signals which are then processed by the first-level trigger, and by two independent pulse height analyses optimized for small (*low energy chain*) and large (*high energy chain*) signals respectively. The low energy chain is amplified with a gain of 32 relative to the high energy chain, after which the two chains are processed identically. The signal in each chain is first integrated and then the amount of integrated signal is stored as a DC level with a sample and hold circuit. The stored DC level is further amplified in two stages each with a gain of four, resulting in a total of six levels of amplification for the two chains as shown in Table 4.2.

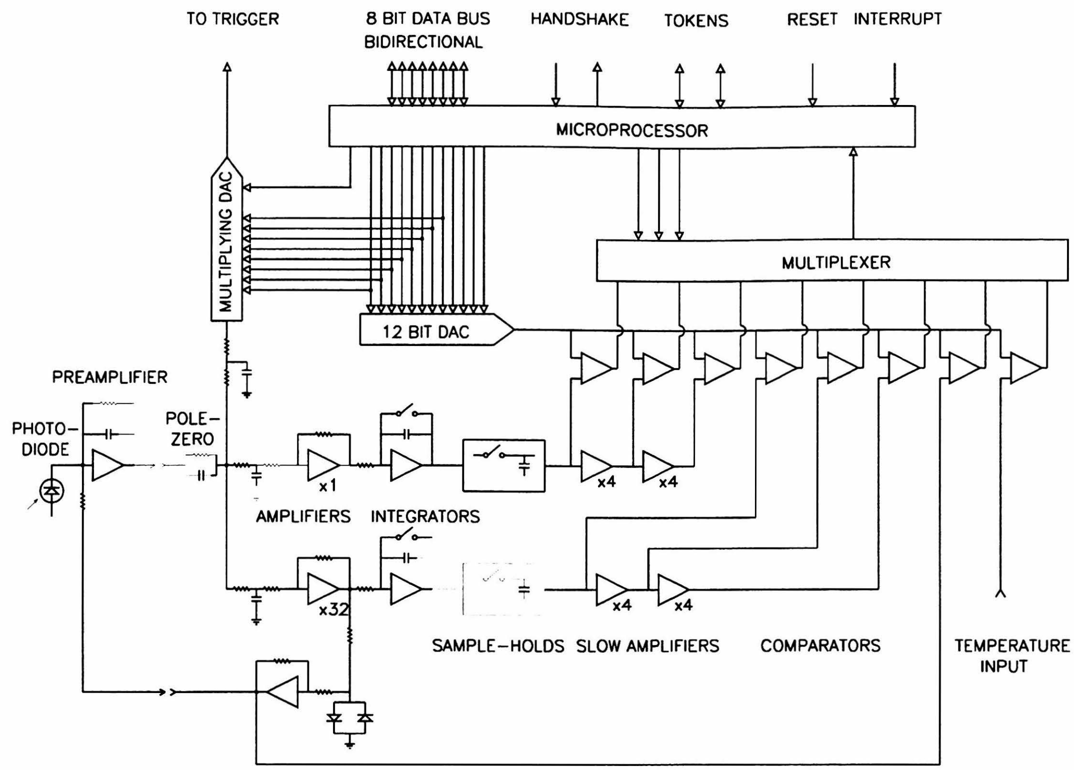

Figure 4.6: Schematic of the ECAL first-level readout showing the front end electronics and analog to digital converter for a single crystal.

4.3.2 Analog to Digital Conversion

The analog to digital converter (ADC) for each crystal's collected light signal is designed to provide accurate measurements over a wide dynamic range (10 MeV–100 GeV) at a minimum cost. This is achieved with a two step digitization supervised by dedicated Hitachi 6305 microprocessor for each crystal (see Figure 4.6). The first step of the digitization is to choose the level of amplification that provides the largest unsaturated signal, where a saturated signal is defined as being larger than 7/8 of the full scale output of the digital-to-analog converter (DAC). The next step is to use a successive approximation algorithm to find the DAC input value for which the corresponding DAC output level is as close as possible to the amplified crystal signal.

		Voltage		Energy	
Comp.	Amp.	Min. Value	Max. Value	Min. Value	Max. Value
1	×1	4 μV	18 mV	0.1 MeV	0.4 GeV
2	×4	18 μV	74 mV	0.4 MeV	1.5 GeV
3	×16	71 μV	290 mV	1.5 MeV	6 GeV
4	×32	0.15 mV	0.6 V	3 MeV	12 GeV
5	×128	0.6 mV	2.5 V	12 MeV	50 GeV
6	×512	2.4 mV	10 V	50 MeV	200 GeV
7	*leakage current*				
8	*identification / supply voltage / temperature sensor*				

Table 4.2: Summary of input signals to the ECAL first-level readout comparators. The first six comparator inputs correspond to different levels of amplification of a crystal's light output signal, for which the approximate voltage and energy ranges of sensitivity are given, as well as the amplification factor relative to the pole zero output level.

The result is a 12-bit digitization which, together with the 9-bit (1:512) selectable gain, corresponds to an effective dynamic range of 21 bits. The 4:1 scaling between different levels of amplification ensures that all signals above about 350 MeV are digitized with at least 10 significant bits, out of the possible 12 bits, which results in a digitization accuracy of at least 0.1%. The digitization accuracy for signals below about 350 MeV is given by the comparator 1 least count, which is about 0.1 MeV. The time required for digitization is 220 μs, and the linearity of the ADC response is better than 1%.

The two additional comparators in each crystal's front end electronics are used to digitize both the photodiode leakage current and one of 12 control signals that monitor power supply voltages, temperature sensors, and board identification resistors. In addition to supervising signal digitization, each crystal's microprocessor applies a programmable scaling to the analog first-level trigger signal, and interfaces with the upper levels of the readout.

4.3.3 Readout Network

The readout network for the ECAL data acquisition is designed to collect together the data from individual crystals (both LUMI and ECAL) into records for each event. The system is implemented with four hierarchical levels, with data buffering and computing capability distributed throughout the network (see Figure 4.7). The lowest level in the readout network consists of groups of first-level microprocessors organized into token-passing rings: each ring covers 60 crystals in the barrel or 48 crystals in an endcap (see Figure 4.8). During normal data-taking, thresholds for each crystal are downloaded to the first-level microprocessors and data are only passed on to higher levels if they exceed this threshold (*sparse scan mode*). The time required to transmit the ECAL data for an event from the first to the second level is determined by the ring containing the largest number of crystals with data above threshold. Each crystal's first-level microprocessor requires 96 μs to transmit its data, or 18 μs to signal that its data is below threshold. The processing time taken for error checking, data formatting, and threshold testing does not contribute to the overall transfer time since each first-level module can buffer data for up to 41 events, and performs these tasks while another module is transmitting.

The next layer of the ECAL readout network consists of 13 VME crates, each containing 16 second-level modules and one third-level module. All modules are commercially available *Mizar* single-board computers based on a Motorola M68010 microprocessor, each with 512K bytes of memory. Each second-level module communicates with a first-level token ring, collecting together the data from up to 60 crystals in its memory. When all 16 second-level modules in a crate have stored the data for an event, the third-level module transfers the combined data to the next layer of the readout network. Second-level modules buffer up to several hundred events, and perform error checking and data reformatting. Third-level modules act only as data movers, with no buffering and minimal processing.

The final layer of the ECAL readout network consists of 13 first-in first-out (FIFO)

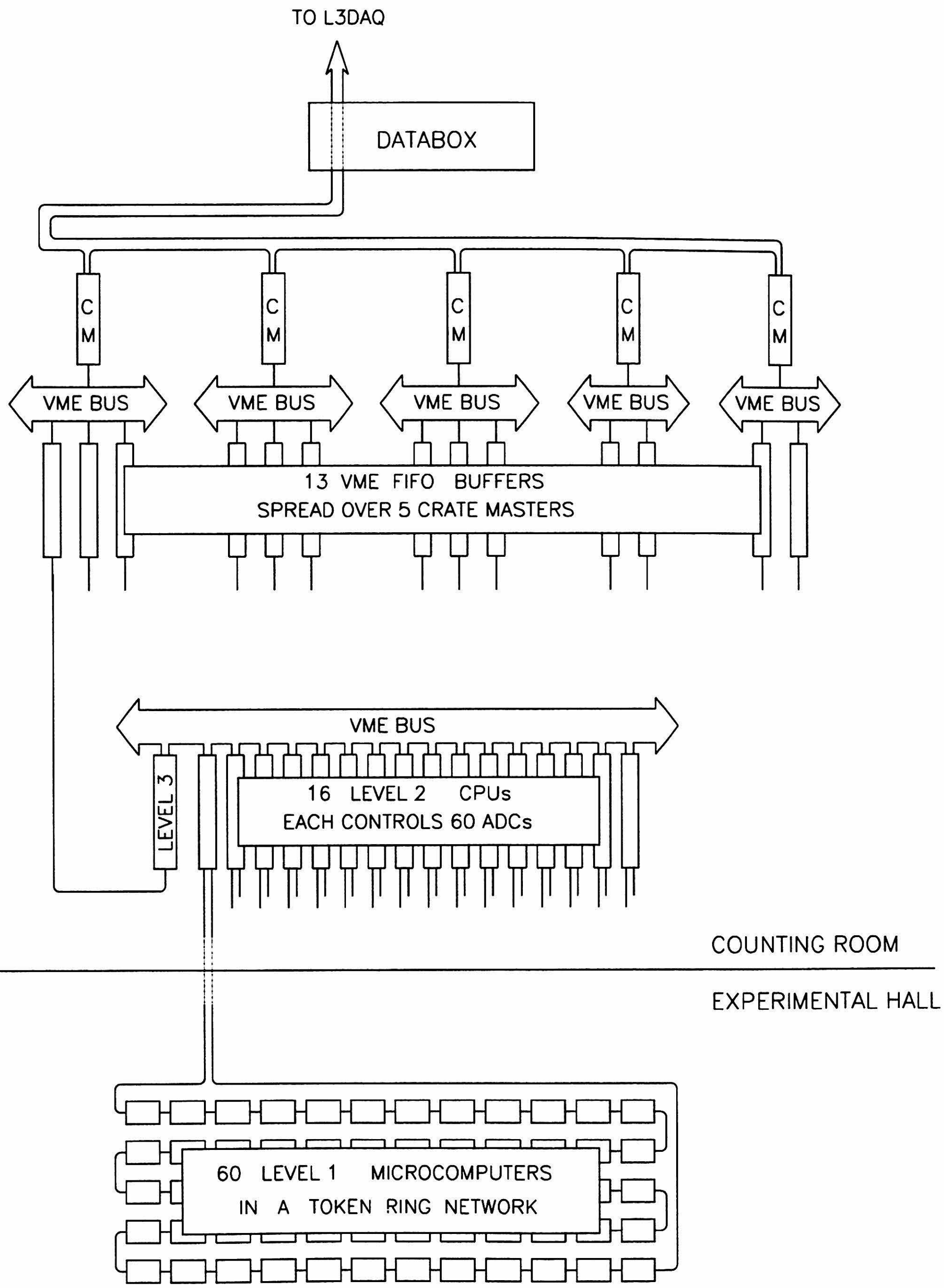

Figure 4.7: Schematic of the ECAL readout network, showing the hierarchical organization into four levels.

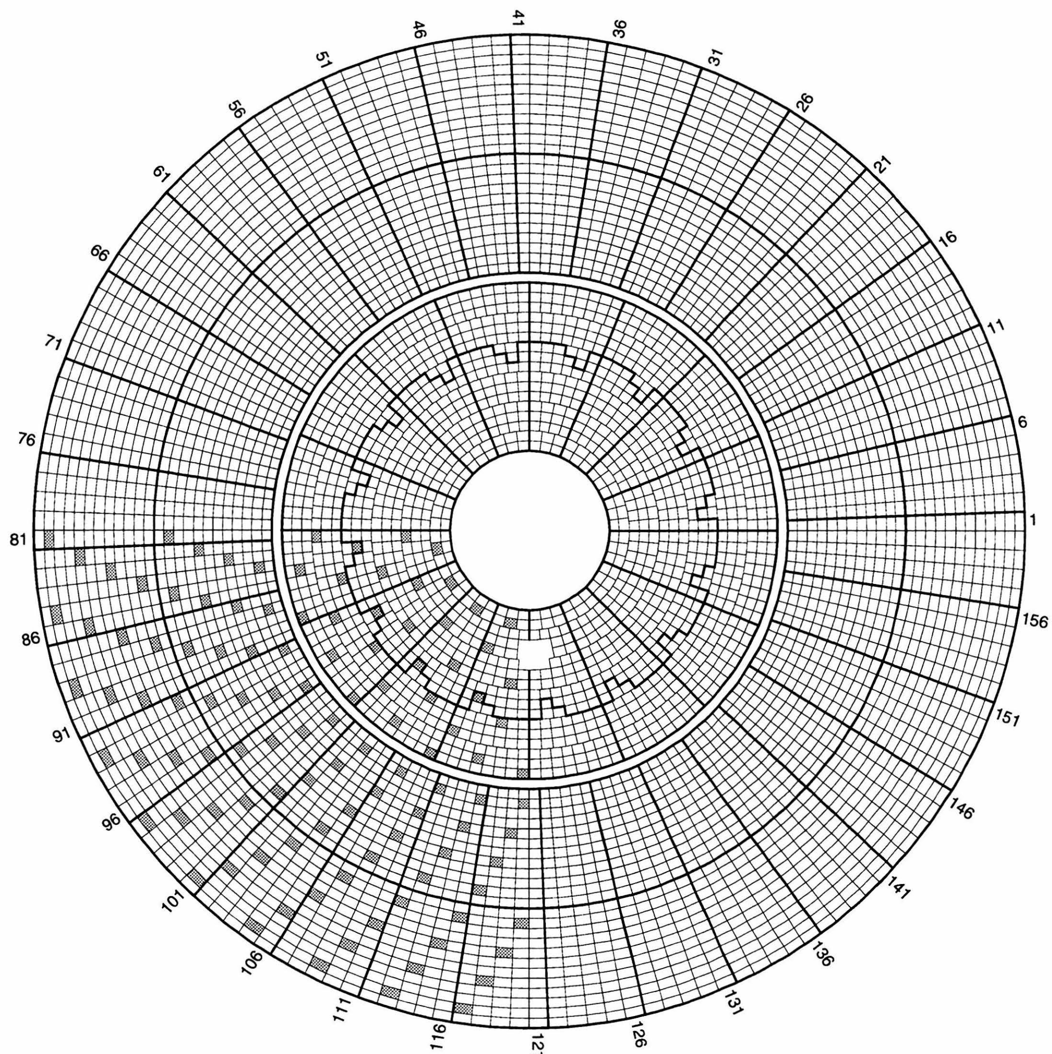

Figure 4.8: Readout map for one side of the ECAL, consisting of a half barrel and an endcap, showing crystals in a schematic r-ϕ projection. The outer radius corresponds to barrel crystals with theta identifier of 1 at $\theta = 90°$, and the inner radius corresponds to endcap crystals with theta identifier of 41 at $\theta = 9.9°$. Numbers around the outer radius correspond to the phi identifiers of crystals in the barrel. Heavy outlines show the grouping of crystals into first-level readout rings. Shaded crystals in the bottom left quadrant mark the position of front- and back-face temperature sensors (which are repeated in all quadrants).

memory modules distributed among 5 VME crates. Each FIFO is filled with the data for up to 960 crystals transmitted by a level three module. When the complete data for an event is available, a crate master in each VME crate supervises its transfer into the L3 event builder.

4.3.4 Temperature Control and Monitoring

The sensitivity of BGO light yield to temperature (-1.55% / °C at 25°) makes careful control and monitoring of crystal temperature necessary in order to achieve and maintain good energy resolution. Temperature control is provided by active thermal shields consisting of brass screens to which copper pipes carrying a silicon-based coolant are soldered. Shields are used to dissipate the heat generated by preamplifiers (0.2 W per channel) and first-level boards (2 W per channel), and to prevent heat transfer from the ECAL to other subdetectors.

Temperature monitoring is provided by 1792 AD590 sensors positioned on the front and back faces of one in 12 crystals (see Figure 4.8). Temperature sensor data is digitized by the first-level modules, using comparator 8 (see Table 4.2), and is read out in the same way as crystal light output data.

4.4 Physics Reconstruction

Physics reconstruction consists of transforming the raw data for an event into physically meaningful units, and then applying pattern recognition algorithms to identify the basic objects of a physics analysis. Reconstruction of ECAL data involves first transforming each crystal's raw ADC signal to an energy value, then analyzing energy deposits to identify clusters that are characteristic of single particles, and finally correlating ECAL energy clusters with tracks and clusters in other subdetectors.

4.4.1 Energy Reconstruction

The transformation of a crystal's raw ADC signal to an energy value takes account of the changing scintillation response of each crystal, due to temperature variations and intrinsic losses associated with aging and radiation damage. The transformation is given by

$$E_i(t) = \left[G_{ij}A_{ij}(t) + B_{ij} - V_{ij}^{(0)}(t)\right] \cdot C_i(t_0, T_0) \cdot F(T, T_0) \cdot \frac{X_i(t)}{X_i(t_0)} ,$$

with variables as given in Table 4.3. The amplifier gains and biases for each channel's comparator are very stable and essentially constant. ADC pedestal values, crystal temperatures, and relative light response coefficients are measured during special calibration runs between data collecting runs, typically once every eight hours. Absolute energy calibration constants for each crystal have been determined at least once: constants for barrels crystals were determined using 2, 10, and 50 GeV electrons in CERN test beams during 1987 and 1988; constants for endcap crystals were determined using 45 GeV electrons from Bhabha scattering, $Z \to e^+e^-(\gamma)$, after installation in L3 in 1991. In the future, absolute calibrations will be determined *in situ* using an RFQ accelerator system developed by Caltech[59–61].

The correction for temperature variations in a crystal's light yield involves adjusting each crystal's signal to an equivalent signal at the reference temperature $T_0 = 18°\text{C}$, to which the absolute calibration constants have also been adjusted. The temperature correction from T to T_0 is parameterized with a linear interpolation between a crystal's front face (T_f) and back face (T_b) temperatures

$$F(T, T_0) = 1 + \kappa \cdot [T_f + c\,(T_b - T_f) - T_0] ,$$

where $\kappa = 1.55\%$ is the temperature coefficient of BGO, and $c = 0.273$ is the interpolation coefficient along the crystal's length. Since only one crystal in 12 is instrumented with temperature sensors (see Figure 4.8), temperatures for the other crystals are determined using fits to sensor values.

	typical value	description
$E_i(t)$	0–50 GeV	crystal energy deposit
$A_{ij}(t)$	0–4095 ADC	raw ADC signal
G_{ij}	3.7–4.5 μV/ADC	amplifier gain
B_{ij}	-130–0 μV	amplifier bias
$V_{ij}^{(0)}$	1–6 mV	ADC pedestal
$C_i(t_0, T_0)$	16–30 keV /μV	absolute energy calibration
$F(T, T_0)$	0.97–1.01	temperature correction function
$X_i(t)$	0.85–1.00	relative light response

Table 4.3: Variables used in the reconstruction of crystal energies. The index i refers to a readout channel and the index j refers to a comparator (1–6) within a readout channel. t,T denote the time and crystal temperature during data acquisition; t_0 specifies the time that the absolute energy calibration was performed; $T_0 = 18°\mathrm{C}$ is the chosen reference temperature.

4.4.2 Particle Reconstruction

The ECAL measures the energy loss of particles traversing BGO, in samples corresponding to the individual crystals. Different types of particles lose energy by different mechanisms and produce different patterns of energy deposition. The design of the ECAL is optimized for photons and electrons which can be precisely reconstructed because they generate characteristic electromagnetic showers with little variation. Hadrons in BGO lose their energy through nuclear interactions which result in diffuse deposits with large fluctuations. Muons do not interact strongly in ECAL and produce small signals that are almost independent of their energy (about 220 MeV for a muon traversing the full length of a crystal).

The first step in particle reconstruction is to identify connected regions of crystals, referred to as *geometrical clusters*, corresponding to the areas of activity (due to one or more particles) in the ECAL. Geometrical clusters are formed by assigning crystals with energy greater than 10 MeV into groups, where each crystal in a group is adjacent to at least one other crystal in the group. Clusters with a total energy of less than 40 MeV are not considered. The definition of adjacency is straightforward in the barrel region and includes diagonal connectivity (each crystal is adjacent to 8 others), however some care is required in the endcap regions where crystals are not aligned in ϕ across different crowns (see Figure 4.5). Clusters are allowed to span the break between the two half barrels, but not the gap between the barrel and endcap regions.

The second step of reconstruction is to identify energy deposits due to individual particles within a geometrical cluster. These are referred to as *bumps* and are formed by first identifying local maxima (*bump crystals*) within a geometrical cluster and then associating each crystal in a geometrical cluster to the nearest such maximum in the same cluster. Bump crystals are required to have energy greater than 40 MeV and also greater than the energies of the 8 neighboring crystals (using the same definition of adjacency as for geometrical clusters). The distance measure used to assign non-bump crystals to their nearest bump crystal is roughly equivalent to the 3-dimensional distance between the crystal centers. If two bump crystals are equidistant from a non-bump crystal, the non-bump crystal is assigned to the most energetic one of the two.

Reconstruction of the energy of the particle that originated a bump assumes that the particle was an electron or a photon, and is based on the quantities

$$S_9 \equiv \sum_{3\times3} E_i \quad , \quad S_{25} \equiv \sum_{5\times5} E_i \, ,$$

where the sums range over crystals in 3×3 and 5×5 matrices centered on the bump crystal, also including those crystals which are assigned to a different bump. Figure 4.9 shows the distributions of S_9 and S_{25}, for 5 and 25 GeV photons simulated in the detector. The extra width of the S_9 distribution, as compared with S_{25}, is due to the greater sensitivity of S_9 to energy leakage effects. This effect can be corrected for since the leakage from a 3×3 matrix of crystals is correlated with the ratio S_1/S_9 (S_1 is the energy of the central bump crystal), which is sensitive to variations in the particle impact parameter over the face of a crystal (see Figure 4.10). The *corrected* *sum-of-9* energy is defined as

$$S_9^c = \frac{S_9}{c_1(\theta) \cdot S_1/S_9 + c_2(\theta)} ,$$

where $c_1(\theta)$ and $c_2(\theta)$ are coefficients chosen to unfold the effect shown in Figure 4.10, with an overall normalization giving $\langle S_9 \rangle \simeq E_\gamma$. Figure 4.9 shows the distributions of S_9^c for 5 and 25 GeV photons simulated in the detector. The correlation in Figure 4.10 is relatively weak for 5 GeV photons, and as a result the improvement in S_9^c over S_9 is small. At higher energies however, the correlation between S_9 and S_1/S_9 is stronger, and results in a S_9^c that is slightly better than S_{25}.

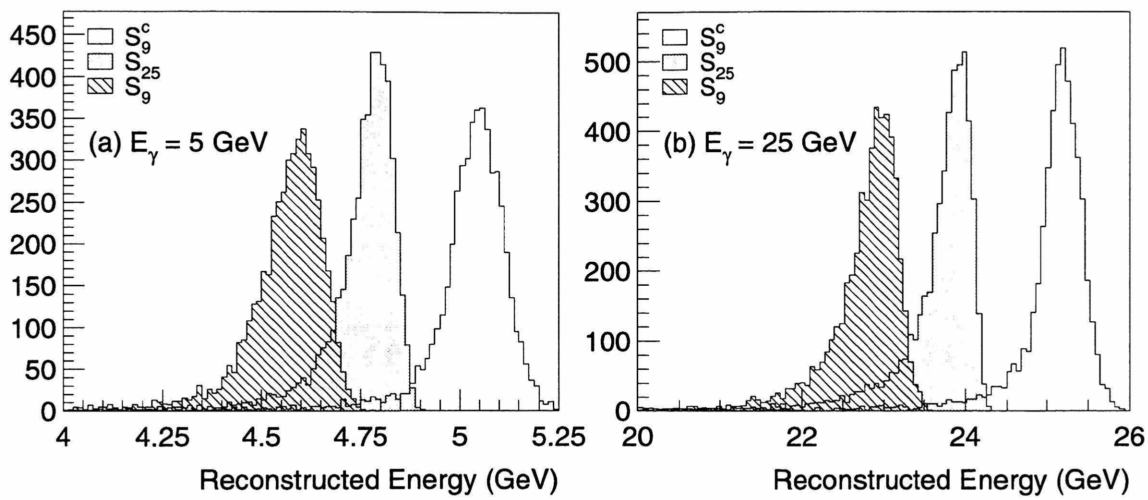

Figure 4.9: Distributions of the reconstructed energy variables S_9, S_{25}, and S_9^c for 5 GeV (a) and 25 GeV (b) photons simulated in the detector.

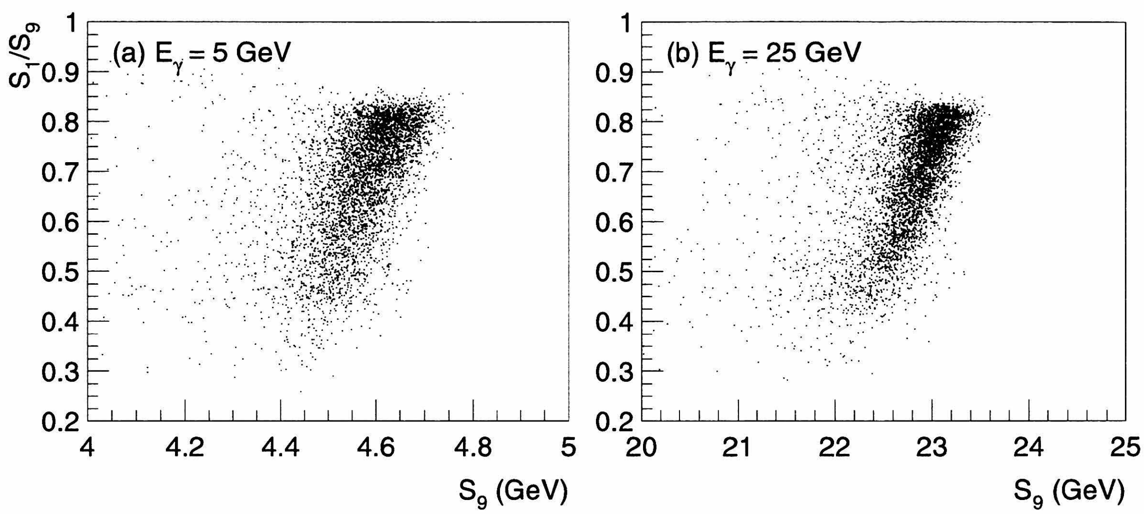

Figure 4.10: Correlation between the reconstructed energy S_9 and the ratio S_1/S_9, for 5 GeV (a) and 25 GeV (b) photons simulated in the detector.

Chapter 5

Event Selection

The physics process that I study in this thesis is $Z \rightarrow q\bar{q}\gamma$: the hadronic decay of a Z boson accompanied by a photon radiated from one of the primary quarks. The dominant backgrounds to this final-state radiation (FSR) process are from neutral hadrons decaying into multi-photon states (mostly $\pi^0 \rightarrow \gamma\gamma$), and, to a smaller extent, from photons radiated by the e^+e^- initial state (ISR). In this chapter, I describe the methods that I have used to select a sample of events that is enriched in FSR. In the next chapter, I describe how I analyze the selected events, accounting for irreducible background contributions and detector effects and estimating uncertainties.

I select events by first choosing hadronic Z decays, and then by further selecting events that contain at least one candidate FSR photon. In the following sections, I describe both of these steps in more detail. I suppress neutral hadronic background from the final event sample by imposing energy and isolation requirements for photon candidates, and by a detailed study of the patterns of the energy deposited in the ECAL. I suppress ISR by restricting my attention to events with $\sqrt{s} \simeq m_{\mathrm{Z}}$, and by rejecting photon candidates in the most forward and backward regions of the detector.

In this chapter, I use the JETSET[62, 63] and HERWIG[64, 65] Monte Carlo models of hadronic Z decay for comparisons with L3 data. Events generated using both of these models were simulated in the L3 detector with the SIL3 program, and then reconstructed using the REL3 program. SIL3 is a detector simulation based on GEANT[66, 67] Version 3.16, and REL3 is the standard L3 reconstruction program used to interpret both real and simulated raw data. The physics performance of JET-

SET has been more extensively studied than that of HERWIG, and a much larger number of JETSET events have been simulated in the L3 detector. For these reasons, and also because HERWIG does not include ISR, I consider JETSET as the primary Monte Carlo for comparisons with L3 data. In all plots showing comparisons of data with Monte Carlo, I normalize the Monte Carlo predictions to the same number of selected hadronic Z decays as observed in data.

5.1 Selection of Hadronic Z Decays

The first step of my analysis is to select a sample of hadronic Z decays. Hadronic decays are characterized by a large number of both charged and neutral particles and are thus easily distinguished from other Z decay modes (Figure 5.1 shows a typical hadronic decay recorded in the L3 detector). I further require that events be recorded at $\sqrt{s} \simeq m_{\mathrm{Z}}$, and during running periods when the relevant components of the detector and data-acquisition system were functioning normally.

5.1.1 Online Trigger

In order for a hadronic Z decay to be recorded, it must first be selected by the online trigger system (see Section 3.2.8). Hadronic events are identified by the logical OR of the first-level energy, scintillator, and TEC triggers, which have efficiencies of 99.93%, 95%, and 95% respectively. The energy trigger requires either a total energy in the calorimeters of at least 25 GeV, or a minimum energy in the central region $42° < \theta < 138°$ of 15 GeV (ECAL+HCAL) or 8 GeV (ECAL only). The scintillator trigger requires a coincidence of at least 5 scintillator hits during a 30 ns interval, which must extend over an azimuthal angular region of at least 90°. The TEC trigger requires that at least two tracks are identified with a maximum acollinearity of 60°.

The hadronic event trigger requires that an event be selected by at least one of the first-level triggers described above. Higher levels of the trigger system filter events to reject those due to electronic noise, beam-gas interactions, and cosmic rays. The overall efficiency for selecting genuine hadronic Z decays with the online trigger is greater than 99.9%.

5.1.2 Selection of Events Produced at the Z Resonance Peak

I require that events be recorded at a center-of-mass energy on the peak of the Z resonance, which I define as

$$91.0 \text{ GeV} < \sqrt{s} < 91.5 \text{ GeV} ,$$

where $\sqrt{s}$ is determined from the operating parameters of the LEP accelerator. This requirement suppresses initial-state bremsstrahlung (see Section 7.1), and thus also minimizes the interference between photons radiated by the initial- and final-states, allowing a meaningful distinction to be made between these two sources.

Figure 5.2(a) shows the distribution of the integrated luminosity recorded by the L3 detector at different center-of-mass energies, between 1991 and 1994. Figure 5.2(b) shows the corresponding number of hadronic events recorded in the on-peak range of energies. The general LEP strategy has been to run on peak during 1992 and 1994, and to scan in energy during 1991 and 1993; as a result, the number of on-peak events collected during 1993 was lower than during the previous year, despite a significant improvement in luminosity. 91.5% of the hadronic event sample—and 81.3% of the luminosity—recorded between 1991 and 1994 is on-peak. The weighted average center-of-mass energy of the on-peak events that I have selected, calculated using weights proportional to the number of hadronic events, is $\langle\sqrt{s}\rangle = 91.248$ GeV.

5.1.3 Detector and Data-Acquisition Status

In order to control systematic uncertainties related to the performance of the detector and the data-acquisition system, I only use events recorded during running periods in which the relevant systems were operating normally. The important detectors for this analysis are the hadron calorimeter (for hadronic event selection), the electromagnetic calorimeter (for hadronic event selection and photon candidate selection), and the central tracking chamber (for neutral bump selection). In addition, I require that the luminosity monitors, the global data-acquisition system, and the energy trigger were operating normally for events to be included in my analysis.

I filter events with detector and data-acquisition problems at three levels: by rejecting all events taken during bad runs, by rejecting individual events within a normal run, and by rejecting individual photon candidates within an otherwise good event (I describe the filtering of photon candidates in Section 5.2.1). A *run* is a series of events taken during part of a single fill of LEP. For the first level of filtering, I define a run to be *bad* when one or more of the systems listed above was not operating normally, as recorded in the online databases or as determined by subsequent analysis. In addition, I reject runs for which the fraction of selected hadronic events with less than four TEC tracks is larger than 20%, since it is unlikely that the TEC was operating normally during such a period. The effect of bad runs on the available data sample from each year is summarized in Table 5.1. There is a general trend of improvement in reliability since 1991, and conditions in 1993 were particularly good.

Within a good run, I apply a second level of filtering that consists of identifying and rejecting events in which the ECAL readout has excessive noise. These events are typically due to large fluctuations in the positions of the pedestals for a group of crystals that share a common power supply, which are induced by pickup from external sources. Figure 5.3 shows a typical event of this class. I identify noisy BGO events using cuts on the number of crystals, N_{cry}, assigned to each bump in an event. For an event to be considered good, I require that it contain no more than four bumps with $N_{\mathrm{cry}} > 30$, and that no bump in the event have

$$N_{\mathrm{cry}} > 35 + 3.5 \times E_{\mathrm{bmp}} \ ,$$

Year	1991	1992	1993	1994	TOTAL
On-peak Runs	1076	2264	1884	4948	10172
Bad Runs	20.8%	17.3%	6.5%	11.7%	13.0%
On-peak Lumi (pb^{-1})	8.6	22.7	15.5	49.9	96.7
Bad Lumi	15.0%	9.5%	2.0%	6.2%	7.1%
Good Runs (events)	310K	793K	509K	1649K	3261K
Noisy BGO Events	2.6%	3.3%	0.4%	0.05%	1.1%

Table 5.1: Summary of detector and data-acquisition status for each of the years 1991–94. The first two rows give the total number of on-peak runs for each year and the fraction of these that I consider bad. The next two rows give the total luminosity recorded on-peak during each year and the fraction of this that I consider bad. The last two rows give the number of events in the $Q\overline{Q}$ stream (see Figure 5.5) of good runs on peak and the fraction of these that I reject for having excessive BGO noise.

where E_{bmp} is the bump's energy in GeV. Figure 5.4 shows the two-dimensional distributions of N_{cry} and E_{bmp} for bumps in data and Monte Carlo events. The Monte Carlo simulation does not account for the effects that lead to noisy BGO events, and the fraction of Monte Carlo events rejected with the cuts described above is less than 0.001%. Table 5.1 summarizes the effect of noisy BGO events on the available data sample: noise conditions have generally improved since 1991. A new method for recovering information from noisy BGO events has recently been developed but it must be applied to raw data during data reconstruction. This method has so far only been applied to the data collected during 1994, and this is the reason for the much smaller fraction of events cut during this year.

As a final level of filtering, I reject certain photon candidates in selected hadronic events because of local problems with the BGO and TEC. I describe this filtering in more detail in Section 5.2.1.

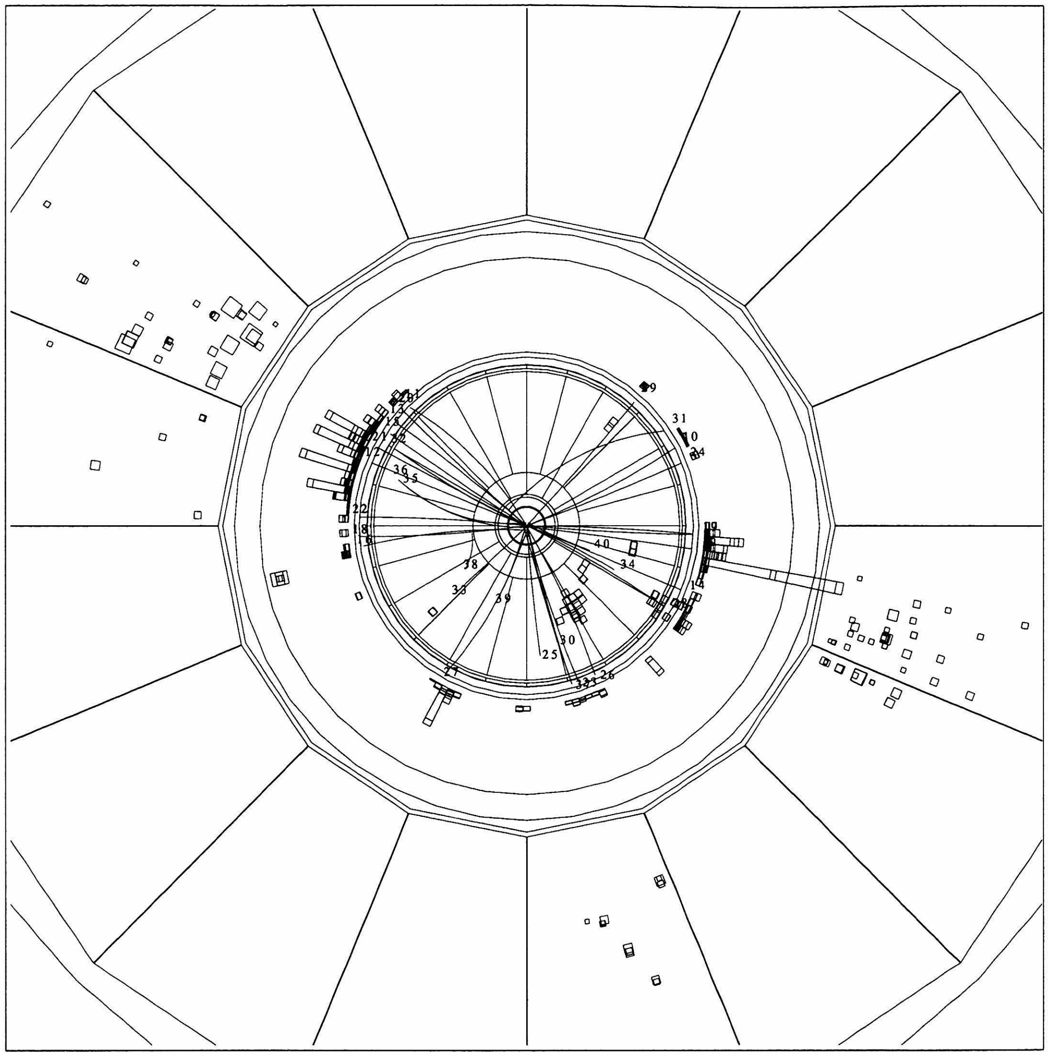

Figure 5.1: A typical hadronic Z decay recorded by the L3 detector, and displayed in the plane perpendicular to the beam axis. The central segmented region of the figure shows tracks reconstructed in the TEC as arcs originating near the nominal vertex. The outer segmented region shows HCAL energy deposits as squares whose size is proportional to the energy deposited. Energy deposits in the ECAL are shown as towers for each crystal, whose height is proportional to the crystal energy. In this projection, barrel crystals appear in the region between the TEC and the HCAL, and endcap crystals are superimposed over the TEC region.

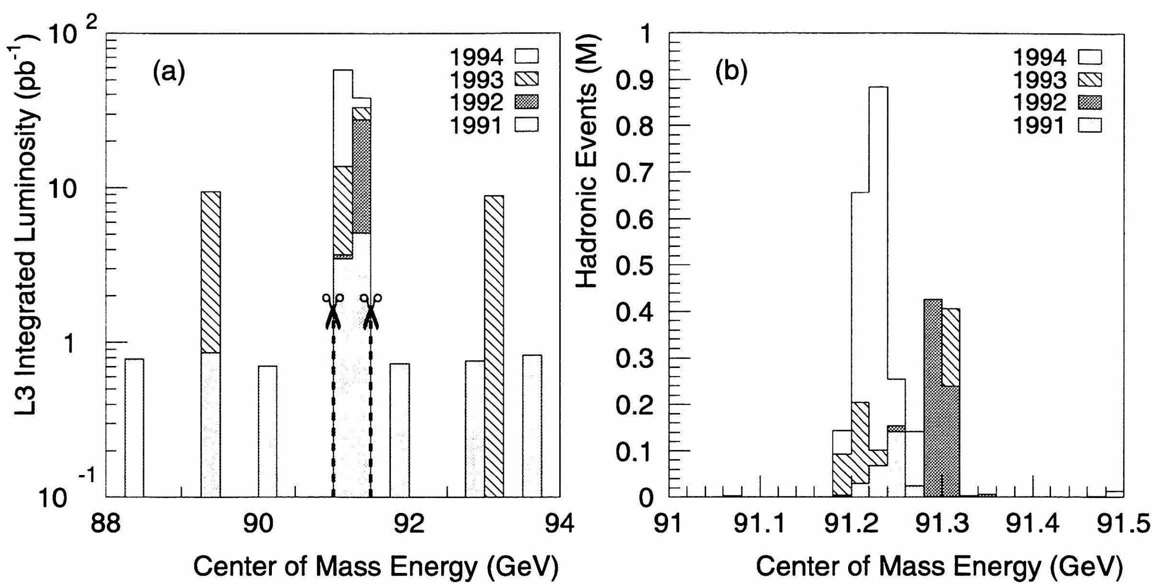

Figure 5.2: Center-of-mass energy distributions of L3 events recorded between 1991 and 1994. Figure (a) shows the integrated luminosity recorded for all energies, on a logarithmic scale, with dashed vertical lines marking the range of energies defined to be on peak. Figure (b) shows the number of hadronic events recorded in the on-peak range of energies, on a linear scale.

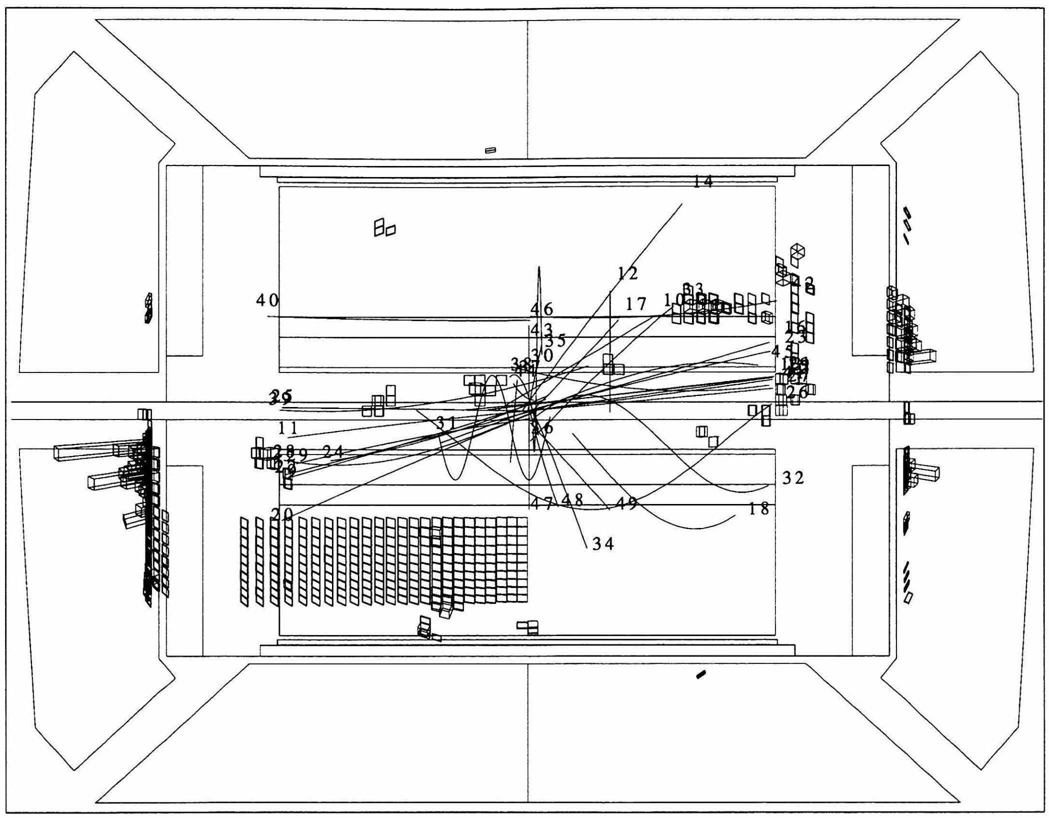

Figure 5.3: Display of a hadronic Z decay event in which excessive ECAL noise is present. The noise is evident as a rectangular region of crystals, all registering a small energy. The event is displayed in the y-z plane, and shows only the TEC and ECAL regions.

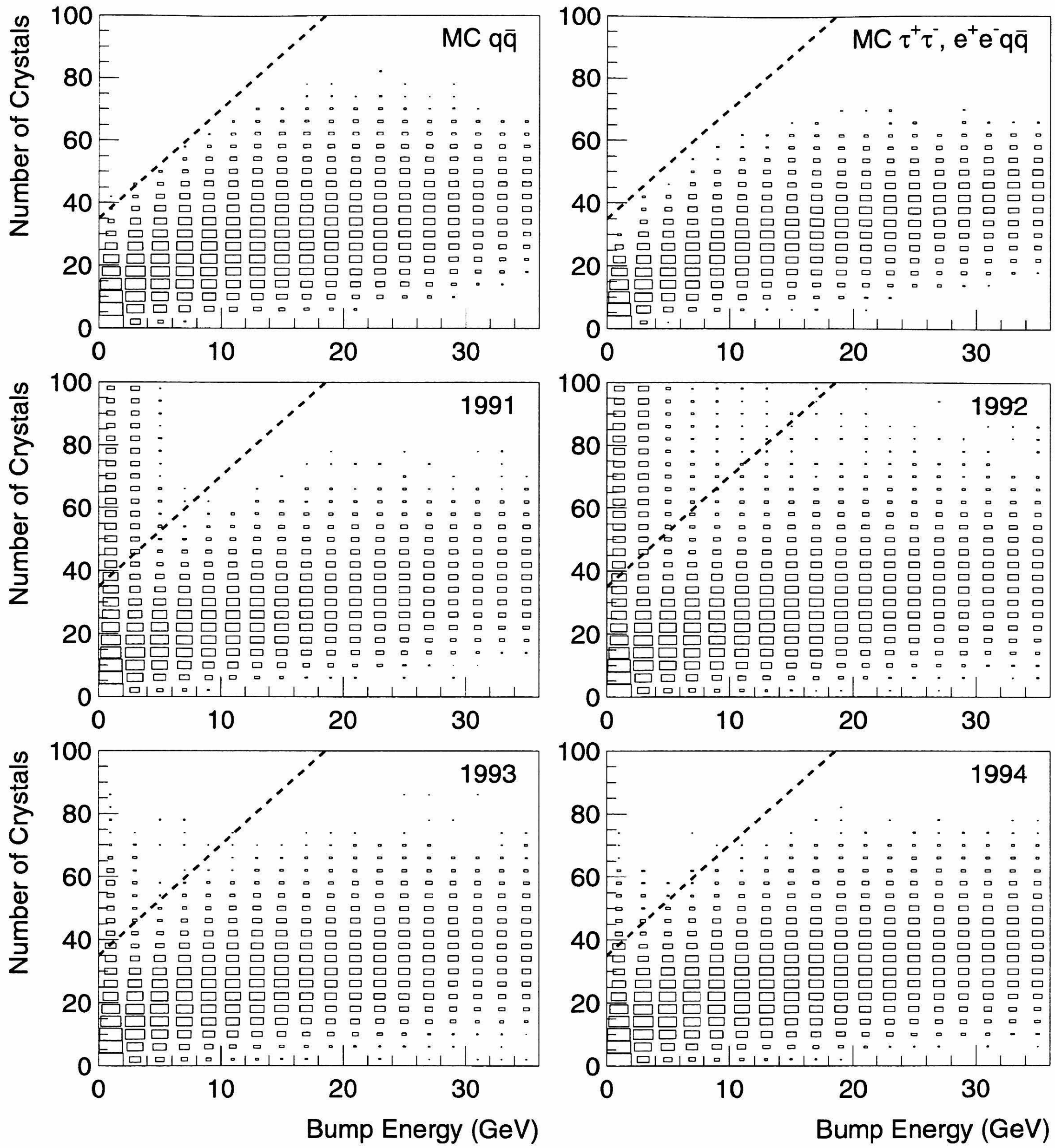

Figure 5.4: Two-dimensional distributions of N_{cry} and E_{bmp} for bumps in Monte Carlo events generated with different final states, and for bumps recorded between 1991 and 1994 in good events of the $\mathrm{Q\overline{Q}}$ stream (see Figure 5.5). The cut $N_{\mathrm{cry}} > 35+3.5\times E_{\mathrm{bmp}}$ is shown as a dashed line. The size of the boxes that are plotted is proportional to the logarithm of the corresponding number of bumps.

5.1.4 Offline Selection

Figure 5.5 gives a schematic overview of the flow of data from the L3 online system to a standard physics analysis. The most important step for my analysis occurs during the first pass of REL3 reconstruction, where each event is assigned to one or more physics split streams in order to simplify subsequent analyses. The relevant stream for hadronic Z decay events is the $\mathrm{Q\overline{Q}}$ stream. The criteria that are used during reconstruction to assign events to this stream are essentially a looser version of the selection cuts that I use in my analysis, and so they have a negligible effect on my analysis and I do not describe them further.

I select hadronic Z decay events from the $\mathrm{Q\overline{Q}}$ stream with two complementary approaches: in the first approach, I use information from reconstructed energy clusters in the calorimeters, and in the second, information from reconstructed tracks. In this analysis, I prefer the first method since it is efficient over a larger fiducial volume, and I reserve the track-based method as an independent check and for estimating systematic uncertainties associated with the event selection (see Section 6.3).

In both the track-based and calorimeter-based selection schemes, a set of energy vectors, $\{\vec{E}_i\}$, is first reconstructed for each event, and these are then used to evaluate the total visible energy

$$E_{vis} \equiv \sum_i^N |\vec{E}_i| \ ,$$

and the longitudinal and perpendicular components of the missing energy vector needed to balance the visible energy

$$\begin{aligned}
\Delta\vec{E} &\equiv -\sum_i^N \vec{E}_i \\
E_{\parallel} &= |\hat{z} \cdot \Delta\vec{E}| \\
E_{\perp} &= \sqrt{(\hat{x} \cdot \Delta\vec{E})^2 + (\hat{y} \cdot \Delta\vec{E})^2} \ .
\end{aligned}$$

In the calorimeter-based selection scheme, energy vectors are reconstructed from individual clusters in the electromagnetic calorimeter, and associated with additional clusters in the hadronic calorimeter that have a similar direction. The direction of an energy vector is determined from the energy-weighted center-of-gravity of the individual calorimeter deposits, and its magnitude is given by

$$E_i = \sum_j g_j E_{i,j} \ ,$$

where $E_{i,j}$ are the raw energies of the clusters associated with an energy vector and the *g-factors*, g_j, are chosen to optimize the resolution for the total visible energy E_{vis} (see Figure 5.6). Typical values for the g-factors lead to the reconstructed energies

$$E_i = \begin{cases} 1.4 \times E_{\mathrm{EC}} + 1.2 \times E_{\mathrm{HC}} & \text{for } 42^\circ < \theta\,(180^\circ - \theta) < 90^\circ \\ 1.7 \times E_{\mathrm{EC}} + 1.1 \times E_{\mathrm{HC}} & \text{for } 18^\circ < \theta\,(180^\circ - \theta) < 42^\circ \\ 1.7 \times E_{\mathrm{EC}} + 1.4 \times E_{\mathrm{HC}} & \text{for } 10^\circ < \theta\,(180^\circ - \theta) < 18^\circ \end{cases} \ ,$$

where the subscripts EC and HC denote the raw energies measured in the electromagnetic and hadronic calorimeters respectively, and the ranges of polar angles correspond to detector regions having different amounts of material. Vectors with a reconstructed energy of less than 100 MeV are dropped from the final list. In the case of a cluster due to a photon or an electron, the g-factors significantly overestimate the particle energy. This is not a serious problem for most hadronic event analyses; however, since I am selecting a sample of events enriched in energetic photons, I force $E_i \equiv E_{\mathrm{EC}}$ for electromagnetic-like bumps, which I define as those with $S_9^c/S_{25}^c > 0.95$ (see Section 4.4.2).

The cuts for selecting hadronic Z decays with the calorimeter-based method are

$$0.6 < \frac{E_{vis}}{\sqrt{s}} < 1.4 \quad , \quad \frac{E_{\|}}{E_{vis}} < 0.4 \quad , \quad \frac{E_{\perp}}{E_{vis}} < 0.4 \quad , \quad N \geq 13 \quad ,$$

where $\sqrt{s}$ is the nominal center-of-mass energy determined by LEP. The distributions of each variable, with the other three cuts applied, are shown in Figs. 5.6–5.9. Each distribution is plotted with both linear and logarithmic scales, and shows the comparison of L3 data with the cummulative (i.e., stacked one on top of the other so that the combined histogram can be directly compared with data) Monte Carlo predictions for different Z decay modes. I use the JETSET Monte Carlo to calculate the dominant decay into hadrons, $\mathrm{Z} \to \mathrm{q\bar{q}}(\gamma)$, the KORALZ[68] Monte Carlo for tau decays, $\mathrm{Z} \to \tau^+\tau^-$, and the DIAG36[69] Monte Carlo[1] for the two-photon process $Z \to \mathrm{e^+e^-q\bar{q}}$.

Small discrepancies between data and Monte Carlo predictions in the distributions of Figures 5.6–5.9 are mostly due to missing backgrounds in the Monte Carlo models, such as cosmic rays and beam-gas interactions, and to incomplete simulation of time-dependent variations of the detector response, such as those induced by readout noise and dead channels. These discrepancies are negligible for the level of precision required here[2].

Energy vectors for the track-based selection are determined from the momentum and direction of reconstructed tracks, with energies calculated assuming a $\pi^\pm$ mass. Tracks with momentum transverse to the incoming beams of less than 100 MeV are ignored. The selection cuts using the track-based method are

$$0.15 < \frac{E_{vis}}{\sqrt{s}} \quad , \quad \frac{E_{\parallel}}{E_{vis}} < 0.75 \quad , \quad \frac{E_{\perp}}{E_{vis}} < 0.75 \quad , \quad N \geq 5 \quad ,$$

and are chosen to be looser than the corresponding calorimeter-based cuts because of a lower efficiency for reconstructing tracks and a poorer resolution for determining track energies. An additional selection cut is applied based on the distribution of track azimuthal angles in an event: the differences in azimuthal angle between azimuthally adjacent pairs of tracks are computed and the *second* largest of these differences must be at most 170°. This cut eliminates events consisting of two back-to-back narrow clusters of tracks, which are characteristic of $\mathrm{Z} \to \tau^+\tau^-$ decays.

[1]Since the DIAG36 Monte Carlo prediction for the absolute rate of hadronic two-photon events is unreliable, I fix its normalization from the data in Figure 5.6, using the region $E_{vis}/\sqrt{s} < 0.3$.

[2]The L3 analysis of hadronic lineshape[70] includes corrections for most of these effects, and obtains a systematic uncertainty on the selection efficiency of $\pm 0.10\%$.

5.1.5 Summary

Table 5.2 summarizes the hadronic event selection statistics for data collected between 1991 and 1994. The total number of selected events using the calorimeter-based method is 2760K. The relative contributions from each year are 9%(91), 24%(92), 16%(93), and 51%(94). Including data from 1990 would add approximately 5% more events, but since the BGO endcaps were not installed during this period, I have not done so.

Year	1991	1992	1993	1994	TOTAL
$Q\overline{Q}$ Stream Events	302K	767K	508K	1649K	3224K
Track Selected	214K	577K	395K	1235K	2421K
	71.0%	75.3%	77.8%	74.9%	75.1%
Calor. Selected	255K	656K	442K	1407K	2760K
	84.5%	85.6%	87.0%	85.4%	85.6%

Table 5.2: Summary of hadronic event selection statistics for data collected during 1991–94. The first row gives the number of *good* events in the $Q\overline{Q}$ reconstruction stream for each year. The next two rows give the number and fraction (of the first row) of events selected using the track-based selection. The last two rows give the number and fraction of events selected using the calorimeter-based selection.

Table 5.3 summarizes the selection statistics for different simulated Monte Carlo processes. I estimate the efficiency of the calorimeter-based selection by taking the average of the results that I obtain with JETSET and HERWIG, finding

$$\varepsilon_{\text{had}} = 97.88 \pm 0.06 \pm 0.38\,\% \ ,$$

where the first error is the combined statistical uncertainty, and the second error is the systematic uncertainty estimated as half the difference between the efficiencies predicted by the two models. The dominant background using the calorimeter-based selection is from $Z \to \tau^+\tau^-$ events in which both taus decay hadronically. Since the expected total background contribution to the final sample is less than 0.25%, I do not consider it further.

Process	Cross Section	Event Generator	Events	Track Selected		Calorimeter Selected	
$Z \to q\bar{q}$	30.5 nb	JETSET	2182K	88.2%	(88.2%)	98.3%	(98.3%)
		HERWIG	730K	87.4%	(87.4%)	97.5%	(97.5%)
$Z \to \tau^+\tau^-$	1.5 nb	KORALZ	84K	1.0%	(0.05%)	4.2%	(0.21%)
$Z \to e^+e^-q\bar{q}$	2.8 nb	DIAG36	110K	2.4%	(0.22%)	0.5%	(0.05%)

Table 5.3: Summary of hadronic event selection statistics for Monte Carlo samples of different processes. All events are generated at $\sqrt{s} = 91.25$ GeV and simulated in the L3 detector. The selected fractions in parentheses are normalized to the hadronic cross section and represent the relative contributions of each process to the final selected event sample.

5.2 Selection of Photon Candidates

After selecting a sample of hadronic Z decays, I identify candidate FSR photons in these events, and then keep only those events with at least one such candidate. I select candidates from the reconstructed ECAL bumps in an event that are not associated with any charged track (I refer to such bumps as *neutral bumps*).

The main source of photons in hadronic events is the decay of neutral mesons (typically $\pi^0 \to \gamma\gamma$); however, in this analysis I am primarily interested in the much smaller contribution from photons radiated by a primary quark. In order to obtain a high-purity sample of these FSR photons, I require that photon candidates

- be isolated from other particles in the event in a cone of opening angle $\alpha_{\text{iso}} =$ 10°–25° (see Section 5.2.3),
- satisfy minimum and maximum energy requirements, 8 GeV $< E_\gamma <$ 44 GeV (see Section 5.2.4),
- be within a restricted fiducial volume, $45° < \theta_\gamma < 135°$ or $17.5° < \theta_\gamma\,(180° - \theta_\gamma) < 35°$ (see Section 5.2.5),

and

- have a pattern of ECAL energy deposits consistent with those expected for a single photon, $p_\gamma > 0.1$ (see Section 5.2.6).

The fiducial volume cut is primarily to reduce the background from photons radiated by the e^+e^- initial state; the remaining cuts serve mostly to reject hadronic background. Figure 5.10 shows an event with a very energetic photon satisfying these requirements. In the following sections I describe each of these cuts in greater detail.

In Figures 5.12, 5.13, and 5.14, which appear below, I show the distributions of each of the three variables on which I cut to select candidates (E_γ, θ_γ, and p_γ) when the other two cuts are applied. I compare L3 data with the predictions of the JETSET Monte Carlo, showing the individual JETSET contributions from FSR photons, ISR photons, and hadronic background. The different Monte Carlo contributions are shown cummulatively in these Figures so that the combined histograms can be directly compared with the data points.

Nearly all of the predicted hadronic background is from neutral hadron decays into photons, but there is a small charged background of 2%–3% consisting of electrons, which are not rejected by a shower-shape analysis, and charged pions. The neutral hadronic background is primarily π^0 (70%–90%, depending on the isolation requirement) with smaller contributions from η, K_S, and K_L. Figure 6.1 in the next chapter shows the predicted energy distributions for the main components of the hadronic background.

5.2.1 Detector and Data-Acquisition Status

In Section 5.1.3, I described the filtering that I apply to runs and events in order to control systematic uncertainties related to the performance of the detector and of the data-acquisition system. In this section, I describe an additional level of filtering that I apply to individual bumps in an event, based on the local performance of the TEC and the ECAL.

For each photon candidate bump, I require that all the crystals in the central 3×3 matrix of of a bump were operating normally and register a non-zero energy, and that the adjacent TEC sectors were also operating normally. The first of these requirements is necessary to ensure consistent performance of the shower shape analysis described in Section 5.2.6, and the second to ensure efficient association between tracks and bumps as described in Section 5.2.2. As described below, I consider three types of problems that can affect the performance of these selection requirements: *dead* ECAL readout rings, isolated *hot* or *dead* BGO crystals, and *dead* TEC half-sectors. Table 5.4 summarizes the deadtime due to each of these effects for data collected between 1991 and 1994, and Figure 5.11 shows the azimuthal-angle dependence of the deadtime.

Year	1991	1992	1993	1994	TOTAL
Bad Rings	0.7%	2.4%	3.1%	1.6%	1.9%
Bad Crystals	7.7%	9.2%	7.8%	7.7%	8.1%
Bad Sectors	13.7%	4.6%	0.6%	4.4%	4.7%
Overall	22.1%	16.2%	11.5%	13.8%	14.8%

Table 5.4: Summary of the average deadtimes due to dead ECAL rings, isolated hot or dead BGO crystals, and dead TEC sectors, during each of the years 1991–94. The last column gives the weighted average deadtimes for the four years, calculated using weights proportional to the number of selected hadronic events in each year.

The first type of problem I consider is related to the first level of the ECAL readout which consists of 192 *rings* (see Section 4.3.3). Each year, a small number—between one and five—of these rings do not provide any data for the crystals they read out: I refer to these rings as *dead*. The second type of problem I consider is the effect of isolated crystals that are either excessively noisy (*hot*) or do not provide any data (*dead*). Both dead rings and hot or dead crystals cause bumps to be rejected by killing crystals in their central 3×3 matrices. The overall deadtime from these problems is 1.9% for dead rings and 8.1% for bad crystals. Note that the actual fraction of

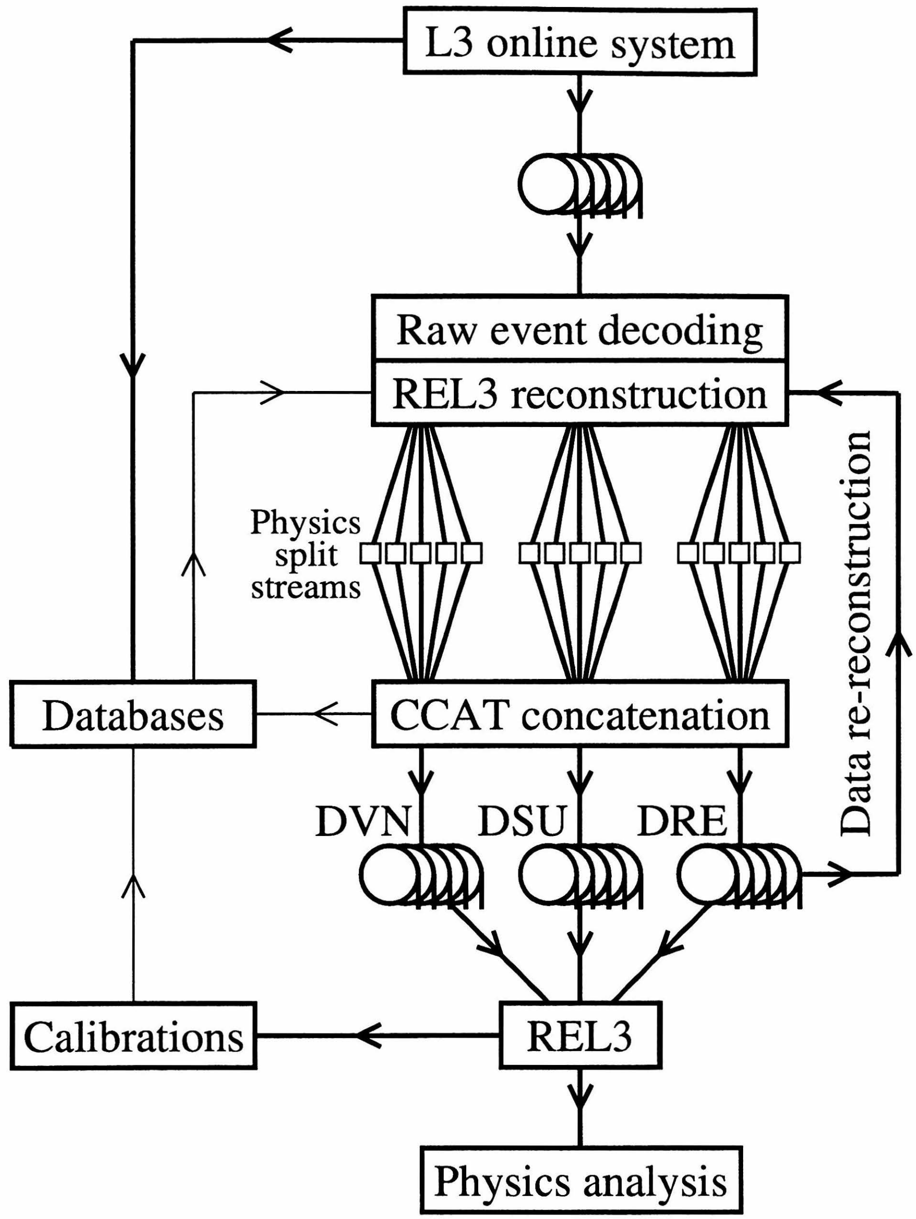

Figure 5.5: Schematic diagram of the flow of L3 data from the online trigger and data-acquisition system (shown at the top), to standard physics analyses (shown at the bottom). Events recorded online are split into physics streams after the first pass of REL3 reconstruction, one of which is the $Q\overline{Q}$ stream that I use for my analysis.

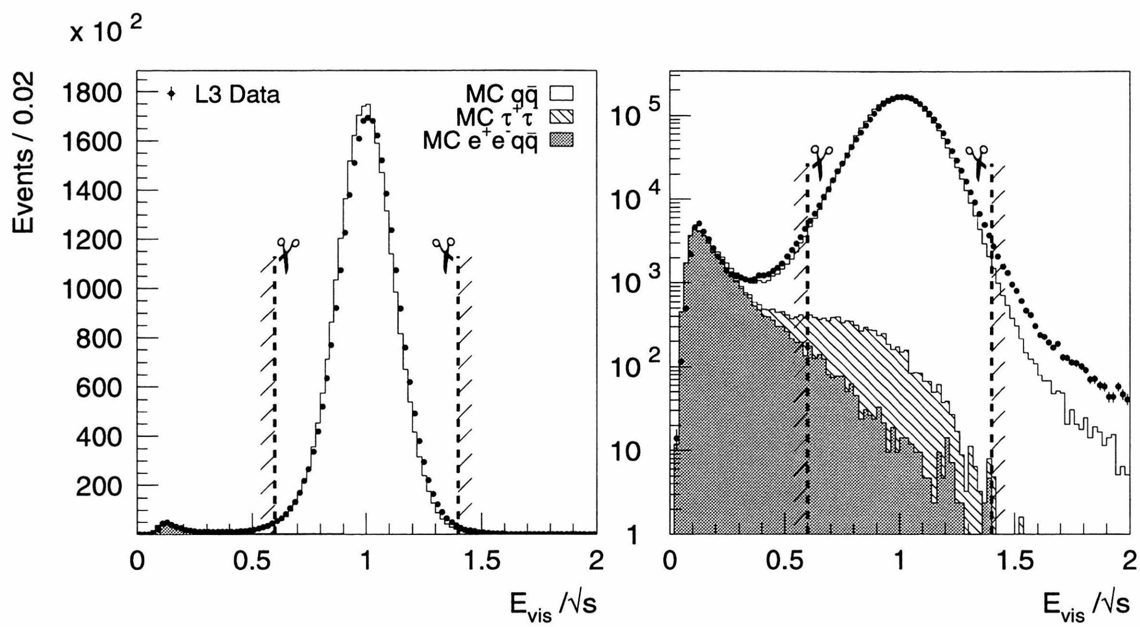

Figure 5.6: Distribution of the visible energy, after all other selection cuts have been applied. The visible energy is calculated with the calorimeter method, and displayed with linear and logarithmic vertical scales.

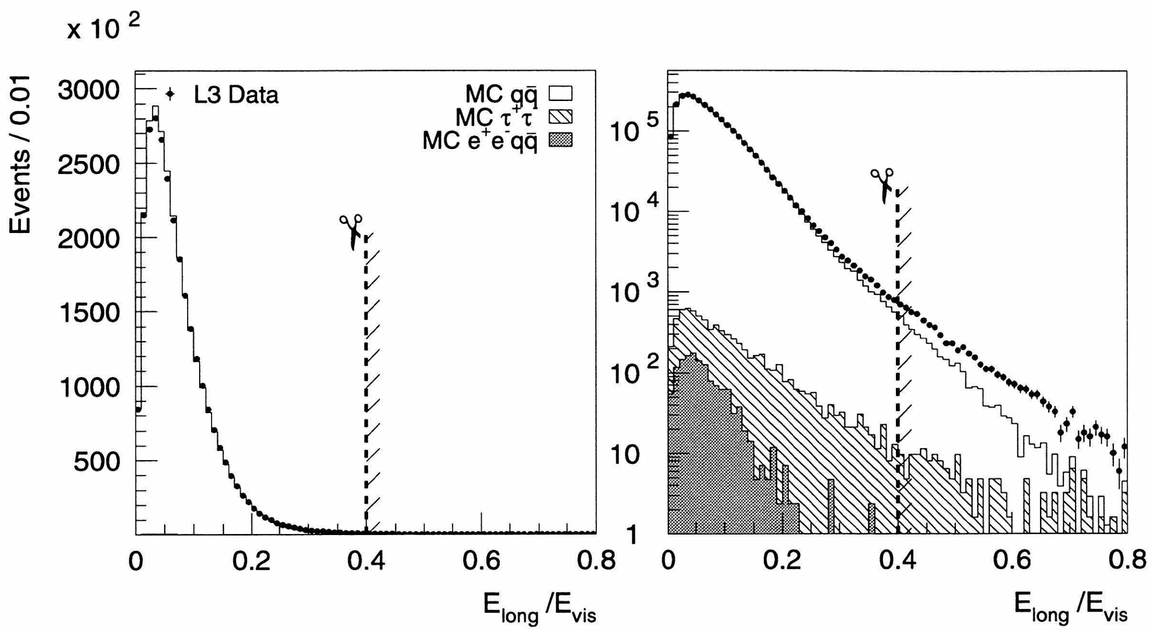

Figure 5.7: Distribution of the longitudinal component of the missing energy vector, after all other selection cuts have been applied. The missing energy is calculated with the calorimeter method, and displayed with linear and logarithmic vertical scales.

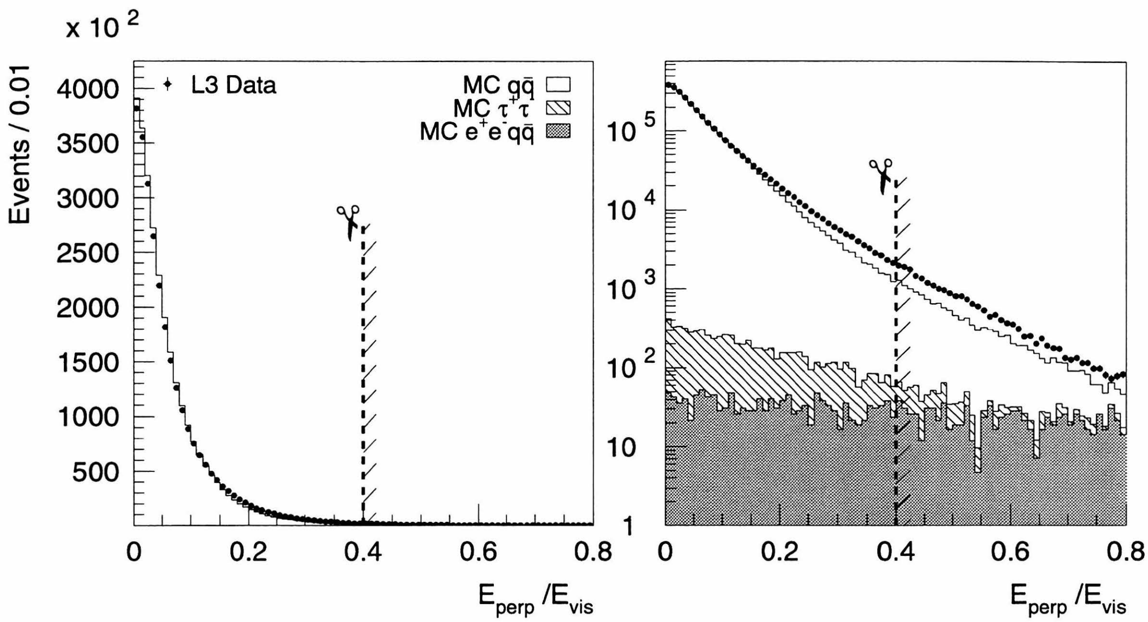

Figure 5.8: Distribution of the perpendicular component of the missing energy vector, after all other selection cuts have been applied. The missing energy is calculated with the calorimeter method, and displayed with linear and logarithmic vertical scales.

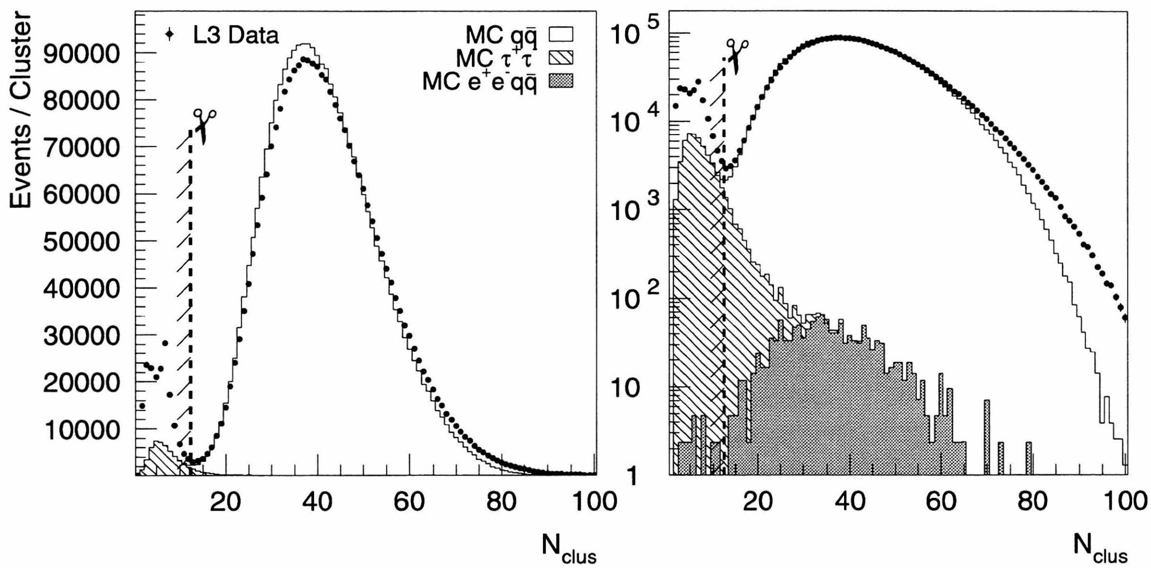

Figure 5.9: Distribution of the number of calorimeter clusters, after all other selection cuts have been applied, displayed with linear and logarithmic vertical scales.

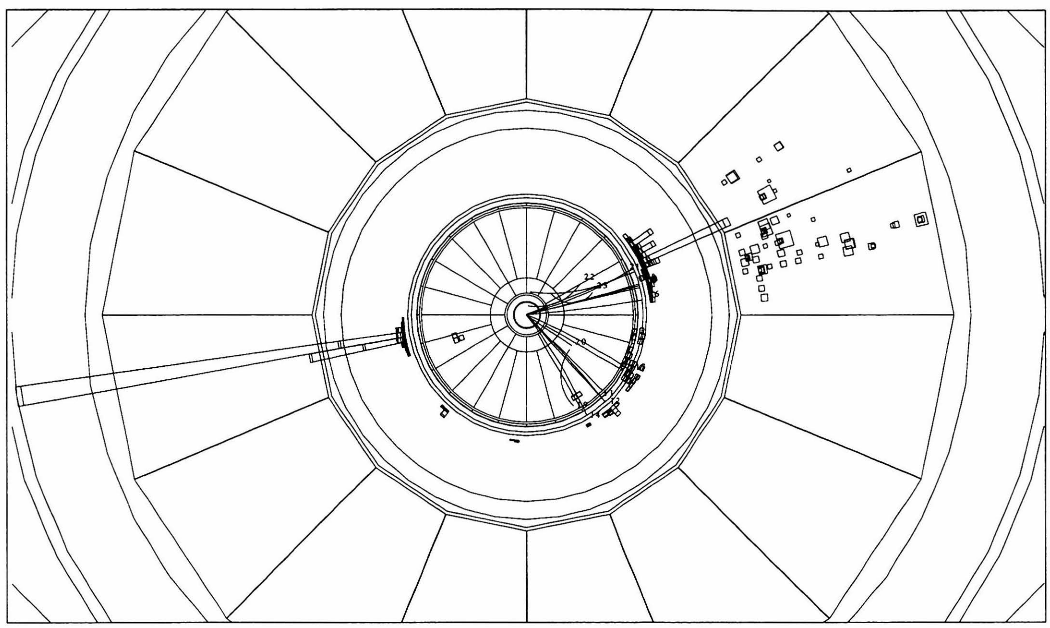

Figure 5.10: Hadronic Z decay with a very energetic photon candidate illustrating the selection criteria used in this analysis. The candidate is not associated with any charged tracks and is isolated from other particles in the event. The event is displayed in the plane perpendicular to the beam axis.

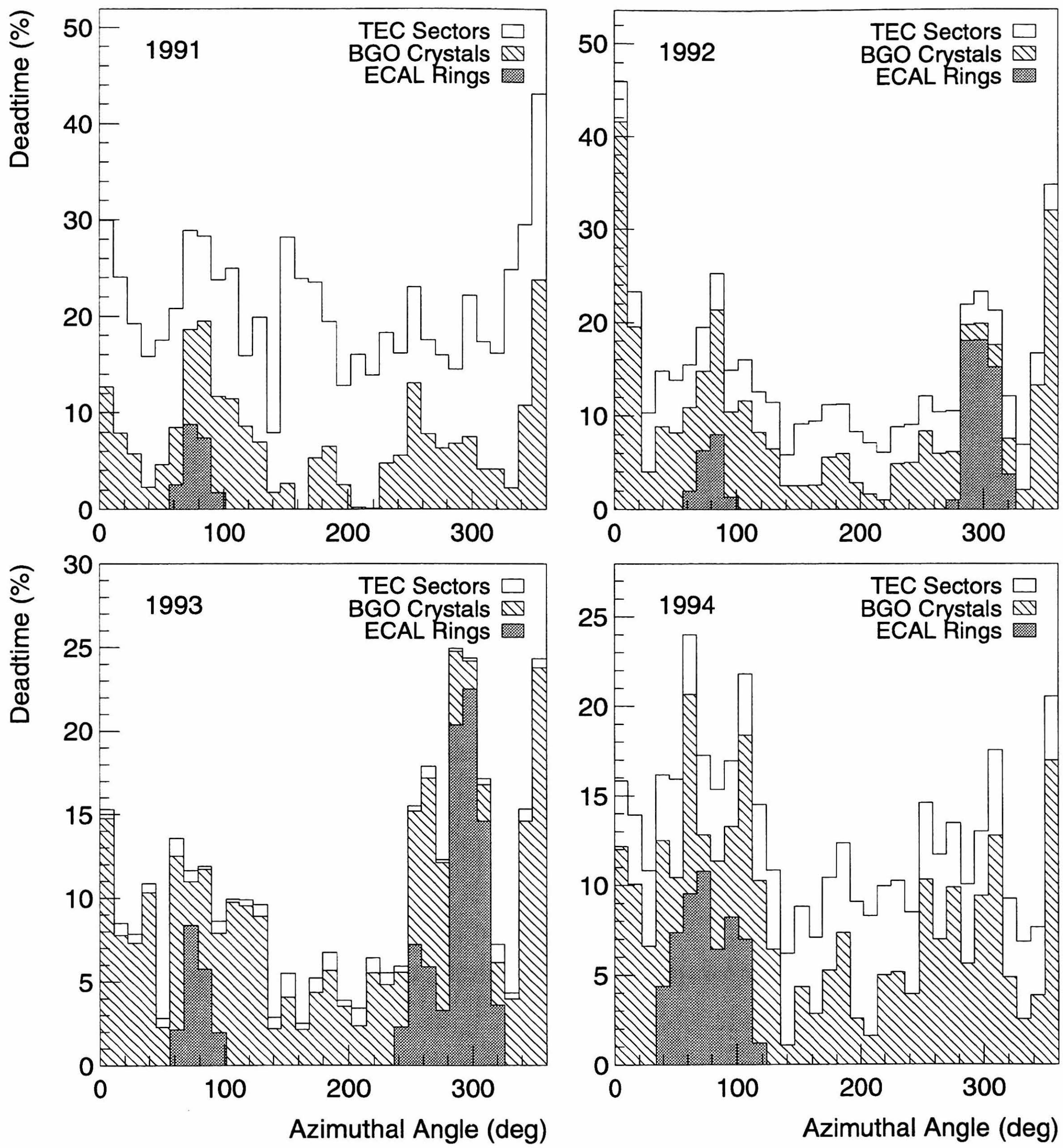

Figure 5.11: Azimuthal distributions of TEC and ECAL deadtimes causing photon candidates to be rejected, during each of the years 1991–94. Note the different vertical scales for each year.

crystals which are bad is less than 1%, but that each isolated bad crystal also kills bumps centered on the neighboring eight crystals in a 3×3 matrix.

The selection of neutral bumps described in Section 5.2.2 requires that both the track and the bump that are due to a single charged particle can be efficiently associated with each other. This association is complicated by the fact that the high-voltage power supplies to each TEC half-sector (24 inner half-sectors and 48 outer half-sectors) can turn off and on again on short timescales. When the high-voltage to a half-sector is turned off, it does not record any tracks so all bumps adjacent to the half-sector appear to be neutral (I refer to such a half-sector as being *dead*). In order to monitor this problem, I use standard files that describe the status of each half-sector during four minute intervals, and which are compiled from high voltage control information stored in the online databases and from analysis of track occupancy in hadronic events. When a half-sector is dead for a fraction of a four-minute interval, it is flagged as dead for the entire interval.

For a bump whose energy-weighted center-of-gravity is located at (θ, ϕ), I require that the adjacent inner TEC half-sectors be active if $\theta < 35°$ or $\theta > 145°$, and that the adjacent outer TEC half-sectors be active if $25° < \theta < 155°$. I define the adjacent inner and outer TEC half-sectors to a bump by matching in ϕ, and then taking a single half-sector if the bump is located its central half-region, away from the boundaries, or otherwise a pair of neighboring half-sectors. When a bump is adjacent to a dead TEC sector, I remove it from the final event sample. The overall deadtime from TEC high-voltage problems is 4.7%.

The detector and data-acquisition problems that I describe above are not included in the detector simulation I use, so I apply efficiency corrections to the Monte Carlo simulated events to account for their effects. This approach then allows direct comparison of distributions obtained from data and Monte Carlo events. I apply corrections to a Monte Carlo event by randomly assigning it a year between 1991 and 1994, using weights proportional to the number of selected hadronic events, and then applying year- and azimuthal-angle-dependent corrections which I obtain from data.

5.2.2 Selection of Neutral Bumps

In order to reject bumps due to charged particles, I require that photon candidate bumps have no associated reconstructed TEC tracks in an event. The matching between bumps and tracks is performed as part of the standard *across-L3* (AXL3) reconstruction, where each bump can be associated with several tracks, but a track is associated with at most one bump. Matching is performed primarily in the plane transverse to the beam, by extrapolating a track's arc to the estimated position of a bump's shower maximum, and then measuring the azimuthal separation $|\Delta\phi|$ at this radius. When the polar angle of a track can be constrained, matching is also performed in θ; however, since track θ coordinates are usually determined to a much lower precision than the corresponding ϕ coordinates, this information serves mostly to reduce combinatorics leading to accidental matches.

5.2.3 Selection of Isolated Bumps

I evaluate the isolation of a photon candidate bump by summing the energy of any other bumps that lie in a cone of half-angle α_{iso} around the candidate, and then requiring that the total energy be less than some maximum value E_{iso}

$$E(\alpha_{\text{iso}}) \equiv \sum_{i \neq \gamma} \Theta(|\hat{\mathbf{n}}_\gamma \cdot \hat{\mathbf{n}}_i| < \cos\alpha_{\text{iso}}) \cdot E_i \leq E_{\text{iso}} \,.$$

I calculate the angles between bumps using direction vectors $\hat{\mathbf{n}}_i$ which point from the L3 origin to the energy-weighted center-of-gravity of a bump. I estimate the energy E_i of a bump appearing within an isolation cone using the sum of the energies of the crystals assigned to the bump. In my analysis, I consider four different isolation requirements: $\alpha_{\text{iso}} = 10°$, $15°$, $20°$, and $25°$. For the maximum energy allowed in a cone, I choose the smallest possible value, $E_{\text{iso}} = 40$ MeV (the standard L3 reconstruction drops any bump with less energy than this value). This amount of energy is large enough relative to the typical readout noise of 1–2 MeV per crystal to be reliably measured, and small enough relative to the energy of photon candidates for clean pattern recognition in the shower-shape analysis.

Note that even when a photon candidate appears isolated in the detector, it can still be accompanied by particles whose total energy is greater than 40 MeV due to two main effects: first, hadrons typically do not deposit all of their energy in the ECAL, and second, charged particles that are produced within the isolation cone can be curved by the L3 magnetic field and deposit their energy outside of the cone. The second of these effects can also cause a genuinely isolated photon to appear non-isolated, when a charged particle trajectory is bent within its isolation cone. I have studied these effects using JETSET Monte Carlo events simulated in the L3 detector, and I find that they are small. The actual total energy accompanying bumps that appear isolated in the detector is less than 40 MeV (400 MeV) for 97.7% (99.9%) of the bumps selected with $\alpha_{\text{iso}} = 10°$ and for 90.0% (99.1%) of the bumps selected with $\alpha_{\text{iso}} = 25°$.

5.2.4 Photon Energy Cut

I estimate the energy of photon candidates with the corrected sum-of-9 energy S_9^c of the corresponding bump (see section 4.4.2). Figure 5.12 shows the energy distributions of candidates selected with all other candidate selection cuts applied. The predicted contributions from both ISR and hadronic background are more strongly peaked at low energies than the FSR contribution, so I apply a minimum energy cut to improve the purity of the final sample. There is a secondary peak in both the ISR and hadronic background contributions at high energies, due to the dynamics of the underlying processes. There is also a slight disagreement at energies near 45 GeV due to the fact that the data is recorded over a range of beam energies while the Monte Carlo events are generated at a fixed energy. In order to suppress this energetic background and to allow comparison between data and Monte Carlo, I also apply a maximum energy cut. The final photon candidate energy requirement is

$$8 \text{ GeV} < E_\gamma < 44 \text{ GeV} .$$

There is a discrepancy between the observed rate of photon candidates and Monte Carlo predictions which is largest for less isolated candidates. In Section 5.2.6, below, I investigate the origin of this discrepancy.

5.2.5 Fiducial Volume Cut

I restrict the fiducial volume of photon candidates using a cut on their polar angle, θ_γ. I estimate θ_γ for a candidate from the position of the energy-weighted center-of-gravity of the corresponding bump, with respect to the L3 origin. The electromagnetic calorimeter covers the region $10^\circ \lesssim \theta_\gamma \lesssim 170^\circ$, with gaps at approximately 40° and 140° between the barrel and endcap regions. Figure 5.13 shows the polar angle distribution of photon candidates selected with all other cuts applied. The predicted contributions from both ISR and hadronic background are strongly peaked in the forward and backward directions. In the case of ISR, this peaking is due to the dynamics of the $e^+e^- \to e^+e^-(\gamma)$ process. In the case of the hadronic background, it is due to the large solid angle subtended by individual crystals near the beampipe, resulting in a lower efficiency for rejecting overlapping $\pi^0 \to \gamma\gamma$ decays with a shower-shape analysis. The hadronic background contribution is also larger near the gap between the barrel and endcap regions, particularly for smaller values of the isolation angle α_{iso}. This effect is due to the inefficiency of the isolation cut in this region, which is proportional to the fraction of the isolation cone that overlaps the gap. In order to improve the purity of the final sample, I restrict photon candidates to the fiducial volume

$$45^\circ < \theta_\gamma < 135^\circ \text{ or } 17.5^\circ < \theta_\gamma\,(180^\circ - \theta_\gamma) < 35^\circ .$$

The discrepancy between data and Monte Carlo predictions mentioned in Section 5.2.4 is again evident in Figure 5.13. In addition to being larger for less isolated

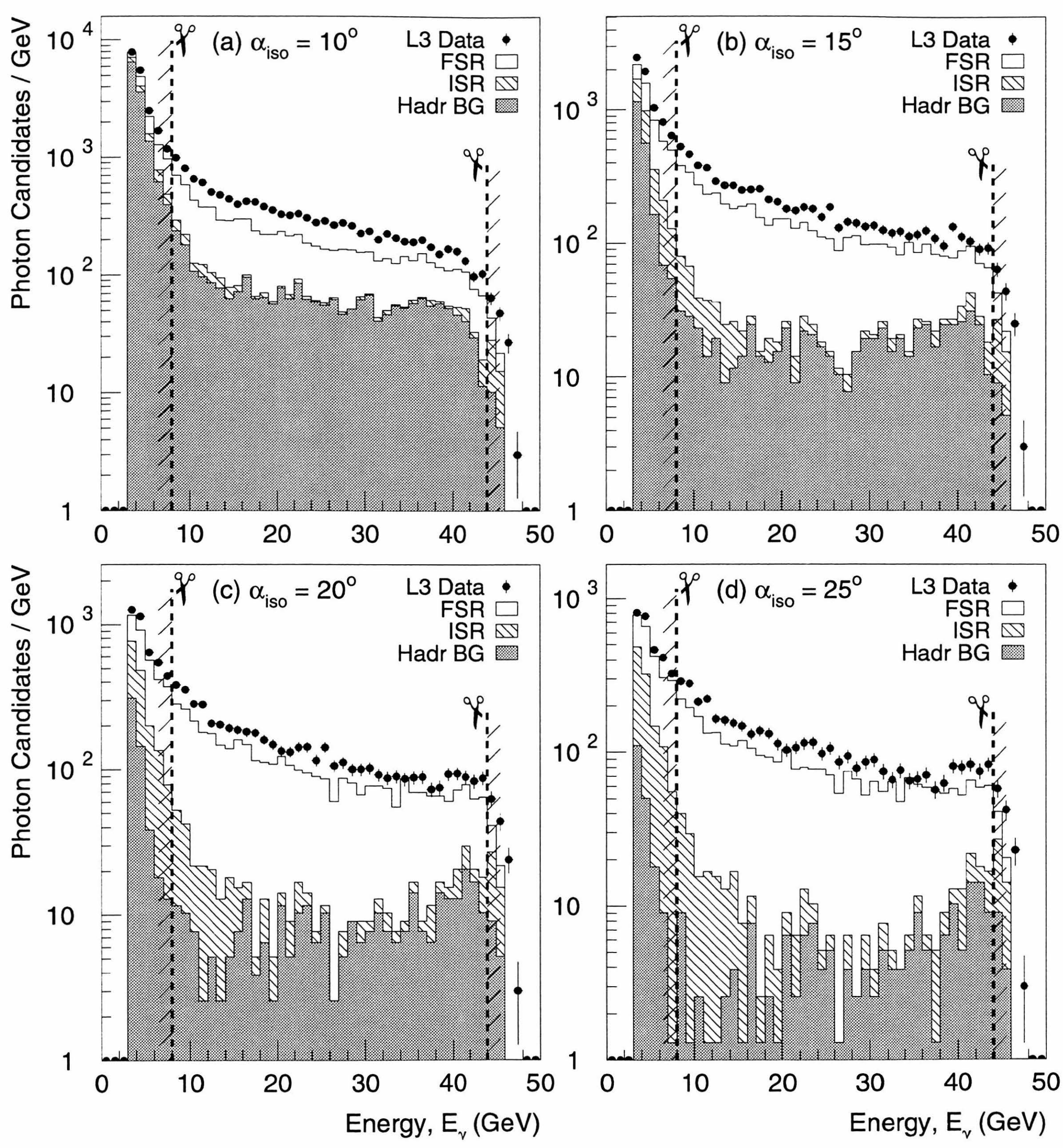

Figure 5.12: Energy distributions of photon candidates, with dashed lines showing the final energy cut: 8 GeV $< E_\gamma <$ 44 GeV. The figures correspond to the isolation requirements $\alpha_{\rm iso} = 10°$ (10), 15° (b), 20° (c), and 25° (d). The Monte Carlo predictions were calculated using JETSET.

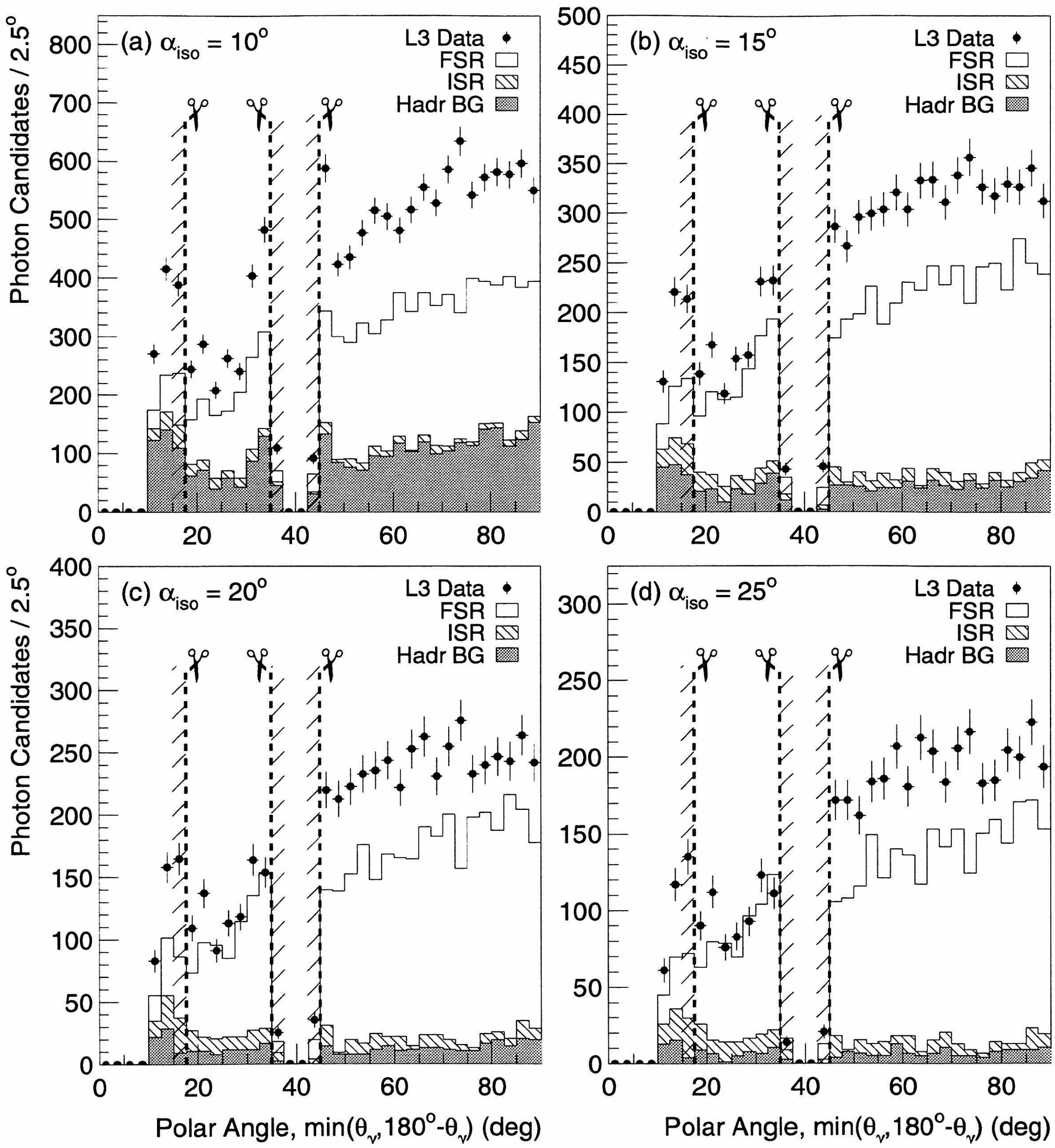

Figure 5.13: Polar angle distributions of photon candidates, with dashed lines showing the final cut: $45° < \theta_\gamma < 135°$ or $17.5° < \theta_\gamma\,(180° - \theta_\gamma) < 35°$. The figures correspond to the isolation requirements $\alpha_{\text{iso}} = 10°$ (a), $15°$ (b), $20°$ (c), and $25°$ (d). The Monte Carlo predictions were calculated using JETSET.

candidates, the discrepancy is also larger in the barrel than in the endcap regions of the ECAL. Note that the detector and data-acquisition problems described in Section 5.2.1 introduce small effects which are non-uniform in polar angle, and these deviations are reflected in Figure 5.13 as well.

5.2.6 Shower-Shape Analysis

The pattern of individual crystal energies in a bump provides a transverse sampling of the shower that develops when a particle passes through the electromagnetic calorimeter (see section 4.1). In the case of electrons and photons, the resulting shower has a characteristic shape that does not depend strongly on the particle energy in the range $E \simeq$ 1–50 GeV. Therefore, it is in principle possible to distinguish between the shower generated by a single photon, and the overlapping showers from almost collinear photons (e.g. from the decay of an energetic π^0). In practice, this approach is limited by how coarsely showers are sampled, which is in turn determined by the crystal transverse dimensions. With fewer samplings of the calorimeter response, it is more difficult to disentangle the effects of varying photon impact parameter and overlapping showers (see Figure A.1 of Appendix A).

To analyze shower shapes in this thesis, I have developed a π^0/γ discriminator based on an artificial neural network, which I call NNDISC. A detailed description of the development and performance of this method is provided in Appendix A; here I only describe aspects relating my analysis. The NNDISC method has better π^0 rejection than previous methods, and is the first that can be used in both the barrel and endcap regions.

The discriminator provides a value between zero and one, which I refer to as p_γ, based on input values derived from the energies of the central 5×5 matrix of crystals of a bump. The distribution of p_γ is ideally flat for bumps due to an isolated photon, so that applying a cut on the minimum value of p_γ has an energy-independent efficiency for selecting isolated photons equal to $1-p_\gamma$. The distribution of p_γ for bumps due to an isolated hadron is peaked near zero, so that a cut on the minimum value of p_γ results in an enriched sample of bumps due to a single photon. Hadronic decays into photons that are either well-separated or almost collinear are not rejected by a shower-shape analysis. The first of these configurations occurs mostly at low energies, and so is suppressed with a minimum energy requirement for photon candidates. The second configuration occurs most frequently at high energies and constitutes an irreducible source of background (I discuss the estimation and subtraction of this background in Section 6.1.2).

Figure 5.14 shows the distributions of p_γ for photon candidates selected with all other cuts applied. The predicted contributions from FSR and ISR are indistinguishable in these distributions, since they both consist of genuine single photons, and are approximately uniformly distributed across the full range of p_γ. The predicted hadronic background contribution is strongly peaked at values of p_γ near zero, but also has a component covering the full range of p_γ, which decreases for larger values of p_γ. In order to reject hadronic background from the final sample, I impose a shower-shape cut of

$$p_\gamma > 0.1 ,$$

and I expect the efficiency of this cut to be 90% for FSR photons.

The large differences between the predicted p_γ distributions of ISR and FSR, and of hadronic background, make it possible to compare data and Monte Carlo separately for these two types of contribution. By comparing data and Monte Carlo in the region $p_\gamma > 0.1$ of Figure 5.14, I find that JETSET underestimates the contribution of ISR and FSR by 10%–30%, and that this discrepancy is larger for less isolated photons. By comparing in the region of p_γ near zero, I find that JETSET underestimates the hadronic background contribution by 20%–100%, and that this discrepancy is larger for more isolated photons. If I assume that the amount of hadronic background with small values of p_γ is representative of the amount with higher values, then I expect similar discrepancies for the hadronic contribution to the final photon candidate sample. This assumption is reasonable for hadrons decaying into overlapping photons, since the main effect that determines the value of p_γ is the kinematics of the decay, which I expect to be reliably described by the Monte Carlo.

5.2.7 Summary

Table 5.5 summarizes the number of photon candidates selected when each of the cuts described above is applied in turn. The observed rate of photon candidates selected per hadronic event (f in Table 5.5) is larger than predicted by the Monte Carlo JETSET and HERWIG. This discrepancy varies between 29%–15% for JETSET and 7%–3% for HERWIG, and is larger for less isolated bumps. If the JETSET ISR prediction is added to the HERWIG prediction, which does not include ISR, then the agreement between data and HERWIG is improved. I select a total of 11785 photon candidates with an isolation of at least 10° from data collected between 1991 and 1994. In the analysis which I describe in the next chapter, I focus on the final energy distributions of photon candidates, selected with four isolation requirements, which are shown in Figure 5.15. Table 5.6 gives the numbers of candidates that I select as a function of energy and isolation, which correspond to the contents of each of the bins of Figure 5.15.

Among the events in which I have selected a photon candidate isolated by at least 10°, there are 34 events with two such photon candidates. Figure 5.16 shows a display of one of these events, recorded during 1994. There is no evidence of a peak in the distribution of the photon-pair invariant masses in these events, within statistical uncertainties. Figure 5.17 shows this distribution for the larger sample of 221 events which I obtain by relaxing the minimum energy requirement from 8 GeV to 3 GeV. The Monte Carlo predictions for the number of events with a pair of photon candidates having $E_\gamma > 8$ GeV are 12 ± 4 (JETSET) and 30 ± 9 (HERWIG).

Selection Cut	L3 DATA		JETSET	HERWIG
$\alpha_{\text{iso}} = 10°$	N	$10^3 \cdot f$	$10^3 \cdot f$	$10^3 \cdot f$
Energy	33519	10.277 ± 0.056	8.781 ± 0.063	10.208 ± 0.092
Fid.Volume	30729	9.422 ± 0.054	8.011 ± 0.061	9.230 ± 0.087
Shwr.Shape	11785	3.613 ± 0.033	2.802 ± 0.036	3.388 ± 0.053
DATA/MC			1.290 ± 0.020	1.066 ± 0.019
$\alpha_{\text{iso}} = 15°$				
Energy	11967	3.669 ± 0.034	3.033 ± 0.037	3.549 ± 0.054
Fid.Volume	10870	3.333 ± 0.032	2.753 ± 0.036	3.213 ± 0.052
Shwr.Shape	6927	2.124 ± 0.026	1.794 ± 0.029	2.071 ± 0.041
DATA/MC			1.184 ± 0.024	1.026 ± 0.024
$\alpha_{\text{iso}} = 20°$				
Energy	7563	2.319 ± 0.027	1.963 ± 0.030	2.231 ± 0.043
Fid.Volume	6871	2.107 ± 0.025	1.802 ± 0.029	2.049 ± 0.041
Shwr.Shape	5224	1.602 ± 0.022	1.398 ± 0.025	1.558 ± 0.036
DATA/MC			1.145 ± 0.026	1.028 ± 0.028
$\alpha_{\text{iso}} = 25°$				
Energy	5551	1.702 ± 0.023	1.459 ± 0.026	1.628 ± 0.037
Fid.Volume	5074	1.556 ± 0.022	1.353 ± 0.025	1.510 ± 0.035
Shwr.Shape	4166	1.277 ± 0.020	1.115 ± 0.023	1.218 ± 0.032
DATA/MC			1.145 ± 0.029	1.048 ± 0.032

Table 5.5: Summary of photon candidate selection cuts giving, for different isolation cuts, the total number N of candidates selected after successive cuts are applied (for L3 DATA) and the fraction $f = N/N_{\text{had}}$ (for L3 DATA, JETSET, and HERWIG) where N_{had} is the number of selected hadronic events. The last row of each section gives the ratios between the values of f for data and Monte Carlo events, for the two Monte Carlo models. All of the errors given are statistical uncertainties.

	Isolation Cut ($\alpha_{\rm iso}$):			
Energy	10°	15°	20°	25°
8–12 GeV	3048	1739	1301	1005
12–16 GeV	1821	1077	796	629
16–20 GeV	1574	920	672	514
20–24 GeV	1284	719	551	439
24–28 GeV	1109	615	476	384
28–32 GeV	928	534	394	328
32–36 GeV	823	467	351	274
36–40 GeV	700	459	330	272
40–44 GeV	498	397	353	321
TOTAL	11785	6927	5224	4166

Table 5.6: Summary of the number of photon candidates selected in different energy intervals (rows) and using different isolation requirements (columns).

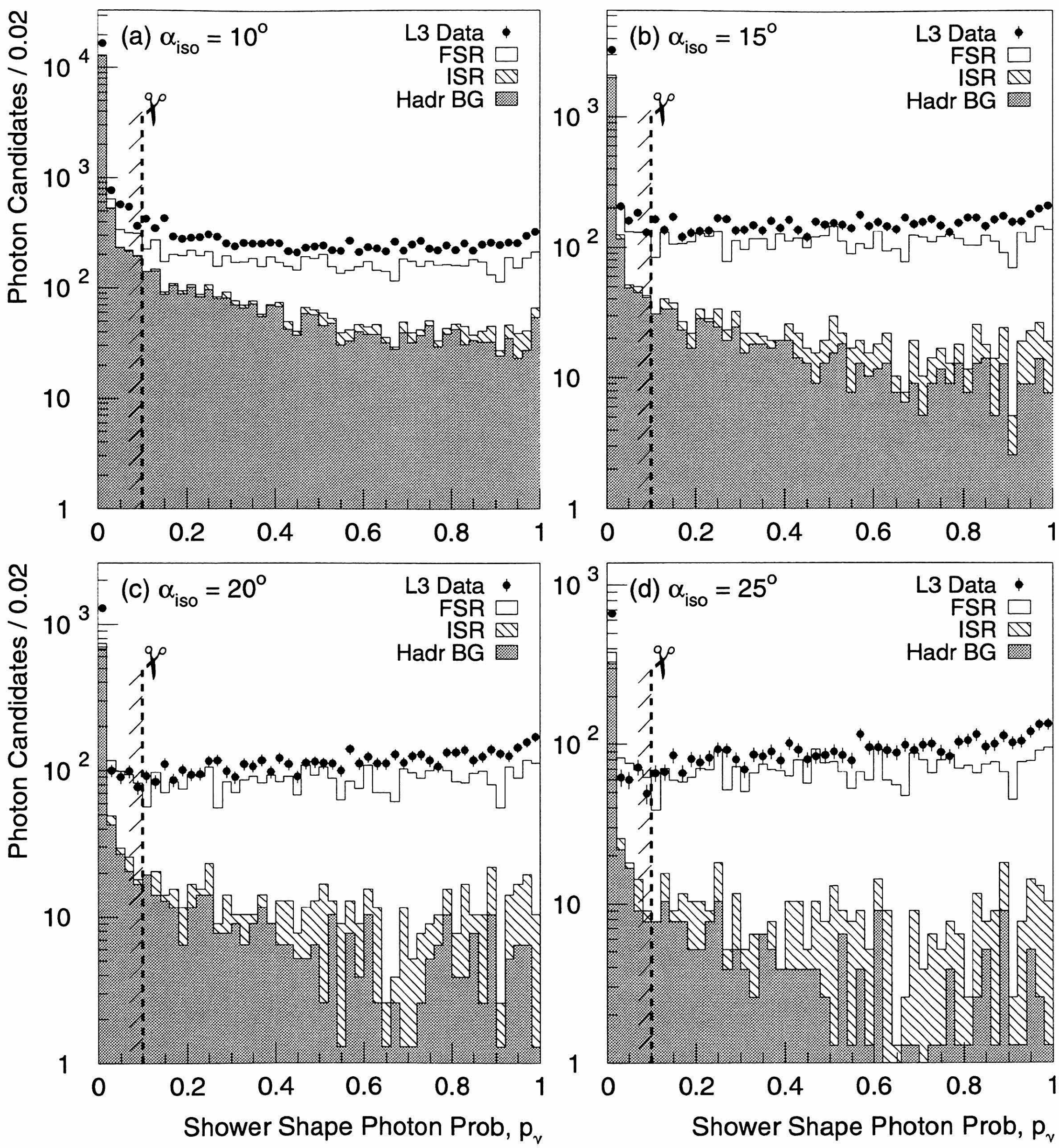

Figure 5.14: Distributions of the π^0/γ discriminator photon probability p_γ for photon candidates, with a dashed line showing the final cut: $p_\gamma > 0.1$. The figures correspond to the isolation requirements $\alpha_{\rm iso} = 10°$ (a), 15° (b), 20° (c), and 25° (d). The Monte Carlo predictions were calculated using JETSET.

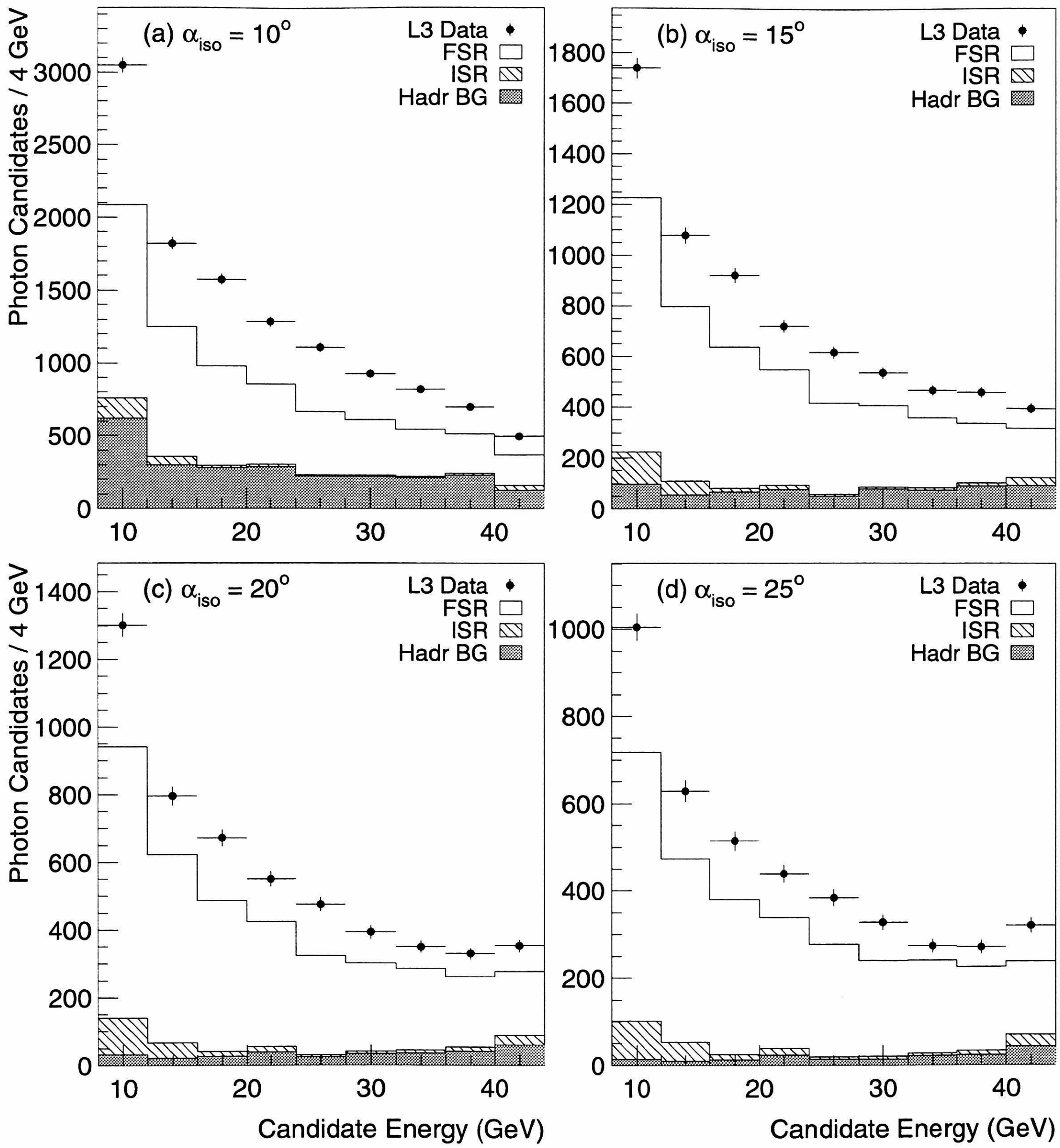

Figure 5.15: Final energy distributions of photon candidates selected with different isolation requirements: $\alpha_{\rm iso} = 10°$ (10), 15° (b), 20° (c), and 25° (d). The Monte Carlo predictions were calculated using JETSET.

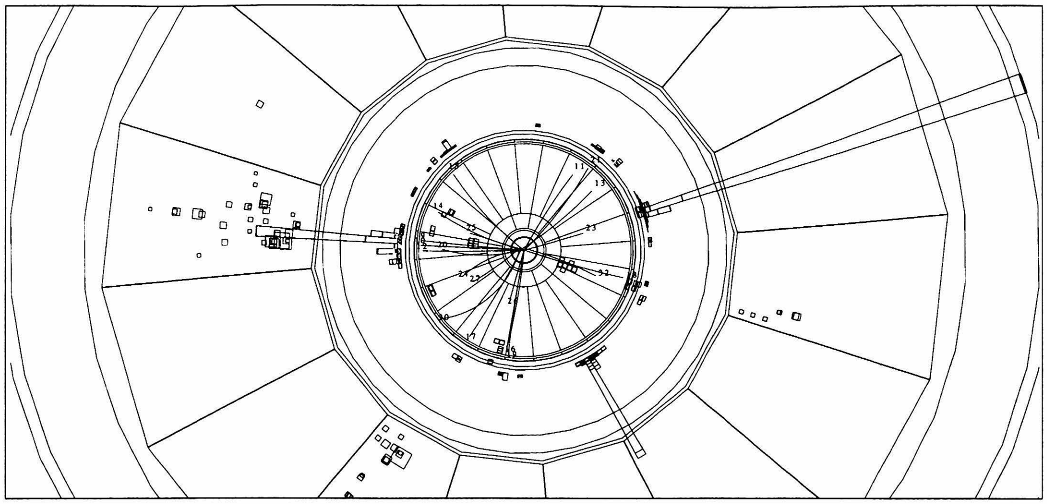

Figure 5.16: Hadronic Z decay recorded during 1994 in which two isolated and energetic FSR photon candidates have been selected. The event is displayed in the plane perpendicular to the beam axis. The energies of the two photon candidates are 29.6 GeV and 10.7 GeV, and their invariant mass is 24.3 GeV.

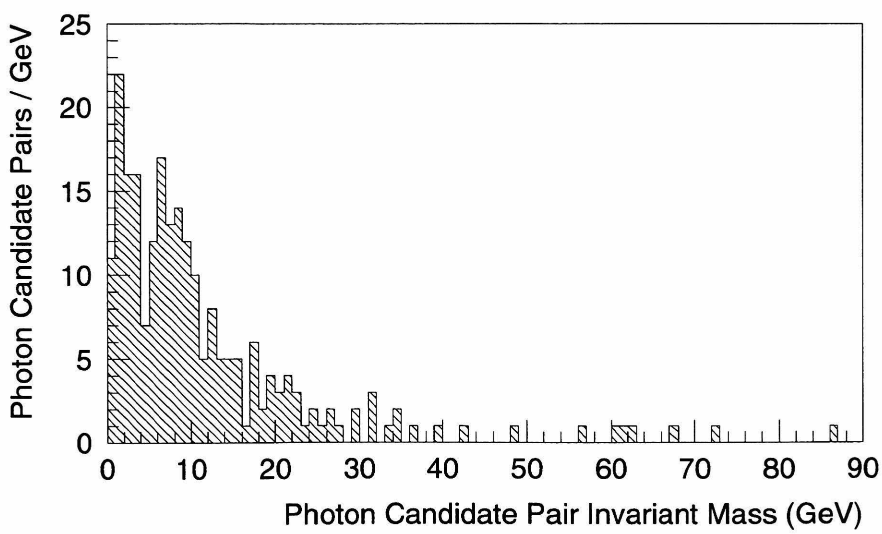

Figure 5.17: Invariant mass distribution of the photon candidate pairs selected with $E_\gamma > 3$ GeV and $\alpha_{\mathrm{iso}} = 10°$. Between 1991 and 1994, 221 events containing such a pair of candidates were recorded.

Chapter 6

Data Analysis

In the previous chapter, I described how I select an event sample that has a high proportion of photons produced by final-state radiation (FSR). In this chapter, I describe how I analyze that sample, obtaining FSR energy distributions that can be compared directly with theoretical models. I also discuss how I estimate the uncertainties in these measured distributions.

My sample of FSR photon candidates includes some irreducible background from both initial-state radiation (ISR) and hadrons (mostly $\pi^0 \rightarrow \gamma\gamma$ decays). Since these contributions are not described by the theoretical calculations that I wish to compare with (see Chapter 7), the first step of my analysis is to estimate these backgrounds and then subtract them. Next, I apply corrections for the limited efficiency and acceptance of my event selection, in order to obtain energy distributions corresponding to what an ideal detector would measure. Finally, I estimate the statistical and systematic uncertainties in my results. In the following sections, I describe each of these steps in more detail.

6.1 Background Subtraction

My photon candidate selection scheme rejects as much of the ISR and hadronic backgrounds as possible, while retaining as much FSR as possible. However, some backgrounds, which cannot be distinguished from genuine FSR on an event-by-event basis, remains in the final sample. I refer to this background as *irreducible*, and must subtract its contribution to my FSR sample statistically. The irreducible ISR background arises because photons from ISR and FSR are fundamentally indistinguishable. The irreducible hadronic background is mostly due to neutral hadron decays into nearly-collinear photons, and to a smaller extent, decays into well-separated photons of which only one is observed in the detector. The first of these decay configurations is important for hadron energies larger than about 5 GeV, and is irreducible because the finite granularity of the calorimeter makes it impossible to resolve the overlapping signals from the two photons. The second configuration is most important for low-energy hadrons and is irreducible because the single detected photon cannot be distinguished from an FSR photon.

6.1.1 Initial-State Radiation

Although it is not possible to distinguish between photons radiated from the initial (e^+e^-) and final ($q\overline{q}$) states on an event-by-event basis, the ISR contribution to any distribution is well-defined when the interference between these two processes is sufficiently small, as is the case at the Z peak. ISR is theoretically well-understood, and can be calculated to high precision for leptonic final states such as $\mu^+\mu^-\gamma$. For hadronic final states, however, the influences of QCD corrections and isolation requirements must be accounted for, and limit the overall precision of a calculation.

I estimate the ISR background contribution to my photon candidate sample using the JETSET[62, 63] Monte Carlo. JETSET models ISR with an $\mathcal{O}(\alpha)$ approximation and improved Born-level corrections to the Z lineshape (see Section 2.1.1.1), and is the only model that can generate ISR in the context of realistic hadronic final states. (The HERWIG[64, 65] Monte Carlo does not describe ISR). To estimate the theoretical uncertainty in the JETSET prediction, I compare it with the prediction of the KORALZ[68] Monte Carlo. KORALZ includes the effects of higher-order electroweak corrections to the Z lineshape; however, it does not describe the QCD evolution of the primary $q\overline{q}$ pair from the Z decay. I perform the comparison at the particle level, without accounting for the effects of the L3 detector (which I expect to be small); my estimate of the overall uncertainty in the JETSET ISR prediction is 15%. Table 6.1 summarizes the JETSET predictions for the number of ISR photons in my candidate sample as a function of both energy and isolation. Note that the statistical uncertainties that I calculate are larger than the square roots of the corresponding numbers of events since the sample of Monte Carlo events that I am using is smaller than my data sample. The fraction of ISR in the sample varies from 2.6% ($\alpha_{\text{iso}} = 10°$) to 5.1% ($\alpha_{\text{iso}} = 25°$). The dominant uncertainty in my ISR background estimate is the theoretical accuracy of JETSET.

	Isolation Cut (α_{iso}):			
Energy	10°	15°	20°	25°
8–12 GeV	142 ± 13	126 ± 13	107 ± 12	88 ± 11
12–16 GeV	59 ± 9	54 ± 8	46 ± 8	44 ± 8
16–20 GeV	15 ± 4	14 ± 4	14 ± 4	12 ± 4
20–24 GeV	18 ± 5	18 ± 5	15 ± 4	15 ± 4
24–28 GeV	9 ± 3	6 ± 3	5 ± 3	5 ± 3
28–32 GeV	8 ± 3	6 ± 3	6 ± 3	6 ± 3
32–36 GeV	10 ± 4	10 ± 4	8 ± 3	5 ± 3
36–40 GeV	13 ± 4	12 ± 4	12 ± 4	10 ± 4
40–44 GeV	31 ± 6	31 ± 6	28 ± 6	27 ± 6
TOTAL	305 ± 20 ± 46	278 ± 19 ± 42	242 ± 18 ± 36	212 ± 17 ± 32

Table 6.1: Summary of the expected ISR contributions to the photon candidate sample, in different intervals of candidate energy and for different isolation requirements. The errors given are statistical uncertainties, except in the final row, where the second error given is the estimated theoretical uncertainty.

6.1.2 Hadronic Background

In a typical hadronic Z decay, most of the photons present are the decay products of neutral hadrons. These photons are usually of low energy and are not isolated, but, because of their high rate, they present a potentially large background to the much smaller signal that I expect from FSR. The main component of this background present in my photon candidate sample is the lightest neutral hadron, π^0, decaying into two photons. I also expect smaller contributions from the decays of other neutral hadrons into photons (mostly η, $\mathrm{K_S}$, and $\mathrm{K_L}$), and from charged hadrons decaying into $\mathrm{e}^\pm$ and $\pi^\pm$. Figure 6.1 shows the predicted energy distributions of the different sources of hadronic background to my photon candidate samples, calculated using the JETSET Monte Carlo (JETSET and HERWIG are in good agreement as to the relative proportions of the different contributions).

The main cuts that I use to eliminate hadronic background are a minimum energy requirement and an isolation requirement. While these cuts are effective, they also select a region of phase space that is not well-understood in hadronization models, so I can not assume that the Monte Carlo predictions of the irreducible hadronic background are reliable. In order to minimize sensitivity to this problem, I study the hadronic background directly with data, using a background-enriched sample that I select from neutral bumps with the same isolation, energy, and fiducial volume cuts as the photon candidate sample, but with a shower shape cut $p_\gamma \leq 0.05$ that *rejects* 95% of genuine isolated photons. I refer to the bumps in this anti-tagged sample as *hadron candidates.* Table 6.2 summarizes the selection statistics for the hadron candidate sample, and Figure 6.2 shows its energy distributions. There is a large discrepancy between the measured rates of hadron candidates and the JETSET predictions.

In order to study hadronic backgrounds, I divide my photon- and hadron candidate samples into sub-samples, which I denote by $\mathcal{S}_i$ and $\overline{\mathcal{S}}_i$ respectively, according to the candidate energies (the index i labels the different energy intervals that I use). Below, I also refer to the larger sample that I select using only energy, isolation, and fiducial-volume cuts, but without any conditions on the shower-shape variable p_γ (which therefore includes both $\mathcal{S}_i$ and $\overline{\mathcal{S}}_i$), which I denote by $\mathcal{S}'_i$. I express the actual

Selection Cut	L3 DATA		JETSET	HERWIG
$\alpha_{\text{iso}} = 10^\circ$	N	$10^3 \cdot f$	$10^3 \cdot f$	$10^3 \cdot f$
Hadr.Sel.	17744	5.440 ± 0.041	4.930 ± 0.048	5.483 ± 0.067
DATA/MC			1.103 ± 0.013	0.992 ± 0.014
$\alpha_{\text{iso}} = 15^\circ$				
Hadr.Sel.	3541	1.086 ± 0.018	0.844 ± 0.020	0.992 ± 0.029
DATA/MC			1.287 ± 0.037	1.094 ± 0.037
$\alpha_{\text{iso}} = 20^\circ$				
Hadr.Sel.	1421	0.436 ± 0.012	0.323 ± 0.012	0.407 ± 0.018
DATA/MC			1.349 ± 0.062	1.071 ± 0.056
$\alpha_{\text{iso}} = 25^\circ$				
Hadr.Sel.	753	0.231 ± 0.008	0.177 ± 0.009	0.229 ± 0.014
DATA/MC			1.302 ± 0.081	1.010 ± 0.071

Table 6.2: Summary of the hadronic background selection for different isolation requirements. The first row in each section gives the number N of hadron candidates selected (for L3 DATA) and the fraction $f = N/N_{\text{had}}$ (for L3 DATA, JETSET, and HERWIG) where N_{had} is the number of selected hadronic events. The second row gives the ratios between the values of f for data and Monte Carlo events, for the two Monte Carlo models. All of the errors are statistical uncertainties.

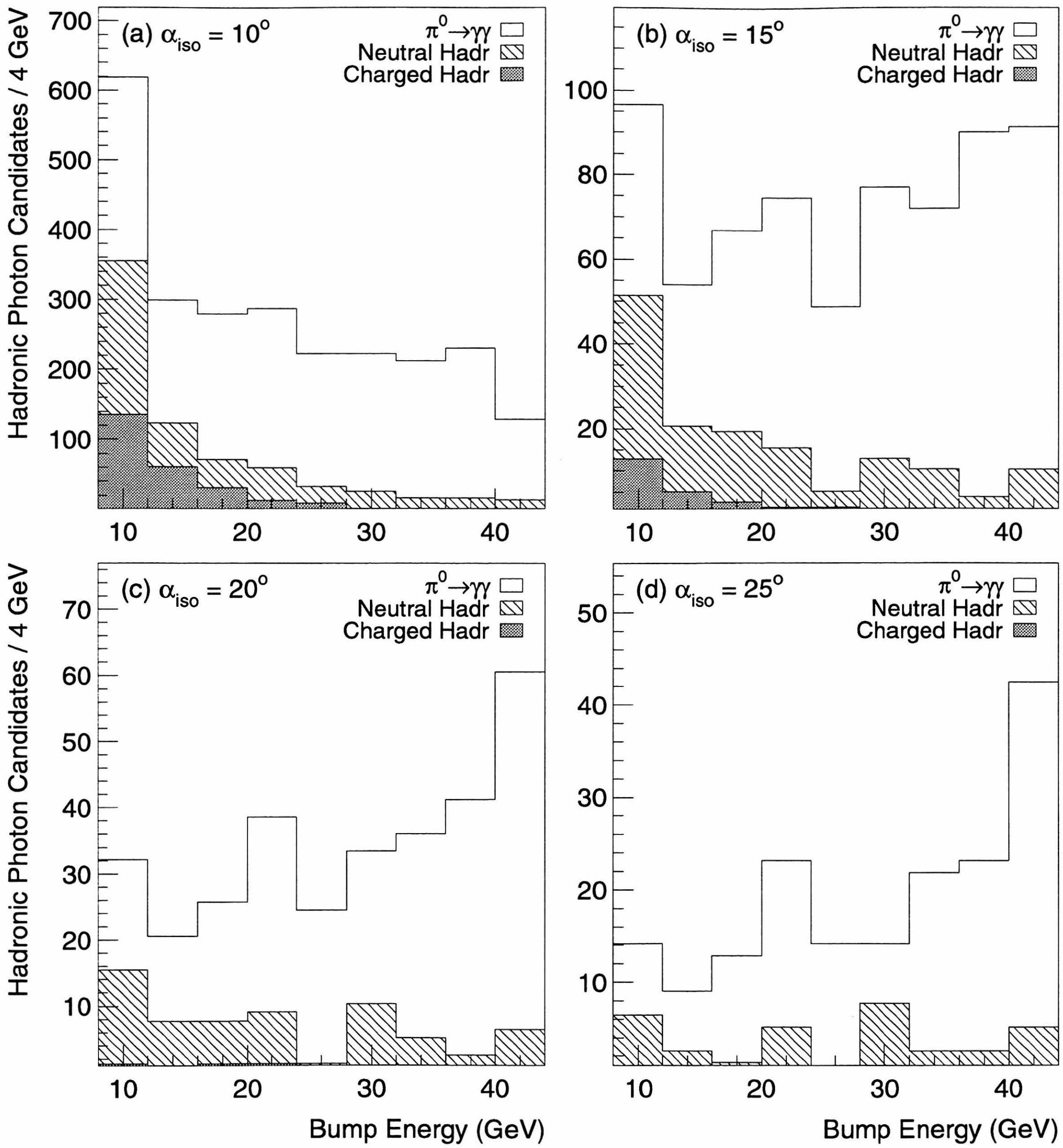

Figure 6.1: Predicted energy distributions of the main components of the hadronic background present in the final photon candidate sample. The different plots correspond to the isolation requirements: $\alpha_{\rm iso} = 10°$ (a), $15°$ (b), $20°$ (c), and $25°$ (d).

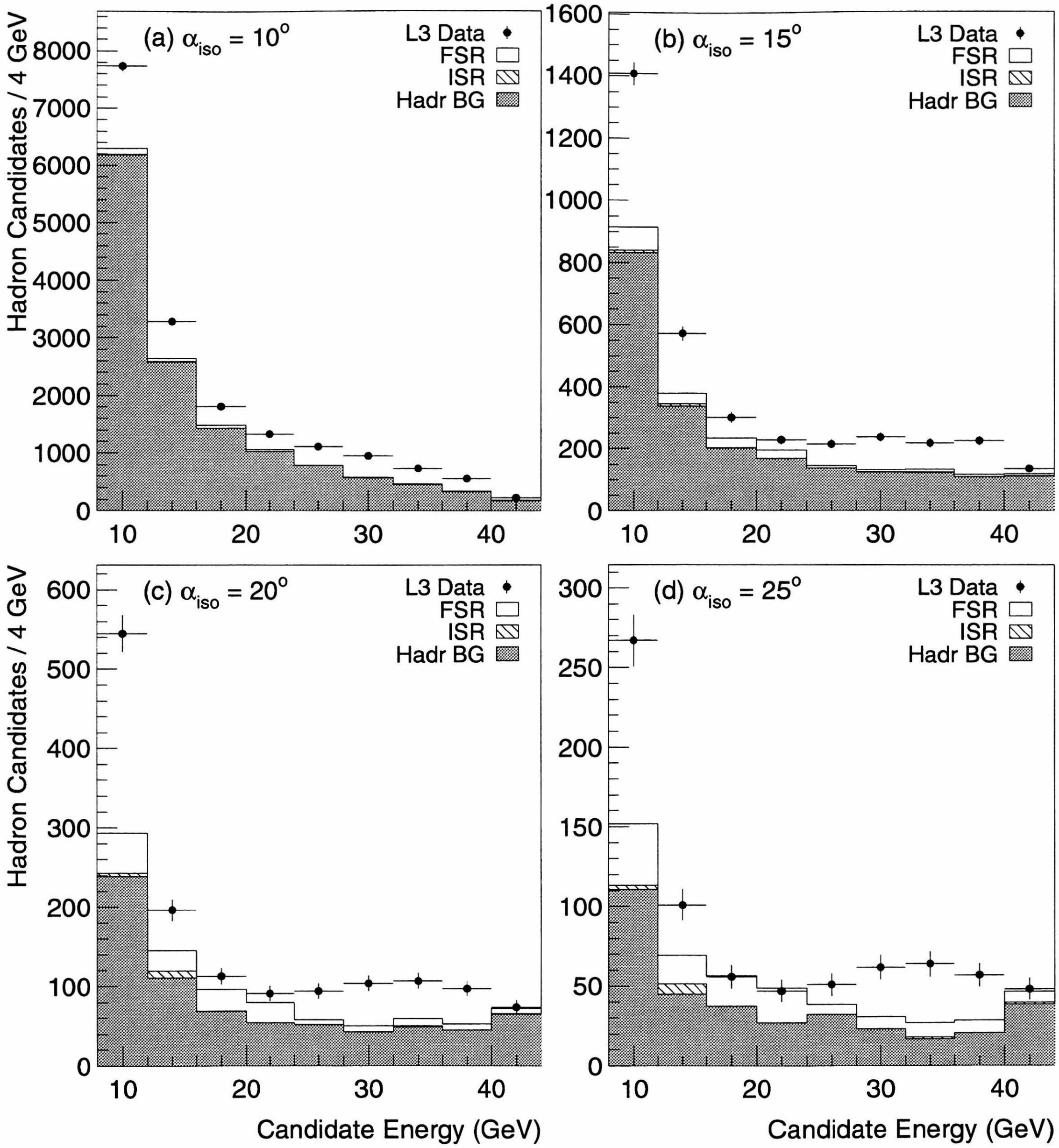

Figure 6.2: Energy distributions of hadron candidates in the hadronic-background enriched samples selected with the same energy and fiducial-volume cuts as the photon candidate sample, but with $p_\gamma \leq 0.05$. The different plots correspond to the isolation requirements: $E_{\rm iso} = 40$ MeV, and $\alpha_{\rm iso} = 10°$ (a), $15°$ (b), $20°$ (c), and $25°$ (d).

hadronic-background contribution, HAD_i, to each sub-sample $\mathcal{S}_i$ as the product of a correction factor, c_i, and the Monte Carlo prediction of this background contribution, $\mathrm{HAD}_i^{(\mathrm{MC})}$,

$$\mathrm{HAD}_i = c_i \times \mathrm{HAD}_i^{(\mathrm{MC})} .$$

I compute the correction factors from the actual number, $\overline{\mathrm{N}}_i$, of hadron candidates in $\overline{\mathcal{S}}_i$, and from the Monte Carlo predictions of the contributions to this sub-sample, which I refer to as $\overline{\mathrm{ISR}}_i^{(\mathrm{MC})}$, $\overline{\mathrm{FSR}}_i^{(\mathrm{MC})}$, and $\overline{\mathrm{HAD}}_i^{(\mathrm{MC})}$,

$$c_i = \frac{\overline{\mathrm{N}}_i - \overline{\mathrm{ISR}}_i^{(\mathrm{MC})} - \overline{\mathrm{FSR}}_i^{(\mathrm{MC})}}{\overline{\mathrm{HAD}}_i^{(\mathrm{MC})}} .$$

Each correction factor thus measures the ratio of the hadronic contribution to $\overline{\mathcal{S}}_i$ in the data to the value predicted by Monte Carlo. Ideally, I would like to know this ratio for the photon candidate sub-sample, $\mathcal{S}_i$. I argue below that the ratio is in fact the same for the two sub-samples. Figure 6.3 shows the correction factors that I obtain using JETSET and HERWIG[1]. The corrections are generally greater than one, and larger for more isolated candidates and for candidates with energies between 28 GeV and 40 GeV.

The two processes responsible for my hadronic background are the production of neutral hadrons and the decay of these hadrons into photons. Although I do not necessarily expect Monte Carlo predictions for production to be reliable, decay is straightforward and I expect it to be correctly described. Therefore, in estimating the actual hadronic background, I only use Monte Carlo predictions for hadrons to calculate decay-dependent quantities, and I extract the values of production-dependent quantities from data.

The dominant hadronic background in my photon candidate sample is from neutral hadrons decaying into overlapping photons. The energy and isolation of these background candidates are the same as those of the decaying hadron, and so depend mostly on how this hadron was produced and not on how it decays. In contrast, the

[1]Since HERWIG does not implement ISR, I use the JETSET ISR predictions for both models.

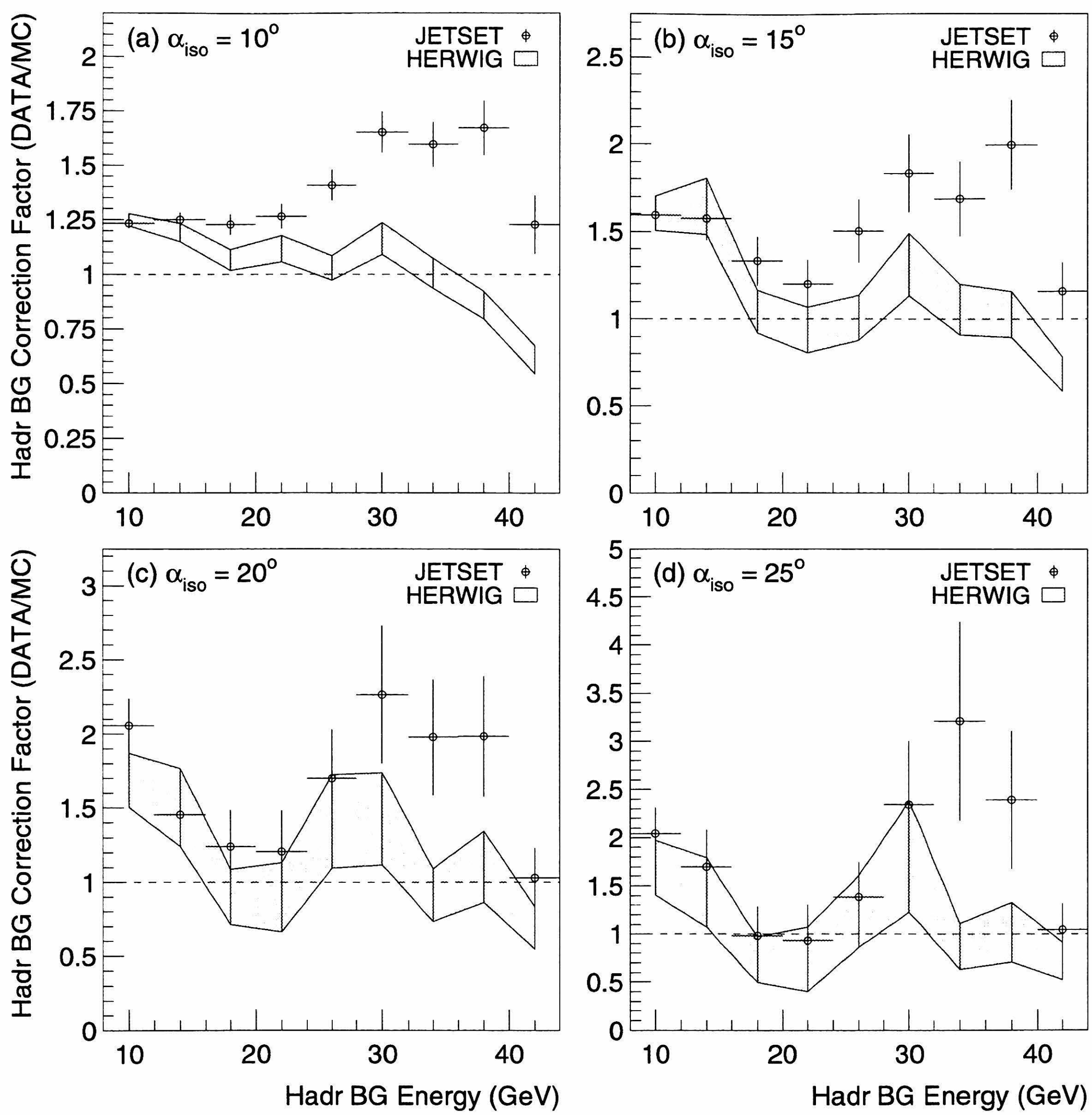

Figure 6.3: Energy dependence of the hadronic-background correction factors, c_i, calculated with JETSET (points) and HERWIG (shaded regions). The errors shown are the combined statistical uncertainties (the HERWIG errors are indicated by the width of the shaded regions). The different plots correspond to the isolation requirements $\alpha_{\mathrm{iso}} = 10°$ (a), 15° (b), 20° (c), and 25° (d).

value of the shower-shape variable, p_γ, depends mostly on how the hadron decays and not on how it was produced. Since it is the value of p_γ that determines which of the two samples, $\mathcal{S}_i$ or $\overline{\mathcal{S}}_i$, a candidate is assigned to, and since these two samples share common hadron-production characteristics (energy and isolation), the *relative* number of hadronic candidates in the two samples

$$\mathrm{HAD}_i^{(\mathrm{MC})}/\overline{\mathrm{HAD}}_i^{(\mathrm{MC})} \;,$$

depends mainly on decay characteristics. Therefore, I can reliably estimate this ratio, which appears in the expression for HAD_i, from Monte Carlo events.

Equivalently, if I compare the distributions of p_γ, between data and Monte Carlo, for the sample $\mathcal{S}'_i$ (which includes both $\mathcal{S}_i$ and $\overline{\mathcal{S}}_i$), then I expect their shapes to agree but their normalizations to differ. I base this expectation on the fact that the hadron-production degrees of freedom are sufficiently constrained in $\mathcal{S}'_i$ that the shapes of the p_γ distributions mainly reflect hadron-decay degrees of freedom. As a result, the correction factor c_i completely specifies the disagreement between data and Monte Carlo within $\mathcal{S}'_i$, and it can be measured using candidates from $\overline{\mathcal{S}}_i$ and then applied to distributions obtained from $\mathcal{S}_i$.

The accuracy of the value of HAD_i that I obtain is limited by two systematic uncertainties: the reliability of the Monte Carlo predictions for $\overline{\mathrm{ISR}}_i$ and $\overline{\mathrm{FSR}}_i$ that I use, and the influence of the hadron production process upon the value of p_γ. I account for the first of these uncertainties by assigning errors of 15% and 30% to $\overline{\mathrm{ISR}}_i$ and $\overline{\mathrm{FSR}}_i$, respectively. I choose the value of 15% based on my earlier comparison between JETSET and KORALZ ISR predictions (see Section 6.1.1) and the value of 30% based on the discrepancy between the numbers of photon candidates (which are mostly FSR) that I select from data and Monte Carlo (see Section 5.2.6). The second uncertainty arises because soft particles that are produced in neighborhood of a candidate can alter the apparent shape of its shower, and thus its value of p_γ. I estimate the size of this effect by comparing the background estimates that I obtain using

JETSET and HERWIG: these two models incorporate different physics assumptions into their hadronization models, and consequently, have different predictions for the production of soft particles. Figure 6.4 shows this comparison, and demonstrates the good agreement between the two models. For my final hadronic-background estimate, I take the average of the values of HAD_i that I obtain using JETSET and HERWIG. Table 6.3 summarizes these final estimates as a function of both energy and isolation. The fraction of hadronic background in the photon candidate sample varies from 28% ($\alpha_{\text{iso}} = 10°$) to 6% ($\alpha_{\text{iso}} = 25°$).

	Isolation Cut (α_{iso}):			
Energy	10°	15°	20°	25°
8–12 GeV	758±31± 9	148±16± 8	55±10±13	20± 6±10
12–16 GeV	373±22± 1	95±13± 8	31± 7± 1	16± 5± 0
16–20 GeV	356±22± 11	80±11±12	22± 6±12	8± 3± 6
20–24 GeV	333±22± 33	69±10±24	34± 8±17	14± 6±11
24–28 GeV	327±22± 13	77±11± 3	41±10± 2	17± 6± 3
28–32 GeV	367±26± 3	132±18±11	68±14± 9	42±13± 7
32–36 GeV	320±24± 21	112±15±12	56±12±17	49±15±24
36–40 GeV	324±26± 63	162±21±20	71±14±13	40±12±18
40–44 GeV	142±15± 17	90±12±17	52±10±12	41± 9± 6
TOTAL	3300±71±124	965±44±94	429±31±96	247±28±70

Table 6.3: Summary of the expected hadronic background contributions to the photon candidate sample, in different intervals of candidate energy, and for different isolation requirements. The errors given are statistical and systematic uncertainties, respectively.

6.1.3 Reconstructed Resonances

The corrections factors that I obtained above are surprisingly large, especially for JETSET. In order to cross-check this apparently significant discrepancy between data and Monte Carlo, I have studied isolated π^0 and η production by reconstructing their decays into two photons. This method has the advantage that the yield of a resonance

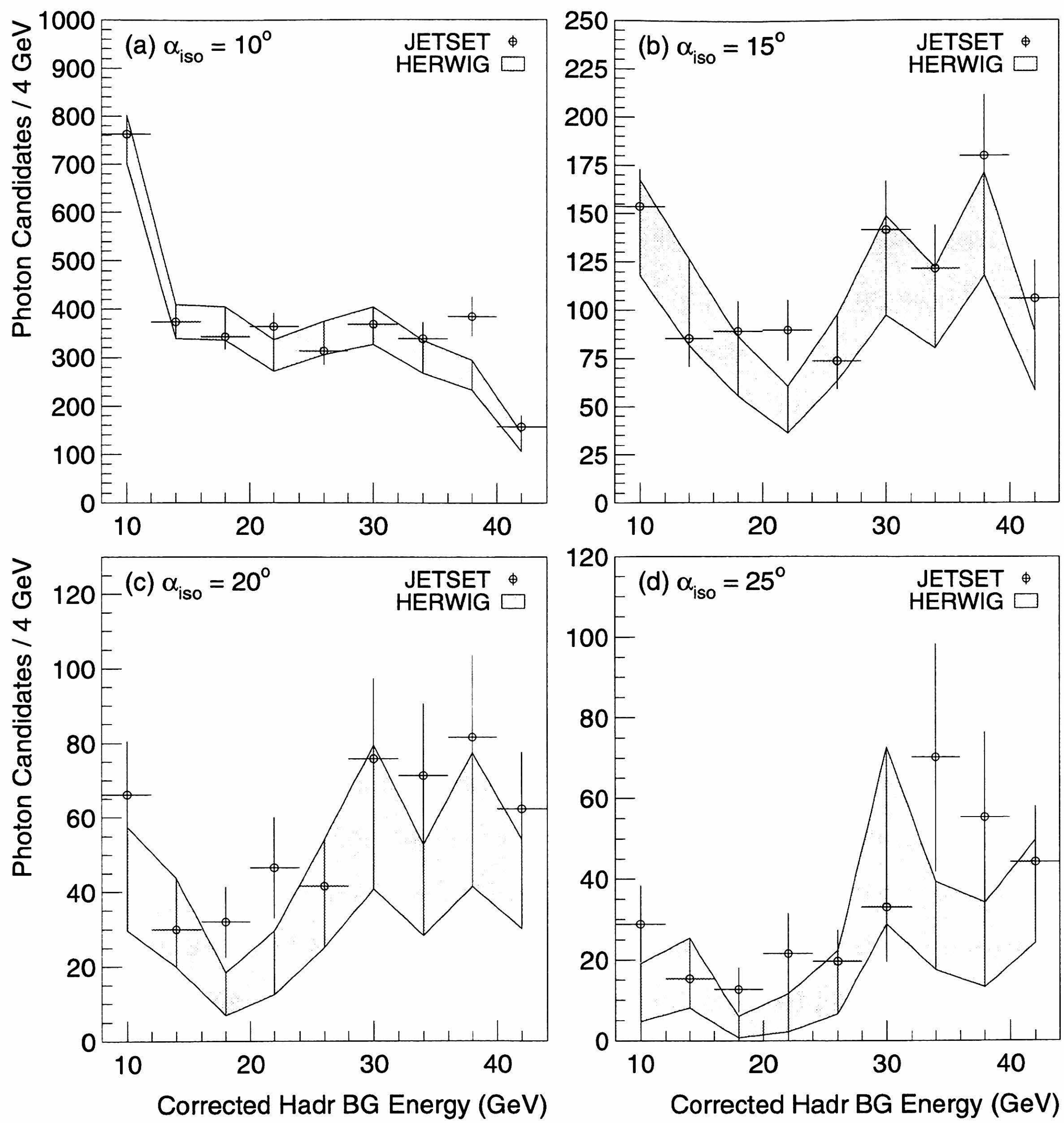

Figure 6.4: Corrected hadronic-background energy distributions obtained with JETSET (points) and HERWIG (shaded regions). The errors shown are the combined statistical uncertainties (the HERWIG errors are indicated by the width of the shaded regions). The different plots correspond to the isolation requirements $\alpha_{\text{iso}} = 10°$ (a), $15°$ (b), $20°$ (c), and $25°$ (d).

can be determined directly from data, without any need to use Monte Carlo events, but has the disadvantage that the reconstruction efficiency decreases rapidly with the energy of the decaying particle.

In order to avoid confusion between the photon candidates in my main analysis and the photons that I select for this study as candidates for reconstruction, I refer to the latter as *decay candidates.* I select decay candidates from bumps reconstructed in the ECAL, and require that they have an energy (S_9^c of the bump) of at least 450 MeV and be separated from the nearest reconstructed track in the event by $|\Delta\phi| > 15$ mrad in the plane transverse to the beam (see Section 5.2.2). In an event with at least two such decay candidates, I consider all possible pairs as *reconstruction candidates.*

I compute the energy and direction of a reconstruction candidate by taking the sum of the energies and momentum vectors of its constituent decay candidates. I compute its isolation in the same way as for a photon candidate. Figure 6.5 shows the invariant-mass distributions of the reconstruction candidates with energies larger than 3 GeV that I select with the same isolation and fiducial-volume cuts as for photon candidates. With an isolation requirement of $\alpha_{\text{iso}} = 10°$, the rate of reconstructed resonances is slightly smaller than is predicted by Monte Carlo; with $\alpha_{\text{iso}} = 25°$, the rate is much larger than predicted. There are small offsets between the positions of the η peak in data and Monte Carlo: these are primarily due to the non-linearity of the ECAL response at low energies, which I have not corrected for, but do not affect the determination of resonance yields and so do not concern me here.

In order to study the energy dependence of the discrepancy between data and Monte Carlo in Figure 6.5, I compare the yields of reconstruction candidates in the π^0 and η peaks for different intervals of reconstruction-candidate energy between 3 GeV and 8 GeV (the upper limit of 8 GeV is determined by the reconstruction efficiency, which decreases rapidly with energy). In each energy interval, I fill separate histograms of the π^0 and η peak regions, which I define to be the ranges

$$\pi^0 \,:\, 80 \text{ MeV} \leq m_{\gamma\gamma} < 300 \text{ MeV} \quad \text{and,} \quad \eta \,:\, 400 \text{ MeV} \leq m_{\gamma\gamma} < 700 \text{ MeV} .$$

I choose histogram bins of equal size in $x_{\gamma\gamma} \equiv \log(m_{\gamma\gamma})$ to improve the separation of the background and π^0 contributions below the π^0 peak[71].

After filling each histogram, I estimate the yield of its associated resonance with a fit to a function, $F = S + B$, which describes separate (resonant) signal and (non-resonant) background contributions. I use a Gaussian in $m_{\gamma\gamma}$ to describe the signal contribution

$$S(m_{\gamma\gamma}) = \frac{N}{\sqrt{2\pi}\sigma} \exp\left[-\frac{1}{2}\left(\frac{m_{\gamma\gamma} - m_0}{\sigma}\right)^2\right] ,$$

and a quadratic in $x_{\gamma\gamma}$ to describe the background contribution

$$B(x_{\gamma\gamma}) = p_0 + p_1 x_{\gamma\gamma} + p_2 x_{\gamma\gamma}^2 .$$

Figure 6.6 shows some examples of these fits for different energy intervals and isolation requirements. I use the MINUIT[72] package to perform the fits.

I define the resonance yield, $Y_j(\pi^0)$ or $Y_j(\eta)$, for each histogram as

$$Y_j = N_{S+B} - N_B ,$$

where N_{S+B} is the number of reconstruction candidates in the invariant-mass interval $|m_{\gamma\gamma} - m_0| < 3\sigma$, and N_B is the amount of background in the same interval that I compute by integrating $B(x_{\gamma\gamma})$ over the same interval (the index j labels the intervals of hadron energy that I use). In order to compare with the correction factors, c_i, that I obtained above, I compute the ratios

$$c_j(\pi^0) = \frac{Y_j(\pi^0)}{Y_j^{(MC)}(\pi^0)} \quad \text{and} \quad c_j(\eta) = \frac{Y_j(\eta)}{Y_j^{(MC)}(\eta)}$$

between data and Monte Carlo yields for both resonances. Table 6.4 gives the values of these ratios that I obtain using four energy intervals spanning the range between 3 GeV and 8 GeV. For both Monte Carlo models, the discrepancy between data and Monte Carlo increases with energy, and is larger for more isolated resonances. The discrepancy is also generally larger for η than for π^0, and the differences between $c_j(\pi^0)$ and $c_j(\eta)$ are larger for HERWIG than for JETSET.

	Isolation Cut (α_{iso}):			
Energy	10°	15°	20°	25°
		JETSET π^0		
3.0–3.5 GeV	0.91±0.01	1.05±0.02	1.26±0.04	1.56±0.08
3.5–4.0 GeV	0.88±0.02	1.13±0.03	1.42±0.06	1.72±0.12
4.0–5.0 GeV	1.00±0.02	1.28±0.03	1.73±0.08	2.22±0.17
5.0–8.0 GeV	1.02±0.02	1.41±0.05	1.97±0.13	2.61±0.29
		JETSET η		
3.0–3.5 GeV	0.93±0.10	0.94±0.09	1.49±0.19	1.60±0.23
3.5–4.0 GeV	0.89±0.10	1.03±0.11	1.51±0.20	1.61±0.31
4.0–5.0 GeV	0.93±0.09	1.55±0.16	2.21±0.32	3.04±0.63
5.0–8.0 GeV	1.26±0.11	1.55±0.19	2.21±0.36	2.74±0.61
		HERWIG π^0		
3.0–3.5 GeV	0.81±0.01	0.87±0.02	1.03±0.04	1.36±0.08
3.5–4.0 GeV	0.82±0.02	0.94±0.03	1.30±0.07	1.65±0.14
4.0–5.0 GeV	0.91±0.02	1.05±0.03	1.33±0.07	1.83±0.17
5.0–8.0 GeV	0.89±0.02	1.25±0.05	1.68±0.13	2.44±0.36
		HERWIG η		
3.0–3.5 GeV	0.98±0.13	1.10±0.14	1.36±0.19	1.88±0.36
3.5–4.0 GeV	1.11±0.16	1.48±0.23	1.68±0.30	1.23±0.27
4.0–5.0 GeV	1.13±0.14	1.39±0.18	1.90±0.30	2.58±0.69
5.0–8.0 GeV	1.79±0.23	1.99±0.34	2.02±0.41	3.02±1.08

Table 6.4: Ratios between the yields obtained from data and Monte Carlo of reconstructed π^0 and η resonances. The first two sections are calculated using the JETSET Monte Carlo, and the last two using HERWIG.

In order to compare the values of $c_j(\pi^0)$ and $c_j(\eta)$ with the correction factors, c_i, that I obtained in the previous section, I have recomputed the c_i between 3 GeV and 10 GeV using energy intervals one GeV wide. I show this comparison in Figures 6.7 (JETSET) and 6.8 (HERWIG). There is good overall agreement between the ratios which I measure using decays into well-separated photons, and those which I measure using decays into almost-collinear photons. This agreement is equally good for JETSET and HERWIG. This result provides further evidence that the corrected hadronic background contributions that I obtained above are reliable.

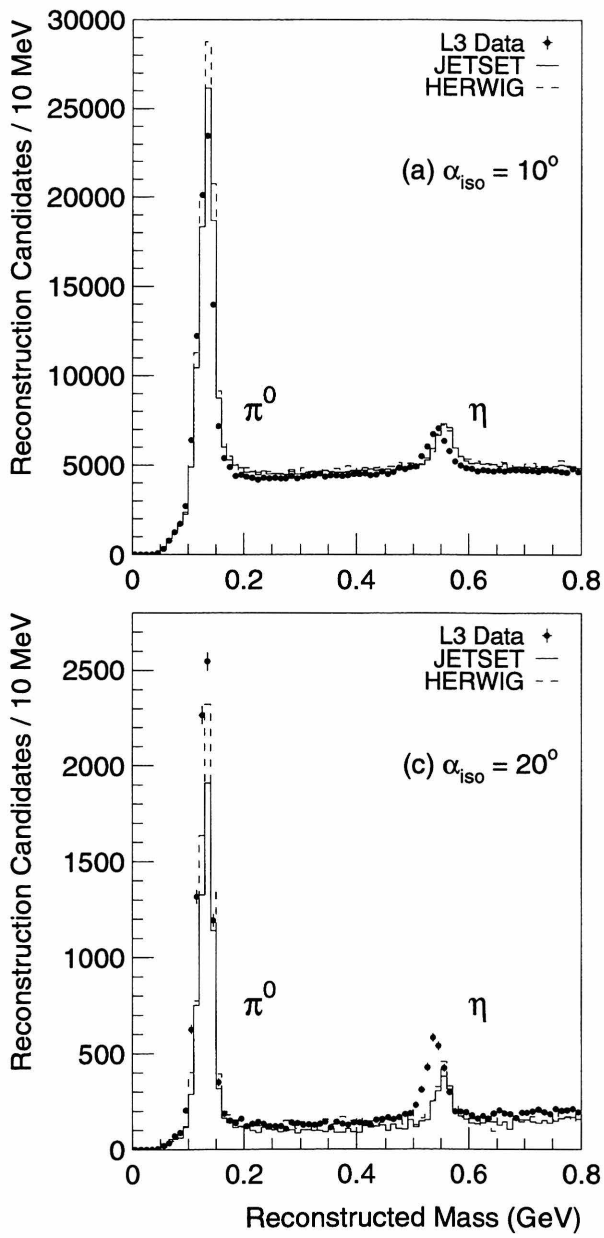

Figure 6.5: Invariant mass distributions of reconstructed photon pairs selected with different isolation requirements: $\alpha_{\text{iso}} = 10°$ (a), $15°$ (b), $20°$ (c), and $25°$ (d). The two peaks correspond to the π^0 ($m_{\gamma\gamma} \simeq 135$ MeV) and η ($m_{\gamma\gamma} \simeq 547$ MeV) resonances.

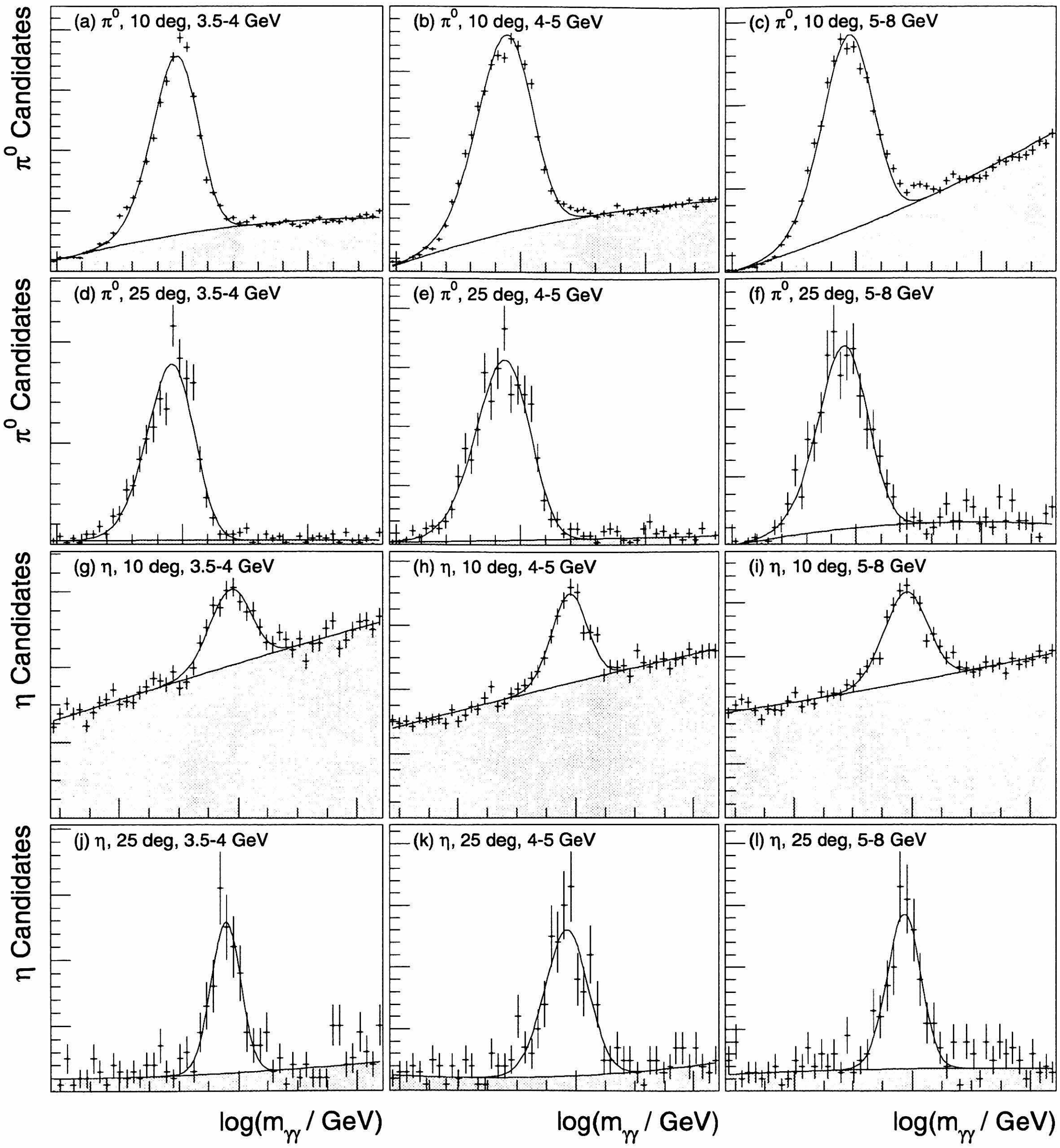

Figure 6.6: Examples of some fits for the yields of reconstructed π^0 and η decays into two photons. Figures (a–f) show the π^0 resonances obtained with 10° isolation (a,b, and c) and 25° isolation (d,e, and f), in three different energy intervals: 3.5 GeV–4 GeV (a,d), 4 GeV–5 GeV (b,e), and 5 GeV–8 GeV (c,f). Figures (g–l) show the corresponding plots for η resonances.

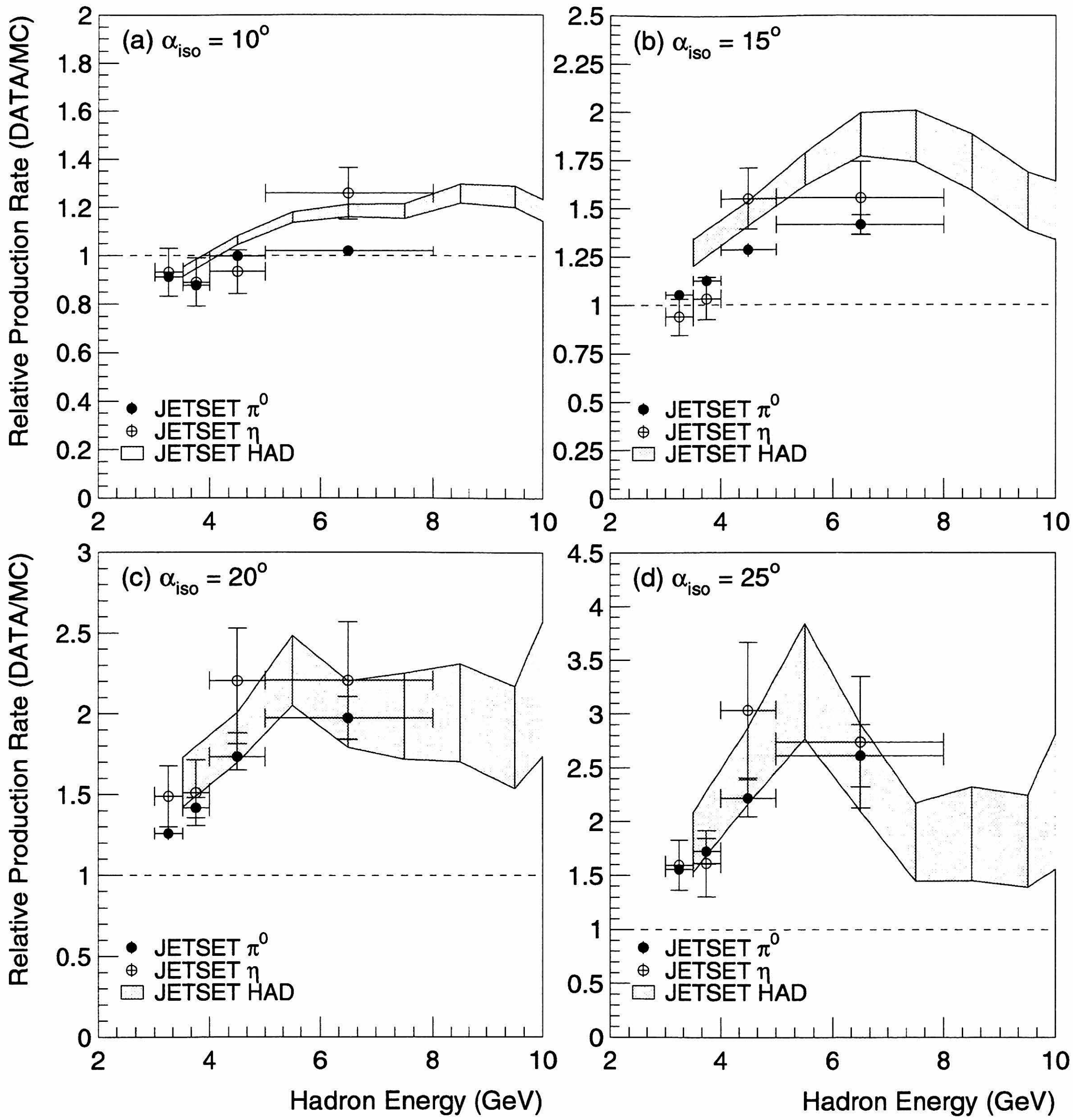

Figure 6.7: Comparison of the discrepancies between the observed rates of isolated hadronic background and the predictions of JETSET, obtained with two different methods. The four figures show, for different isolation requirements, the ratios (DATA/MC) obtained for the reconstructed yields of π^0 (solid data points) and η (hollow data points), and for the rates of neutral hadron decays into overlapping photons (shaded regions).

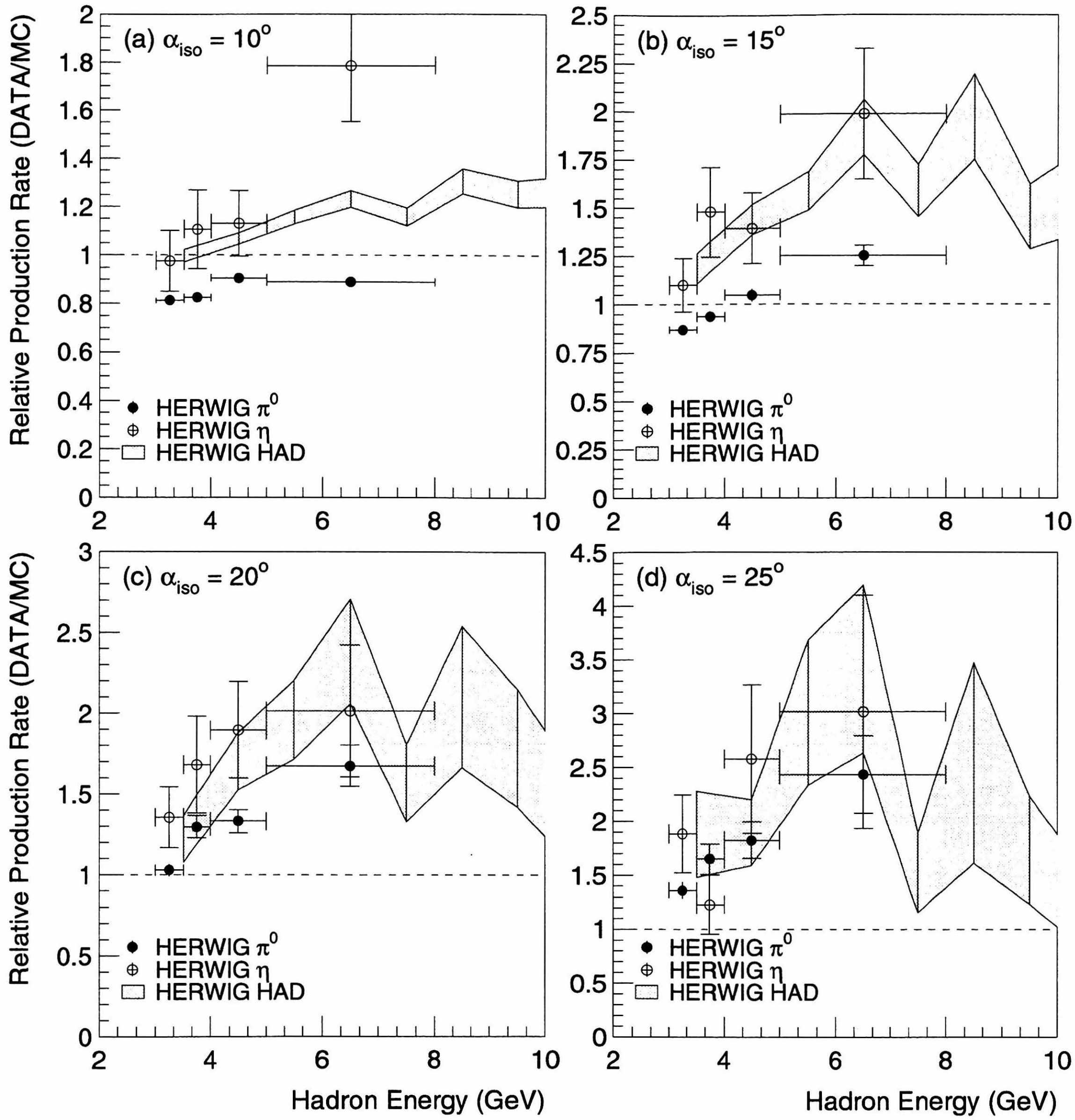

Figure 6.8: Comparison of the discrepancies between the observed rates of isolated hadronic background and the predictions of HERWIG, obtained with two different methods. The four figures show, for different isolation requirements, the ratios (DATA/MC) obtained for the reconstructed yields of π^0 (solid data points) and η (hollow data points), and for the rates of neutral hadron decays into overlapping photons (shaded regions).

6.1.4 Summary

Figure 6.9 shows the photon candidate energy distributions that I measure, together with my final estimates of the background contributions. The ISR contribution is concentrated at low energies, with a small secondary peak at energies $E_\gamma \simeq \sqrt{s}/2$, and is almost independent of the isolation requirement. In contrast, the hadronic contribution decreases rapidly with the isolation requirement, and has a nearly flat energy distribution. I calculate final FSR energy distributions for the different isolation requirements by subtracting the estimated backgrounds from the photon candidate data. Table 6.5 gives a summary of these estimated contributions and of the final FSR samples. The FSR purity of the photon candidate samples varies from 69% (α_{iso} = 10°) to 89% (α_{iso} = 25°).

	$\alpha_{\text{iso}} = 10°$	$\alpha_{\text{iso}} = 15°$	$\alpha_{\text{iso}} = 20°$	$\alpha_{\text{iso}} = 25°$
DATA	11785	6927	5224	4166
−ISR	2.6%	4.0%	4.6%	5.1%
	$\pm 0.2\% \pm 0.4\%$	$\pm 0.3\% \pm 0.6\%$	$\pm 0.3\% \pm 0.7\%$	$\pm 0.4\% \pm 0.8\%$
−HAD	28.0%	13.9%	8.2%	5.9%
	$\pm 0.6\% \pm 1.1\%$	$\pm 0.6\% \pm 1.4\%$	$\pm 0.6\% \pm 1.8\%$	$\pm 0.7\% \pm 1.7\%$
=FSR	69.4%	82.1%	87.2%	89.0%
	$\pm 1.1\% \pm 1.4\%$	$\pm 1.4\% \pm 2.0\%$	$\pm 1.5\% \pm 2.5\%$	$\pm 1.7\% \pm 2.5\%$

Table 6.5: Summary of the estimated background contributions to the photon candidate samples selected with different isolation requirements, and of the final background-corrected FSR samples. The two errors given for each quantity are statistical and systematic uncertainties.

6.2 Acceptance and Efficiency Corrections

As the final step in preparing distributions that can be compared directly with theoretical models, I correct for the limited acceptance and efficiency of my event selection. In particular, I unfold the effects of my fiducial-volume, shower-shape, and hadronic-

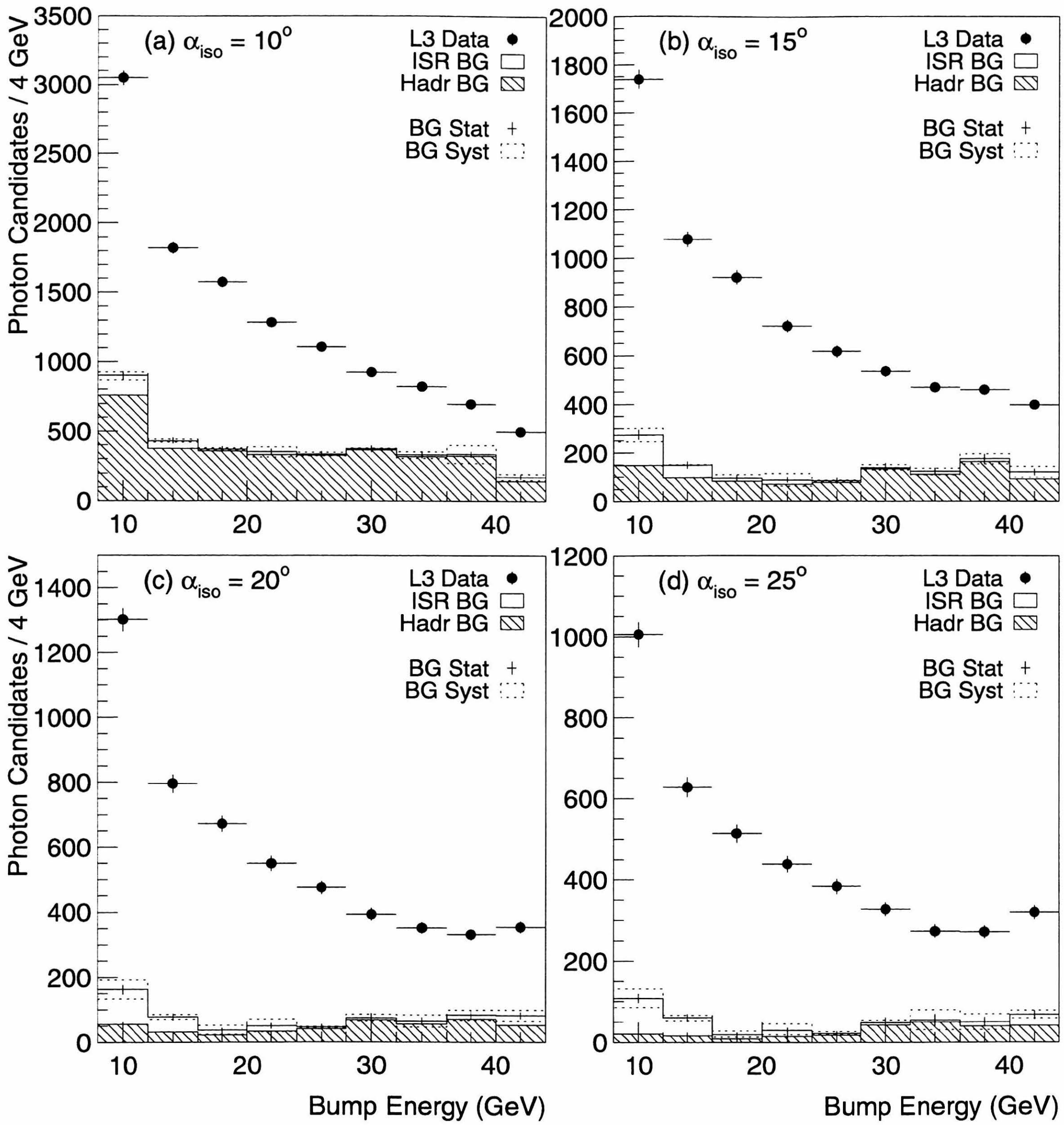

Figure 6.9: Energy distributions of photon candidates together with the final estimates of the background contributions. The figures correspond to the different isolation requirements $\alpha_{\text{iso}} = 10°$ (a), 15° (b), 20° (c), and 25° (d). The errors shown for the data are statistical uncertainties, and for the combined background, are statistical (error bars) and systematic (dotted boxes) uncertainties.

event-selection cuts and I correct for the inefficiencies of my neutral-bump selection. Finally, I obtain the energy distribution of isolated FSR that an ideal detector would measure.

I refer to the actual FSR energy distributions that I measure after background subtraction as *detector-level*, and the corresponding distributions that would be measured by an ideal detector as *particle-level* (and denote these with a tilde). The most general transformation of a binned distribution $\{y_i\}$ from particle level to detector level is given by

$$y_i = \sum_j m_{ij} \tilde{y}_j \ ,$$

where the coefficient m_{ij} gives the fraction of the events which are in bin j at the particle level that are expected to appear in bin i at the detector level. The values of m_{ij} are generally obtained by a simulation of the effects of the detector on Monte-Carlo generated events. Off-diagonal coefficients ($i \neq j$) measure the amount of bin-to-bin migration between the particle and detector levels.

Figure 6.10 shows the distribution of the difference between the energies of FSR photon candidates measured on the particle and detector levels, which I obtain by simulating the effects of the L3 detector on Monte-Carlo generated events. The spread in this difference is independent of the isolation requirement, and is small enough that bin-to-bin migration is negligible for the bin width of 4 GeV that I use[2]. Therefore, I neglect the off-diagonal coefficients of the general transformation, above, and use for my transformation from detector to particle level the equation

$$\tilde{y}_i = \frac{1}{\varepsilon_i} y_i$$

where $\varepsilon_i \equiv m_{ii}$ is the overall efficiency of my event selection for FSR photons with energies in bin i. I refer to this correction procedure as *bin-by-bin unfolding.* The distributions in Figure 6.10 are offset from zero by about 80 MeV. Since this offset is much less than the bin width I have chosen, I do not make any correction for it.

[2]The bin-to-bin migration would be negligible with a bin width as small as 1 GeV. I choose the

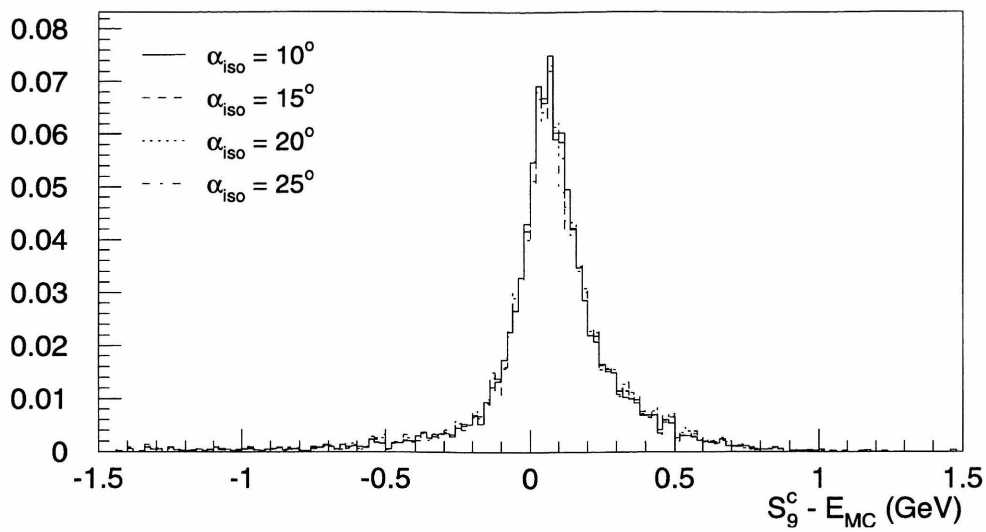

Figure 6.10: Distribution of the difference between the energy of a photon candidate at the particle level (taken directly from the Monte Carlo generator) and measured by the detector using the corrected sum-of-9 energy. The normalized distributions for candidates selected with different isolation requirements are superimposed.

I define my bin-by-bin correction coefficients to be

$$\varepsilon_i \equiv \frac{\mathrm{DET}_i}{\mathrm{GEN}_i},$$

where GEN_i is number of FSR photons whose energies fall in the i-th bin and that I select at the particle level, and DET_i is the number of FSR photon candidates in the same energy bin that I select at the detector level. The cuts that I apply at the particle level define what my final unfolded distributions measure. Since these cuts must be defined in terms of particle four-vectors, they cannot include those photon candidate selection cuts that depend intrinsically on the detector response. This restriction means, for example, that it is not meaningful to apply a shower-shape cut at the particle level, but that cuts on the photon energy and direction can be applied at particle level. In order to minimize the sensitivity of the detector corrections to

larger bin width of 4 GeV in order to reduce the statistical fluctuations in each bin.

ambiguities in the Monte Carlo description of FSR, the particle-level cuts should select a sample of FSR that is *representative* of my photon candidate sample. This second restriction means, for example, that an isolation cut should be applied at the particle level, since otherwise, the accuracy of the unfolding of the isolation cut will depend on an accurate Monte Carlo description of non-isolated FSR.

I select FSR at the particle level using the same energy and isolation cuts that I apply to select photon candidates. Since the total energy of the particles within the isolation cone of a photon is generally larger than the corresponding total energy of bumps, I use $\widetilde{E}_{\text{iso}} = 100$ MeV at the particle level (the tilde distinguishes between the particle-level and detector-level parameters) in order to approximately match the value $E_{\text{iso}} = 40$ MeV that I use at the detector level (see Section 5.2.3). Figure 6.11 shows the efficiencies, ε_i, that I obtain using these particle-level cuts. There is good agreement between JETSET and HERWIG, and the efficiencies are independent of energy within statistical errors. I calculate the final correction coefficients, $1/\varepsilon_i$, by taking the average of the coefficients that I obtain with JETSET and HERWIG, and I estimate the systematic uncertainty of my unfolding procedure by comparing the results I obtain by using either JETSET or HERWIG.

The event-selection criteria that my bin-by-bin unfolding corrects for are

- the shower-shape cut, $p_\gamma > 0.1$ (see Section 5.2.6),
- the requirements for selecting a good neutral bump, which include the effects of detector problems (see Section 5.2.1) and of accidental matches with a track (see Section 5.2.2),
- the hadronic Z decay selection cuts (see Section 5.1.4),

and

- the fiducial-volume cut, $45° < \theta_\gamma < 135°$ or $17.5° < \theta_\gamma\,(180° - \theta_\gamma) < 35°$ (see Section 5.2.5).

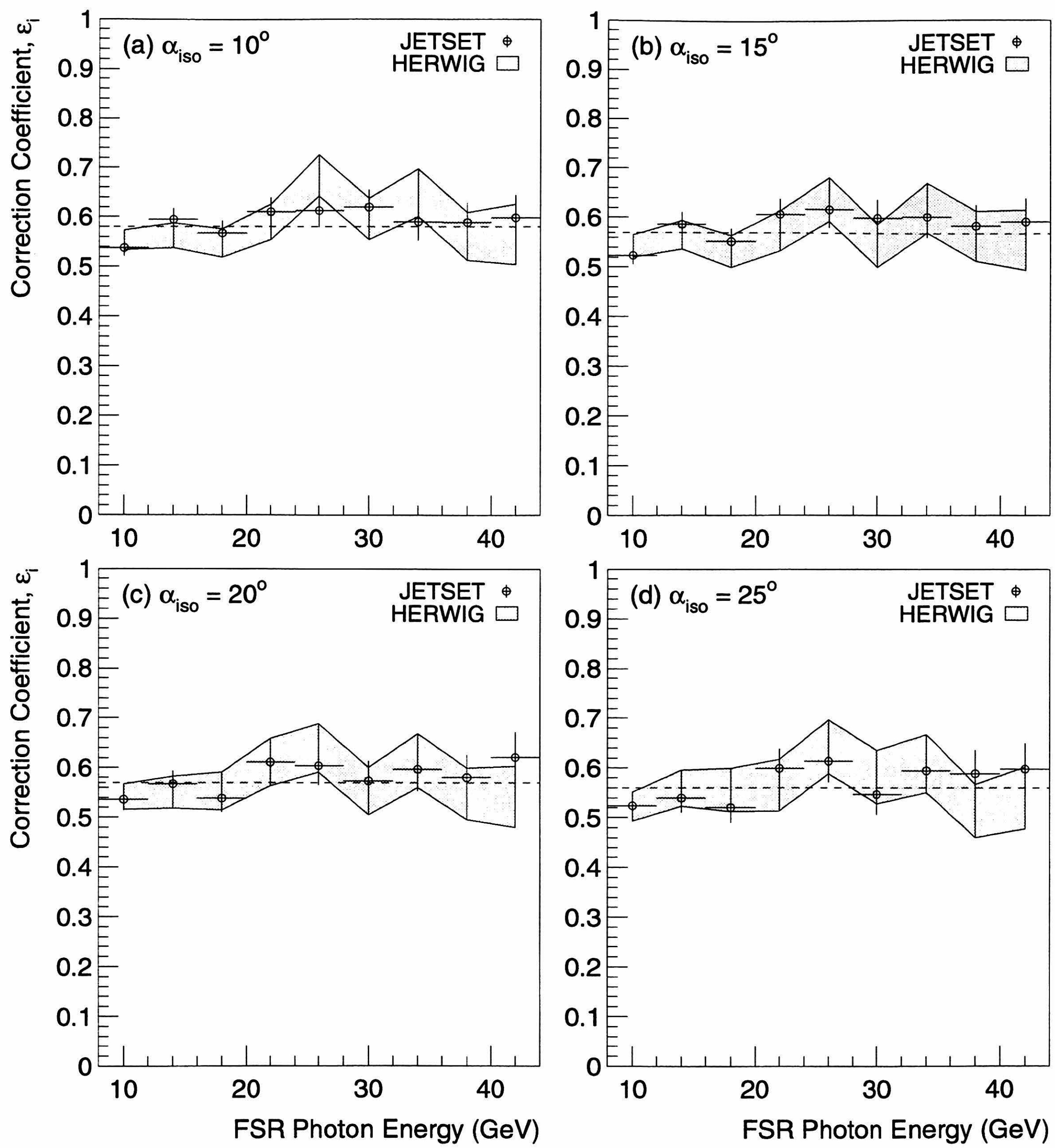

Figure 6.11: Event-selection efficiencies as a function of energy for different isolation requirements, obtained with JETSET (data points) and HERWIG (shaded regions). The horizontal dashed lines correspond to the energy-averaged efficiencies given in Table 6.6. The errors shown are combined statistical uncertainties.

I have determined the efficiencies of these cuts separately, and I find that in all cases, there is good agreement between JETSET and HERWIG, and that the efficiencies are independent of energy within statistical errors. Table 6.6 summarizes the energy-averaged efficiencies that I calculate for each of the selection criteria listed above. The largest contribution to the inefficiency of my event selection arises from my requirement that an isolated FSR photon produce a good neutral bump, and this inefficiency is mostly due to detector problems (see Section 5.2.1). The efficiency of my shower-shape cut agrees with the value of 90% that I expect (see Section 5.2.6). My efficiency for selecting hadronic Z decays that contain an isolated and energetic FSR photon is consistent with the value that I obtained in Section 5.1.5 for the inclusive hadronic event sample.

	Isolation Cut (α_{iso}):			
Correction For	$10°$	$15°$	$20°$	$25°$
Shwr. Shape	90.4±1.1%	90.9±1.3%	91.5±1.4%	91.3±1.6%
Neutral Bump	78.5±0.9%	76.4±1.0%	75.4±1.1%	74.3±1.2%
Hadr. Event	99.1±1.0%	99.0±1.2%	99.0±1.3%	98.9±1.4%
Fiducial Vol.	82.3±0.9%	82.5±1.0%	83.0±1.1%	83.1±1.2%
All FSR	57.8±0.7%	56.7±0.8%	56.7±0.9%	55.8±1.0%
u-type FSR	57.8±0.9%	56.5±1.0%	56.6±1.1%	55.6±1.2%
d-type FSR	57.8±1.3%	57.2±1.4%	57.0±1.6%	56.2±1.7%

Table 6.6: Energy-averaged efficiencies of the different aspects of my event selection described in the text. The values given are the averages of the values obtained using JETSET and HERWIG. The errors given are the combined statistical uncertainties. The last two rows give the overall efficiencies for FSR photons radiated by an up- or down-type quark, respectively.

In Chapter 8, I will use the unfolded energy distributions that I calculate here to determine parameters which are sensitive to the relative proportions of FSR photons radiated from up- and down-type quarks. Therefore, it is important to check whether the event selection and data analysis that I am using introduces any bias into these proportions. More precisely, if the efficiencies of my selection for FSR photons radiated by a primary up- or down-type quark pair are ε_{u} and ε_{d}, respectively, then the unfolding coefficient I will calculate is

$$\varepsilon = \varepsilon_{\mathrm{u}} \cdot f_{\mathrm{u}} + \varepsilon_{\mathrm{d}} \cdot f_{\mathrm{d}} \ ,$$

where f_{u} and f_{d} are the relative proportions of up- and down-type quarks at the particle level in the Monte Carlo model ($f_{\mathrm{u}} + f_{\mathrm{d}} = 1$). Therefore, if ε_{u} and ε_{d} are not equal, and the Monte Carlo values of f_{u} and f_{d} are not correct, then the unfolding will bias the proportions of up- and down-type quark contributions. In order to study this problem, I have calculated the separate efficiencies, ε_{u} and ε_{d}, using both JETSET and HERWIG (see the last two rows of Table 6.6 and Figure 6.12). I find that $\varepsilon_{\mathrm{u}} = \varepsilon_{\mathrm{d}}$ for both models, within statistical uncertainties, so that I do not expect any bias in my results.

By applying the acceptance and efficiency corrections that I describe above, I obtain FSR energy distributions whose normalizations measure the total number of FSR photons that would be recorded by an ideal detector between 1991 and 1994. In order to compare with theoretical models, I multiply these distributions by $1/N_{\mathrm{had}}$, so that they measure the number of FSR photons per hadronic Z decay. I estimate the number of hadronic Z decays corresponding to the data collected between 1991 and 1994 using

$$N_{\mathrm{had}} = \frac{1}{\varepsilon_{\mathrm{had}}} \cdot N_{\mathrm{sel}} \ ,$$

where N_{sel} is the number of selected hadronic events given in Table 5.2 and $\varepsilon_{\mathrm{had}}$ is the estimated hadronic event selection efficiency given in Section 5.1.5. The additional errors introduced by this procedure from the uncertainties on $\varepsilon_{\mathrm{had}}$ and N_{sel} are negligible.

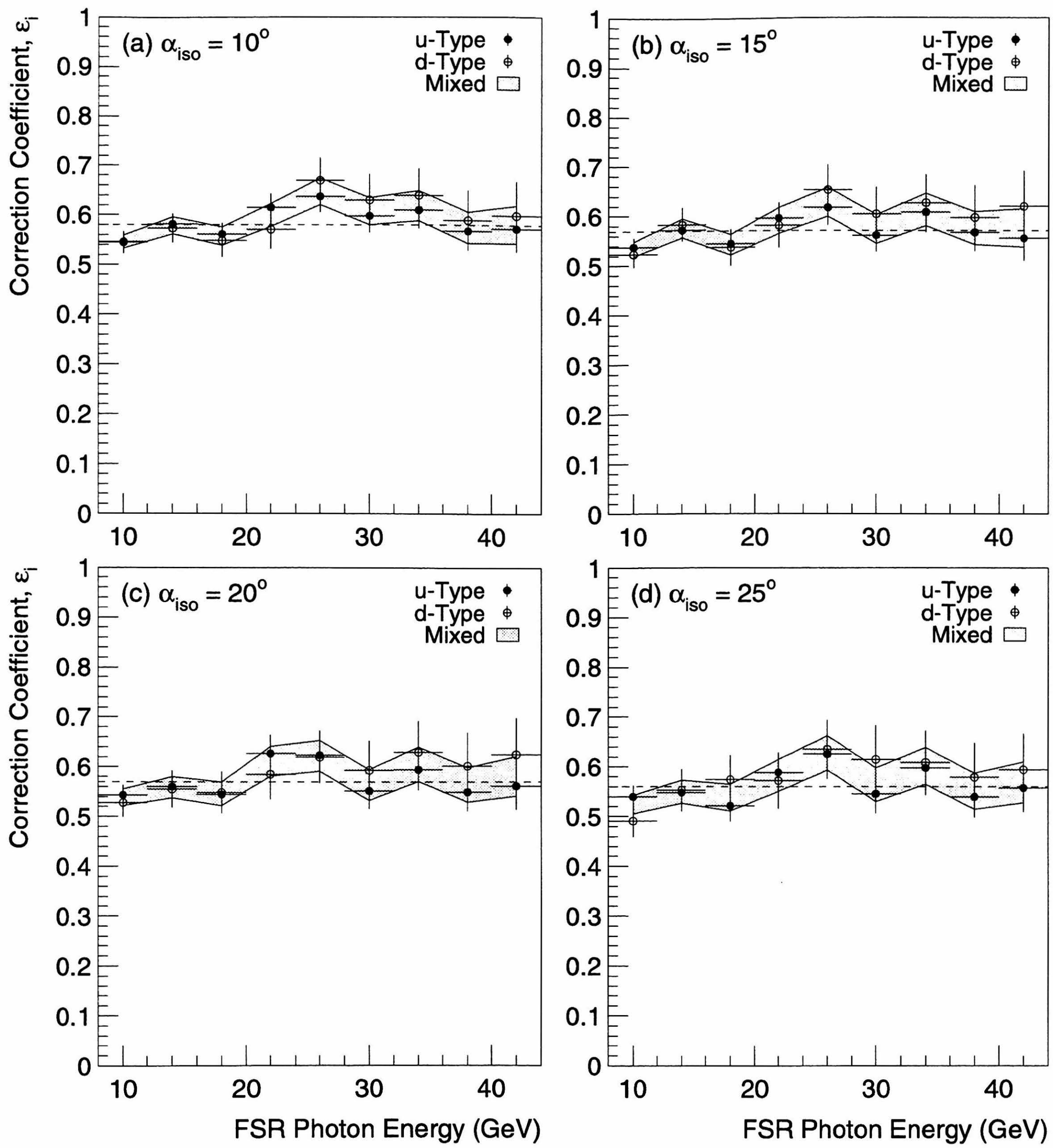

Figure 6.12: Comparison of the efficiencies of my event selection with different isolation requirements, obtained using different combinations of flavors for the quark radiating an FSR photon: up-type quarks (solid data points), down-type quarks (hollow data points), and all quarks (shaded regions). The horizontal dashed lines correspond to the overall correction coefficients given in Table 6.6. The errors given are combined statistical uncertainties.

6.3 Analysis Uncertainties

The final isolated FSR energy distributions that I obtain should not depend on the details of my event selection and data analysis, within the uncertainties that I assign. In this section, I describe the possible sources of error that I consider, and how I calculate the uncertainties in my results.

The final rate of isolated FSR per hadronic Z decay, R_i, that I calculate in each energy bin, labeled by the index i, is

$$R_i = \left(N_i - \mathrm{ISR}_i^{(\mathrm{MC})} - c_i \cdot \mathrm{HAD}_i^{(\mathrm{MC})}\right) \cdot \frac{1}{\varepsilon_i} \cdot \frac{1}{N_{\mathrm{had}}} ,$$

where N_i is the number of photon candidates that I select in energy bin i (see Section 5.2), $\mathrm{ISR}_i^{(\mathrm{MC})}$ is my estimate of the ISR background (see Section 6.1.1), $c_i \cdot \mathrm{HAD}_i^{(\mathrm{MC})}$ is my estimate of the hadronic background (see Section 6.1.2), and ε_i is the analysis efficiency that I calculate (see Section 6.2).

I use standard techniques[73] to calculate the statistical uncertainties in R_i, which are due to the number of events in the data and Monte Carlo event samples that I am using, obtaining

$$\left(\frac{\delta R_i}{R_i}\right)^2 = \frac{(\delta N_i)^2 + (\delta \mathrm{ISR}_i^{(\mathrm{MC})})^2 + (\mathrm{HAD}_i^{(\mathrm{MC})} \cdot \delta c_i)^2 + (c_i \cdot \delta \mathrm{HAD}_i^{(\mathrm{MC})})^2}{\left(N_i - \mathrm{ISR}_i^{(\mathrm{MC})} - c_i \cdot \mathrm{HAD}_i^{(\mathrm{MC})}\right)^2} + \left(\frac{\delta \varepsilon_i}{\varepsilon_i}\right)^2 + \left(\frac{\delta N_{\mathrm{had}}}{N_{\mathrm{had}}}\right)^2 ,$$

where I use the notation δx for the statistical error in x. The largest contributions to these uncertainties are from the number of photon candidates that I select from data (δN_i) and the number of events in the Monte Carlo event samples that I use to calculate acceptance and efficiency corrections ($\delta \varepsilon_i$).

I estimate the sensitivity of my results to any Monte Carlo model inaccuracies by observing how the results change when I use different models or rescale the predictions of one model. In particular, I have studied the systematic effects on my results of the following changes in my analysis (I define $R \equiv \sum_i R_i$):

- increasing (decreasing) the values of $\mathrm{ISR}_i^{(\mathrm{MC})}$ and $\overline{\mathrm{ISR}}_i^{(\mathrm{MC})}$ in each energy bin by 15%, which decreases (increases) the value of R,
- increasing (decreasing) the value of $\overline{\mathrm{FSR}}_i^{(\mathrm{MC})}$ in each bin by 30%, which increases (decreases) the value of R,
- using JETSET (HERWIG) to estimate the hadronic background, which decreases (increases) the value of R,
- using JETSET (HERWIG) to estimate the acceptance and efficiency corrections, which decreases (increases) the value of R,

and

- using JETSET (HERWIG) to estimate N_{had} for rescaling the results, which increases (decreases) the value of R.

I estimate the overall systematic error in my results from all of these effects by repeating my analysis using first, the set of changes that each increase the value of R, obtaining values R_i^+, and then, the set of changes that each decrease R, obtaining R_i^-. Finally, I assign a systematic error on the value of R_i of

$$\Delta R_i^{mc} = \frac{1}{2}\left|R_i^+ - R_i^-\right| ,$$

and on the value of R of

$$\Delta R^{mc} = \frac{1}{2}\sum_i \left(R_i^+ - R_i^-\right) .$$

The largest contributions to these uncertainties is from my subtraction of hadronic background. The errors on the total FSR rate due to any possible Monte Carlo bias, ΔR^{mc}, are between 2.6% and 3.5%.

I estimate the sensitivity of my results to the event selection that I use by repeating my analysis with the following changes:

- using the track-based hadronic event selection, instead of the calorimeter-based method (see Section 5.1.4),
- using only the barrel region of the detector ($45° < \theta < 135°$), instead of also including the endcap regions (see Section 5.2.5),
- changing the detector-level maximum allowed energy within an isolation cone from 40 MeV to 100 MeV (see Section 5.2.3),
- using data from either 1994 only or from 1991–93 only,
- either removing the shower-shape cut which I use to select photon candidates, or else tightening the cut from $p_\gamma > 0.1$ to $p_\gamma > 0.45$ (see Section 5.2.6),

and

- relaxing the shower-shape cut which I use to select hadron candidates from $p_\gamma \leq 0.05$ to $p_\gamma \leq 0.45$ (see Section 6.1.2).

Each of these changes influences the FSR purity and efficiency of my analysis: for example, the changes in the shower-shape cut for selecting photon candidates that I consider vary the purity (efficiency) for $\alpha_{\text{iso}} = 10°$ between 40% and 78% (64% and 38%). Figure 6.13 shows the variations in the isolated FSR rates that I observe.

The largest variations in Figure 6.13 are from changing the hadronic event selection method from calorimeter-based to track-based, and changing the shower-shape cut that I use to select photon candidates. I consider that the first of these variations overestimates the systematic uncertainty due to my event selection since I have not corrected for TEC problems that influence the track-based method. In my standard analysis, these problems only affect my selection of neutral bumps, and I have corrected for them in this case (see Section 5.2.2). I assign a systematic error due to my event selection equal to half of the difference between the results that I obtain by either removing the shower-shape cut that I use to select photon candidates, or else tightening the cut to $p_\gamma > 0.45$,

$$\Delta R_i^{sel} = \frac{1}{2}\left|R_i(\text{no } p_\gamma \text{ cut}) - R_i(p_\gamma > 0.45)\right|$$

and

$$\Delta R^{sel} = \frac{1}{2}\left|\sum_i \left\{R_i(\text{no } p_\gamma \text{ cut}) - R_i(p_\gamma > 0.45)\right\}\right| .$$

I do not consider tightening the shower-shape cut further since this would reduce the predicted hadronic background in my photon candidate sample to a level where my method of estimating the actual hadronic background is excessively sensitive to statistical fluctuations. The errors on the total FSR rate due to my event selection, ΔR^{sel}, are between 2.2% and 3.6%.

I assign overall systematic errors on my results by combining in quadrature the errors that I estimate due to Monte Carlo biases and to my event selection

$$\Delta R_i \equiv \sqrt{(\Delta R_i^{mc})^2 + (\Delta R_i^{sel})^2} \quad \text{and} \quad \Delta R \equiv \sqrt{(\Delta R^{mc})^2 + (\Delta R^{sel})^2} .$$

Table 6.7 summarizes the final statistical and systematic uncertainties on R that I calculate, and the contributions to these errors from from each step of my analysis. The statistical uncertainty varies between 2.0% and 2.6%, and the systematic uncertainty varies between 4.1% and 4.5%. The combined statistical and systematic uncertainty is between 4.7% and 5.0% and does not depend strongly on the isolation cut.

6.4 Summary of Analysis Results

Table 6.8 gives rates of isolated FSR photons that I calculate as a function of both the photon energy and the isolation requirement, after subtracting irreducible background, applying acceptance and efficiency corrections, and renormalizing to the number of hadronic Z decays. These results are also plotted in Figure 6.14. I measure the

Step	$\alpha_{\text{iso}} = 10°$	$\alpha_{\text{iso}} = 15°$	$\alpha_{\text{iso}} = 20°$	$\alpha_{\text{iso}} = 25°$
Evt.Sel.	$\pm 1.3 \pm 3.6\%$	$\pm 1.5 \pm 2.2\%$	$\pm 1.6 \pm 2.5\%$	$\pm 1.7 \pm 2.8\%$
ISR Sub.	$\pm 0.2 \pm 0.6\%$	$\pm 0.3 \pm 0.7\%$	$\pm 0.4 \pm 0.8\%$	$\pm 0.5 \pm 0.9\%$
HAD Sub.	$\pm 0.9 \pm 1.5\%$	$\pm 0.8 \pm 1.6\%$	$\pm 0.7 \pm 2.1\%$	$\pm 0.7 \pm 1.9\%$
Eff.Cor.	$\pm 1.2 \pm 0.2\%$	$\pm 1.4 \pm 0.8\%$	$\pm 1.6 \pm 0.3\%$	$\pm 1.7 \pm 0.1\%$
Rescale	$\pm 0.0 \pm 0.4\%$	$\pm 0.0 \pm 0.4\%$	$\pm 0.0 \pm 0.4\%$	$\pm 0.0 \pm 0.4\%$
Total	$\pm 2.0 \pm 4.5\%$	$\pm 2.2 \pm 4.1\%$	$\pm 2.4 \pm 4.3\%$	$\pm 2.6 \pm 4.3\%$

Table 6.7: Summary of the estimated fractional errors in the total rates of isolated FSR, R, due to different analysis steps. Each row gives the contributions of statistical (first error) and systematic (second error) uncertainties for one step of my analysis. The last row gives the combined total uncertainties.

total rate of isolated final-state radiation with energy between 8 GeV and 44 GeV to be

$$\boxed{\frac{\mathrm{BR}(\mathrm{Z} \to \mathrm{q}\bar{\mathrm{q}}\gamma)}{\mathrm{BR}(\mathrm{Z} \to \mathrm{q}\bar{\mathrm{q}})} \equiv R = \begin{cases} 5.02 \pm 0.10(\mathrm{stat}) \pm 0.22(\mathrm{syst}) \times 10^{-3} & \alpha_{\text{iso}} = 10° \\ 3.56 \pm 0.08(\mathrm{stat}) \pm 0.15(\mathrm{syst}) \times 10^{-3} & \alpha_{\text{iso}} = 15° \\ 2.85 \pm 0.07(\mathrm{stat}) \pm 0.12(\mathrm{syst}) \times 10^{-3} & \alpha_{\text{iso}} = 20° \\ 2.36 \pm 0.06(\mathrm{stat}) \pm 0.10(\mathrm{syst}) \times 10^{-3} & \alpha_{\text{iso}} = 25° \end{cases},}$$

where I define isolation by requiring that the total hadronic energy within a cone of half-angle α_{iso} about the photon direction be less than 100 MeV. This is one of the main results of this thesis.

	Isolation Cut (α_{iso}):			
Energy	10°	15°	20°	25°
8–12 GeV	1397± 54± 61	975±41± 11	750±35± 21	608±32± 19
12–16 GeV	851± 39± 74	572±29± 29	456±26± 22	367±23± 19
16–20 GeV	766± 39± 12	541±30± 31	413±25± 21	326±22± 23
20–24 GeV	551± 33± 47	380±24± 28	291±20± 12	249±19± 2
24–28 GeV	423± 28± 35	300±21± 5	245±18± 5	204±16± 8
28–32 GeV	323± 28± 10	245±22± 23	201±19± 19	176±18± 14
32–36 GeV	282± 26± 11	200±19± 7	168±16± 10	129±16± 17
36–40 GeV	224± 26± 49	176±21± 24	156±18± 18	143±16± 11
40–44 GeV	198± 21± 20	170±19± 20	166±18± 22	158±17± 4
TOTAL	5016±102±224	3560±78±147	2847±67±122	2360±62±101

Table 6.8: Summary of the final FSR rates that I calculate as a function of energy, after background subtraction, acceptance and efficiency corrections, and normalization to the number of hadronic Z decays. The rates are expressed as number of isolated FSR photons per million hadronic Z decays. The errors given are statistical and systematic uncertainties, respectively.

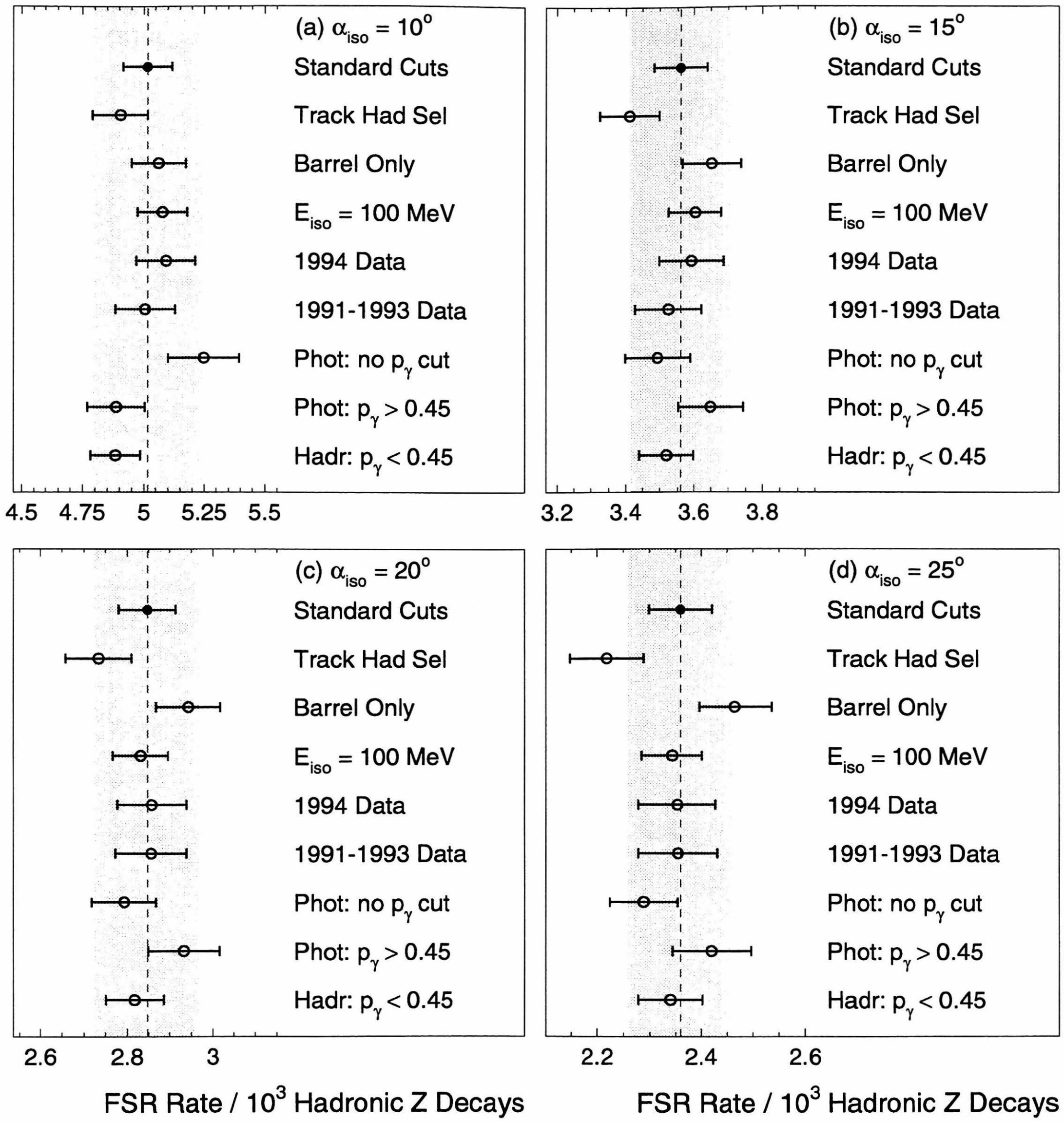

Figure 6.13: Summary of the isolated FSR rates obtained with different changes to the event selection. The top point in each plot shows the results obtained with the standard selection, and the dotted vertical lines show the central values of the standard selection. The error bars on each point are combined statistical uncertainties. The widths of the shaded vertical bands show the combined systematic errors, ΔR, that I assign.

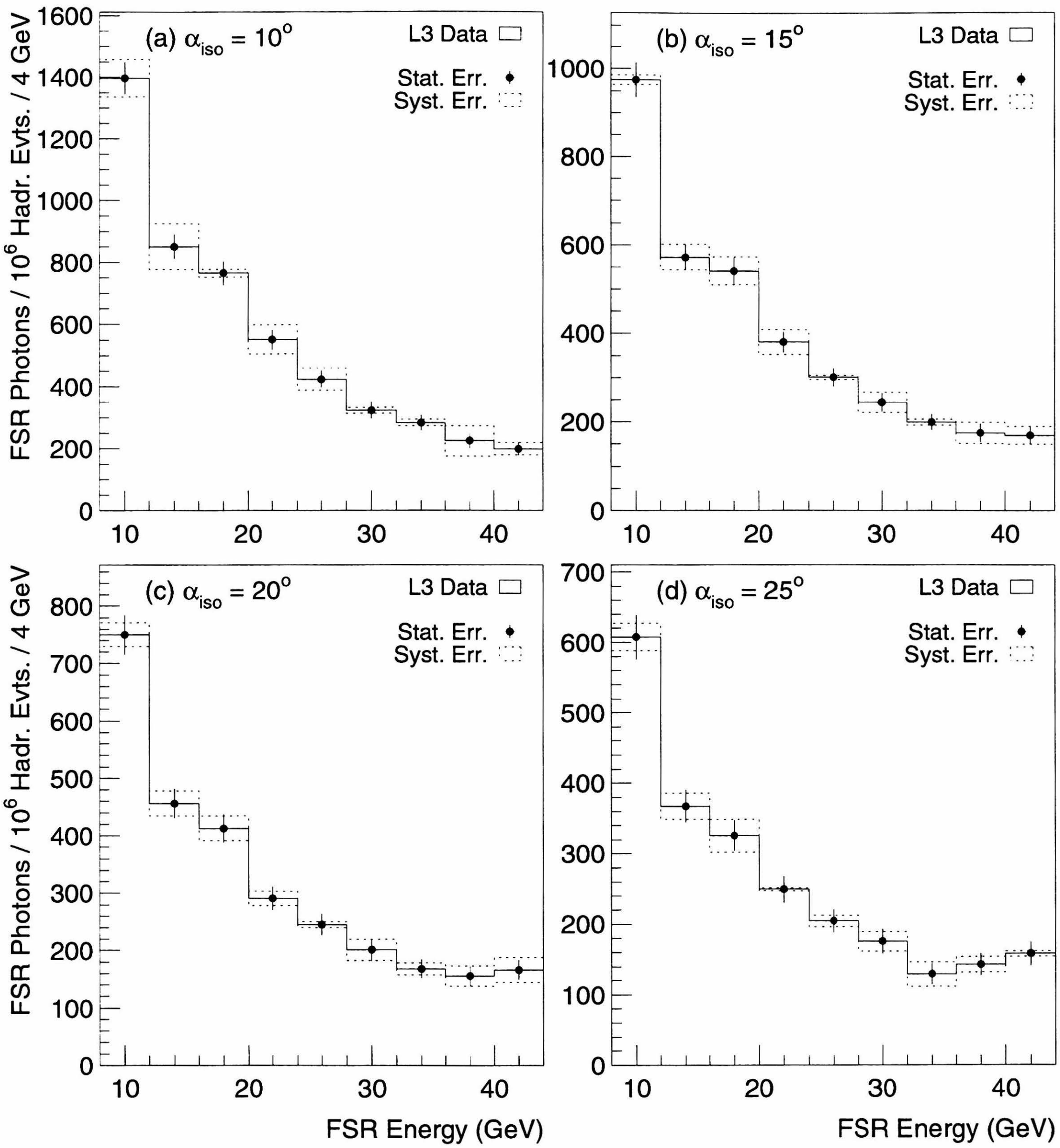

Figure 6.14: Energy distributions of isolated FSR, after background subtraction, acceptance and efficiency corrections, and normalization to the number of hadronic Z decays. The error bars show the combined statistical uncertainties and the dotted boxes show the combined systematic uncertainties.

Chapter 7

Theoretical Models

In the previous chapter, I described how I measured the energy distributions of the isolated photons that are radiated by primary quarks in hadronic Z decays, $Z \to q\overline{q}\gamma$. In this chapter, I consider how to treat this final-state radiation (FSR) process theoretically. In particular, I describe how I calculate the energy distributions that correspond to the ones I measure. In the next chapter, I will compare my experimental results with these theoretical predictions in order to determine the values of the up- and down-type quark couplings to the Z boson ($\overline{c}_{\mathrm{u}}$ and $\overline{c}_{\mathrm{d}}$) and to the photon (${Q_{\mathrm{u}}}^2$ and ${Q_{\mathrm{d}}}^2$), and to evaluate the accuracy of different theoretical methods.

Theoretical models of final-state radiation were first formulated[74] in the context of low-energy e^+e^- reactions where photon exchange rather than Z exchange dominates. However, experimental studies at these energies[75–78] were limited by a large background from initial-state radiation (ISR). Since 1989, it has been possible to perform more detailed studies of FSR at the Z resonance where ISR is suppressed and the event rate is high. These new studies required a new generation of theoretical models. The first such model[79] was based on a next-to-lowest order matrix-element calculation. Comparisons[80, 81] between this calculation and data revealed that a successful model must implement photon isolation in a way that matches the experimental cuts as closely as possible. Since this first calculation, several new models have been described[82–85] that are all based on the same matrix-element approach but that offer different schemes for isolating a photon. My original calculation is described in Reference [83] and is the basis of the results obtained in Reference [86]. Below, I describe the calculation that I have performed for this thesis which is specifically matched to the experimental cuts that I apply here.

My general approach to describing final-state radiation theoretically is to treat the process $e^+e^- \rightarrow$ hadrons $+ \gamma$ as consisting of the following independent steps, which I show schematically in Figure 7.1:

- the annihilation of an initial e^+e^- pair into a Z boson, possibly including radiation of an initial-state bremsstrahlung photon, and the decay of this Z boson into a primary $q\bar{q}$ pair,
- the perturbative evolution of the primary $q\bar{q}$ pair, in which an FSR photon is radiated, as well as gluons which can themselves radiate other gluons,

and

- the non-perturbative evolution of the quarks and gluons into hadrons, some of which will decay into multi-photon states.

I refer to these phases of evolution as electroweak, perturbative, and non-perturbative, respectively, and describe them in more detail in the following sections. In the previous chapter, I described how I subtract the contributions of ISR (see Section 6.1.1) and hadronic background (see Section 6.1.2) from the distributions that I measure. In this chapter, I focus on the description of FSR.

In this chapter, as in the previous chapter, I define the isolation of a photon at the particle level (instead of at the detector level) using a cut, $\widetilde{E}_{\text{iso}}$, on the maximum total energy of particles allowed within a cone of half-angle α_{iso} about the photon direction. In the following sections, I generally consider the value of $\widetilde{E}_{\text{iso}} = 100$ MeV to be fixed, and so I do not explicitly include it as a variable in the expressions I give. Where I give results that depend on the center-of-mass energy, $\sqrt{s}$, I use the weighted average from the events that I use in my data analysis, $\langle\sqrt{s}\rangle = 91.248$ GeV.

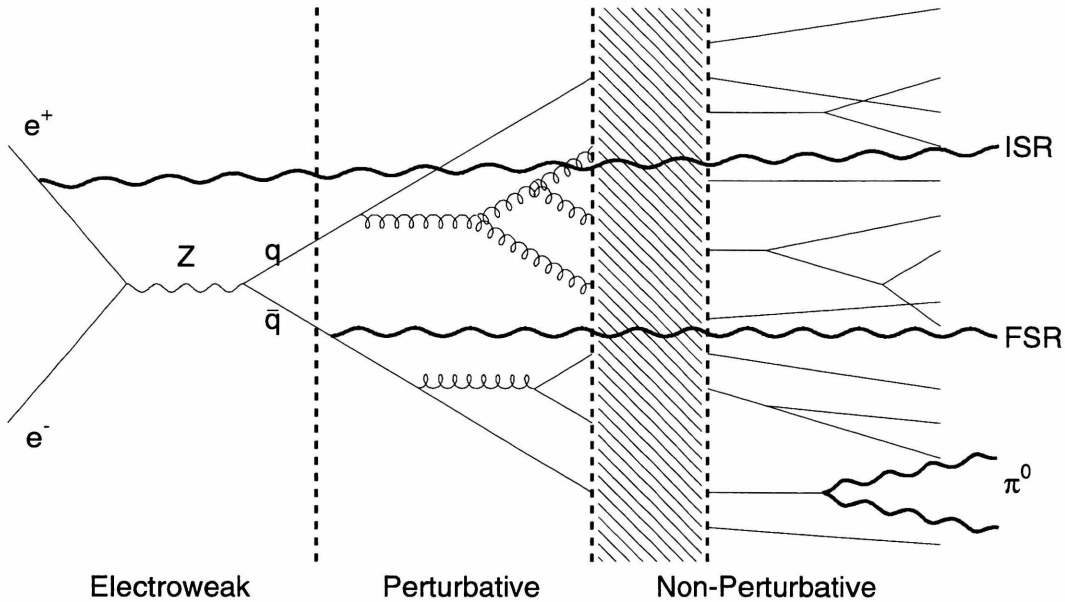

Figure 7.1: A schematic diagram of the process $e^+e^- \to$ hadrons+γ, showing the three different phases of evolution. The sources of photons shown are initial-state radiation (ISR), final-state radiation (FSR), and hadron decays (π^0).

7.1 Electroweak Processes

The first step towards producing an FSR photon is the electroweak reaction $e^+e^- \to Z \to q\overline{q}(\gamma)$, which I show schematically on the left-hand side of Figure 7.1. I have already described this process in Section 2.1.1.1, so here I only review its main features and introduce the terminology that I will use in later sections.

In order to treat the production of a primary $q\overline{q}$ pair and its subsequent evolution independently, I neglect the interference between photons radiated by the initial and final states. This simplification is justified at the Z resonance, since energetic ISR is strongly suppressed there, and thus, so is the interference between energetic ISR and energetic FSR. ISR is suppressed because the probability that an electron emits a photon before annihilating is proportional to the ratio of the e^+e^- annihilation cross sections after and before emitting the photon

$$\frac{\sigma(s \cdot (1 - x_\gamma))}{\sigma(s)} \,,$$

where $x_\gamma = 2E_\gamma/\sqrt{s}$ is the scaled energy of the ISR photon. At the Z resonance, this probability decreases rapidly with increasing E_γ because of the decreasing cross section, $\sigma(m_{\mathrm{Z}} \cdot (1 - x_\gamma))$, below the resonance peak.

I express the energy distribution of isolated FSR from each quark flavor as the product of an electroweak factor, $\sigma_{\mathrm{q\overline{q}}}(s)$, and a second factor, $f_{\mathrm{q}}(\sqrt{s}, \alpha_{\mathrm{iso}}, E_\gamma)$, which describes the subsequent evolution of the primary $\mathrm{q\overline{q}}$ pair

$$\frac{d\sigma}{dE_\gamma}(s, \alpha_{\mathrm{iso}}, E_\gamma) = \sum_{\mathrm{q=u,d,c,s,b}} \sigma_{\mathrm{q\overline{q}}}(s) \times f_{\mathrm{q}}(\sqrt{s}, \alpha_{\mathrm{iso}}, E_\gamma) \,.$$

At the peak of the Z resonance, the electroweak factor can be calculated to high accuracy using the improved Born approximation (see Section 2.1.1.1)

$$\sigma_{\mathrm{q\overline{q}}}(s) = \frac{1}{3s}\left[\frac{G_F m_{\mathrm{Z}}^2}{8\pi}\right]^2 N_C\, \overline{c}_{\mathrm{e}}\overline{c}_{\mathrm{q}} \left|\frac{s}{s - m_{\mathrm{Z}}^2 + is\Gamma_{\mathrm{Z}}/m_{\mathrm{Z}}}\right|^2 ,$$

where $G_F \simeq 1.166392 \times 10^{-5}\ \mathrm{GeV}^{-2}$ is the Fermi constant, whose value is measured from muon decays[73], and $N_C = 3$ is the number of colors in QCD. The parameters $\overline{c}_{\mathrm{e}}$ and $\overline{c}_{\mathrm{q}}$ that appear in this expression are the effective couplings of electrons and quarks, respectively, to the Z boson; they are related to the vector- and axial-couplings, $\overline{g}_V^{\mathrm{f}}$ and $\overline{g}_A^{\mathrm{f}}$ (see Section 2.1.1.1), by

$$\overline{c}_{\mathrm{f}} \equiv 4\left(\overline{g}_V^{\mathrm{f}\,2} + \overline{g}_A^{\mathrm{f}\,2}\right) \,.$$

I use the term *effective* here to indicate that these parameters do not correspond to the bare couplings of the Standard Model Lagrangian, but rather, they also include the effects of higher-order virtual corrections renormalized at the Z-mass scale.

Taking the expression for $\sigma_{\mathrm{q\overline{q}}}(s)$, above, to be the defining relationship between the effective couplings and the cross section allows a determination of those couplings to be made from a measurement of the cross section. This approach relies on only minimal assumptions about the underlying theory, and is one that I follow in the next chapter. Alternatively, by using the framework of the Standard Model, the effective couplings can all be derived from two flavor-independent parameters, $\sin^2\overline{\theta}_W$ and ρ_{eff}, according to

$$\overline{c}_{\text{f}} = \rho_{\text{eff}}\left[1 + \left(1 - 4|Q_{\text{f}}|\sin^2\overline{\theta}_W\right)^2\right] .$$

This approach has the advantage that the values of the quark couplings can be predicted using the values of $\sin^2\overline{\theta}_W$ and ρ_{eff} which are determined from the forward-backward asymmetries of Z decay into leptons (see, for example, Reference [70]). In the next chapter, I will compare this prediction with my results. I will also use the relationship between the electroweak parameters, $\sin^2\overline{\theta}_W$ and ρ_{eff}, and the quark charges, Q_{q}, in order to determine the values of the quark charges.

The bare couplings of quarks to the Z boson — those that appear in the Standard Model Lagrangian and which I denote c_{q} — only depend on the charge of a quark, so that $c_{\text{u}} = c_{\text{s}}$ and $c_{\text{d}} = c_{\text{c}} = c_{\text{b}}$. In principle, however, the higher-order corrections that are incorporated into the effective couplings introduce flavor-dependent effects. In practice, these effects are negligible except for the heaviest accessible flavor, bottom, for which the vertex corrections involving a virtual top quark must be taken into account. The effect of a heavy top quark, calculated at leading order in the top-quark mass, can be expressed using an overall correction factor which is applied to the b-quark effective coupling[18], $\overline{c}_{\text{b}} = (1 - \Delta\rho_{\text{b}})\overline{c}_{\text{d}}$, with

$$\Delta\rho_{\text{b}} = \frac{G_F m_{\text{t}}^2}{2\sqrt{2}\pi^2} \simeq (4.18 \times 10^{-7}\ \text{GeV}^{-2})\, m_{\text{t}}^2 .$$

A top quark mass[1] of $m_{\text{t}} = 180$ GeV yields a value of $\overline{c}_{\text{b}}$ that is 1.35% smaller than the value of $\overline{c}_{\text{d}}$. Finally, the set of five effective quark couplings can, to a good approximation, be parameterized using only two independent couplings, $\overline{c}_{\text{u}}$ and $\overline{c}_{\text{d}}$:

$$\overline{c}_{\text{s}} = \overline{c}_{\text{u}} \quad , \quad \overline{c}_{\text{c}} = \overline{c}_{\text{d}} \quad , \quad \text{and,} \quad \overline{c}_{\text{b}} = (1 - \Delta\rho_{\text{b}})\overline{c}_{\text{d}} .$$

[1]I use the weighted average of the recent top-quark masses determined by the CDF Collaboration, 176 ± 13 GeV [87], and the DØ Collaboration, 199 ± 30 GeV [88], obtaining $m_{\text{t}} = 180 \pm 12$ GeV.

I refer to the quarks with charge +2/3 (−1/3) as *up-type* (*down-type*), and I refer to $\bar{c}_{\mathrm{u}}$ and $\bar{c}_{\mathrm{d}}$ as the up- and down-type couplings, respectively.

The expression I use for the isolated FSR energy distribution depends on the parameters of the primary $\mathrm{q\bar{q}}$ pair through the factor $\bar{c}_{\mathrm{q}}$. Therefore, the total cross section for hadronic Z decays is obtained from this expression by replacing $\bar{c}_{\mathrm{q}}$ with the summed contributions from each accessible flavor, $2\bar{c}_{\mathrm{u}} + (3 - \Delta\rho_{\mathrm{b}})\bar{c}_{\mathrm{d}}$, and the remaining electroweak contributions are the same. I exploit this fact by rescaling to the total hadronic cross section,

$$\frac{1}{\sigma_{\mathrm{had}}}\frac{d\sigma}{dE_\gamma}(s, \alpha_{\mathrm{iso}}, E_\gamma) = \frac{1}{2\bar{c}_{\mathrm{u}} + (3 - \Delta\rho_{\mathrm{b}})\bar{c}_{\mathrm{d}}} \sum_{\mathrm{q}} \bar{c}_{\mathrm{q}} \times f_{\mathrm{q}}(\sqrt{s}, \alpha_{\mathrm{iso}}, E_\gamma) \ ,$$

which simplifies the calculation that follows. Note that the only electroweak parameters in this expression are the quark couplings to the Z boson, $\bar{c}_{\mathrm{q}}$. Therefore, by choosing this normalization for both my measured distributions and my calculation, and then comparing these, I am able to measure a constraint on the quark coupling parameters without reference to any other electroweak parameters (such as the Z boson mass or width).

Since the experimental energy distributions that I measure, R_i (see Section 6.3), are binned, the actual quantities that I will calculate for comparison are the integrals over each bin

$$\mathbb{R}_i = \frac{1}{2\bar{c}_{\mathrm{u}} + (3 - \Delta\rho_{\mathrm{b}})\bar{c}_{\mathrm{d}}} \sum_{\mathrm{q}} \bar{c}_{\mathrm{q}} \times \mathbb{R}_{\mathrm{q},i} \ .$$

I define the contribution from each quark flavor as

$$\mathbb{R}_{\mathrm{q},i} \equiv \int_{E_i}^{E_i+\Delta E} dE_\gamma \cdot f_{\mathrm{q}}(\sqrt{s}, \alpha_{\mathrm{iso}}, E_\gamma) \ ,$$

and I calculate these contributions using $\sqrt{s} = 91.248$ GeV, $\alpha_{\mathrm{iso}} = 10°$–$25°$, and $\Delta E = 4$ GeV. I use the notation $\mathbb{R}$ to denote those quantities that I calculate, to distinguish them from those that I measure, and I do not explicitly indicate the dependence of $\mathbb{R}_i$ and $\mathbb{R}_{\mathrm{q},i}$ on α_{iso}.

7.2 Perturbative Processes

The second step that I consider in FSR production is the perturbative evolution of a primary $\mathrm{q\overline{q}}$ pair. The main process in this evolution is gluon radiation, from both the primary quarks and from previously radiated gluons. A photon can also be emitted from a primary quark — this is the process that I refer to as final-state radiation — but it occurs less frequently than gluon emission because the quark-photon coupling, $Q_\mathrm{q}^2\alpha$, is small compared with the quark-gluon coupling, $C_F\alpha_S$.

While the coupling strengths for photon and gluon radiation differ, the dynamics are similar: the radiated particle is typically of low energy and produced at a small angle with respect to the quark. Therefore, most of the photons radiated by a quark do not meet the minimum energy and isolation requirements that I apply in my analysis, and so the process that I study experimentally is suppressed relative to inclusive FSR production. However, when a quark *does* radiate an energetic and isolated photon, it is most likely that it does so before radiating any energetic gluons, to which it would have lost energy. As a result, I expect that energetic gluon radiation is not an important effect in the production of isolated and energetic FSR.

My goal is to perform a perturbative calculation of the function f_q, which I defined in Section 7.1, and the associated binned quantities, $\mathbb{R}_{\mathrm{q},i}$. The contributions to these calculations that I consider are the emission of a single photon, which results in an overall factor of $Q_\mathrm{q}^2\alpha/(2\pi)$, and the emission of both real and virtual gluons, which are associated with factors proportional to the strong coupling, α_S. A complete perturbative calculation of f_q that includes these contributions can be expanded in powers of α_S and a logarithm, $L = \log y$, as

$$f_\mathrm{q} = \frac{Q_\mathrm{q}^2\alpha}{2\pi}\sum_{n=0}^{\infty}\sum_{k=0}^{2n} c_{n,k}\cdot\alpha_S^n\cdot L^k\ ,$$

which is shown schematically in Figure 7.2 (I define the variable y, which is associated with gluon radiation, in Section 7.2.2). I consider two complementary approaches for systematically generating this expansion: row-wise and column-wise.

LO, $\mathcal{O}(\alpha_s)$	$\alpha_s L^2$	$\alpha_s L$	α_s					
NLO, $\mathcal{O}(\alpha_s^2)$	$\alpha_s^2 L^4$	$\alpha_s^2 L^3$	$\alpha_s^2 L^2$	$\alpha_s^2 L$	α_s^2			
NNLO, $\mathcal{O}(\alpha_s^3)$	$\alpha_s^3 L^6$	$\alpha_s^3 L^5$	$\alpha_s^3 L^4$	$\alpha_s^3 L^3$	$\alpha_s^3 L^2$	$\alpha_s^3 L$	α_s^3	
$\vdots$	$\vdots$	$\vdots$	$\vdots$	$\vdots$	$\vdots$	$\vdots$	$\vdots$	$\ddots$
	LL	NLL	NNLL	...				

Figure 7.2: Schematic representation of the terms in a perturbative QCD expansion. The rows correspond to orders of a matrix-element expansion, with expansion parameter α_S. The columns correspond to orders of a leading-logarithm expansion, with expansion parameter $1/L$.

Adding together the terms in each row, k, of Figure 7.2 yields the contribution to f_q that is proportional to α_S^k. Since the strong coupling is a small parameter ($\alpha_S \simeq 0.1$), the successive contributions from the rows $k = 1, 2, \dots$ provide a series of improving approximations to f_q. I refer to this as the matrix-element approach for calculating f_q, and I refer to the first approximation ($k = 1$) as the lowest order (LO), the second ($k = 2$) as the next-to-lowest order (NLO), and so on. I describe this approach in more detail in Section 7.2.1, below. For some observables, the value of the logarithm, $L = \log y$, can be large. If L is too large ($L \gg 1$), a perturbative expansion no longer converges and the observable is not perturbatively calculable. However, for a range of moderately large values, $1 \lesssim L \lesssim \alpha_S^{-1/2}$, the matrix-element approach converges, but slowly, and it is necessary to use $1/L$ as an expansion parameter instead of α_S. This approach, which I refer to as the leading-logarithm method, consists of taking the successive contributions from the columns of Figure 7.2 as a series of approximations to f_q. I describe this method in more detail in Section 7.2.2. There, I also argue that the leading-logarithm method is less appropriate than the matrix-element method for calculating the energy distribution of isolated FSR.

7.2.1 Matrix-Element Calculations

In this section, I describe how I calculate the energy distribution of isolated FSR using a matrix-element method. First, I derive the calculation at lowest order, which is $\mathcal{O}(\alpha)$, and then I describe how I extend this calculation to next-to-lowest order, which is $\mathcal{O}(\alpha_S\alpha)$. For the lowest-order calculation, I first assume that the radiating quark is massless, and then I calculate the corrections due to finite mass effects.

7.2.1.1 FSR Production at Lowest Order

The differential cross section that describes the annihilation of an e^+e^- pair into a Z boson, and then the subsequent Z decay into a final state evolving from a primary $q\bar{q}$ pair, can be written

$$d\sigma_{q\bar{q}} = \frac{1}{s - m_Z^2} L_{\mu\nu} H^{\mu\nu} \cdot d\Phi \ ,$$

where the tensors $L_{\mu\nu}$ and $H^{\mu\nu}$ describe the initial- and final-state currents, respectively, and $d\Phi$ describes the phase space available to the final state. Averaging out all angular correlations between the initial and final states, and normalizing to the the total cross section, reduces the cross section to

$$\frac{1}{\sigma_{q\bar{q}}} d\sigma = \frac{4\pi^2}{\sqrt{s}} g_{\mu\nu} H^{\mu\nu} \cdot d\Phi \ .$$

The final-state current from a $q\bar{q}$ pair, together with a radiated photon, is described, at lowest order, by the tensor

$$H^{\mu\nu} = \sum_{\text{pol}} (h_1^\mu + h_2^\mu) \cdot (h_1^\nu + h_2^\nu)^* \ ,$$

where the summation is over all polarization states of the final-state particles, and the h_i^μ are the currents associated with the diagrams of Figure 7.3

$$h_1^\mu = \frac{Q_q e}{2\,(q_2 \cdot k)} \bar{u}(q_1, \lambda_1)\, \gamma^\mu\, (m - \not{q}_2 - \not{k})\, \not{\epsilon}^*(\lambda)\, v(q_2, \lambda_2)$$
$$h_2^\mu = \frac{Q_q e}{2\,(q_1 \cdot k)} \bar{u}(q_1, \lambda_1)\, \not{\epsilon}^*(\lambda)\, (m + \not{q}_1 + \not{k})\, \gamma^\mu\, v(q_2, \lambda_2) \ .$$

The phase space for the three-body decay is

$$d\Phi = \frac{1}{(2\pi)^3}\,\frac{1}{8\sqrt{s}}\,dE_1 dE_2$$

where E_1 and E_2 are the quark and anti-quark energies respectively, measured in the Z decay rest frame.

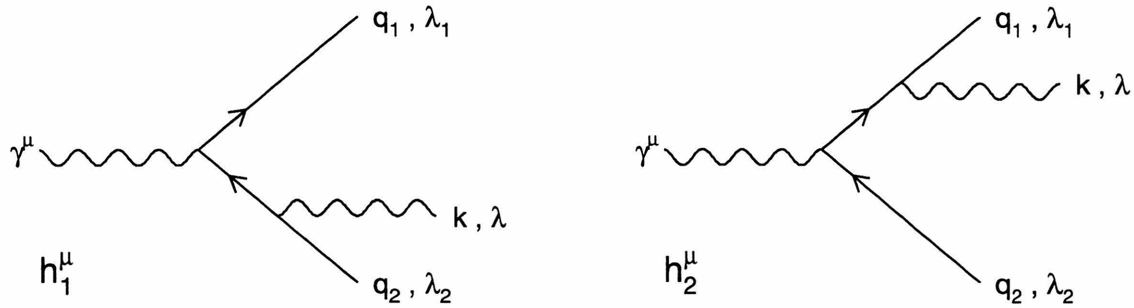

Figure 7.3: Lowest-order diagrams for the process $Z \to q\bar{q}\gamma$, showing the labeling used in the text for the momenta (q_1, q_2, k) and spins $(\lambda_1, \lambda_2, \lambda)$ of the quark, anti-quark, and photon respectively.

The cross section is expressed most compactly in terms of dimensionless scaled energies, which I define for the quark and antiquark as

$$x_1 \equiv \frac{2E_1}{\sqrt{s}} = 1 - 2(q_2 \cdot k)/s \quad , \quad x_2 \equiv \frac{2E_2}{\sqrt{s}} = 1 - 2(q_1 \cdot k)/s \ ,$$

and for the photon as

$$x_\gamma \equiv \frac{2E_\gamma}{\sqrt{s}} = 1 - (q_1 + q_2)^2/s = 2 - x_1 - x_2 \ .$$

In addition, it is convenient to define a scaled quark mass, $\mu^2 \equiv 2m_{\rm q}^2/s$, and the angular variable $t \equiv \min(t_1, t_2)$, where

$$t_i = \frac{1 - x_j}{x_\gamma x_i} = \frac{1 - \beta_i \cos\theta_{i,\gamma}}{2} \ ,$$

and $\beta_i \equiv |\vec{p}_i|/E_i$.

The lowest-order differential cross section for FSR production from a quark with charge Q_{q} and scaled mass μ, in terms of the scaled quark energies, is then

$$\begin{aligned}\frac{1}{\sigma_{\mathrm{q\bar{q}}}}\frac{d\sigma^{(\mathrm{LO})}}{dx_1 dx_2} = \frac{Q_{\mathrm{q}}^2\alpha}{2\pi}\Bigg\{&\frac{x_1^2+x_2^2}{(1-x_1)(1-x_2)} \\ &-\mu^2(3-x_1-x_2)\left[\frac{1}{(1-x_1)^2}+\frac{1}{(1-x_2)^2}\right] \\ &-\mu^4\left[\frac{1}{(1-x_1)^2}+\frac{1}{(1-x_2)^2}+\frac{2}{(1-x_1)(1-x_2)}\right]\Bigg\}\,,\end{aligned}$$

where I use the superscript (LO) to denote a quantity that is calculated at lowest order, $\mathcal{O}(\alpha)$, in perturbation theory. The kinematically-allowed phase space is described by

$$\sqrt{2}\,\mu \leq x_1\,,\, x_2 \leq 1 \quad \text{and} \quad x_1 + x_2 \geq 1 + 2\mu^2\,,$$

and is shown in Figure 7.4. The cross section diverges when either $x_1 \to 1$ or $x_2 \to 1$.

7.2.1.2 Lowest-Order Energy Distributions for Massless Quarks

In this section, I calculate the energy distribution of isolated FSR from massless quarks using the cross section I calculated in the previous section. Since the lowest-order calculation does not describe a realistic hadronic final state, the experimental photon isolation requirement must be reinterpreted in terms of the quark final state: I define isolation here by requiring that no quark be present in a cone of half-angle α_{iso} around the photon direction

$$t \geq t_0 \equiv (1-\cos\alpha_{\mathrm{iso}})/2\,.$$

Figure 7.4 shows the effect this cutoff has on the allowed phase space for isolated FSR emission. The cut regulates most of the singular behavior of the cross section, except when $x_\gamma \to 0$ ($x_1 \to 1$ and $x_2 \to 1$) and $tx_\gamma \to 1$ ($x_i \to 0$ and $x_j \to 1$).

The lowest-order differential cross section for FSR production from a massless quark with charge Q_{q}, in terms of the variables x_γ and t, is

$$\frac{1}{\sigma_{\mathrm{q\bar{q}}}}\frac{d\sigma^{(\mathrm{LO})}}{dx_\gamma dt} = \frac{Q_{\mathrm{q}}^2\alpha}{\pi}\left\{\frac{(1-x_\gamma)^2+(1+tx_\gamma^2)^2-4tx_\gamma(1-tx_\gamma+tx_\gamma^2)}{tx_\gamma(1-t)(1-tx_\gamma)^2}\right\}\,.$$

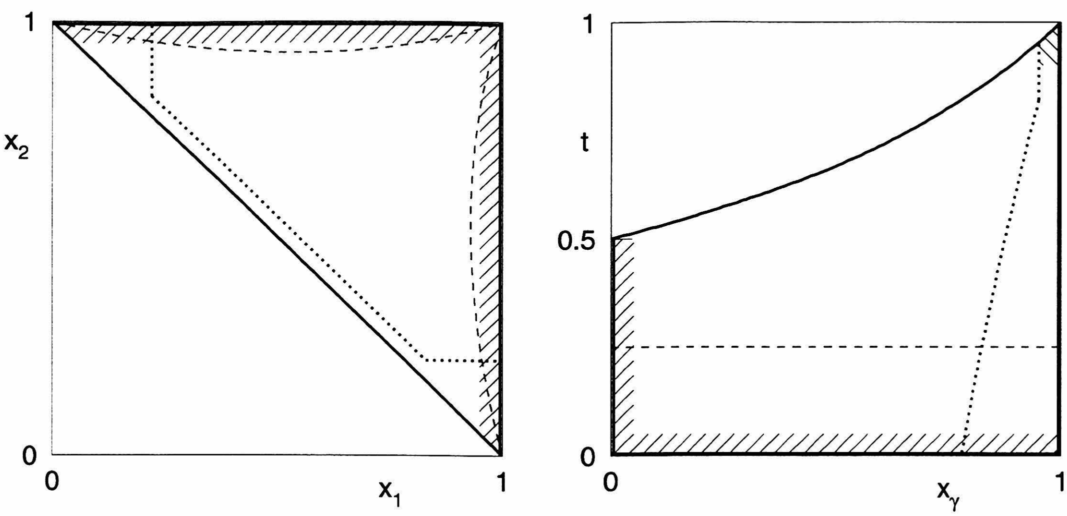

Figure 7.4: Lowest-order phase space for the decay $Z \longrightarrow q\bar{q}\gamma$. The left-hand diagram shows the phase space in terms of the scaled quark-energies x_1 and x_2. The right-hand diagram shows the phase space in terms of the scaled photon energy x_γ and the angular variable t. The regions of phase space where the matrix element diverges are indicated with hatched areas. The kinematically allowed regions for massless quarks are indicated with solid outlines. Dotted lines show the additional constraints for a massive quark (a value of $m_q = 10$ GeV was chosen for clarity). The isolation constraint $t \geq t_0$ is indicated with dashed lines (a value of $\alpha_{\text{iso}} = 60°$ was chosen for clarity).

I obtain the isolated FSR energy distribution by integrating out the angular variable t from the lower cutoff $t_{\text{min}} = t_0$ up to the kinematic limit $t_{\text{max}} = 1/(2 - x_\gamma)$

$$\frac{1}{\sigma_{q\bar{q}}} \frac{d\sigma^{(\text{LO})}}{dx_\gamma} = \int_{t_0}^{1/(2-x_\gamma)} \frac{1}{\sigma_{q\bar{q}}} \frac{d\sigma^{(\text{LO})}}{dx_\gamma dt} dt \ ,$$

which yields

$$\frac{1}{\sigma_{q\bar{q}}} \frac{d\sigma^{(\text{LO})}}{dx_\gamma} = \frac{Q_q^2 \alpha}{\pi} \left\{ x_\gamma - 2 + 2\frac{1 - x_\gamma}{1 - t_0 x_\gamma} + \frac{2 - 2x_\gamma + x_\gamma^2}{x_\gamma} \cdot \log \frac{1 - t_0}{t_0(1 - x_\gamma)} \right\} \ .$$

With a further integration of the isolated FSR energy distribution over an energy interval $x_{\text{min}} < x_\gamma < x_{\text{max}}$, I obtain

$$\int_{x_{\text{min}}}^{x_{\text{max}}} \frac{1}{\sigma_{q\bar{q}}} \frac{d\sigma^{(\text{LO})}}{dx_\gamma} dx_\gamma = \frac{Q_q^2 \alpha}{2\pi} \left[F(x_{\text{max}}, t_0) - F(x_{\text{min}}, t_0) \right] \ ,$$

with

$$F(x,t_0) = \frac{4}{t_0}\left[1 - t_0 - t_0 \log(\frac{1-t_0}{t_0})\right] x + \left[1 + \log(\frac{1-t_0}{t_0})\right] x^2$$
$$+ 4 \log(\frac{1-t_0}{t_0}) \log x + 4 \left(\frac{1-t_0}{t_0^2}\right) \log(1 - t_0 x)$$
$$+ \frac{1}{2}(x-4)(x-2) + (x-3)(1-x)\log(1-x) + 4\,\mathrm{Li}_2(x) ,$$

where the dilogarithm function, $\mathrm{Li}_2(x)$, is given by

$$\mathrm{Li}_2(x) = \int_0^x \frac{\log|1-z|}{z} dz = \sum_{k=1}^{\infty} \frac{x^k}{k^2} .$$

This energy distribution is related to the function, f_{q}, which I defined in Section 7.1, by

$$f_{\mathrm{q}}(\sqrt{s}, \alpha_{\mathrm{iso}}, E_\gamma) =$$
$$\frac{2}{\sqrt{s}} \frac{1}{\sigma_{\mathrm{q\bar{q}}}} \left\{ \frac{d\sigma^{(\mathrm{LO})}}{dx_\gamma} + \mathcal{O}(\mu^2\alpha) + \mathcal{O}(\alpha_s\alpha) \right\} \otimes \left\{ \text{non-perturbative effects} \right\} ,$$

and is thus a lowest-order approximation to this function. Similarly, the energy integral that I perform provides lowest-order approximations to the binned quantities, $\mathbb{R}_{\mathrm{q},i}$, which are

$$\mathbb{R}_{\mathrm{q},i}^{(\mathrm{LO})} = \frac{Q_{\mathrm{q}}^2\alpha}{2\pi} \left[F(x_i + \Delta x, t_0) - F(x_i, t_0)\right] ,$$

where I define $x_i \equiv 2E_i/\sqrt{s}$ and $\Delta x \equiv 2\Delta E/\sqrt{s}$. Since the contributions to $\mathbb{R}_i$ from each quark flavor are the same when all quarks are considered to be massless, $\mathbb{R}_i$ is given at lowest order by

$$\mathbb{R}_i^{(\mathrm{LO})} = \frac{2\bar{c}_{\mathrm{u}} {Q_{\mathrm{u}}}^2 + (3 - \Delta\rho_{\mathrm{b}})\bar{c}_{\mathrm{d}} {Q_{\mathrm{d}}}^2}{2\bar{c}_{\mathrm{u}} + (3 - \Delta\rho_{\mathrm{b}})\bar{c}_{\mathrm{d}}} \mathbb{R}_{\mathrm{q},i}^{(\mathrm{LO})} .$$

In Figure 7.5(a), I show my lowest-order approximation to f_{q} as a function of both energy and isolation, and I also superimpose my binned predictions of $\mathbb{R}_{\mathrm{q},i}^{(\mathrm{LO})}$. In Figure 7.5(b), I show the integral of f_{q} over the range 8 GeV $< E_\gamma <$ 44 GeV, which I use for my data analysis, as a function of the isolation cut, α_{iso}. I performed my calculations with the overall scale factor, $Q_{\mathrm{q}}^2\alpha/(2\pi)$, set to one, so that my results do not depend on the type of quark or on the values of any coupling constants.

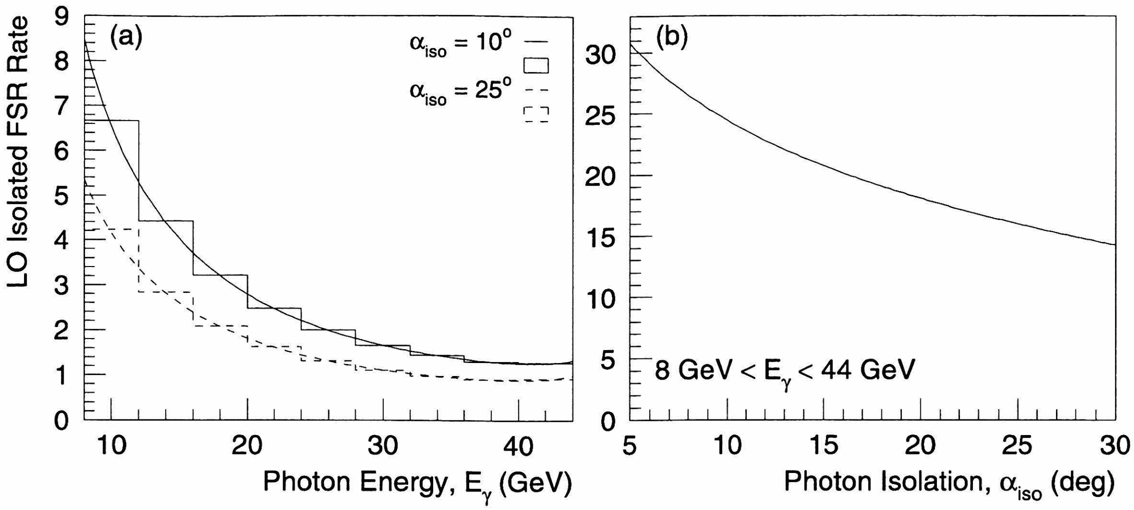

Figure 7.5: Isolated FSR rates for a single quark flavor calculated at lowest order, and shown as functions of the photon energy for two different isolations (a), and the photon isolation for 8 GeV $< E_\gamma <$ 44 GeV (b). In (a), I compare the differential energy distributions, $\Delta E \cdot f_{\mathrm{q}}^{(\mathrm{LO})}$, (smooth curves) with the binned distributions, $\mathbb{R}_{\mathrm{q},i}^{(\mathrm{LO})}$ (histograms). The results were obtained by dividing out the overall factor, $Q_{\mathrm{q}}^2\alpha/(2\pi)$ (see Figures 7.19 and 7.20 for results that include all couplings).

7.2.1.3 Lowest-Order Corrections for Quark Masses

In this section, I consider how quark masses change the results that I presented above. I will express the effects of quark mass on the energy distribution of isolated FSR as a correction factor that I apply to the distribution I calculate for a massless quarks. Since it is not technically feasible to calculate quark-mass effects explicitly at higher orders, I will use my lowest-order correction to estimate the size of these effects at higher orders.

Mass corrections in perturbative calculations generally arise from restrictions on the phase space available to the final state, and from additional terms in the matrix element proportional to powers of μ. The expressions above for the dimensionless variables x_1, x_2, x_γ, and t are still valid for massive quarks, and so the three-body phase-space factor, $d\Phi$, does not change. However, the phase-space limits are reduced — as Figure 7.4 shows — so the isolated FSR rate is lower at higher photon energies.

For the calculation I will perform, it is convenient to divide phase space into two regions (see Figure 7.6), according to whether the range of allowed values for x_1 and x_2 at a fixed value of x_γ is determined by the isolation cut (region A) or by the kinematic boundary (region B). The boundary between these two regions occurs at

$$x'_\gamma = \frac{1 - 2m_q/\sqrt{s}}{1 - 2t_0 m_q/\sqrt{s}} \ .$$

In region A, it is most convenient to use the variables x_γ and t; in region B, the variables x_1 and x_2 are most convenient.

The FSR energy distribution that I calculate for region A depends on the isolation cut that I apply, $t \geq t_0$. The interpretation of this cut is slightly modified when quark masses are taken into account, since

$$t_i = \frac{1 - \beta_i \cos\theta_{i,\gamma}}{2} = \frac{1 - \cos\theta_{i,\gamma}}{2} + \mathcal{O}(\frac{\mu}{x_i})^2 \ .$$

This correction increases the probability that a photon is considered to be isolated when the nearest quark is very soft ($E_i \to m_q$), and therefore approximately incorporates the experimental requirement that the energy within an isolation cone be above some minimum value. In region B, the energy distribution is independent of the isolation cut t_0, but depends instead on a parameter, d_0, through the kinematic constraint

$$x_\gamma + |x_1 - x_2| \leq d_0 \ ,$$

with

$$d_0 \equiv 2(1 - \sqrt{2}\mu) \ .$$

Below, I give the results of my calculation of the lowest-order differential energy distribution, including quark-mass effects, in the form

$$\begin{aligned}\frac{d\sigma^{(\mathrm{LO})}}{dx_\gamma}(x_\gamma, \alpha_{\mathrm{iso}}, \mu) = &\left[\frac{d\sigma_A}{dx_\gamma}(x_\gamma, t_0) + \frac{d\sigma'_A}{dx_\gamma}(x_\gamma, t_0, \mu)\right] \cdot \Theta(x_\gamma < x'_\gamma) \\ &+ \left[\frac{d\sigma_B}{dx_\gamma}(x_\gamma, d_0) + \frac{d\sigma'_B}{dx_\gamma}(x_\gamma, d_0, \mu)\right] \cdot \Theta(x_\gamma \geq x'_\gamma) \ ,\end{aligned}$$

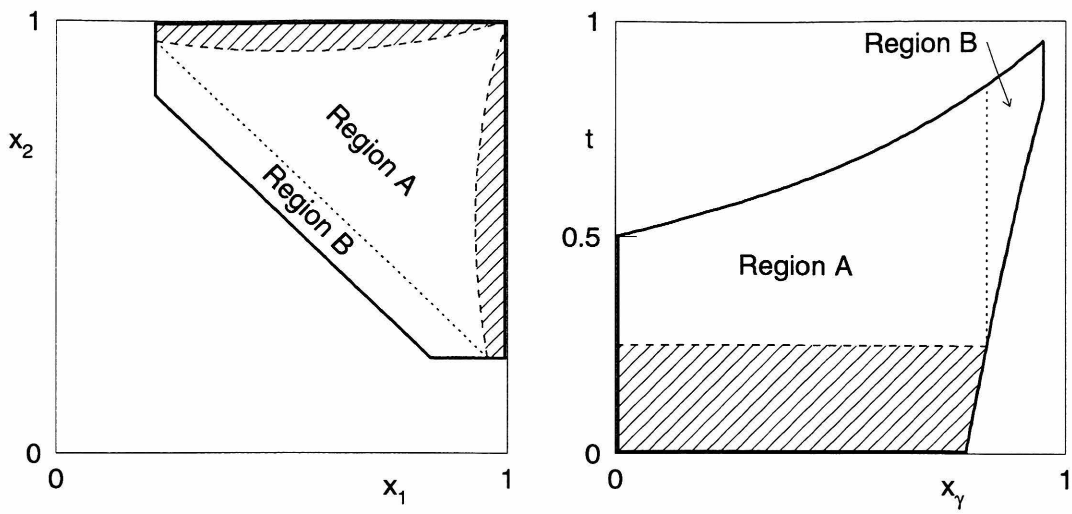

Figure 7.6: Division of the lowest-order phase space for decay $Z \to q\bar{q}\gamma$ into two regions for the purposes of calculating the energy distribution of isolated FSR produced by massive quarks. The left-hand diagram shows the phase space in terms of the scaled quark energies x_1 and x_2. The right-hand diagram shows the phase space in terms of the scaled photon energy x_γ and the angular variable t. The kinematically allowed regions for massive quarks are indicated with solid outlines (a value of $m_q = 10$ GeV was chosen for clarity). The isolation constraint $t \geq t_0$ is indicated with dashed lines (a value of $\alpha_{\text{iso}} = 60°$ was chosen for clarity) and the phase space that is cut is indicated as a dashed area. Dotted lines indicate the boundary between regions A and B.

where the theta functions select the expressions appropriate for either region A or region B. The first term in each large bracket represents the contribution of the massless lowest-order matrix element (and so only depends on quark masses through changes in the available phase space), and the second (primed) term represents the contributions of the mass-dependent corrections to the lowest-order matrix element. I use a similar decomposition for the function, $F(x, \alpha_{\text{iso}}, \mu)$, which I obtain by integrating this differential energy distribution.

By performing the energy integral of the matrix element for massless quarks in region A, I obtain the same results as in the previous section,

$$\frac{1}{\sigma_{q\bar{q}}}\frac{d\sigma_A}{dx_\gamma}(x_\gamma, t_0) = \frac{1}{\sigma_{q\bar{q}}}\frac{d\sigma^{(LO)}}{dx_\gamma}(x_\gamma, t_0) \quad \text{and,} \quad F_A(x, t_0) = F(x, t_0) ,$$

since neither the integrand nor the integration limits depend on the quark mass. Performing the energy integration on the massless matrix element in region B gives

$$\frac{1}{\sigma_{q\bar{q}}}\frac{d\sigma_B}{dx_\gamma}(x_\gamma, d_0) = \frac{Q_q^2\alpha}{\pi}\left\{\frac{2 - 2x_\gamma + x_\gamma^2}{x}\log\frac{d_0}{d_0 - 2x_\gamma} + x_\gamma - d_0\right\} ,$$

and

$$\begin{aligned} F_B(x, d_0) = &- 4x + \frac{3}{2}x(x - d_0) + x(x-4)\log\frac{d_0}{2x - d_0} + \frac{d_0}{4}(d_0 - 8)\log(2x - d_0) \\ &+ 4\log d_0 \log x - 4\log(2x - d_0)\log\frac{2x}{d_0} - 4\,\mathrm{Li}_2(1 - \frac{2x}{d_0}) . \end{aligned}$$

The additional mass-dependent terms in the lowest-order matrix element give a negative contribution, that is, they reduce the isolated FSR rate. Performing the integration of these terms, I obtain, in region A

$$\begin{aligned} \frac{1}{\sigma_{q\bar{q}}}\frac{d\sigma'_A}{dx_\gamma}(x_\gamma, t_0, \mu) = &-\frac{Q_q^2\alpha}{\pi}\left\{\mu^2\frac{(1+x_\gamma)(1-t_0x_\gamma)(1-2t_0x_\gamma)}{(1-t_0)t_0(1-x_\gamma)x_\gamma}\right. \\ &\left.+\mu^4\left[-1 + \frac{2}{x_\gamma} - \frac{1-x_\gamma}{x_\gamma(1-t_0)} - \frac{2-x_\gamma}{x_\gamma(1-x_\gamma)} + \frac{1}{t_0x_\gamma(1-x_\gamma)} + \frac{2}{x_\gamma}\log\frac{1-t_0}{t_0(1-x_\gamma)}\right]\right\} , \end{aligned}$$

and, in region B

$$\begin{aligned} \frac{1}{\sigma_{q\bar{q}}}\frac{d\sigma'_B}{dx_\gamma}(x_\gamma, d_0, \mu) = &-\frac{Q_q^2\alpha}{\pi}\left\{4\mu^2\frac{(d_0 - x_\gamma)(1+x_\gamma)}{d_0(2x_\gamma - d_0)}\right. \\ &\left.+ 4\mu^4\left[\frac{d_0 - x}{d_0(2x_\gamma - d_0)} + \frac{1}{x_\gamma}\,\mathrm{atanh}\frac{d_0 - x_\gamma}{x_\gamma}\right]\right\} . \end{aligned}$$

Performing a further energy integration of these energy distributions, I obtain, in region A

$$\begin{aligned} F'_A(x, t_0, \mu) = &-\mu^2\left[\frac{t_0x^2}{1-t_0} - 4\left(\frac{1-t_0}{t_0}\right)\log(1-x) + \frac{2(1-2t_0)}{t_0(1-t_0)}\log x\right] \\ &- \mu^4\left\{\frac{2t_0x}{1-t_0} - 2\left(\frac{1-t_0}{t_0}\right)\log(1-x) + 4\mathrm{Li}_2(x)\right. \\ &\left.+ \frac{2}{t_0(1-t_0)}\left[1 - 2t_0 + 2t_0(1-t_0)\log\frac{1-t_0}{t_0}\right]\log x\right\} , \end{aligned}$$

and, in region B

$$F'_B(x,d_0,\mu) = -\mu^2\left[2\frac{x(d_0-2)}{d_0} - 2\frac{x^2}{d_0} + (2+d_0)\log(2x-d_0)\right]$$
$$-\mu^4\left[2\log(2x-d_0) - 4\frac{x}{d_0} + 8\,\mathrm{atanh}(1-\frac{d_0}{x})\,\log\frac{d_0}{x}\right.$$
$$\left. -4\log(1-\frac{d_0}{2x})\log\frac{d_0}{x} + 2\log^2\frac{d_0}{x} - 4\,\mathrm{Li}_2(\frac{d_0}{2x})\right] .$$

A comparison of the lowest-order energy distributions that I have calculated, with and without quark masses taken into account, reveals the following general features:

- both the reduction in phase space due to quark masses and the additional terms in the matrix element proportional to mass reduce the rate of isolated FSR,
- the reduction in the rate is greater for photons that are more energetic or less isolated,

and

- the dominant effect of nonzero quark masses is proportional to μ^2, so that, to a good approximation, quark-mass corrections scale with m_q^2.

I also note that when $x_\gamma \to 1$ or $\alpha_{\rm iso} \to 0$, the negative contributions from the mass-dependent terms diverge faster than the positive contributions from the mass-independent terms. As a result, the net lowest-order cross section eventually takes on negative values for sufficiently energetic and isolated photons. This behavior signals that a lowest-order calculation of mass corrections is not reliable over the full range of photon energy and isolation.

In order to evaluate the expressions that I give above, I must specify the values of the quark masses. These values are not well defined, since they can not be measured directly. Instead, quark masses must be determined from hadron properties, and thus depend on exactly how they are defined in relation to these properties. The s-quark mass has been estimated[73] to be between 100 MeV and 300 MeV, from the mass differences between strange and non-strange hadrons. The mass ratios, $m_{\mathrm{u}}/m_{\mathrm{d}}$ and $m_{\mathrm{s}}/m_{\mathrm{d}}$, have been extracted from the pion and kaon masses masses using chiral symmetry[73], and give a u-quark mass between 2 MeV and 8 MeV, and a d-quark mass between 5 MeV and 15 MeV. The c-quark mass has been estimated from charmonium and D-meson masses, using $\overline{\mathrm{MS}}$ perturbation theory, to be between 1.0 GeV and 1.6 GeV. The b-quark mass has been estimated from bottomonium and B-meson masses, using similar techniques, to be between 4.1 GeV and 4.5 GeV. The top-quark mass has recently been estimated by both the CDF[87] and DØ[88] collaborations from T-meson masses, and their combined result is 180 $\pm$ 12 GeV; however, the t quark is not kinematically accessible at LEP.

I express the lowest-order energy distribution, with mass effects included, as the product of the lowest-order distribution for massless quarks that I derived in the previous section and a mass correction factor

$$\frac{d\sigma^{(\mathrm{LO})}}{dx_\gamma}(x_\gamma, \alpha_{\mathrm{iso}}, \mu) = \frac{d\sigma^{(\mathrm{LO})}}{dx_\gamma}(x_\gamma, \alpha_{\mathrm{iso}}) \times [1 - M(x_\gamma, \alpha_{\mathrm{iso}}, \mu)] \ .$$

The value of $M(x_\gamma, \alpha_{\mathrm{iso}}, \mu)$ is then positive, since mass corrections reduce the FSR rate, and increases with increasing photon energy or decreasing photon isolation. In Figure 7.7, I show the value of M as a function of both energy and isolation for two quark masses: 1 GeV, which is the lower limit of the estimated c-quark mass, and 4.5 GeV, which is the upper limit of the b-quark mass. I observe that the scaling of mass corrections with m_{q}^2 is a good approximation for all of the accessible quark flavors when the photon energy is below 41 GeV (the scaling approximation improves with decreasing mass, so it is sufficient to verify it for the heaviest quarks). The breakdown of scaling for b quarks above 41 GeV is due to the transition from region A to region B, and arises because the mass correction in region B is independent of the isolation cut. The results in Figure 7.7 show that the mass corrections due to light quarks (u, d, or s) are negligible. Using a quark mass of 300 MeV and requiring 10° isolation (these choices provide an upper bound on the size of light-quark mass corrections to my calculation), the correction reaches a maximum value of 2% at 44 GeV, and the overall correction to the total rate of isolated FSR between 8 GeV and 44 GeV is less than 0.2%.

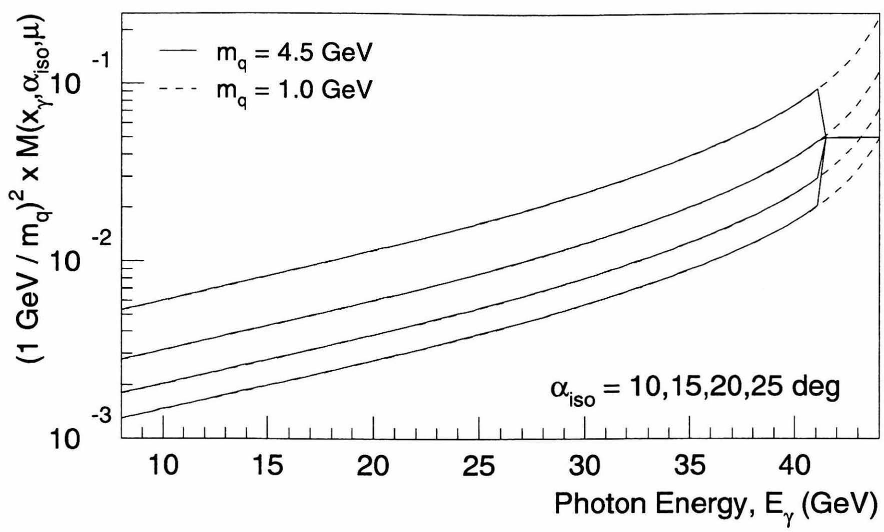

Figure 7.7: The dependence of the scaled lowest-order mass correction, $(1\ \mathrm{GeV}/m_q)^2 \times M(x_\gamma, \alpha_{\mathrm{iso}}, \mu)$, on photon energy and isolation. Solid lines give the corrections for a quark mass of 4.5 GeV, and dashed lines for a mass of 1 GeV. The four curves are, from top to bottom, for the isolation cuts α_{iso} = 10°, 15°, 20°, and 25°.

Figure 7.8 shows the total rate of isolated FSR, with energies between 8 GeV and 44 GeV, that I calculate as a function of the isolation cut, for different quark masses. The mass corrections are small for the light quarks, as well as for the c quark, in the range of isolation cuts that I use in my experimental analysis. The rate of isolated FSR from b quarks that I calculate diverges from the rates that I calculate for other quarks for isolation cuts less than about 20°. I interpret this behavior as a breakdown of the lowest-order approximation that I am using, and I consider my calculated b-quark mass corrections to be unreliable for $\alpha_{\mathrm{iso}} \lesssim 20°$.

In order to compare my full theoretical prediction, including the effects of finite quark mass, with my experimental results, I express my lowest-order calculation of

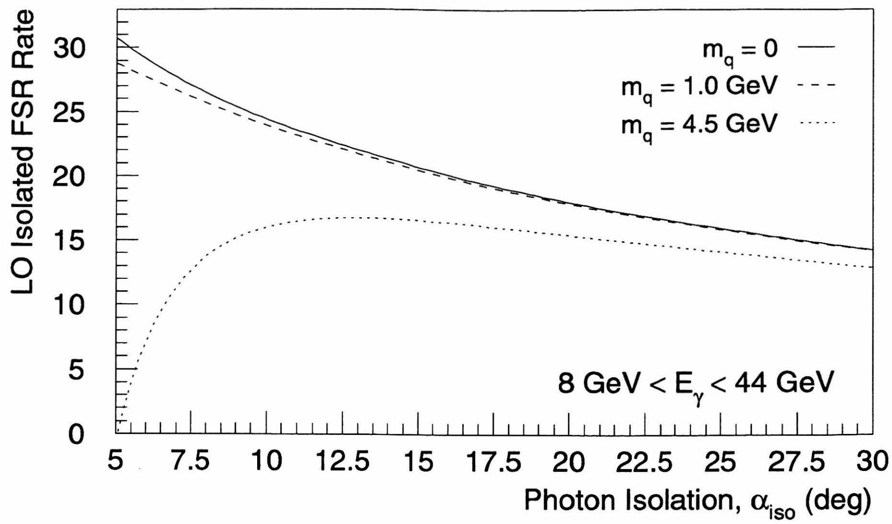

Figure 7.8: Rates of isolated FSR calculated at lowest-order and shown as a function of the isolation, $\alpha_{\rm iso}$, including mass effects for three different quark masses: zero (solid curve), 1 GeV (dashed curve), and 4.5 GeV (dotted curve). The results were obtained by dividing out the overall factor, $Q_{\rm q}^2\alpha/(2\pi)$.

$\mathbb{R}_{{\rm q},i}$ as the product of the result I obtain with a massless calculation, $\mathbb{R}_{{\rm q},i}^{\rm (LO)}$, and a mass correction factor which scales explicitly with quark mass

$$\mathbb{R}_{{\rm q},i}^{\rm (LO)}(m_{\rm q}) \equiv \mathbb{R}_{{\rm q},i}^{\rm (LO)} \times \left[1 - m_{\rm q}^2 M_i\right] .$$

(I use the notational convention that when a quark-mass dependence is not explicitly shown for a quantity, then the quantity is calculated assuming zero mass.) In Figure 7.9, I show the dependence of M_i on the photon energy interval, labeled by the index i, and the isolation cut, $\alpha_{\rm iso}$.

When I add together the contributions to the isolated FSR energy distribution from the five accessible quark flavors, I assume that the light quarks (u, d, and s) have zero mass, and thus obtain

$$\mathbb{R}_i^{\rm (LO)} = \frac{(2 - m_{\rm c}^2 M_i)\overline{c}_{\rm u}{Q_{\rm u}}^2 + (2 + (1-\Delta\rho_{\rm b})(1 - m_{\rm b}^2 M_i))\overline{c}_{\rm d}{Q_{\rm d}}^2}{2\overline{c}_{\rm u} + (3 - \Delta\rho_{\rm b})\overline{c}_{\rm d}} \mathbb{R}_{{\rm q},i}^{\rm (LO)} .$$

Since the mass correction, M_i, that I calculate is a function of energy, this expression no longer has the simple form of an electroweak factor multiplied by the energy distribution of FSR from a single quark flavor. However, the overall effect of quark-mass corrections is small in the range of isolations, $\alpha_{\text{iso}} \gtrsim 20°$, where I can calculate them reliably. Therefore, I introduce an average mass correction, $\langle M \rangle$, that does not depend on energy

$$\langle M \rangle \equiv \sum_i \frac{\mathbb{R}^{(\text{LO})}_{\text{q},i} \cdot M_i}{\mathbb{R}^{(\text{LO})}_{\text{q},i}} .$$

The values of this average correction that I calculate are

$$\langle M \rangle = \begin{cases} 2.05\ \%/\text{GeV}^2 & \alpha_{\text{iso}} = 10° \\ 1.07\ \%/\text{GeV}^2 & \alpha_{\text{iso}} = 15° \\ 0.68\ \%/\text{GeV}^2 & \alpha_{\text{iso}} = 20° \\ 0.49\ \%/\text{GeV}^2 & \alpha_{\text{iso}} = 25° \end{cases} .$$

Replacing the energy-dependent correction, M_i, in the expression for $\mathbb{R}^{(\text{LO})}_i$, above, with the average correction, $\langle M \rangle$, and neglecting terms proportional to $\Delta\rho_{\text{b}} \cdot \langle M \rangle$, I obtain

$$\mathbb{R}^{(\text{LO})}_i = \frac{(2 - m_{\text{c}}^2 \langle M \rangle)\overline{c}_{\text{u}} {Q_{\text{u}}}^2 + (3 - \Delta\rho_{\text{b}} - m_{\text{b}}^2 \langle M \rangle)\overline{c}_{\text{d}} {Q_{\text{d}}}^2}{2\overline{c}_{\text{u}} + (3 - \Delta\rho_{\text{b}})\overline{c}_{\text{d}}} \mathbb{R}^{(\text{LO})}_{\text{q},i} .$$

7.2.1.4 Higher-Order Corrections

At higher orders in perturbation theory, the lowest-order diagrams of Figure 7.3 are modified with additional particles, which can either appear in the final state or form internal loops. Because of the large value of the strong coupling α_S, the most important corrections are associated with diagrams having additional gluons. Corrections from diagrams with additional photons or other particles are much smaller, and I do not consider them here. The complexity of a QCD calculation increases very rapidly with increasing order, and so in practice, only a few orders can be calculated. Here, I extend my lowest-order, $\mathcal{O}(\alpha)$, calculation by one order in the strong coupling, to

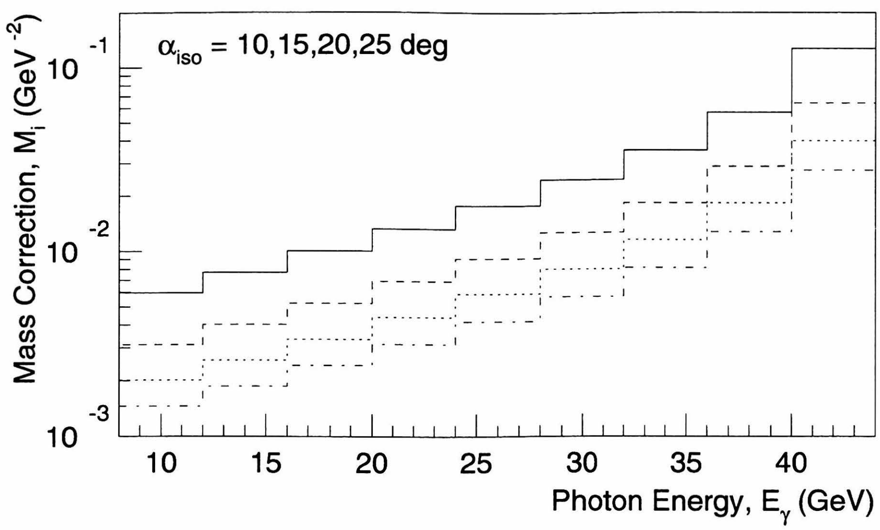

Figure 7.9: Dependence of the binned quark-mass corrections, M_i, on the photon energy interval, labeled by the index i, and the photon isolation. The results are calculated at lowest order for the isolations, from top to bottom, $\alpha_{\rm iso} = 10°$, $15°$, $20°$, and $25°$.

obtain a next-to-lowest-order, $\mathcal{O}(\alpha_S\alpha)$, prediction for the isolated FSR energy distribution.

Below, I use the notation $d\sigma^{(\rm NLO)}/dx_\gamma$ for the $\mathcal{O}(\alpha_S\alpha)$ contribution to the isolated FSR energy distribution, and I refer to it as both the next-to-lowest-order contribution and the leading-order QCD correction. By combining this contribution with the lowest-order contribution that I calculated in the previous sections, I obtain a more accurate approximation to $f_{\rm q}$, of the form

$$f_{\rm q}(\sqrt{s}, \alpha_{\rm iso}, E_\gamma) = \frac{2}{\sqrt{s}}\frac{1}{\sigma_{\rm q\bar{q}}}\left\{\frac{d\sigma^{(\rm LO)}}{dx_\gamma} + \frac{d\sigma^{(\rm NLO)}}{dx_\gamma} + \mathcal{O}(\alpha_S^2\alpha)\right\} \otimes \left\{\text{non-perturbative effects}\right\},$$

and a corresponding approximation to the binned quantities, $\mathbb{R}_{{\rm q},i}$, of the form

$$\mathbb{R}_{{\rm q},i} = \left\{\mathbb{R}_{{\rm q},i}^{(\rm LO)} + \mathbb{R}_{{\rm q},i}^{(\rm NLO)} + \mathcal{O}(\alpha_S^2\alpha)\right\} \otimes \left\{\text{non-perturbative effects}\right\}.$$

The leading-order QCD corrections to isolated FSR production correspond to diagrams with one additional gluon, which can either appear in the final state (see Figure 7.10) or else form a loop between quark lines (see Figure 7.11). I refer to the $\mathcal{O}(\alpha_S\alpha)$ matrix elements for producing the final states $q\overline{q}g\gamma$ and $q\overline{q}\gamma$ as $\mathcal{M}_4$ and $\mathcal{M}_3$, respectively. The NLO contribution to isolated FSR production is given by

$$d\sigma^{(\mathrm{NLO})} = \mathcal{M}_3\Theta_3 \cdot d\Phi_3 + \mathcal{M}_4\Theta_4 \cdot d\Phi_4 \ ,$$

where $d\Phi_n$ represents $n-$body phase space and Θ_n implements photon energy and isolation cuts for an $n-$body final state.

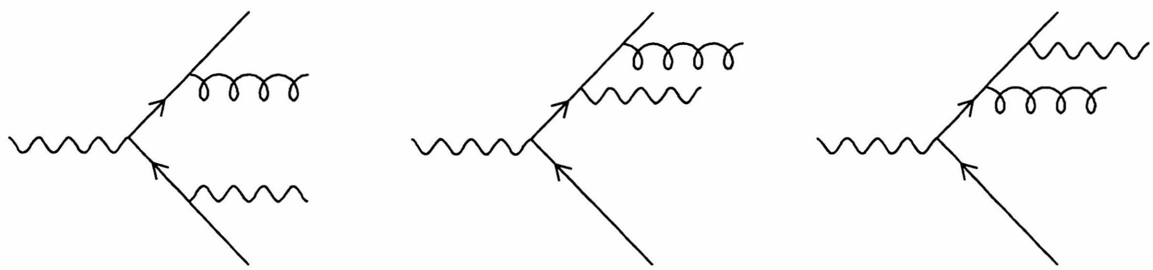

Figure 7.10: Leading-order QCD diagrams for the process $Z \to q\overline{q}g\gamma$, which contribute to the matrix element $\mathcal{M}_4$. The complete set of diagrams also includes the permutation $q \leftrightarrow \overline{q}$.

Since the perturbative descriptions of gluon and photon radiation from quarks differ only by coupling constants, the matrix elements $\mathcal{M}_3$ and $\mathcal{M}_4$ can be deduced from the corresponding $\mathcal{O}(\alpha_S^2)$ matrix elements for the process $e^+e^- \to q\overline{q}g(g)$, which have already been calculated[89–91]. I obtain $\mathcal{M}_3$ and $\mathcal{M}_4$ from the results given for massless quarks in Reference [91] by setting the color factor N_C to zero, in order to eliminate contributions from the triple-gluon vertex, and by performing the substitution

$$\left(C_F\frac{\alpha_S}{2\pi}\right)^2 \to N_s \cdot Q_q^2\frac{\alpha}{2\pi} \cdot C_F\frac{\alpha_S}{2\pi} \ ,$$

which converts one (qqg) vertex into a (qqγ) vertex, and cancels the symmetrization factor $1/N_s$ for identical bosons in the $\mathcal{O}(\alpha_S^2)$ calculation[82] ($N_s = 1$ and 2 for the

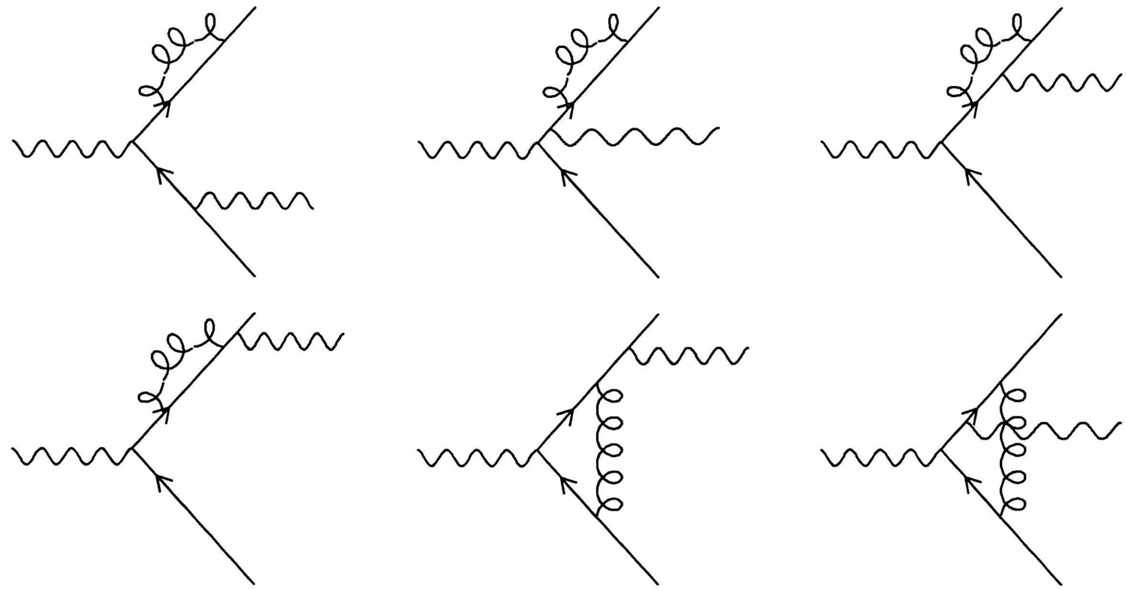

Figure 7.11: Leading-order QCD diagrams for the process $Z \to q\bar{q}\gamma$, which contribute to the matrix element $\mathcal{M}_3$. The complete set of diagrams also includes the permutation $q \leftrightarrow \bar{q}$.

$q\bar{q}\gamma$ and $q\bar{q}g\gamma$ final states, respectively).

After averaging over angular correlations between the initial and final states, the massless four-body phase space is described by five parameters which are conventionally chosen from the set of six scaled invariant masses

$$y_{ij} \equiv \frac{(p_i + p_j)^2}{s} ,$$

with $i > j$. The scaled energies $x_i = 2E_i/\sqrt{s}$ and the angular variables $t_{ij} = (1 - \cos\theta_{ij})/2$ are related to the scaled invariant masses by

$$x_i \equiv 1 - y_{jkl} \quad , \quad t_{ij} = \frac{y_{ij}}{x_i x_j} ,$$

where I use the notation $y_{ijk} \equiv y_{ij} + y_{ik} + y_{jk}$. The phase-space limits are determined by the constraints $0 \le y_{ij} \le 1$ and the conservation equation

$$\sum_{i>j} y_{ij} = 1 .$$

The $\mathcal{O}(\alpha_s\alpha)$ contributions from the $\mathrm{q\bar{q}}\gamma$ and $\mathrm{q\bar{q}g}\gamma$ final states are individually divergent, but combine to give a finite result. In order to obtain numerical results, it is convenient to first isolate the singularities from each contribution and then cancel them analytically. Divergences in the $\mathcal{O}(\alpha_s\alpha)$ $\mathrm{q\bar{q}g}\gamma$ matrix element, $\mathcal{M}_4$, are due to configurations in which the gluon is either very soft, or else, is almost collinear with the quark or anti-quark. In both of these configurations, the gluon is essentially unresolved, and so a general strategy for canceling singularities is to define *physical* cross sections (which I denote with a tilde) in terms of resolved-particle final states, which are then individually finite.

The choice of finite physical cross sections is not unique and introduces a *renormalization scheme* uncertainty into the results of a calculation. I use the method of Reference [91], where the matrix element for the $\mathrm{q\bar{q}g}\gamma$ final state is expressed as a sum of single-pole terms that are related to each other by permutations of the particle labels

$$\mathcal{M}_4 = \frac{1}{y_{\mathrm{qg}}} \cdot P + \frac{1}{y_{\mathrm{\bar{q}g}}} \cdot P(\mathrm{q} \leftrightarrow \mathrm{\bar{q}}) + \frac{1}{y_{\mathrm{q}\gamma}} \cdot P(\mathrm{g} \leftrightarrow \gamma) + \frac{1}{y_{\mathrm{\bar{q}}\gamma}} \cdot P(\mathrm{q} \leftrightarrow \mathrm{\bar{q}}, \mathrm{g} \leftrightarrow \gamma) ,$$

and where P remains finite when a single $y_{ij} \to 0$. In order to extract the singular contribution from $\mathrm{q\bar{q}g}\gamma$ final states, unresolved gluons are defined with explicit phase-space cuts of $y_{\mathrm{qg}} < y_0$ and $y_{\mathrm{\bar{q}g}} < y_0$ for the first and second terms given above. The corresponding poles in $y_{\mathrm{q}\gamma}$ and $y_{\mathrm{\bar{q}}\gamma}$ are regulated by the photon energy and isolation requirements, and so do not need to be explicitly cut. For small values of y_{qg}, the leading singular behavior of $\mathcal{M}_4$ is due to the $1/y_{\mathrm{qg}}$ pole-term and is given by

$$\frac{1}{y_{\mathrm{qg}}} \left[\frac{2y_{\mathrm{q\bar{q}g}}}{y_{\mathrm{qg}}v + y_{\mathrm{q\bar{q}g}}(1-v)} - v - 1 \right] \cdot d\sigma^{(\mathrm{LO})}(x_1, x_2) ,$$

where

$$v = \frac{y_{\mathrm{q\bar{q}}}}{1 - y_{\mathrm{q\bar{q}g}} - y_{\mathrm{qg}}} .$$

The factor $d\sigma^{(\mathrm{LO})}(x_1, x_2)$ appearing above is the lowest-order cross section evaluated with the effective three-body variables, x_1 and x_2, that I obtain by considering the quark and gluon together as a single particle. The mapping of degenerate four-particle configurations with an unresolved gluon into three-particle phase-space is only well-defined up to terms proportional to $y_{\mathrm{qg}} < y_0$. However, by choosing y_0 to be sufficiently small, this uncertainty is numerically insignificant. I choose a mapping that does not alter the photon energy

$$x_1 \equiv 1 - y_{\bar{\mathrm{q}}\gamma} + y_{\mathrm{qg}} \quad , \quad x_2 \equiv 1 - y_{\mathrm{qg}\gamma} \quad , \quad x_\gamma \equiv 1 - x_1 - x_2 = 1 - y_{\mathrm{q}\bar{\mathrm{q}}\mathrm{g}} \; .$$

In the limit $y_{\mathrm{qg}} \to 0$, the four-particle phase space factor reduces into a product of the unresolved gluon phase space and a three-particle phase space factor

$$d\Phi_4 = d\Phi_3 \cdot dv\, d\phi\, dy_{\mathrm{qg}} \; ,$$

so that the singular contribution from $\mathcal{M}_4$ can be evaluated analytically by integrating over the unresolved gluon degrees of freedom. Performing this integration yields an expression in terms of three-body variables

$$\mathcal{M}_{4\to 3} = 2 \int dy_{\mathrm{qg}} \int dv \int d\phi\; P \cdot \Theta(y_{\mathrm{qg}} < y_0) \; ,$$

where the extra factor of two accounts for the permutation $\mathrm{q} \leftrightarrow \bar{\mathrm{q}}$. The pole terms of this singular contribution exactly cancel the pole terms of the virtual corrections at each point in the $\mathrm{q}\bar{\mathrm{q}}\gamma$ phase space, so that the physical cross sections are given by

$$d\tilde{\sigma}_3(y_0) = \{\mathcal{M}_3 + \mathcal{M}_{4\to 3}\}\, \Theta_3 \cdot d\Phi_3$$

and

$$\begin{aligned} d\tilde{\sigma}_4(y_0) = \Bigg\{ & \frac{1}{y_{\mathrm{qg}}} P \cdot \Theta(y_{\mathrm{qg}} > y_0) + \frac{1}{y_{\mathrm{qg}}} P(\mathrm{q} \leftrightarrow \bar{\mathrm{q}}) \cdot \Theta(y_{\mathrm{qg}} > y_0) + \\ & \frac{1}{y_{\mathrm{q}\gamma}} P(\mathrm{g} \leftrightarrow \gamma) + \frac{1}{y_{\bar{\mathrm{q}}\gamma}} P(\mathrm{q} \leftrightarrow \bar{\mathrm{q}}, \mathrm{g} \leftrightarrow \gamma) \Bigg\} \; . \end{aligned}$$

For small values of y_0, the physical cross sections asymptotically approach

$$d\tilde{\sigma}_4(y_0) \to \log^2 y_0 + \frac{3}{2} \log y_0 \quad \text{and,} \quad d\tilde{\sigma}_3(y_0) \to -d\tilde{\sigma}_4(y_0) \; ,$$

and so are individually very sensitive to the value of the cutoff parameter y_0. However, their sum is independent of the cutoff value.

The functions Θ_3 and Θ_4, introduced above, implement cuts on photon isolation and energy, and so should be defined to match the corresponding experimental cuts as closely as possible. In the previous section, I defined the cuts for the $\mathrm{q\bar{q}}\gamma$ final state as

$$\Theta_3 \equiv \Theta(x_\gamma > x_0) \cdot \Theta(t_\mathrm{q} > t_0) \cdot \Theta(t_{\bar{\mathrm{q}}} > t_0) \ ,$$

and so an obvious extension to the $\mathrm{q\bar{q}g}\gamma$ final state is

$$\Theta_4 = \Theta_3 \cdot \Theta(t_\mathrm{g} > t_0) \ .$$

This choice is in fact not possible since it restricts the gluon phase space sufficiently to modify the leading behavior of $d\tilde{\sigma}_4(y_0)$ and thus introduces a y_0-dependence into the sum $d\tilde{\sigma}_3(y_0) + d\tilde{\sigma}_4(y_0)$.

In order to obtain a QCD correction that is independent of the cutoff parameter, Θ_4 must allow gluons up to some energy, E', within the isolation cone of the photon,

$$\Theta_4 = \Theta_3 \cdot (1 - \Theta(t_\mathrm{g} > t_0) \cdot \Theta(x_\mathrm{g} < x')) \ ,$$

where $x' = 2E'/\sqrt{s}$. This approach treats quarks and gluons differently and thus does not match the experimental isolation requirement. Therefore, I also allow soft quarks within the isolation cone by using

$$\begin{aligned}\Theta_4 =& \Theta(x_\gamma > x_0) \cdot (1 - \Theta(t_\mathrm{q} > t_0) \cdot \Theta(x_\mathrm{q} < x')) \cdot \\ & (1 - \Theta(t_{\bar{\mathrm{q}}} > t_0) \cdot \Theta(x_{\bar{\mathrm{q}}} < x')) \cdot (1 - \Theta(t_\mathrm{g} > t_0) \cdot \Theta(x_\mathrm{g} < x')) \ .\end{aligned}$$

The additional contributions to $d\tilde{\sigma}_4$ that are due to soft quarks within the photon isolation cone diverge as $x_\gamma \to 1$, so I require a cut on the maximum photon energy in order to use this isolation scheme. I already apply such a cut in my experimental selection. Note that the final isolation scheme that I choose still does not exactly match my experimental scheme, since I analytically remove regions of four-body phase space where $y_{\rm qg} \leq y_0$. Therefore, I treat any soft gluons or quarks in an isolation cone differently in my calculation depending on their invariant masses with other partons in the event.

Since an analytic calculation of the $\mathcal{O}(\alpha_S\alpha)$ corrections is not technically feasible with my choice of isolation scheme, I evaluate the corrections using the VEGAS[92] Monte Carlo integration algorithm. I calculate the value of each $\mathbb{R}^{(\rm NLO)}_{{\rm q},i}$ as the sum of the contributions from the three- and four-body physical cross sections. Since these contributions are separately divergent as the cutoff parameter, y_0, approaches zero, decreasing the value of this cutoff involves a cancelation between larger values, and thus results in a larger numerical uncertainty in the result. Increasing the cutoff, however, increases the theoretical error in the result due to missing sub-leading contributions in my calculation, which are proportional to the cutoff. The final choice of value for y_0 is a compromise between these two sources of error.

Figure 7.12 shows the corrections that I calculate, in different energy intervals and for different isolations, as a function of the cutoff parameter. I choose the value $y_0 = 10^{-6}$ as a suitable compromise between the effects that I described above, and I use this value to calculate the results that I present below. I use a value of $E' = 100$ MeV for the maximum energy of a soft particle allowed within an isolation cone. Although this value matches the value of the cut, $\widetilde{E}_{\rm iso}$, that I use in my analysis, the effects of these cuts are different since they are applied to different final states (quarks and gluons, or hadrons). This difference is due to non-perturbative processes, which I will consider further in section 7.3.

Figure 7.13 shows the final binned $\mathcal{O}(\alpha_S\alpha)$ corrections to the isolated FSR energy distribution that I calculate. The corrections are generally negative, since gluon radiation reduces the energy of a quark that might later radiate a photon and increases the number of particles in the final state: both of these effects reduce the probability that a photon is energetic and isolated. The corrections are largest for less energetic photons.

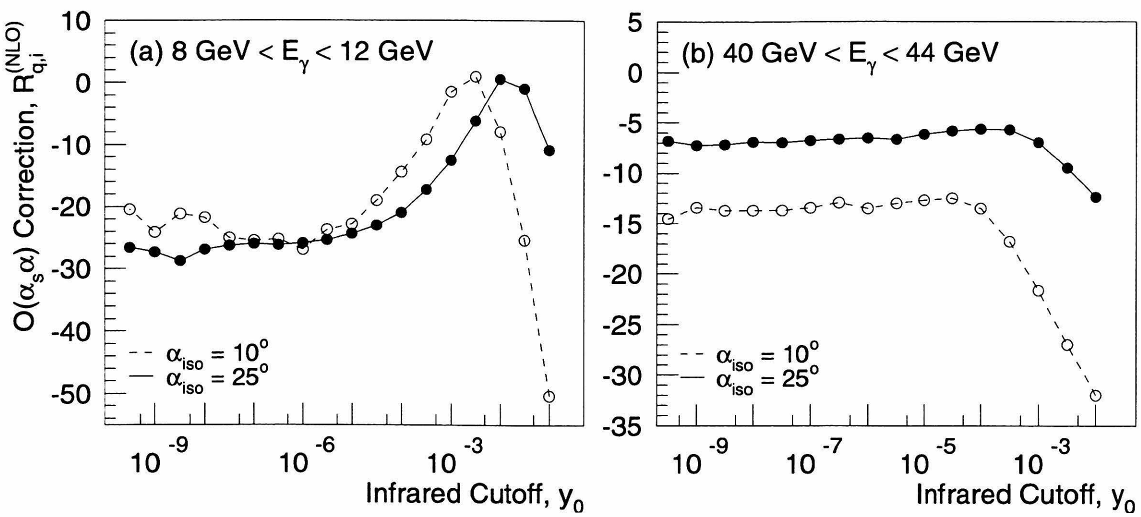

Figure 7.12: Dependence of the $\mathcal{O}(\alpha_S\alpha)$ QCD corrections to the isolated FSR energy distribution for a single quark flavor on the infrared cutoff parameter, y_0. The results were obtained by dividing out the overall factor, $C_F\alpha_S/(2\pi)\cdot\alpha/(2\pi)$, and by using a soft-parton cutoff, E', of 100 MeV.

The QCD corrections that I show in Figure 7.13 are calculated by dividing out the overall factor, $C_F\alpha_S/(2\pi)\cdot\alpha/(2\pi)$. However, for a realistic calculation that can be compared with data, the values of the couplings, α_S and α, must be specified. Since these couplings are free parameters in the Standard Model, they must be determined by comparing experimental results with theoretical predictions. In the case of the quark-photon coupling, α, this comparison is straightforward and provides an unambiguous and precise result, $\alpha \simeq 1/137.036$[73]. However, in the case of the quark-gluon coupling, α_S, the necessary QCD calculations are difficult to perform and require significant approximations. As a result, the values of α_S that are obtained using these approximate calculations are *effective* values: they differ from the *true* value — the value that would be obtained from a comparison with an ideal complete calculation — in a way that approximately compensates for the theoretical approximations that were used. Therefore, in order to best describe my experimental results, my $\mathcal{O}(\alpha_S\alpha)$ calculation requires an effective value for α_S, which will, in general, differ

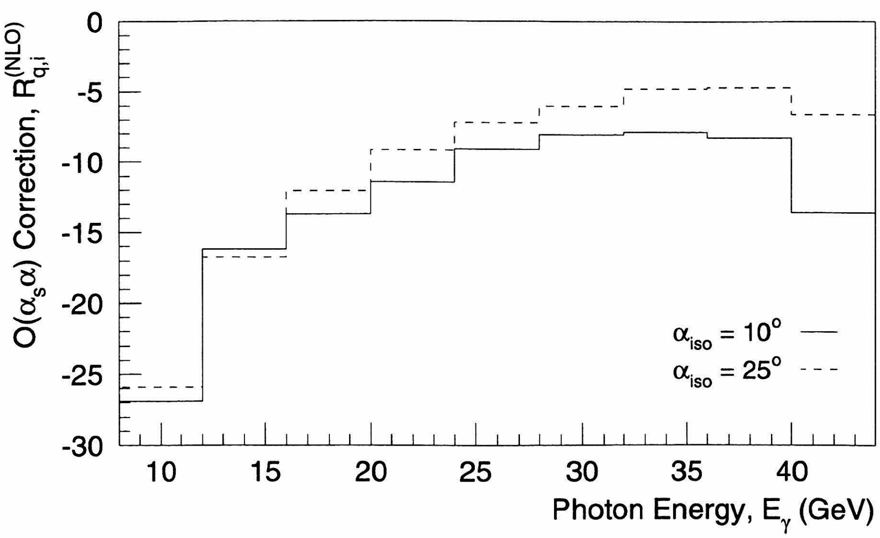

Figure 7.13: QCD corrections to the binned isolated FSR energy distribution calculated at $\mathcal{O}(\alpha_S\alpha)$. The two histograms are calculated for $\alpha_{\text{iso}} = 10°$ (solid) and 25° (dashed). The results were obtained by dividing out the overall factor, $C_F\alpha_S/(2\pi) \cdot \alpha/(2\pi)$ (see Figures 7.19 and 7.20 for results that include all couplings), and by using a soft-parton cutoff, E', of 100 MeV.

from the true value. However, since I have no *a priori* knowledge of how this best effective value for my calculation differs from the true value, I take instead the best estimate of the true value of α_S that is available. For this best estimate, I take the value $\alpha_S = 0.124 \pm 0.009$[93], which was obtained by comparing global event shape distributions, measured by L3 in hadronic Z decays, with the predictions of a calculation that combines $\mathcal{O}(\alpha_S^2)$ matrix elements with some leading-logarithm corrections. Note that the error of ± 0.009 that is quoted on this value is an estimate of how much this value might differ from the true value of α_S. However, the difference between this result and the best effective value for my calculation could be larger than this error.

7.2.2 Leading-Logarithm Calculations

In this section, I describe the leading-logarithm approach to calculating the energy distribution of isolated FSR. The advantage of this approach is that it includes the main effects of gluon radiation to all orders in the strong coupling, and thus provides a good description of QCD corrections. I will show that the disadvantage of this approach is that it does not necessarily give a good description of isolated and energetic photon radiation from a quark.

The logarithms, $L = \log y$, that appear in the perturbative expansion of f_{q} (see Figure 7.2) represent the leading singular behavior, $1/y$, of the cross section caused by soft and collinear radiation ($y \rightarrow 0$). Because quarks couple more strongly to gluons than to photons, this radiation consists mostly of gluons; however, the final states that I am interested in calculating must also contain at least one radiated photon. Each radiated gluon or photon that is either soft or collinear contributes one factor of L, and radiation that is both soft and collinear contributes a factor of L^2. I define the variable y as the combined scaled invariant mass of the radiated particle (gluon or photon) and the radiating particle (quark or gluon), although other definitions are also possible.

The leading-logarithmic contributions to FSR production are proportional to $\alpha_s^k \cdot L^{2k}$, and thus correspond to diagrams without internal loops and in which every radiated gluon or photon is both soft and collinear. Therefore, in the leading-logarithm approximation (LLA), the quark and anti-quark of a primary $\mathrm{q\bar{q}}$ pair evolve independently through a sequence of soft and collinear branching processes, $a \rightarrow bc$, as shown schematically in Figure 7.14. Since the LLA describes the radiation at each branch using an approximation that incorporates the leading singular behavior of the cross section, it is not necessarily a good approximation for radiation that is either hard or isolated. In particular, I do not expect the LLA to provide a good description of the isolated and energetic photon radiation that I study experimentally. For this reason, I consider the matrix-element approach to calculating FSR production, which

I described in the previous section, to be more reliable than the leading-logarithm approach, which I describe here.

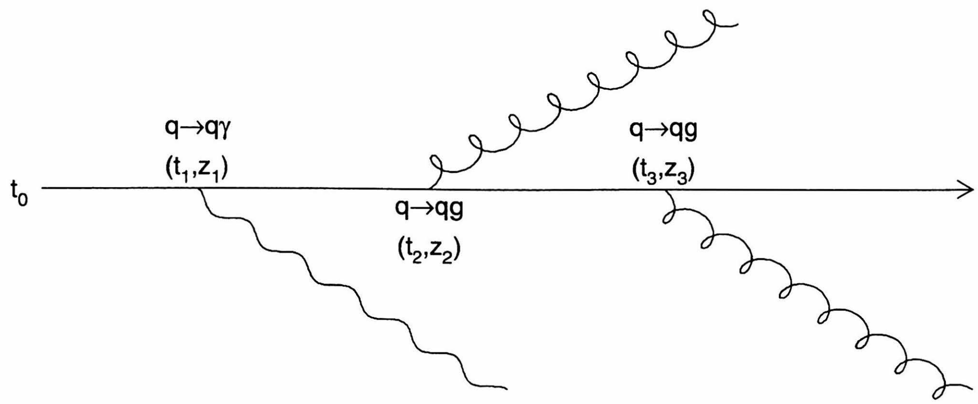

Figure 7.14: A schematic diagram of the leading-logarithm-approximation evolution of the primary quark (or anti-quark) produced from a Z decay.

The kinematics at each branch of the LLA evolution, shown in Figure 7.14, are parameterized using two variables, t_i and z_i. In the limit of soft and collinear kinematics, the variable $t = \log(Q^2/Q_0^2)$ can be identified with the *virtuality* of the primary quark (or anti-quark): its initial value is set by the hard scattering scale, $Q^2 \simeq m_Z^2$, and then its value decreases at each subsequent branch

$$t_0 > t_1 > t_2 > t_3 > \ldots ,$$

as the primary quark becomes less virtual, $Q^2 \to 0$. In the same soft and collinear limit, the variable z corresponds to the energy sharing between the decay products of each branch, and takes on values near zero when the radiated particle is soft. The exact definitions of the branching variables, t and z, are somewhat arbitrary: different choices agree in the soft and collinear limit, but yield numerically different results.

The LLA cross section for FSR production is given by the sum of the quark and anti-quark contributions

$$d\sigma^{(\mathrm{LLA})} = d\sigma_{\mathrm{q}}^{(\mathrm{LLA})} + d\sigma_{\overline{\mathrm{q}}}^{(\mathrm{LLA})} ,$$

whose separate contributions are in turn obtained by multiplying together contributions from each branch

$$\frac{1}{\sigma} d\sigma_{\mathrm{q}}^{(\mathrm{LLA})} = \prod_i \frac{dt_i}{t_i} P_{a\to bc}(z_i) dz_i .$$

The functions $P_{a\to bc}(z)$ are the Altarelli-Parisi splitting kernels[94] and depend on the type of branch that occurs. The $q \to \mathrm{qg}$ and $q \to \mathrm{q}\gamma$ kernels differ only by an overall factor, and are given by

$$P_{\mathrm{q}\to\mathrm{qg}}(z) = \frac{C_F \alpha_S}{2\pi} \frac{1+(1-z)^2}{z} \quad \text{and} \quad P_{\mathrm{q}\to\mathrm{q}\gamma}(z) = \frac{Q_{\mathrm{q}}^2 \alpha}{2\pi} \frac{1+(1-z)^2}{z} .$$

The $\mathrm{g} \to \mathrm{gg}$ kernel is given by

$$P_{\mathrm{g}\to\mathrm{gg}}(z) = \frac{N_C \alpha_S}{2\pi} \frac{(1-z(1-z))^2}{z(1-z)} .$$

The LLA factors associated with each branch are divergent when either t_i or z_i approaches zero. Therefore, it is necessary to apply cutoffs on both the decreasing sequence of virtualities at each branch, $t_i > t_0$, as well as on the minimum value of the energy sharing at each branch, $z > z_0$. The first of these cutoffs can be interpreted as setting the scale, Λ, at which non-perturbative effects must be considered, $t_0 \simeq \log(\Lambda^2/Q_0^2)$. The second cutoff regulates the infrared divergence of the matrix element and so plays a role analogous to that of the parameter y_0, which I described in Section 7.2.1.

7.2.2.1 Parton-Shower Programs

In this section, I describe how an LLA calculation can be performed using a Monte Carlo program. I consider two such programs in particular — JETSET[62, 63], and HERWIG[64, 65] — and I describe their predictions for isolated FSR production.

Since, in the LLA, branchings are independent of one another (except for the requirement of decreasing virtuality), there are no quantum-mechanical interference effects and the dynamics of the process can be described using probabilities. As a result, a LLA calculation can be performed by averaging over an ensemble of *events* that are generated according to appropriate probability distributions. This method is an example of a Monte Carlo event generator, and I refer to programs that use this method as *parton-shower* programs.

The necessary probability distributions for a parton-shower program are given by the Altarelli-Parisi splitting kernels, given above, and the Sudakov form factor[95]

$$S(t_0, t) = \exp\left\{ -\int_{t_0}^{t} \frac{dt'}{t'} \int dz\, P_{a\to bc}(z) \right\} ,$$

which expresses the probability that a parton evolves from an initial virtuality, t_0, to a lower value, t, without branching. A Monte Carlo implementation of the LLA consists of generating events in which the primary quark and anti-quark each evolve separately by a sequence of branches, with the values of t_i and z_i at each branch chosen according to these probability distributions.

There is some freedom in the exact definitions of the branching variables and of the cutoffs in these variables, and, as a result, different parton-shower programs yield different predictions. These differences are formally of next-to-leading order in the LLA and so are only numerically significant when calculating observables for which the LLA is not a good approximation. Below, I show that these differences are large when calculating the energy distribution of isolated FSR. I use the parton-shower programs JETSET and HERWIG for these calculations, although other programs are available that also implement FSR[96, 97]. JETSET and HERWIG both use

$$z \equiv E_c/(E_b + E_c) ,$$

but implement different choices for the virtuality:

$$\text{JETSET:} \quad t \equiv (p_b + p_c)^2 \quad , \quad \text{HERWIG:} \quad t \equiv \frac{p_b \cdot p_c}{z(1-z)} .$$

An important feature of both JETSET and HERWIG, which influences their predictions of isolated FSR production, is that they reweight the first branch of both the primary quark and anti-quark in order to approximately reproduce the appropriate lowest-order matrix element at that branch ($\mathcal{O}(\alpha_S)$ in the case of an initial $q \to \mathrm{qg}$ branch, or $\mathcal{O}(\alpha)$ for an initial $q \to \mathrm{q}\gamma$ branch). As a result, this first branch is not generated according to the LLA, but rather, according to a hybrid matrix-element / leading-logarithm method. Figure 7.15 shows a comparison of the energy distributions of isolated FSR predicted by JETSET and HERWIG with the results of my $\mathcal{O}(\alpha_S\alpha)$ matrix-element calculation, and reveals that while HERWIG is in good agreement with the matrix-element calculation, JETSET and HERWIG are not in agreement with each other. I take this disagreement between the two parton-shower programs as an indication that the description of isolated FSR production in the LLA is sensitive to subleading effects. Because of this sensitivity, the LLA is not appropriate for describing the type of events that I study experimentally. I attribute the good agreement between HERWIG and my matrix-element calculation to a fortuitous choice of branching variables and to the procedure of reweighting the first branch that HERWIG implements.

Although parton-shower programs are not suitable for describing the actual process of photon radiation from a quark, I expect them to provide a reliable description of the QCD corrections to this process. Therefore, it is interesting to compare the corrections, $\mathbb{R}_{\mathrm{q},i}^{(\mathrm{NLO})}$, that I calculated in Section 7.2.1, using the $\mathcal{O}(\alpha_S\alpha)$ matrix element, with a similar correction calculated in the LLA, which I refer to as $\mathbb{R}_{\mathrm{q},i}^{(\mathrm{LLA})}$. In order to make this comparison, I select a sample of events that are generated according to an effective lowest order for the LLA which approximately corresponds to the lowest order of my matrix-element calculation. I define this set to consist of events in which a photon is radiated at one of the first branches, and I measure the energy distributions of isolated FSR in these events using two different methods. First, I ignore all other subsequent branches, so that the final state consists of a $\mathrm{q\overline{q}}$ pair together with

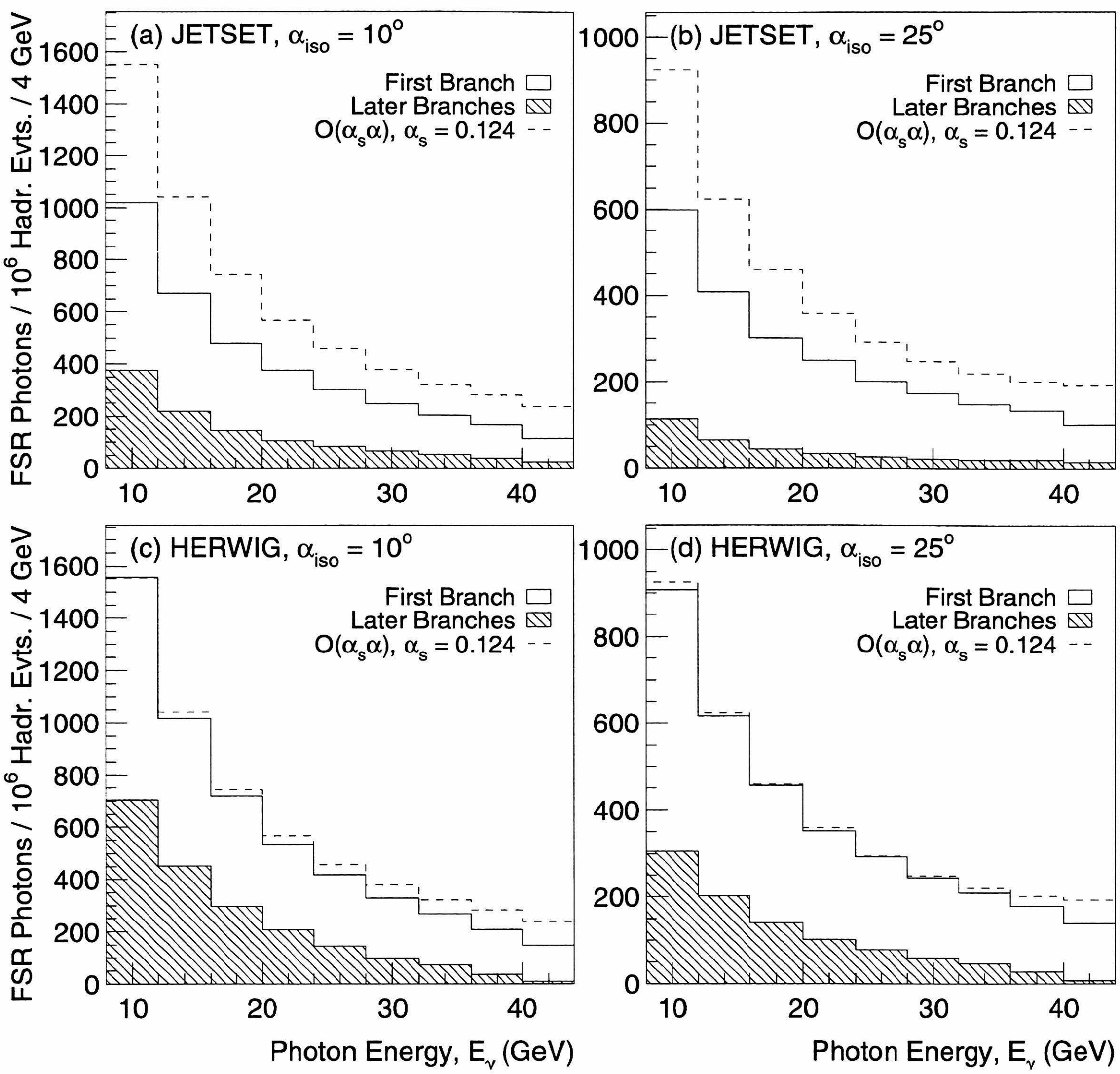

Figure 7.15: Energy distributions of isolated FSR predicted by the parton-shower programs JETSET (a,b) and HERWIG (c,d). Figures (a) and (c) are the predictions with an isolation cut of $\alpha_{\text{iso}} = 10°$, and Figures (b) and (d) are the predictions for $\alpha_{\text{iso}} = 25°$. The unfilled areas of each histogram are the predicted contributions from photons that are radiated at the first branch of the primary quark or anti-quark. The hatched areas are the predicted contributions from all later branches. The solid histogram shows the combined contributions from all branches. The dashed histogram shows the predictions of my $\mathcal{O}(\alpha_S\alpha)$ calculation, which I obtain with $\alpha_S = 0.124$ and using Standard Model quark couplings.

a radiated photon, and measure the photon isolation from the quark and anti-quark only, obtaining a binned energy distribution which I refer to as $\mathbb{R}^{(lo)}_{\mathrm{q},i}$. Then, I include all the particles that are radiated in subsequent branches when I measure photon isolation, and I obtain a second binned energy distribution for these events which I refer to as $\mathbb{R}^{(lo+qcd)}_{\mathrm{q},i}$. Finally, I define the LLA QCD correction, which I will use to compare with the matrix-element QCD correction, as

$$\mathbb{R}^{(\mathrm{LLA})}_{\mathrm{q},i} \equiv \frac{\mathbb{R}^{(lo+qcd)}_{\mathrm{q},i} - \mathbb{R}^{(lo)}_{\mathrm{q},i}}{\mathbb{R}^{(lo)}_{\mathrm{q},i}} \times \mathbb{R}^{(\mathrm{LO})}_{\mathrm{q},i} ,$$

where $\mathbb{R}^{(\mathrm{LO})}_{\mathrm{q},i}$ is the lowest-order matrix-element distribution that I calculated in Section 7.2.1.

Figure 7.16 shows a comparison of the QCD corrections that I obtain using the matrix-element and leading-logarithm methods. I use two different values of α_S in order to calculate the matrix-element QCD correction, $\mathbb{R}^{(\mathrm{NLO})}_{\mathrm{q},i}$. The first of these values is my best estimate of the true value, $\alpha_S \simeq 0.124$. The second value that I use is an optimized effective value, α_S^{eff}, that I determine by minimizing the differences between $\mathbb{R}^{(\mathrm{NLO})}_{\mathrm{q},i}$ and of $\mathbb{R}^{(\mathrm{LLA})}_{\mathrm{q},i}$ for each value of α_{iso}. These values then approximately incorporate the effect of missing higher orders in my calculation. The effective values that I obtain with this method are:

$$\alpha_S^{eff} = \begin{cases} 0.040 & \alpha_{\mathrm{iso}} = 10^\circ \\ 0.068 & \alpha_{\mathrm{iso}} = 15^\circ \\ 0.098 & \alpha_{\mathrm{iso}} = 20^\circ \\ 0.122 & \alpha_{\mathrm{iso}} = 25^\circ \end{cases} .$$

A large difference between the effective and true values indicates that higher-order corrections are important. Thus, I conclude that the effect of the higher-order QCD corrections that I do not calculate is important for $\alpha_{\mathrm{iso}} = 10^\circ$, but can be neglected, to a good approximation, for $\alpha_{\mathrm{iso}} = 25^\circ$. In Figure 7.17, I show the difference between the NLO and LLA corrections that I obtain with $\alpha_{\mathrm{iso}} = 10^\circ$ and 25°, using the effective

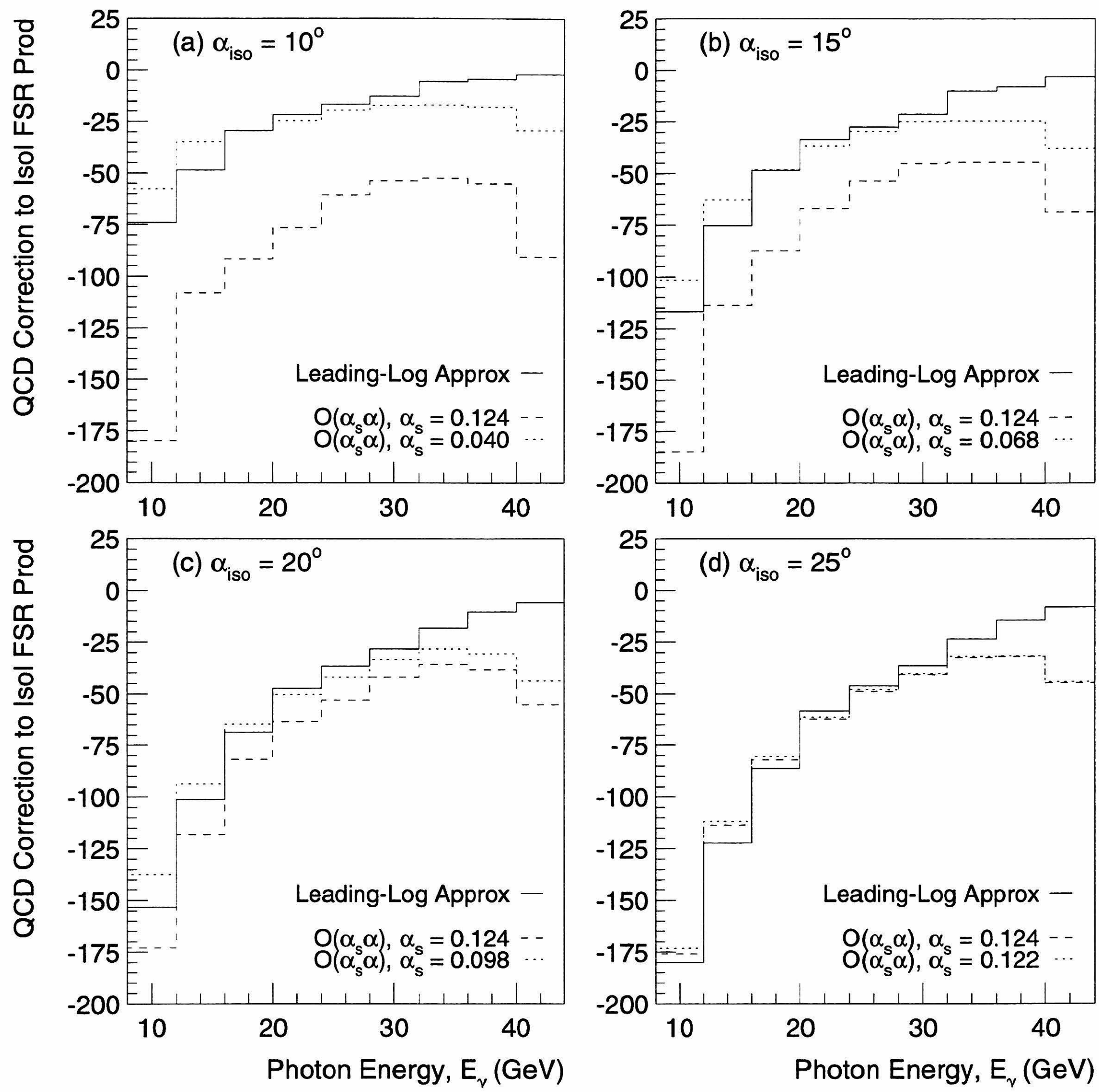

Figure 7.16: Comparison of the QCD corrections to isolated FSR production calculated using a parton-shower program (solid line) and an $\mathcal{O}(\alpha_S\alpha)$ matrix-element calculation (dashed and dotted lines). The dashed lines are calculated using a fixed value of the strong coupling, $\alpha_S = 0.124$. The dotted lines are calculated using a value of α_S that best matches the parton-shower result for each value of the isolation cut, α_{iso}.

α_S for the NLO calculation. These differences reveal that for a given isolation cut, the missing higher-order corrections are most important at high photon energies. I estimate that for photon energies between 8 GeV and 32 GeV and using an isolation cut of $\alpha_{\text{iso}} = 25°$ (10°), the error in my NLO calculation due to missing higher-order corrections is approximately 5% (25%).

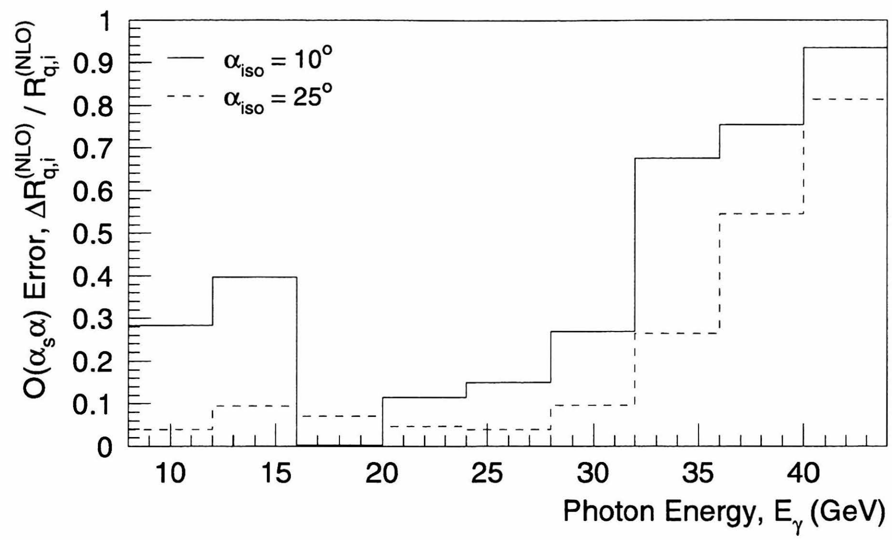

Figure 7.17: Estimated systematic uncertainty in the NLO QCD corrections that I calculate due to missing higher-order contributions. The solid (dashed) line shows the relative error, $\Delta\mathbb{R}^{(\text{NLO})}_{q,i}/\mathbb{R}^{(\text{NLO})}_{q,i}$, that I calculate with $\alpha_{\text{iso}} =$ 10° (25°), where $\Delta\mathbb{R}^{(\text{NLO})}_{q,i} \equiv |(\mathbb{R}^{(\text{NLO})}_{q,i} - \mathbb{R}^{(\text{LLA})}_{q,i}|$ and I calculate $\mathbb{R}^{(\text{NLO})}_{q,i}$ using $\alpha_S = \alpha_S^{eff}$.

7.3 Non-Perturbative Processes

In the previous section, I have described how I calculate the energy distribution of isolated FSR using perturbation theory. In this section, I first outline a theoretical framework for extending this calculation to include non-perturbative effects, and then, I estimate the size of these effects using phenomenological models.

According to the factorization theorem, perturbative and non-perturbative effects can be calculated separately and then combined with a convolution to obtain a physical cross section. For the energy distribution of isolated FSR, this factorization is given by

$$\frac{d\sigma}{dE_\gamma} = \sum_{p=\mathrm{q},\bar{\mathrm{q}},\mathrm{g},\gamma} \int_{m_p}^{\sqrt{s}/2} dE_p \int_0^1 dz\, \delta(E_\gamma - zE_p) \left\{ D_{\gamma/p}(z,\mu_f) \cdot \frac{d\hat{\sigma}_p}{dE_p}(E_p,\mu_f) \right\} ,$$

where $D_{\gamma/p}$ is the *fragmentation function* that describes the non-perturbative production of an isolated photon from a parton, p, with a fraction z of p's energy, and $d\hat{\sigma}/dE_\gamma$ is the perturbatively-calculated cross section for producing an isolated parton p with an energy of E_p. The separation between the perturbative and non-perturbative contributions in this framework is parameterized by a *factorization scale*, μ_f. Since this separation is not precisely defined, the choice of the factorization scale is arbitrary and this arbitrariness introduces an uncertainty into an approximate calculation. However, in an ideal complete calculation that made no approximations, the scale-dependencies of the individual contributions would cancel, and the resulting physical cross section would be independent of μ_f.

In the factorization, above, the photon isolation requirement is implemented separately in the calculations of the perturbative and non-perturbative contributions. Therefore, using this factorization implies that when a parton, p, (which is either a photon itself or else fragments into one) is isolated with respect to the other partons in the event, then the only hadrons which might destroy this isolation are those that are produced from p itself. This condition is not strictly satisfied, however, since hadrons that are produced by the fragmentation of other partons can also appear in the isolation cone of p, but I expect that this is a small effect for the range of isolation cone sizes that I study experimentally.

The energy distribution that I calculated with perturbation theory in Section 7.2 can be recovered from the factorized expression that I give above by defining the fragmentation functions to be

$$D_{\gamma/\gamma}(z) = \delta(1-z) \quad \text{and, for } p \neq \gamma, \quad D_{\gamma/p}(z) = 0 \ .$$

Therefore, non-perturbative effects (within the theoretical framework that I describe here) are due to the differences between these trivial fragmentation functions and the actual fragmentation functions. The actual fragmentation functions cannot be calculated with presently available techniques, and so require experimental input in order to be determined. Since this experimental input is not currently available, the theoretical framework that I have outlined here does not yield quantitative predictions of the non-perturbative contributions to my calculation. Therefore, I now turn to phenomenological fragmentation models.

7.3.1 Fragmentation Models

Although the present theoretical understanding of non-perturbative phenomena does not yield quantitative predictions, several phenomenological models of the fragmentation process have been developed that do. These models do not provide much insight into the theoretical aspects of hadronization but they are able to reproduce experimental results with relatively few parameters[98].

In order to estimate the non-perturbative contributions to my matrix-element calculation, I use the LUND string-fragmentation model[62, 63] and the HERWIG cluster-fragmentation model[64, 65]. I express the effect of non-perturbative contributions as a correction factor, H_i, that I apply to my perturbative calculation

$$\mathbb{R}_{q,i} = \left[\mathbb{R}_{q,i}^{(\mathrm{LO})} + \mathbb{R}_{q,i}^{(\mathrm{NLO})} + \mathcal{O}(\alpha_s^2\alpha)\right] \times H_i \ .$$

L3 has compared the distributions of global event shape variables, measured in hadronic Z decays, with the predictions of several different combinations of a perturbative calculation with a fragmentation model[98]. For each of these combinations, we determined optimized values of the model parameters. In Table 7.1, I summarize the optimized fragmentation-model parameters that we obtained for the combination of the JETSET $\mathcal{O}(\alpha_s^2)$ matrix-element model with the string-fragmentation model (I refer to this as the LUND+ME combination), and for the combination of the HERWIG parton-shower model with the cluster-fragmentation model (I refer to this as the CLUS+PS combination). Two string-fragmentation model parameters, which I refer to as σ_q and b, were used to tune the predictions of the LUND+ME combination in order to best describe experimental results. The first parameter, σ_q, is the width of the Gaussian transverse-momentum distribution for primary hadrons. The parameters, a and b, describe the distribution of longitudinal momenta for primary hadrons according to the Lund symmetric fragmentation function

$$f(z) \propto \frac{(1-z)^a}{z} \exp\left[-\frac{b(p_T^2+m^2)}{z}\right] .$$

(The value of a was held fixed at 0.5 during the tuning process.) The CLUS+PS combination was tuned using only one fragmentation-model parameter, which I refer to as M_{max}. This parameter determines the maximum allowed mass of a cluster that is made from two quarks whose combined mass is M_{12}, according to the constraint

$$M_{clus}^2 < M_{max}^2 + M_{12}^2 .$$

Model Combination	Model Parameter	Default Value	Tuned Value
LUND+ME	σ_q	0.35 GeV	0.50 GeV
	b	0.90 GeV^{-2}	0.42 GeV^{-2}
CLUS+PS	M_{max}	3.35	3.00

Table 7.1: Optimized values of parameters for the string- and cluster-fragmentation models, which were determined by tuning different combinations of a perturbative model (ME or PS) and a non-perturbative model (LUND or CLUS) in order to best describe the distributions of global hadronic event shapes.

The LUND+ME and CLUS+PS combinations involve significantly different perturbative final states. With the LUND+ME combination, the string-fragmentation model is applied to a final state containing at most four particles. With the CLUS+PS combination, the cluster-fragmentation model is applied to a final state that consists of 10–20 particles. For this reason, I expect that the string-fragmentation model, with the LUND+ME tuned parameters, is the the most appropriate for calculating the non-perturbative corrections to my calculation, which — like the JETSET ME model — involves final states of at most four particles. I also calculate these corrections using the cluster-fragmentation model, with the CLUS+PS tuned parameters. I take the difference between the corrections that I obtain with these two models as an estimate of sensitivity of my corrections to the details of a particular model.

My method for calculating the hadronization corrections, H_i, is to randomly generate FSR events according to the $\mathcal{O}(\alpha)$ matrix element, and then apply one of the fragmentation models that I have described. First, I generate events in which the photon has an energy between 8 GeV and 44 GeV and is isolated from the quark and anti-quark by at least 5°. (I use a minimum isolation of 5°, rather than my usual 10°, in order to account for events that are more isolated after hadronization than before.) Next, I apply a fragmentation model that converts the quark and anti-quark into hadrons. Finally, I calculate the energy distributions of those photons which are isolated with respect to the hadrons in the event, obtaining binned rates which I refer to as $\mathbb{R}_{\mathrm{q},i}^{(\mathrm{HAD})}$. I define the binned hadronization correction as the ratio between the hadron-level energy distribution that I obtain and the lowest-order energy distribution that I calculate with the same matrix element as I used to generate my events

$$H_i \equiv \mathbb{R}_{\mathrm{q},i}^{(\mathrm{HAD})} / \mathbb{R}_{\mathrm{q},i}^{(\mathrm{LO})} \ .$$

In Figure 7.18, I compare the corrections that I obtain using the string- and cluster-fragmentation models. The corrections are large; however, there is good agreement between the two models. Since these models are based on significantly different theoretical assumptions and use parameters that are tuned for very different perturbative final states, I consider that my estimated corrections are reliable.

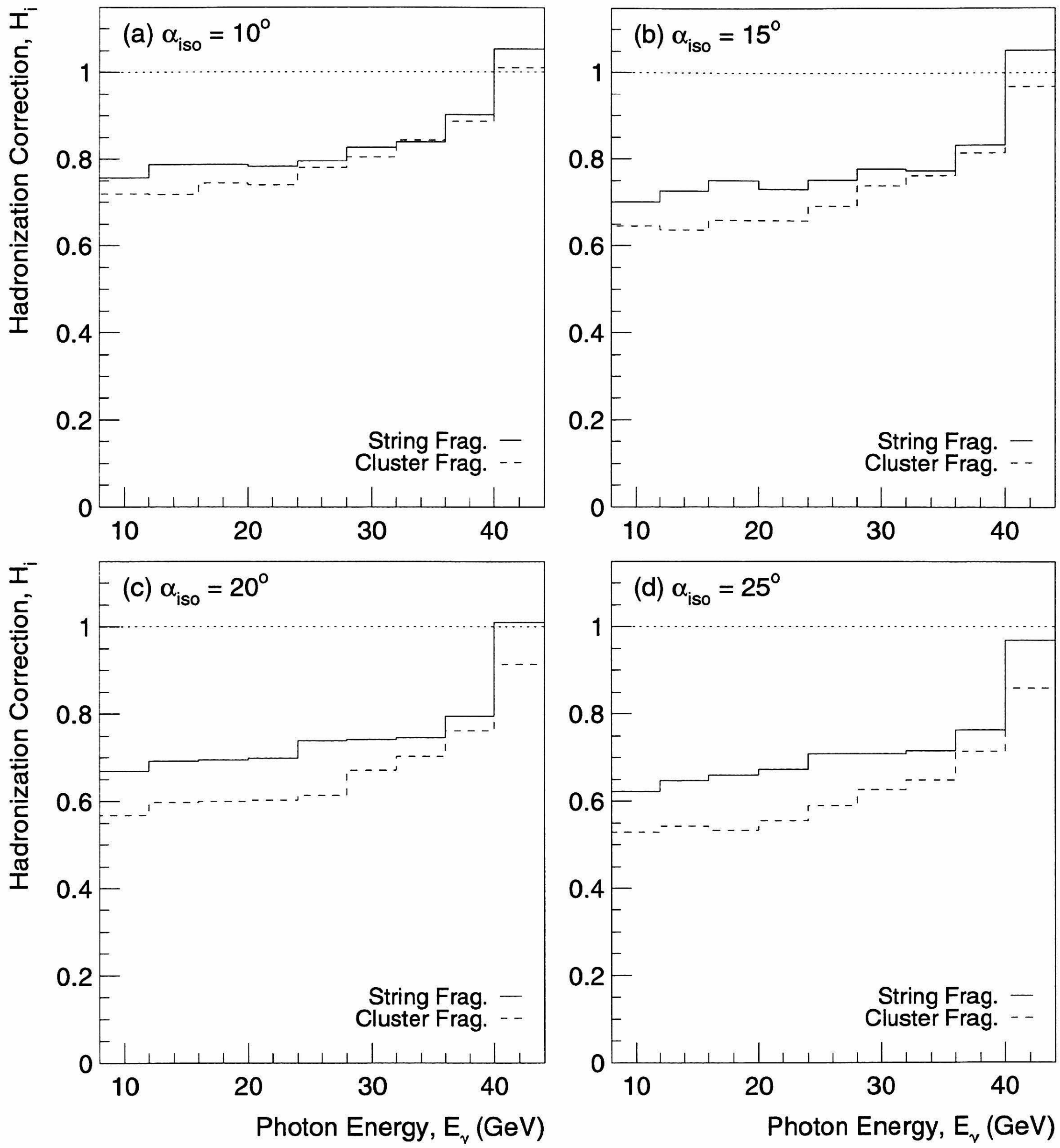

Figure 7.18: Hadronization corrections, H_i, to the energy distribution of isolated FSR. The corrections were obtained with the string-fragmentation model (solid histogram) using LUND+ME tuned parameters, and with the cluster-fragmentation model (dashed histogram) using CLUS+PS tuned parameters.

7.4 Summary and Discussion of Uncertainties

In this chapter, I have described how I treat the production of isolated FSR theoretically, in terms of three independent phases: an electroweak phase, a perturbative phase, and a non-perturbative phase. My goal has been to calculate the binned energy distributions, $\mathbb{R}_i$, that I will compare with my experimental results in the next chapter.

In Section 7.1, I argued that, to a good approximation, my calculation can be separated into an electroweak factor that depends on the quark couplings and a second factor that describes the evolution of a primary $\mathrm{q\overline{q}}$ pair. In Section 7.2, I described two complementary methods for calculating how a primary $\mathrm{q\overline{q}}$ pair evolves in perturbation theory. I argued that the matrix-element method is the more appropriate of these two methods for my calculation, and in Section 7.2.1, I described the matrix-element calculation that I have performed including terms up to $\mathcal{O}(\alpha_S\alpha)$ and quark-mass effects. In Section 7.3, I first described a theoretical framework for including non-perturbative effects in my calculation, and then I calculated the size of these effects using two fragmentation models.

The final form of the binned energy distributions that I calculate, and which I will use in the next chapter to compare with my experimental results, is

$$\mathbb{R}_i = \mathcal{C}_{\mathrm{q\overline{q}}\gamma} \times \left[\mathbb{R}^{(\mathrm{LO})}_{\mathrm{q},i} + \mathbb{R}^{(\mathrm{NLO})}_{\mathrm{q},i}\right] \times H_i \ ,$$

where I define the quark-coupling factor

$$\mathcal{C}_{\mathrm{q\overline{q}}\gamma} \equiv \frac{(2 - m_{\mathrm{c}}^2\langle M\rangle)\overline{c}_{\mathrm{u}}Q_{\mathrm{u}}{}^2 + (3 - \Delta\rho_{\mathrm{b}} - m_{\mathrm{b}}^2\langle M\rangle)\overline{c}_{\mathrm{d}}Q_{\mathrm{d}}{}^2}{2\overline{c}_{\mathrm{u}} + (3 - \Delta\rho_{\mathrm{b}})\overline{c}_{\mathrm{d}}} \ .$$

In Figure 7.19, I show these distributions for different isolation cuts, which I calculate using values of $\mathcal{C}_{\mathrm{q\overline{q}}\gamma}$ that I obtain in the framework of the Standard Model (see Section 8.1.2). For comparison, I also show the different approximations to $\mathbb{R}_i$ that I calculate by first setting H_i to one (which gives the $\mathcal{O}(\alpha_S\alpha)$ approximation) and then, also setting α_S to zero (which gives the $\mathcal{O}(\alpha)$ approximation). In Figure 7.20, I show my predictions for the total rate of isolated FSR

$$\mathbb{R} \equiv \sum_{i=1}^{9} \mathbb{R}_i \ ,$$

together with the same two approximations for comparison.

The main theoretical uncertainties in the FSR energy distributions that I calculate are from

- my estimate of quark-mass effects, which is unreliable for small isolation cuts,
- the uncertainty in the value of α_S that I use to calculate $\mathbb{R}_i^{(\mathrm{NLO})}$,
- the effect of missing higher-order contributions in perturbation theory, which are $\mathcal{O}(\mu^2 \alpha_S \alpha)$ and $\mathcal{O}(\alpha_S^2 \alpha)$,

and,

- my estimate of the non-perturbative corrections, H_i, which I calculate with a phenomenological model.

The first of these uncertainties is difficult to quantify, but can be avoided by using an isolation cut of at least 20° (see Section 7.2.1.3). For smaller isolation cuts, the value of the b-quark correction, $m_b^2 \langle M \rangle$, can be truncated to avoid introducing a large unphysical effect (this is the approach that I use in Section 8.1.2). The second and third uncertainties are related since, to some extent, an adjustment of the value of α_S that I use can compensate for the effect of missing higher orders (see Section 7.2.1.4). Therefore, I estimate the uncertainty due to both of these effects by varying the value of α_S. The range of α_S values that I consider is between

$$\alpha_S^{min} \equiv \min(\alpha_S^{eff}\,,\, 0.124 - \Delta\alpha_S) \quad \text{and} \quad \alpha_S^{max} \equiv \max(\alpha_S^{eff}\,,\, 0.124 + \Delta\alpha_S)\ ,$$

where α_S^{eff} is the optimized effective value that I determined in Section 7.2.2.1, and $\Delta\alpha_S = 0.018$ is twice the error on the value, $\alpha_S = 0.124$, that is quoted in Reference

[93]. I estimate the uncertainty due to the factors, H_i, that I apply, by using two different models to calculate these factors (see Section 7.3). For my best estimate of H_i, I use the values that I obtain with the LUND+ME model,

$$H_i \equiv H_i^{LUND+ME} \; .$$

I assign a theoretical uncertainty on this estimate equal to half of the difference between the LUND+ME and CLUS+PS corrections

$$\Delta H_i \equiv \frac{1}{2} \left| H_i^{LUND+ME} - H_i^{CLUS+PS} \right| \; .$$

The uncertainties that I calculate by varying α_S and the hadronization corrections are indicated by the size of the bands that I show in Figures 7.19 and 7.20.

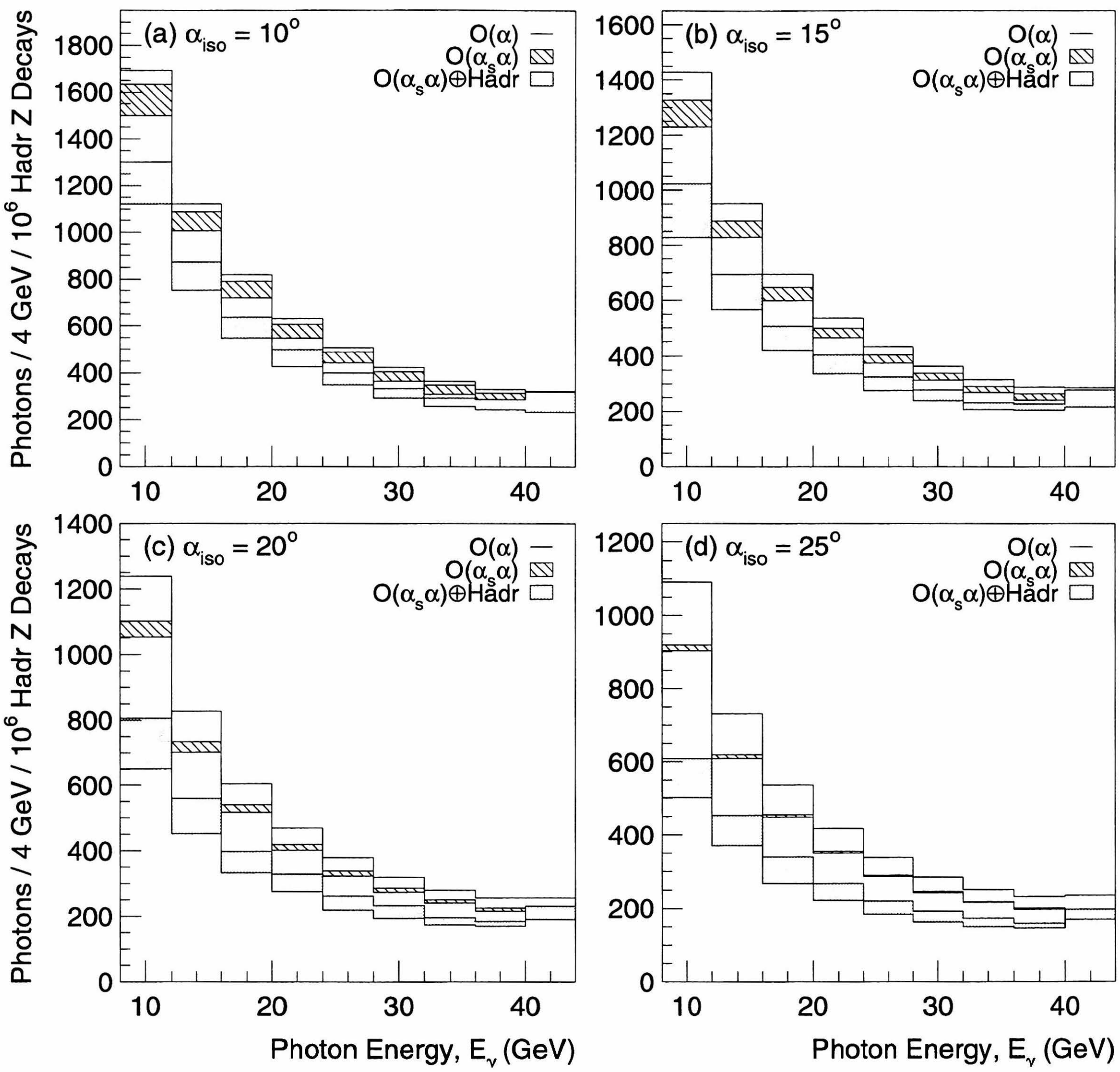

Figure 7.19: Energy distributions of isolated FSR calculated using different theoretical approximations. The matrix-element perturbative predictions are shown as a solid histogram (lowest order) and a hatched region (next-to-lowest order). The size of the hatched region is the theoretical uncertainty that I estimate by varying α_S. The final prediction, which includes non-perturbative effects, is shown as a shaded region. The size of this shaded region is the theoretical uncertainty that I estimate by varying α_S and by using different fragmentation models. These results were obtained using values of the quark couplings that I calculate in the Standard Model (see Section 8.1).

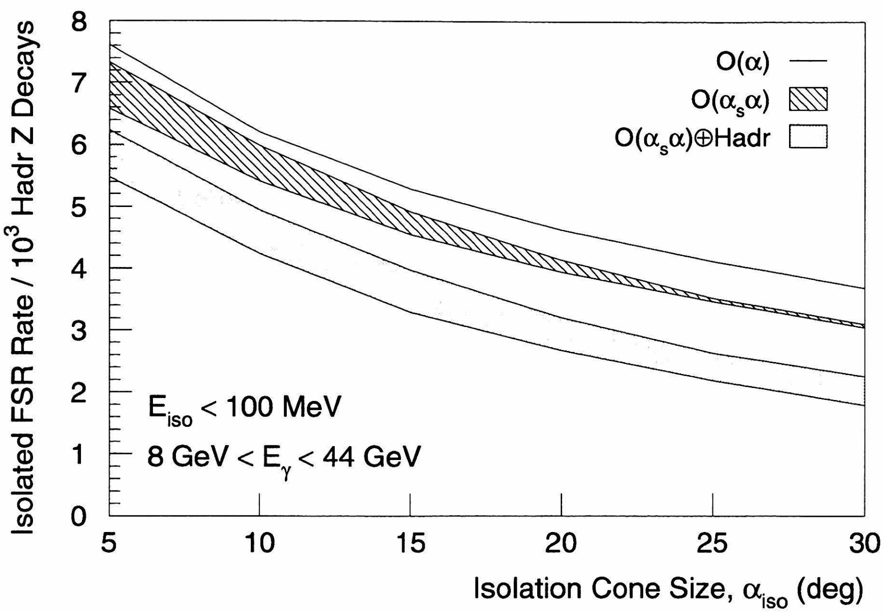

Figure 7.20: Rates of isolated FSR with energies between 8 GeV and 44 GeV, as a function of the isolation cut, calculated using different theoretical approximations. The matrix-element perturbative predictions are shown as a solid curve (lowest order) and a hatched region (next-to-lowest order). The size of the hatched region is the theoretical uncertainty that I estimate by varying α_S. The final prediction, which includes non-perturbative effects, is shown as a shaded region. The size of this shaded region is the theoretical uncertainty that I estimate by varying α_S and by using different fragmentation models. These results were obtained using values of the quark couplings that I calculate in the Standard Model (see Section 8.1).

Chapter 8

Results

In this chapter, I measure the couplings of up-type and down-type quarks to the Z boson and to the photon. I do so by combining two independent constraints on these couplings. A measurement of the inclusive rate of hadronic Z decays[1] (see Figure 8.1(a)) constrains the combination

$$\mathcal{C}_{\mathrm{q\bar{q}}} \simeq 2 \cdot \overline{c}_{\mathrm{u}} + 3 \cdot \overline{c}_{\mathrm{d}} \; .$$

A measurement of the fraction of hadronic Z decays that are accompanied by final-state radiation (see Figure 8.1(b)), constrains the combination

$$\mathcal{C}_{\mathrm{q\bar{q}\gamma}} \simeq \frac{2 \cdot \overline{c}_{\mathrm{u}} \cdot Q_{\mathrm{u}}{}^2 + 3 \cdot \overline{c}_{\mathrm{d}} \cdot Q_{\mathrm{d}}{}^2}{2 \cdot \overline{c}_{\mathrm{u}} + 3 \cdot \overline{c}_{\mathrm{d}}} \; .$$

In this chapter, I first review the L3 measurement of the Z lineshape parameters, and derive the relationship between $\mathcal{C}_{\mathrm{q\bar{q}}}$ and these parameters. Next, I compare my experimental results from Chapter 6 with my theoretical predictions from Chapter 7, and thus measure $\mathcal{C}_{\mathrm{q\bar{q}\gamma}}$. Finally, I combine the two constraints on the quark couplings, using two alternative sets of assumptions, in order to determine their values. The method that I use to obtain the quark-Z couplings was first proposed in Reference [99].

[1] Inclusive hadronic Z decays include those decays that accompanied by a photon, but this FSR contribution is negligible since it is suppressed by a factor of $\alpha/(2\pi) \simeq 0.1\%$.

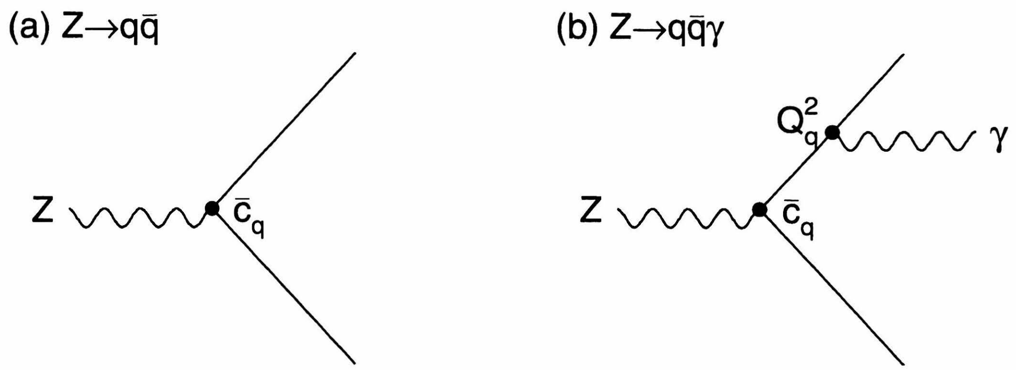

Figure 8.1: Diagrams for the two Z decay processes that I use to constrain the quark couplings to the Z boson and the photon: inclusive decays into quarks (a), and exclusive decays into quarks that are accompanied by a radiated photon (b).

8.1 Lineshape Constraints

In this section, I derive constraints on the quark couplings from cross sections and asymmetries measured at the Z peak (I refer to these as *lineshape* measurements). First, I review the five-parameter fit that L3 has performed to its lineshape data. Then, I calculate the constraint $\mathcal{C}_{\mathrm{q\bar{q}}}$ on the couplings using the results of this fit. Finally, I calculate the Standard Model values of the couplings, $\bar{c}_{\mathrm{u}}$ and $\bar{c}_{\mathrm{d}}$, and of the constraint, $\mathcal{C}_{\mathrm{q\bar{q}}\gamma}$, in order to compare with the results that I obtain later in this chapter.

8.1.1 Lineshape Fit

L3 has measured the leptonic and hadronic cross sections and the leptonic forward-backward charge asymmetries at the Z peak, using 117.8 pb^{-1} of data collected during 1990–94[58]. In order to extract the electroweak parameters of Z decay, we perform a fit of this lineshape data to a model, ZFITTER[19], that assumes lepton universality but otherwise makes a minimum of assumptions about the underlying theory. The five parameters of this fit are chosen to be as uncorrelated as possible. They are the Z mass and total width, m_Z and Γ_Z, the Born-level peak hadronic cross section,

$$\sigma_{\rm had} = \frac{12\pi}{m_Z^2}\frac{\Gamma_\ell \Gamma_{\rm had}}{\Gamma_Z^2} ,$$

the ratio of the hadronic to the leptonic partial widths, $R_\ell = \Gamma_{\rm had}/\Gamma_\ell$, and the leptonic forward-backward charge asymmetry at $s = m_Z^2$, A_{FB}^ℓ. The results of the fit are[58]

$$m_Z = 91.1936 \pm 0.0036 \text{ GeV} \quad , \quad \Gamma_Z = 2.5022 \pm 0.0054 \text{ GeV} ,$$

$$\sigma_{\rm had} = 41.483 \pm 0.108 \text{ nb} \quad , \quad R_\ell = 20.812 \pm 0.076 \quad , \quad A_{FB}^\ell = 0.0186 \pm 0.0030 ,$$

and the correlations between these parameters[2] are given in Table 8.1. In Figure 8.2, I show our measured hadronic cross sections at different center-of-mass energies. I also superimpose the resonance curve that ZFITTER predicts using the fitted parameter values. There is good agreement between our lineshape measurements and the fit.

	Γ_Z	$\sigma_{\rm had}$	R_ℓ	A_{FB}^ℓ
m_Z	$+.053$	$-.068$	$-.019$	$+.086$
Γ_Z		$-.317$	$-.038$	$+.000$
$\sigma_{\rm had}$			$+.148$	$+.004$
R_ℓ				$-.008$

Table 8.1: Matrix of the correlation coefficients between the five parameters used in the lineshape fit to the hadronic and leptonic cross sections and the leptonic asymmetries.

8.1.2 Derived Parameters

In the Improved Born Approximation (see Section 2.1.1.1), the partial width for a Z to decay into hadrons is related to the the effective quark electroweak couplings, $\bar{c}_u$ and $\bar{c}_d$, by

$$\Gamma_{\rm had} = \frac{N_C G_F}{24\pi\sqrt{2}} m_Z^3 (1 + \delta_{\rm QCD}) \left[2 \cdot \bar{c}_u + (3 - \Delta\rho_b) \cdot \bar{c}_d\right] ,$$

[2] All of the errors that I quote on quantities that are derived from lineshape parameters take account of these correlations.

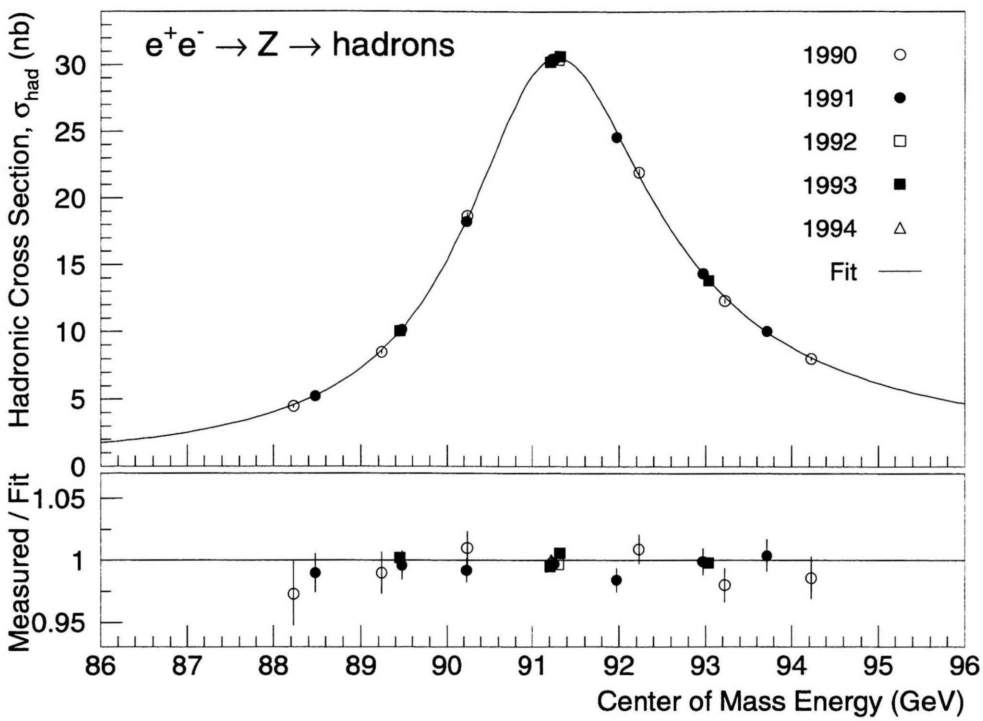

Figure 8.2: L3's measured cross sections at different center-of-mass energies for the reaction $e^+e^- \longrightarrow Z \longrightarrow$ hadrons (data points) and the fitted model (solid curve) generated by ZFITTER. The lower part of the figure shows the ratios between the measured and fitted values on an expanded scale.

where $N_C = 3$ is the number of colors in QCD, and $G_F \simeq 1.166392 \times 10^{-5}$ GeV^{-2}[73] is the Fermi constant. The term δ_{QCD} incorporates QCD final-state corrections, and has been calculated[100] using a series expansion in the strong coupling, α_S, to be

$$\delta_{\text{QCD}} = 1.060 \cdot \frac{\alpha_S}{\pi} + 0.9 \cdot \left(\frac{\alpha_S}{\pi}\right)^2 - 15 \cdot \left(\frac{\alpha_S}{\pi}\right)^3 + \mathcal{O}(\alpha_S^4)\ .$$

I substitute the value of α_S that we obtained from fits to global event-shape distributions measured in hadronic Z decays[3], $\alpha_S = 0.124 \pm 0.009$[93], and obtain

$$\delta_{\text{QCD}} = (4.34 \pm 0.30)\ \%\ .$$

[3] I use the value of α_S obtained from hadronic event shapes, rather than the value $\alpha_S = 0.127 \pm 0.008$ that is obtained from the hadronic width of the Z [58], since this first value is uncorrelated with the lineshape-fit parameters that I am using.

The parameter $\Delta\rho_{\rm b}$ incorporates $\rm b\overline{b}$ vertex corrections that involve a heavy top quark (see Section 7.1), and is approximately 1.35% for a top quark mass of 180 GeV [87, 88].

A measurement of $\Gamma_{\rm had}$ constrains the values of the quark couplings to the Z boson, $\overline{c}_{\rm u}$ and $\overline{c}_{\rm d}$. I express this constraint as

$$\mathcal{C}_{\rm q\overline{q}} = 2 \cdot \overline{c}_{\rm u} + (3 - \Delta\rho_{\rm b}) \cdot \overline{c}_{\rm d} \ ,$$

and calculate its value using

$$\mathcal{C}_{\rm q\overline{q}} \equiv \frac{\Gamma_{\rm had}}{m_{\rm Z}^3} \frac{24\pi\sqrt{2}}{N_C G_F} \frac{1}{1 + \delta_{\rm QCD}} \ .$$

The hadronic partial width is not one of the five parameters of our lineshape fit, but it is related to these parameters by

$$\Gamma_{\rm had} = \left(\frac{\sigma_{\rm had} R_\ell}{12\pi} \right)^{1/2} \frac{\Gamma_{\rm Z} m_{\rm Z}}{\hbar c} \ .$$

Thus, the coupling constraint, $\mathcal{C}_{\rm q\overline{q}}$, can be expressed in terms of the lineshape fit parameters as

$$\mathcal{C}_{\rm q\overline{q}} = \frac{\Gamma_{\rm Z}}{m_{\rm Z}^2} \frac{(96\pi\sigma_{\rm had} R_\ell)^{1/2}}{N_C G_F (1 + \delta_{\rm QCD})\hbar c} \ .$$

I substitute the fitted parameter values into this expression, and obtain

$$\mathcal{C}_{\rm q\overline{q}} = 6.886 \pm 0.020 \ .$$

In the Standard Model, the couplings of quarks and leptons to the Z boson are related to the two universal parameters, $\sin^2\overline{\theta}_W$ and $\rho_{\rm eff}$, according to

$$\overline{c}_{\rm f} = \rho_{\rm eff} \left[1 + \left(1 - 4|Q_{\rm f}| \sin^2\overline{\theta}_W \right)^2 \right] \ .$$

In the following, when I refer to a result as being obtained within the framework of the Standard Model — I use the superscript (SM) to denote such results — I am assuming that this relationship holds, and that the quark charges are $Q_{\rm u} = +2/3$ and $Q_{\rm d} = -1/3$. As an example, the constraint that I obtained above was not obtained within the framework of the Standard Model.

The effective electroweak mixing angle, $\sin^2\overline{\theta}_W$, and the effective ratio of the neutral to charged weak current couplings, ρ_{eff}, are related to the lineshape parameters by

$$\sin^2\overline{\theta}_W = \frac{1}{4} - \frac{1}{4}\cdot\left(\frac{3 - 2A^{\ell}_{FB} - \sqrt{9 - 12A^{\ell}_{FB}}}{2A^{\ell}_{FB}}\right)^{1/2},$$

and

$$\rho_{\text{eff}} = \frac{(3 + \sqrt{9 - 12A^{\ell}_{FB}})\Gamma_{\text{Z}}}{\hbar c G_F m_{\text{Z}}^2}\left(\frac{8\pi\sigma_{\text{had}}}{3R_{\ell}}\right)^{1/2}.$$

I substitute the fitted values of the lineshape parameters into these expressions, and obtain[4]

$$\sin^2\overline{\theta}_W = 0.2302 \pm 0.0016 \quad \text{and} \quad \rho_{\text{eff}} = 1.007 \pm 0.003\,.$$

In Table 8.2, I give the correlations that I calculate between the three parameters: $\sin^2\overline{\theta}_W$, ρ_{eff}, and $\mathcal{C}_{\text{q}\overline{\text{q}}}$. If I assume the framework of the Standard Model, then, using the values of $\sin^2\overline{\theta}_W$ and ρ_{eff} that I obtained above, I calculate

$$\overline{c}_{\text{u}}^{\,(\text{SM})} = 1.1574 \pm 0.0039 \quad \text{and} \quad \overline{c}_{\text{d}}^{\,(\text{SM})} = 1.4911 \pm 0.0044\,.$$

	$\sin^2\overline{\theta}_W$	ρ_{eff}
$\mathcal{C}_{\text{q}\overline{\text{q}}}$	+.006	+.149
$\sin^2\overline{\theta}_W$		+.345

Table 8.2: Matrix of correlation coefficients between three parameters that I derive from the five-parameter lineshape fit.

In Section 8.2, I place a second constraint on the quark couplings which I refer to as $\mathcal{C}_{\text{q}\overline{\text{q}}\gamma}$. This constraint is expressed in terms of the couplings as

$$\mathcal{C}_{\text{q}\overline{\text{q}}\gamma} = \frac{(2 - m_{\text{c}}^2\langle M\rangle)\overline{c}_{\text{u}}Q_{\text{u}}^{\,2} + (3 - \Delta\rho_{\text{b}} - m_{\text{b}}^2\langle M\rangle)\overline{c}_{\text{d}}Q_{\text{d}}^{\,2}}{2\overline{c}_{\text{u}} + (3 - \Delta\rho_{\text{b}})\overline{c}_{\text{d}}},$$

[4]The values that I obtain here are not exactly the same as those given in Reference [58], $\sin^2\overline{\theta}_W = 0.2302 \pm 0.0016$ and $\rho_{\text{eff}} = 1.005 \pm 0.003$, since the measurements of the tau polarization and the forward-backward asymmetry in $\text{b}\overline{\text{b}}$ events were also taken into account there.

where m_c and m_b are the c- and b-quark masses, respectively, and $\langle M \rangle$ is the mass correction that I calculated in Section 7.2.1.3. I will measure the value of $\mathcal{C}_{q\bar{q}\gamma}$ by comparing my experimental results on isolated FSR with my theoretical predictions, not assuming the framework of the Standard Model in doing so. For comparison with this result, I now calculate $\mathcal{C}_{q\bar{q}\gamma}$ within the framework of the Standard Model. I use the central values of the estimated quark masses that are given in Reference[73], which are $m_c = 1.3$ GeV and $m_b = 4.3$ GeV. Finally, I obtain[5]

$$\mathcal{C}^{(\mathrm{SM})}_{q\bar{q}\gamma} = \begin{cases} 0.2187 & \alpha_{\mathrm{iso}} = 10^\circ \\ 0.2200 & \alpha_{\mathrm{iso}} = 15^\circ \\ 0.2211 & \alpha_{\mathrm{iso}} = 20^\circ \\ 0.2222 & \alpha_{\mathrm{iso}} = 25^\circ \end{cases} .$$

The errors in these values are negligible since most of the error in the numerator and denominator of the expression for $\mathcal{C}_{q\bar{q}\gamma}$ is correlated and thus cancels in their ratio.

8.2 Comparison of Data with Theory

In this section, I compare the isolated FSR energy distributions that I measured in Chapter 6 with the predictions for these distributions that I calculated in Chapter 7. First, I perform this comparison using the values of the quark couplings that I calculate within the framework of the Standard Model. Then, I consider these couplings to be free parameters and I use fits to measure the constraint, $\mathcal{C}_{q\bar{q}\gamma}$, on their values.

[5]Since the b-quark mass correction that I calculate is not reliable for $\alpha_{\mathrm{iso}} \lesssim 20^\circ$, I truncate the value of $m_b^2 \langle M \rangle$ at a maximum value of 15%. This procedure increases the value of $\mathcal{C}^{(\mathrm{SM})}_{q\bar{q}\gamma}$ that I calculate with $\alpha_{\mathrm{iso}} = 10^\circ$ (15°) by 2.5% (-0.5%).

8.2.1 Standard Model Comparison

In this section, I compare my experimental results with the theoretical predictions that I calculate within the framework of the Standard Model. I calculate these predictions using my $\mathcal{O}(\alpha_S\alpha)$ matrix-element calculation that also includes non-perturbative corrections. For completeness, I also compare with the predictions of the JETSET[62, 63] and HERWIG[64, 65] Monte Carlo programs, which both combine a parton-shower model with a fragmentation model, although I do not consider that these programs are appropriate for describing FSR.

I refer to the rate of isolated FSR that I measure in an energy bin, i, as R_i (see Section 6.3). I express my matrix-element prediction of this rate, within the framework of the Standard Model, as

$$\mathbb{R}_i = \mathcal{C}^{(\mathrm{SM})}_{\mathrm{q\bar{q}}\gamma} \times \left[\mathbb{R}^{(\mathrm{LO})}_{\mathrm{q},i} + \mathbb{R}^{(\mathrm{NLO})}_{\mathrm{q},i}\right] \times H_i \ ,$$

where $\mathbb{R}^{(\mathrm{LO})}_i$ and $\mathbb{R}^{(\mathrm{NLO})}_i$ are the $\mathcal{O}(\alpha)$ and $\mathcal{O}(\alpha_S\alpha)$ contributions that I calculate (see Section 7.2), and H_i incorporates non-perturbative corrections (see Section 7.3). I estimate the theoretical uncertainty in this prediction by varying the value of α_S that I use to calculate $\mathbb{R}^{(\mathrm{NLO})}_i$ and by comparing different methods for estimating the correction factors, H_i (see Section 7.3.1).

Figure 8.3 shows the comparison of my measured FSR energy distributions with the matrix-element and Monte Carlo predictions. Figure 8.4 shows the same comparison for the total rate of isolated FSR with energies between 8 GeV and 44 GeV, as a function of the isolation cut. There is good overall agreement between my experimental results and my Standard Model matrix-element predictions. This agreement appears slightly worse with an isolation cut of $\alpha_{\mathrm{iso}} = 10°$, although this discrepancy may be due to heavy-quark mass corrections which I can not calculate reliably at α_{iso} $= 10°$, and which are not included in my theoretical error estimate. The JETSET and HERWIG Monte Carlo programs both predict a lower rate of isolated FSR than I observe. More significantly, there is a large discrepancy between the predictions of these two programs. I attribute this disagreement to the fact that the leading-logarithm approximation, which both programs use for their perturbative calculations, is not appropriate for describing isolated FSR production.

8.2.2 Fitted Comparisons

In this section, I do not assume the framework of the Standard Model, so that the values of the quark couplings are unconstrained. With this approach, $\mathcal{C}_{q\bar{q}\gamma}$ and α_S become free parameters of my matrix-element prediction,

$$\mathbb{R}_i(\mathcal{C}_{q\bar{q}\gamma}, \alpha_S) = \mathcal{C}_{q\bar{q}\gamma} \times \left[\mathbb{R}^{(\mathrm{LO})}_{q,i} + \mathbb{R}^{(\mathrm{NLO})}_{q,i}(\alpha_S)\right] \times H_i \ ,$$

which I can determine using a fit to my measured distributions, R_i. I perform two types of fits: first, I allow both $\mathcal{C}_{q\bar{q}\gamma}$ and α_S to vary freely, and then, I constrain α_S and allow only $\mathcal{C}_{q\bar{q}\gamma}$ to vary. The two-parameter fit allows me to test the consistency of the QCD corrections that I calculate. The one-parameter fit provides the best measurement of $\mathcal{C}_{q\bar{q}\gamma}$.

I define a chi-square function for fitting my predictions, $\mathbb{R}_i$, to my experimental results, R_i, as

$$\chi^2(\mathcal{C}_{q\bar{q}\gamma}, \alpha_S) \equiv \sum_{i=1}^{9} \left[\frac{R_i - \mathbb{R}_i(\mathcal{C}_{q\bar{q}\gamma}, \alpha_S)}{\delta R_i}\right]^2 \ ,$$

where δR_i are the statistical errors of my data analysis (see Section 6.3). For the two-parameter fit, I simultaneously minimize this chi-square with respect to $\mathcal{C}_{q\bar{q}\gamma}$ and α_S. For the one-parameter fit, I minimize the chi-square with respect to $\mathcal{C}_{q\bar{q}\gamma}$ only, holding α_S fixed. I define the fitted parameter values as the location of these minima

$$\chi^2(\mathcal{C}^{(\mathrm{FIT})}_{q\bar{q}\gamma}, \alpha^{(\mathrm{FIT})}_S) \equiv \chi^2_{min} \quad \text{or} \quad \chi^2(\mathcal{C}^{(\mathrm{FIT})}_{q\bar{q}\gamma}, \alpha_S) \equiv \chi^2_{min} \ ,$$

and study the statistical errors in these fitted values using contours of constant chi-square[73]

$$\chi^2(\mathcal{C}_{q\bar{q}\gamma}, \alpha_S) = \chi^2_{min} + \Delta\chi^2 \ .$$

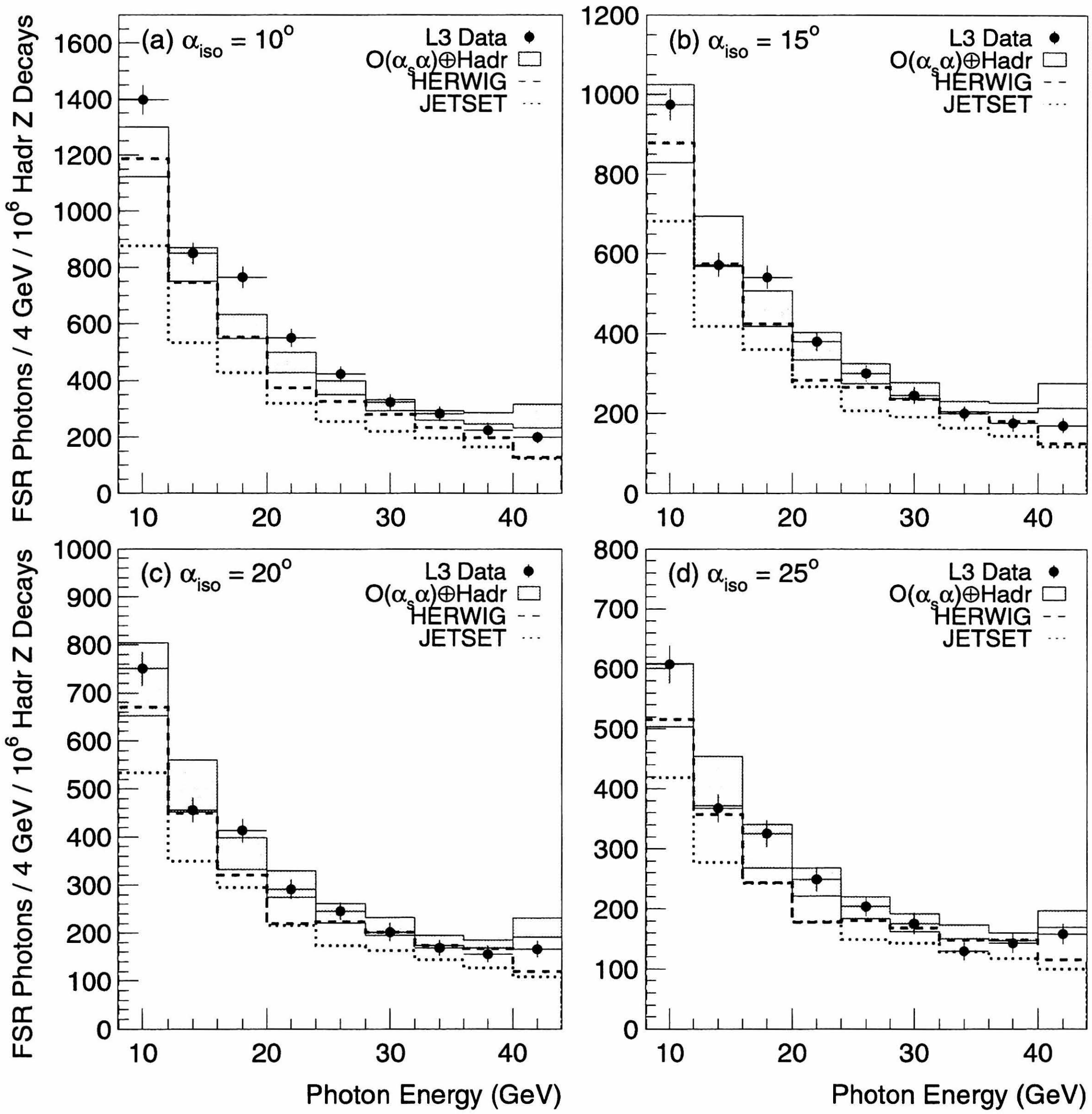

Figure 8.3: Comparison of my measured isolated FSR energy distributions with the predictions of different theoretical models. The measured distributions are shown as data points with statistical errors. My matrix-element prediction is shown as a shaded region whose size indicates the estimated theoretical uncertainty. The HERWIG and JETSET predictions are shown as dashed and dotted histograms, respectively.

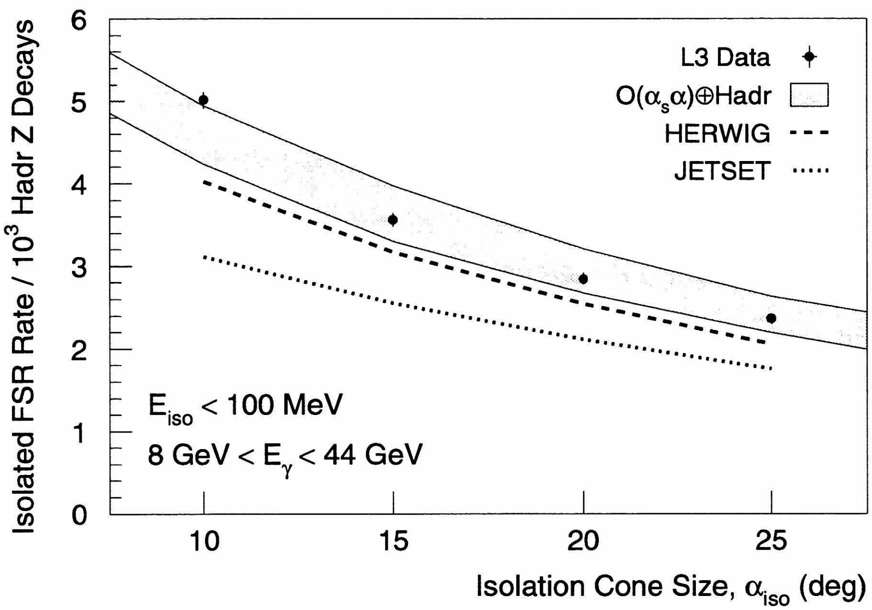

Figure 8.4: Comparison of my measured isolated FSR rates at different isolation cuts with the predictions of different theoretical models. The measured distributions are shown as data points with statistical errors. The matrix-element prediction is shown as a shaded region whose size indicates the estimated theoretical uncertainty. The HERWIG and JETSET predictions are shown as dashed and dotted curves, respectively.

The energy distribution that I measure for each isolation cut has nine bins. Therefore, the one- and two-parameter fits that I perform to each distribution have eight and seven degrees of freedom, respectively. The distributions that I measure using different isolation cuts are correlated and as a result, so are the fitted parameters that I obtain from them.

8.2.2.1 Two-Parameter Fits

In this section, I describe the fits that I perform using two free parameters: $\mathcal{C}_{q\bar{q}\gamma}$ and α_S. The first of these parameters influences the normalization of the predicted energy distribution but not its shape. The second parameter influences both its normalization and its shape. The results of these fits, using different isolation cuts, are summarized in Table 8.3. Figure 8.5 shows a comparison of my measured energy distributions with the predictions that I calculate using the fitted parameters. Figure 8.6 shows the contours of the 68% and 90% statistical-error regions in $\mathcal{C}_{q\bar{q}\gamma}$ and α_S.

$\alpha_{\rm iso}$	$\mathcal{C}^{(\rm FIT)}_{q\bar{q}\gamma}$	$\alpha^{(\rm FIT)}_S$	$\chi^2_{min}/\rm DF$
10°	0.294	0.253	16.7/7
15°	0.279	0.285	16.2/7
20°	0.281	0.293	9.6/7
25°	0.216	0.123	13.7/7

Table 8.3: Results of two-parameter fits to the energy distributions of isolated FSR with different isolation cuts. Note that my chi-square only includes statistical errors and so does not measure the overall goodness of the fits.

The fitted energy distributions are in good agreement with my measurements, within the statistical errors of my data analysis. The fitted parameter values that I obtain using different isolation cuts are consistent with each other, within statistical uncertainties, except for $\alpha_{\rm iso} = 10°$. This consistency check indicates that my calculation correctly predicts the evolution of the FSR energy distribution between 25° and 15°, but becomes less reliable at smaller isolation cuts. The fitted parameter

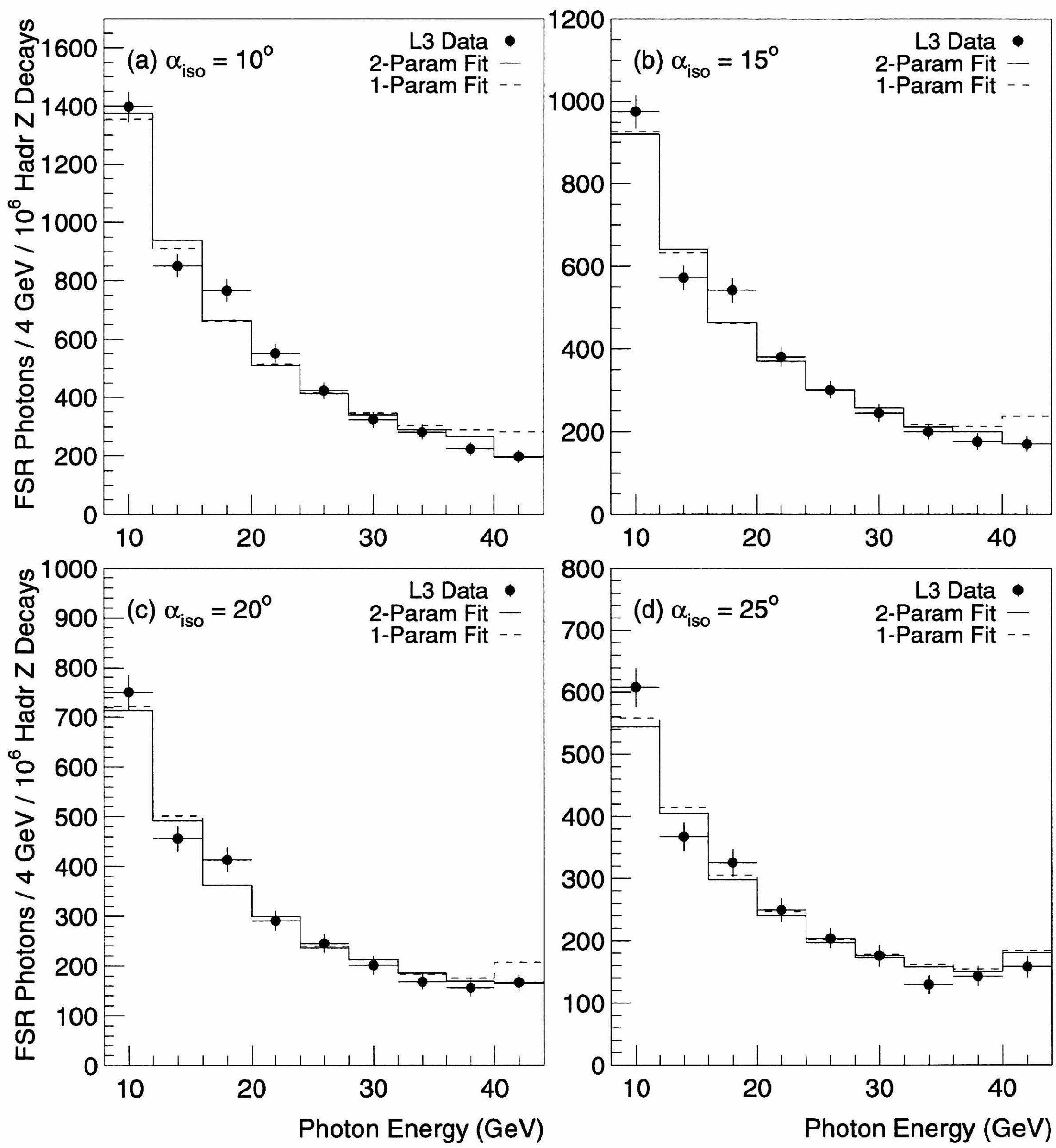

Figure 8.5: Comparison of my measured isolated FSR energy distributions (data points showing statistical errors) with the predictions that I calculate using fitted parameter values. The solid and dashed histograms are calculated using the two- and one-parameter fit results, respectively.

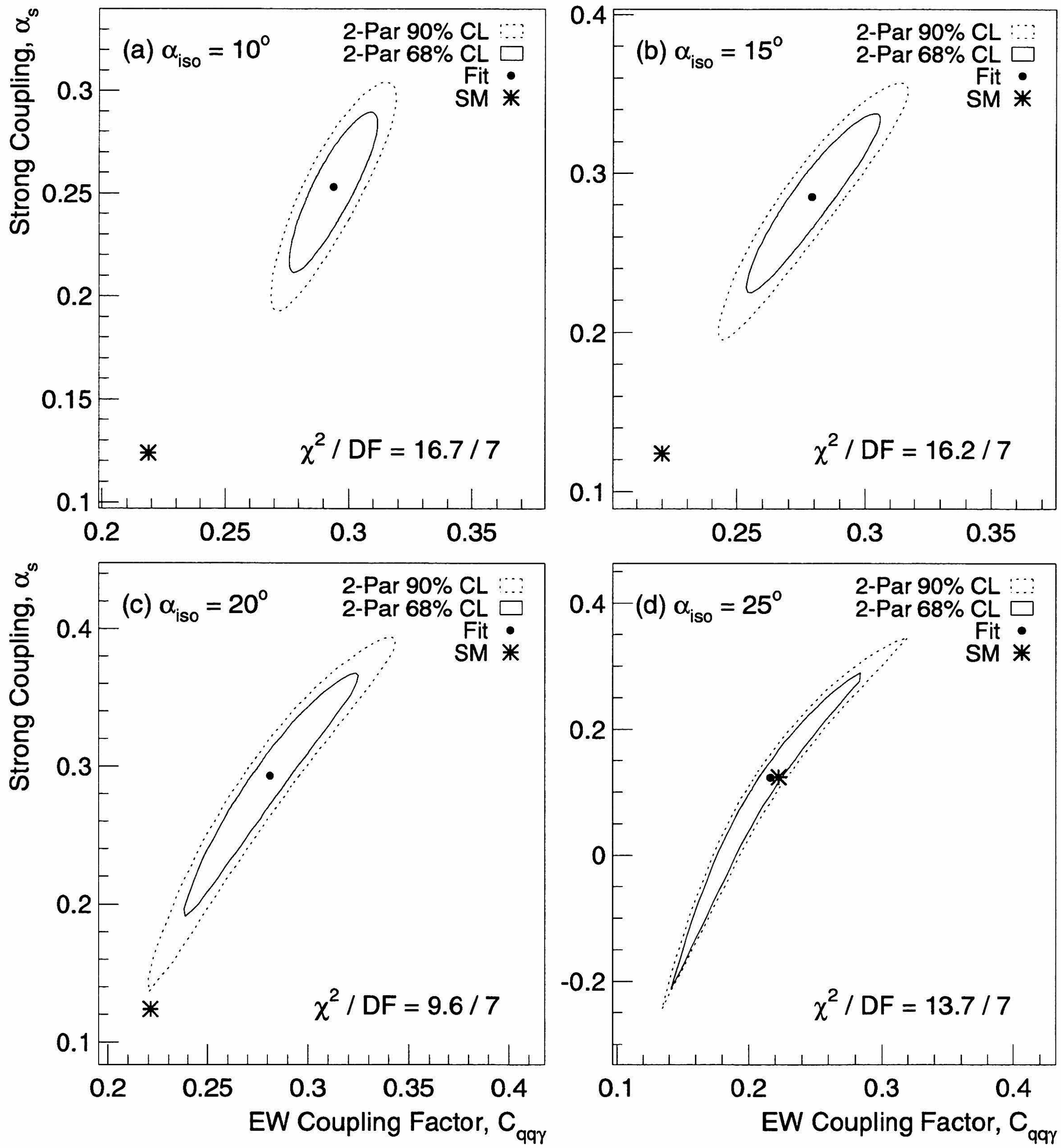

Figure 8.6: Confidence-level contours of the two-parameter fits to isolated FSR energy distributions with different isolation cuts. The solid (dotted) contours show the 68% (90%) confidence-level *statistical-error* regions. The fitted values of the parameters are shown with a filled circle. The Standard Model values of the parameters are shown with an asterisk. Note the different scales used for each plot.

values are only consistent with the Standard Model (within statistical uncertainties) for $\alpha_{\text{iso}} = 25°$. The discrepancy at lower α_{iso} indicates a systematic problem with the two-parameter model that I am using rather than an incompatibility between the measurements and the Standard Model. In particular, in order to perform the fit with α_S a free parameter, I assume that with an appropriate choice of this parameter, my $\mathcal{O}(\alpha_S\alpha)$ calculation correctly describes the QCD corrections to the energy distribution. However, this assumption is only valid if the higher-order corrections that I do not calculate are negligible. In Section 7.2.2.1, I compared two methods for estimating QCD corrections: the $\mathcal{O}(\alpha_S\alpha)$ matrix element and a leading-logarithm approximation. I concluded that higher-order QCD corrections are important with a 10° isolation cut, but can, to a good approximation, be neglected with a 25° cut. This conclusion is reinforced by the good agreement between the fitted and Standard Model values of $\mathcal{C}_{q\bar{q}\gamma}$ and α_S with $\alpha_{\text{iso}} = 25°$. In Section 7.2.2.1, I also concluded that the QCD corrections that I calculate are less reliable at high energies. I have repeated my two-parameter fits using only energy bins between 8 GeV and 30 GeV. The parameter values that I obtain from these restricted fits are in better agreement with the Standard Model.

The statistical-error regions that I show in Figure 8.6 span large intervals of $\mathcal{C}_{q\bar{q}\gamma}$ and α_S because there is a strong positive correlation between the effects of these parameters: an increase in $\mathcal{C}_{q\bar{q}\gamma}$ can be compensated by an increase in α_S. Because of this correlation, a fit that makes no *a priori* assumptions about the value of α_S yields a large uncertainty in the value of $\mathcal{C}_{q\bar{q}\gamma}$. Therefore, in order to measure $\mathcal{C}_{q\bar{q}\gamma}$ as accurately as possible, I now turn to a one-parameter fit in which I use the value of α_S determined by other measurements.

8.2.2.2 One-Parameter Fits

In this section, I describe the fits that I perform by allowing the quark coupling factor $\mathcal{C}_{q\bar{q}\gamma}$ to vary, but fixing the value of the strong coupling, α_S. To obtain my best estimate of the value of $\mathcal{C}_{\mathrm{q\bar{q}}\gamma}$, I fit using $\alpha_S = 0.124$[93]. In addition to the statistical errors on $\mathcal{C}_{\mathrm{q\bar{q}}\gamma}$ that I calculate from the chi-square, I estimate experimental and theoretical systematic uncertainties. I estimate the experimental systematic errors by repeating the fit using the two limit distributions that I measure, R_i^+ and R_i^-, instead of the central-value distribution, R_i, and by changing the shower-shape cut that I use to select photon candidates (see Section 6.3). I estimate the theoretical systematic errors by varying the value of α_S and the hadronization corrections, H_i, that I use in my calculation. The extreme values of α_S that I use are α_S^{min} and α_S^{max} which I defined in Section 7.4. The extreme sets of hadronization corrections that I use are $H_i + \Delta H_i$ and $H_i - \Delta H_i$, where ΔH_i is the theoretical uncertainty that I defined in Section 7.4. The results of my one-parameter fits are summarized in Table 8.4. Figure 8.5 shows a comparison of my measured energy distributions with the fitted energy distributions.

The largest systematic errors that I calculate are due to the uncertainties of my calculation. I combine the variations that I observe by changing α_S or the corrections, H_i, into a single asymmetric theoretical error by taking the maximum deviation for both of these effects, separately for the upper and lower errors. With an isolation cut of $\alpha_{\mathrm{iso}} = 10°$, the uncertainty due to missing higher-order QCD corrections dominates; with $\alpha_{\mathrm{iso}} = 25°$, the uncertainty due to the non-perturbative corrections dominates. I calculate a symmetric experimental systematic error by adding in quadrature the average variations that I observe by replacing R_i with either R_i^+ or R_i^-, and by changing my shower-shape cut. Finally, I obtain

$$\mathcal{C}_{\mathrm{q\bar{q}}\gamma}^{(\mathrm{FIT})} = \begin{cases} 0.249 \pm 0.005 \pm 0.012 \,{}^{+0.007}_{-0.024} & \alpha_{\mathrm{iso}} = 10° \\ 0.222 \pm 0.005 \pm 0.008 \,{}^{+0.012}_{-0.015} & \alpha_{\mathrm{iso}} = 15° \\ 0.217 \pm 0.005 \pm 0.008 \,{}^{+0.016}_{-0.014} & \alpha_{\mathrm{iso}} = 20° \\ 0.217 \pm 0.005 \pm 0.008 \,{}^{+0.020}_{-0.017} & \alpha_{\mathrm{iso}} = 25° \end{cases},$$

where the errors are statistical and systematic experimental uncertainties and theo-

Isolation Cut:	10°	15°	20°	25°
		Central-value fit		
$\mathcal{C}^{(\mathrm{FIT})}_{\mathrm{q\bar{q}}\gamma}$	0.249	0.222	0.217	0.217
$\delta\mathcal{C}^{(\mathrm{FIT})}_{\mathrm{q\bar{q}}\gamma}$	±0.005	±0.005	±0.005	±0.005
χ^2_{min}/DF	34.6/8	28.3/8	14.8/8	13.7/8
		Systematic error fits		
$R_i \to R_i^+$	+0.007	+0.008	+0.008	+0.007
$R_i \to R_i^-$	−0.006	−0.007	−0.008	−0.007
$p_\gamma > 0.45$	−0.011	+0.002	+0.004	+0.003
no p_γ cut	+0.010	−0.002	−0.003	−0.005
$\alpha_S \to \alpha_S^{max}$	+0.006	+0.005	+0.006	+0.006
$\alpha_S \to \alpha_S^{min}$	−0.024	−0.015	−0.008	−0.006
$H_i \to H_i - \Delta H_i$	+0.007	+0.012	+0.016	+0.020
$H_i \to H_i + \Delta H_i$	−0.006	−0.011	−0.014	−0.017
		Standard Model predictions		
$\mathcal{C}^{(\mathrm{SM})}_{\mathrm{q\bar{q}}\gamma}$	0.219	0.220	0.221	0.222

Table 8.4: Results of one-parameter fits to the energy distributions of isolated FSR with different isolation cuts. The first section of the table gives the fitted values, statistical errors, and minimum chi-squares that I obtain with my central-value fit. The next section gives the systematic shifts in the fitted values that occur when changing the experimental or theoretical input to the fit. The final section repeats the Standard Model values that I calculated in Section 8.1.2.

retical uncertainties, respectively.

In order to determine the quark couplings, I would like to use a single value of $\mathcal{C}_{\mathrm{q\bar{q}}\gamma}$ that represents my best estimate based on the results of my one-parameter fits. The results that I obtain using different isolation cuts are in good agreement with each other, within the errors that I assign; however, since the measured distributions with different isolation cuts are strongly correlated, so are the fit results. Therefore, there is little advantage to combining the results that I obtain with different isolation cuts, and so instead, I choose the results for a single isolation cut. The factors that I consider in making this choice are the minimum chi-square values and theoretical uncertainties for different isolation cuts. I define my chi-square using statistical errors only, so its minimum value measures the goodness of fit within statistical uncertainties. The minimum values that I obtain are considerably larger for $\alpha_{\rm iso} = 10°$ and $15°$ than for $\alpha_{\rm iso} = 20°$ and $25°$. This trend indicates that systematic effects are more important for smaller isolation cuts, and so, based on the minimum chi-square values, I prefer to use $\alpha_{\rm iso} = 20°$ or $25°$. Of these two, I choose $\alpha_{\rm iso} = 20°$ because it has the smaller theoretical uncertainty. My best estimate of $\mathcal{C}_{\rm q\bar{q}\gamma}$ is therefore

$$\mathcal{C}_{\rm q\bar{q}\gamma} = 0.217 \pm 0.005 \pm 0.008 \pm 0.015 \; ,$$

where the errors are statistical and systematic experimental uncertainties and theoretical uncertainties, respectively, and I use a symmetric error to describe the average theoretical uncertainty.

8.3 Determination of Quark Coupling Constants

In the previous sections, I have determined the values of two constraints, $\mathcal{C}_{\rm q\bar{q}}$ and $\mathcal{C}_{\rm q\bar{q}\gamma}$, on the quark couplings to the Z boson and the photon. In this section, I describe how I combine these constraints under different assumptions in order to determine the values of these couplings.

In Section 8.1.2, I derived the value

$$\mathcal{C}_{\rm q\bar{q}} = 6.886 \pm 0.020$$

from the L3 lineshape-fit parameters. This result constrains the quark-Z couplings, $\bar{c}_{\rm u}$ and $\bar{c}_{\rm d}$, according to

$$\mathcal{C}_{\rm q\bar{q}} = \mathcal{N}_{\rm u} \cdot \bar{c}_{\rm u} + \mathcal{N}_{\rm d} \cdot \bar{c}_{\rm d} \; .$$

The coefficients $\mathcal{N}_{\rm u} = 2$ and $\mathcal{N}_{\rm d} = 3 - \Delta\rho_{\rm b}$ count the number of up- and down-type quarks that are kinematically accessible at $\sqrt{s} \simeq 91$ GeV ($\Delta\rho_{\rm b} \simeq 1.3\%$ incorporates top-quark corrections to $\rm b\bar{b}$ production).

In Section 8.2.2.2, I measured the value (with errors combined in quadrature)

$$\mathcal{C}_{\mathrm{q\bar{q}}\gamma} = 0.217 \pm 0.018 \; ,$$

by fitting my measured FSR energy distribution with $\alpha_{\mathrm{iso}} = 20°$ to my theoretical prediction for this distribution. This result constrains the quark couplings to the Z boson, $\bar{c}_{\mathrm{u}}$ and $\bar{c}_{\mathrm{d}}$, and the photon, ${Q_{\mathrm{u}}}^2$ and ${Q_{\mathrm{d}}}^2$, according to

$$\mathcal{C}_{\mathrm{q\bar{q}}\gamma} = \frac{\mathcal{F}_{\mathrm{u}} \cdot \bar{c}_{\mathrm{u}} \cdot {Q_{\mathrm{u}}}^2 + \mathcal{F}_{\mathrm{d}} \cdot \bar{c}_{\mathrm{d}} \cdot {Q_{\mathrm{d}}}^2}{\mathcal{N}_{\mathrm{u}} \cdot \bar{c}_{\mathrm{u}} + \mathcal{N}_{\mathrm{d}} \cdot \bar{c}_{\mathrm{d}}} \; .$$

The coefficients $\mathcal{F}_{\mathrm{u}}$ and $\mathcal{F}_{\mathrm{d}}$ are similar to $\mathcal{N}_{\mathrm{u}}$ and $\mathcal{N}_{\mathrm{d}}$, but include the additional suppression factors for c and b quarks that I calculated in Section 7.2.1.3. They are given by

$$\mathcal{F}_{\mathrm{u}} = 2 - m_c^2 \langle M \rangle \quad \text{and} \quad \mathcal{F}_{\mathrm{d}} = 3 - \Delta\rho_{\mathrm{b}} - m_c^2 \langle M \rangle \; .$$

The two constraints, $\mathcal{C}_{\mathrm{q\bar{q}}}$ and $\mathcal{C}_{\mathrm{q\bar{q}}\gamma}$, are functions of four parameters: $\bar{c}_{\mathrm{u}}$, $\bar{c}_{\mathrm{d}}$, ${Q_{\mathrm{u}}}^2$, and ${Q_{\mathrm{d}}}^2$. Therefore, it is not possible to simultaneously solve for all of these parameters. Instead, I make two alternative sets of assumptions in order to first, solve for $\bar{c}_{\mathrm{u}}$ and $\bar{c}_{\mathrm{d}}$, and then, solve for ${Q_{\mathrm{u}}}^2$ and ${Q_{\mathrm{d}}}^2$.

8.3.1 Quark Couplings to the Z Boson

In order to determine the quark couplings, $\bar{c}_{\mathrm{u}}$ and $\bar{c}_{\mathrm{d}}$, I assume the Standard Model quark charges,

$$Q_{\mathrm{u}} = +2/3 \quad \text{and} \quad Q_{\mathrm{d}} = -1/3 \; ,$$

but I do not make any assumptions about the relationship between $\bar{c}_{\mathrm{u}}$ and $\bar{c}_{\mathrm{d}}$ and the parameters $\sin^2\overline{\theta}_W$ and ρ_{eff}. I express the constraints on $\bar{c}_{\mathrm{u}}$ and $\bar{c}_{\mathrm{d}}$ that I use as

$$\Delta_{\mathrm{q\bar{q}}}(\bar{c}_{\mathrm{u}}, \bar{c}_{\mathrm{d}}) = 0 \quad \text{and} \quad \Delta_{\mathrm{q\bar{q}}\gamma}(\bar{c}_{\mathrm{u}}, \bar{c}_{\mathrm{d}}) = 0 \; ,$$

where I define

$$\Delta_{\mathrm{q\bar{q}}}(\bar{c}_{\mathrm{u}}, \bar{c}_{\mathrm{d}}) \equiv \mathcal{N}_{\mathrm{u}} \cdot \bar{c}_{\mathrm{u}} + \mathcal{N}_{\mathrm{d}} \cdot \bar{c}_{\mathrm{d}} - \mathcal{C}_{\mathrm{q\bar{q}}} \; ,$$

and

$$\Delta_{q\bar{q}\gamma}(\bar{c}_u, \bar{c}_d) \equiv \left(\mathcal{F}_u \mathcal{Q}_u{}^2 - \mathcal{C}_{q\bar{q}\gamma}\mathcal{N}_u\right) \cdot \bar{c}_u + \left(\mathcal{F}_d \mathcal{Q}_d{}^2 - \mathcal{C}_{q\bar{q}\gamma}\mathcal{N}_d\right) \cdot \bar{c}_d \, .$$

In Figure 8.7, I show the 68% confidence-level contours in $\bar{c}_u$ and $\bar{c}_d$ that correspond to each of these constraints.

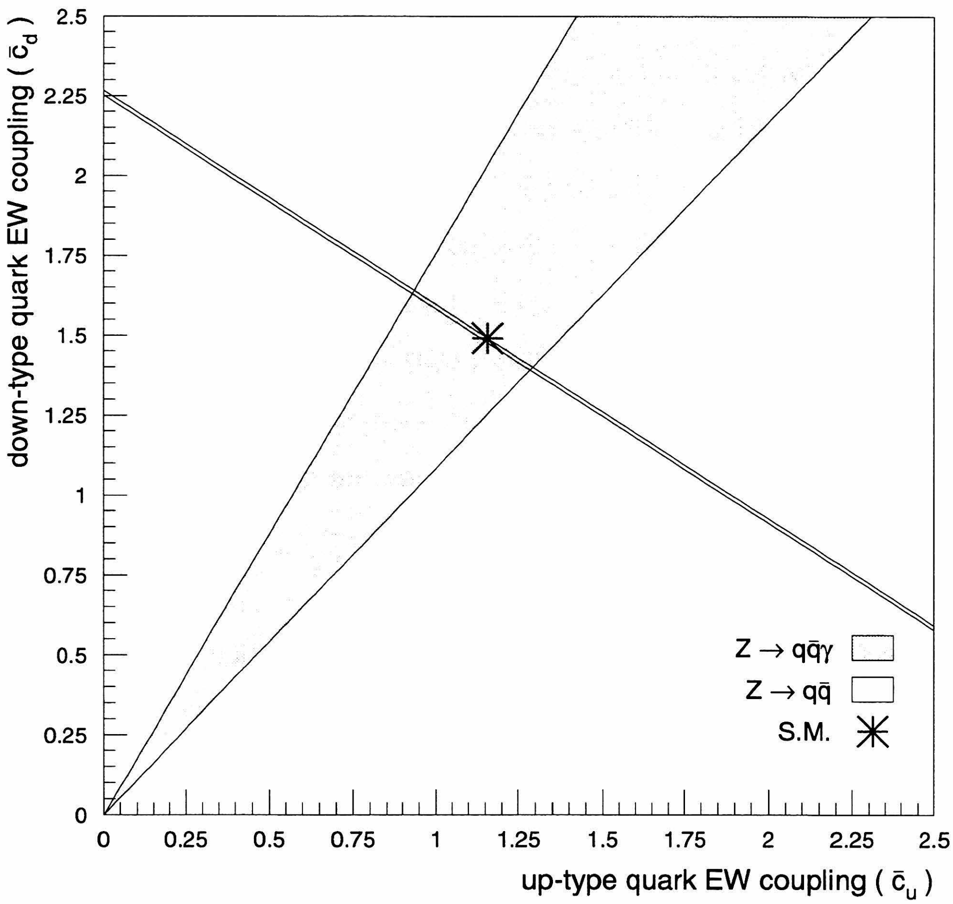

Figure 8.7: Constraints on the effective couplings of up- and down-type quarks to the Z boson, $\bar{c}_u$ and $\bar{c}_d$, obtained from the relative rate of isolated and energetic FSR in hadronic Z decays (shaded region), and from lineshape fits (outlined region). The values of $\bar{c}_u$ and $\bar{c}_d$ determined in the framework of the Standard Model are shown as an asterisk.

By solving the simultaneous linear equations for $\bar{c}_u$ and $\bar{c}_d$, above, I obtain

$$\bar{c}_u = \frac{\mathcal{C}_{q\bar{q}}\left(\mathcal{F}_d \mathcal{Q}_d{}^2 - \mathcal{N}_d \mathcal{C}_{q\bar{q}\gamma}\right)}{\mathcal{N}_u \mathcal{F}_d \mathcal{Q}_d{}^2 - \mathcal{N}_d \mathcal{F}_u \mathcal{Q}_u{}^2} \quad \text{and} \quad \bar{c}_d = \frac{\mathcal{C}_{q\bar{q}}\left(\mathcal{F}_u \mathcal{Q}_u{}^2 - \mathcal{N}_u \mathcal{C}_{q\bar{q}\gamma}\right)}{\mathcal{N}_d \mathcal{F}_u \mathcal{Q}_u{}^2 - \mathcal{N}_u \mathcal{F}_d \mathcal{Q}_d{}^2} \, .$$

Substituting the values of $\mathcal{C}_{q\bar{q}}$ and $\mathcal{C}_{q\bar{q}\gamma}$ into these expressions, I calculate $\bar{c}_u = 1.1095$ and $\bar{c}_d = 1.5158$. In order to estimate the uncertainties in the couplings, I define a combined chi-square for the simultaneous constraints

$$\chi^2(\bar{c}_u, \bar{c}_d) \equiv \left[\frac{\Delta_{q\bar{q}}(\bar{c}_u, \bar{c}_d)}{\delta\Delta_{q\bar{q}}}\right]^2 + \left[\frac{\Delta_{q\bar{q}\gamma}(\bar{c}_u, \bar{c}_d)}{\delta\Delta_{q\bar{q}\gamma}}\right]^2 ,$$

where $\delta\Delta_{q\bar{q}}$ and $\delta\Delta_{q\bar{q}\gamma}$ are the errors on the individual constraints that I derive from the errors on $\mathcal{C}_{q\bar{q}}$ and $\mathcal{C}_{q\bar{q}\gamma}$. Figure 8.8 shows the 68% and 90% two-parameter error regions that I calculate using contours of $\chi^2(\bar{c}_u, \bar{c}_d) = \Delta\chi^2$ (χ^2_{min} is equal to zero since the constraints can be solved exactly). I set $\Delta\chi^2$ equal to 2.28 and 4.61 for the 68% and 90% confidence-level contours, respectively. I define the one-parameter error bounds on $\bar{c}_u$ ($\bar{c}_d$) by locating the the minimum and maximum values of $\bar{c}_u$ ($\bar{c}_d$) on the $\chi^2 = 1$ contour[73]. I find that these errors are, to a good approximation, symmetric.

Finally, I determine the up- and down-type quark couplings to the Z boson to be

$$\boxed{\bar{c}_u = 1.11 \pm 0.17 \quad \text{and} \quad \bar{c}_d = 1.52 \pm 0.11 \ .}$$

This is one of the main results of this thesis. These values are consistent with the Standard Model values that I calculated above

$$\bar{c}_u^{(SM)} = 1.1574 \pm 0.0039 \quad \text{and} \quad \bar{c}_d^{(SM)} = 1.4911 \pm 0.0044 \ .$$

8.3.2 Quark Couplings to the Photon

In order to determine the quark couplings to the photon, Q_u^2 and Q_d^2, I assume that their couplings to the Z boson, $\bar{c}_u$ and $\bar{c}_d$, are given by

$$\bar{c}_q = \rho_{\text{eff}} \left[1 + \left(1 - 4|Q_q| \sin^2\bar{\theta}_W\right)^2\right] ,$$

using the Standard Model values of $\sin^2\bar{\theta}_W$ and ρ_{eff} that I calculated above. I express the constraints on Q_u and Q_d that I use as

$$\Delta_{q\bar{q}}(Q_u, Q_d) = 0 \quad \text{and} \quad \Delta_{q\bar{q}\gamma}(Q_u, Q_d) = 0 \ ,$$

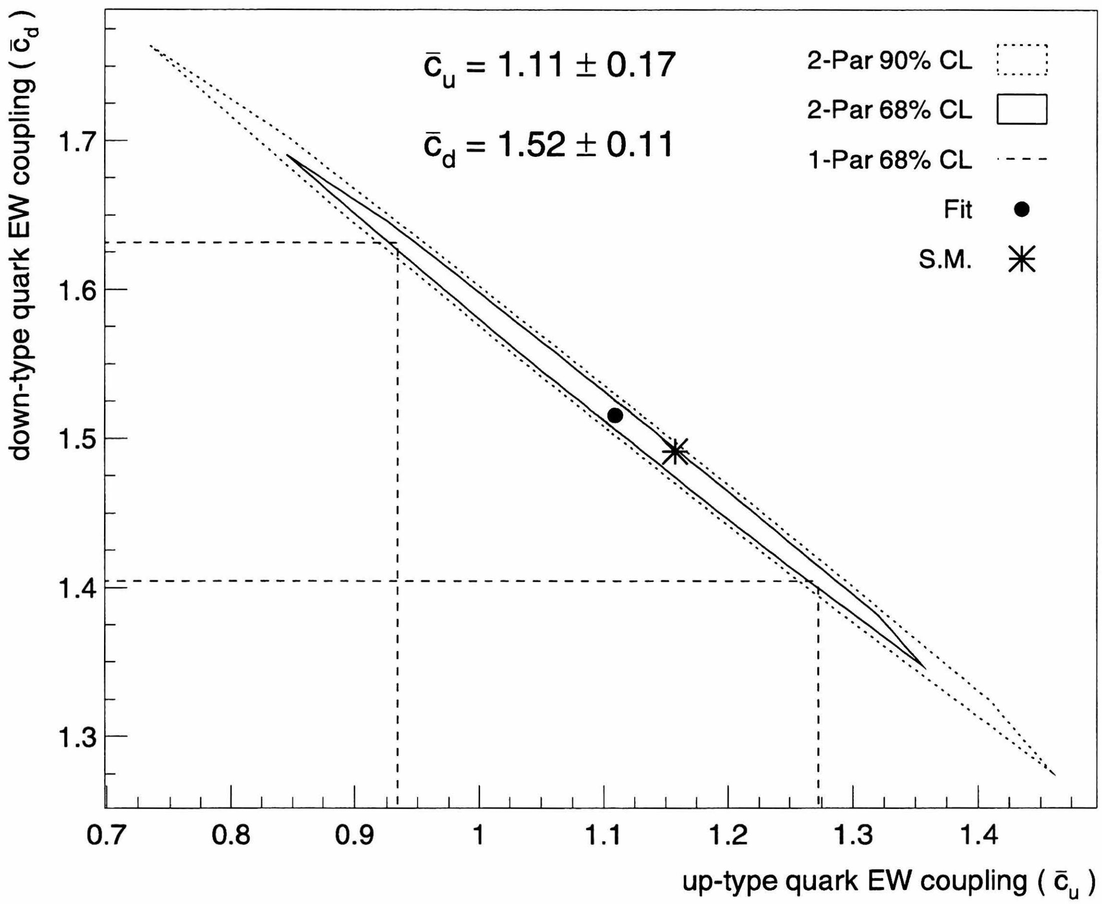

Figure 8.8: One- and two-parameter error regions in $\bar{c}_u$ and $\bar{c}_d$. The two-parameter regions are defined as the areas contained within contours of constant chi-square, $\chi^2(\bar{c}_u, \bar{c}_d) = \Delta\chi^2$, with $\Delta\chi^2 = 2.28$ (4.61) for the 68% (90%) confidence-level errors. The one-parameter errors are defined by the bounding box of the $\chi^2 = 1$ contour. The fitted values of $\bar{c}_u$ and $\bar{c}_d$ are shown with a filled circle, and their Standard Model values are shown with an asterisk.

where I define

$$\Delta_{q\bar{q}}(Q_u, Q_d) \equiv \mathcal{N}_u \left(|Q_u| - \frac{1}{4\sin^2\overline{\theta}_W} \right)^2 + \mathcal{N}_d \left(|Q_d| - \frac{1}{4\sin^2\overline{\theta}_W} \right)^2 - \frac{\mathcal{C}_{q\bar{q}} - (\mathcal{N}_u + \mathcal{N}_d)\rho_{\text{eff}}}{16\sin^4\overline{\theta}_W \rho_{\text{eff}}} ,$$

and

$$\Delta_{q\bar{q}\gamma}(Q_u, Q_d) \equiv \left(\mathcal{F}_u {Q_u}^2 - \mathcal{C}_{q\bar{q}\gamma}\mathcal{N}_u\right) \cdot \left[1 - 4|Q_u|\sin^2\overline{\theta}_W + 8{Q_u}^2\sin^4\overline{\theta}_W\right] + \left(\mathcal{F}_d {Q_d}^2 - \mathcal{C}_{q\bar{q}\gamma}\mathcal{N}_d\right) \cdot \left[1 - 4|Q_d|\sin^2\overline{\theta}_W + 8{Q_d}^2\sin^4\overline{\theta}_W\right] .$$

These constraints do not depend on the signs of the quark charges, and so by combining them, I am only able to determine their magnitudes, $|Q_u|$ and $|Q_d|$. In Figure 8.9, I show the 68% confidence-level contours in $3|Q_u|$ and $3|Q_d|$ that correspond to each of the constraints. I express my results in terms of three times the charge magnitudes so that the corresponding Standard Model values are integers: $3|Q_u| = 2$ and $3|Q_d| = 1$.

By solving the simultaneous non-linear equations for the quark charges, above, I obtain two solutions:

$$3|Q_u| = 1.8971 \quad \text{and} \quad 3|Q_d| = 1.0579 ,$$

or

$$3|Q_u| = 0.8566 \quad \text{and} \quad 3|Q_d| = 1.7684 .$$

The second of these solutions is not compatible with the results of Reference [101] (see Section 9.2.3) so I do not consider it further. In order to estimate the uncertainties in values that I obtain from the first solution, I define a combined chi-square for the simultaneous constraints

$$\chi^2(Q_u, Q_d) \equiv \frac{1}{1-\kappa} \left\{ \chi^2_{q\bar{q}}(Q_u, Q_d) + \chi^2_{q\bar{q}\gamma}(Q_u, Q_d) - 2\kappa\sqrt{\chi^2_{q\bar{q}}(Q_u, Q_d)\chi^2_{q\bar{q}\gamma}(Q_u, Q_d)} \right\} ,$$

where $\chi^2_{\mathrm{q\bar{q}}}(Q_{\mathrm{u}}, Q_{\mathrm{d}})$ and $\chi^2_{\mathrm{q\bar{q}}\gamma}(Q_{\mathrm{u}}, Q_{\mathrm{d}})$ are the chi-squares of the individual constraints,

$$\chi^2_{\mathrm{q\bar{q}}}(Q_{\mathrm{u}}, Q_{\mathrm{d}}) \equiv \left[\frac{\Delta_{\mathrm{q\bar{q}}}(Q_{\mathrm{u}}, Q_{\mathrm{d}})}{\delta\Delta_{\mathrm{q\bar{q}}}}\right]^2 \quad \text{and} \quad \chi^2_{\mathrm{q\bar{q}}\gamma}(Q_{\mathrm{u}}, Q_{\mathrm{d}}) \equiv \left[\frac{\Delta_{\mathrm{q\bar{q}}\gamma}(Q_{\mathrm{u}}, Q_{\mathrm{d}})}{\delta\Delta_{\mathrm{q\bar{q}}\gamma}}\right]^2$$

and $\kappa \simeq 0.25\%$ is the correlation coefficient between the values of $\Delta_{\mathrm{q\bar{q}}}$ and $\Delta_{\mathrm{q\bar{q}}\gamma}$ that I derive from the values given in Table 8.2. I calculate two-parameter error regions and one-parameter asymmetric errors using the same methods that I described in Section 8.3.1.

Finally, I determine the up- and down-type quark couplings to the photon to be

$$\boxed{3|Q_{\mathrm{u}}| = 1.90\ ^{+0.25}_{-0.46} \quad \text{and} \quad 3|Q_{\mathrm{d}}| = 1.06\ ^{+0.26}_{-0.11}\ .}$$

This is one of the main results of this thesis. These values are consistent with the Standard Model values

$$3|Q_{\mathrm{u}}| = 2 \quad \text{and} \quad 3|Q_{\mathrm{d}}| = 1\ .$$

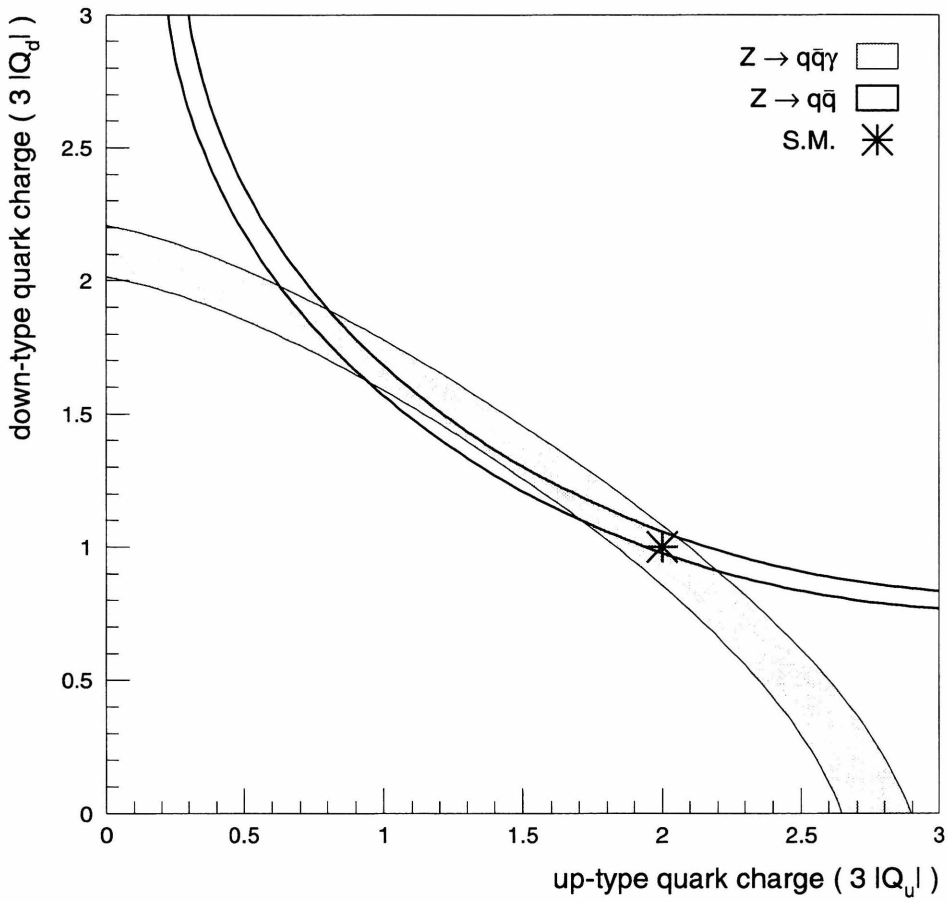

Figure 8.9: Constraints on three times the magnitude of the charges of up- and down-type quarks, $3|Q_{\mathrm{u}}|$ and $3|Q_{\mathrm{d}}|$, obtained from the relative rate of isolated and energetic FSR in hadronic Z decays (shaded region), and from lineshape fits (outlined region). The Standard Model values of $3|Q_{\mathrm{u}}|$ and $3|Q_{\mathrm{d}}|$ are shown as an asterisk.

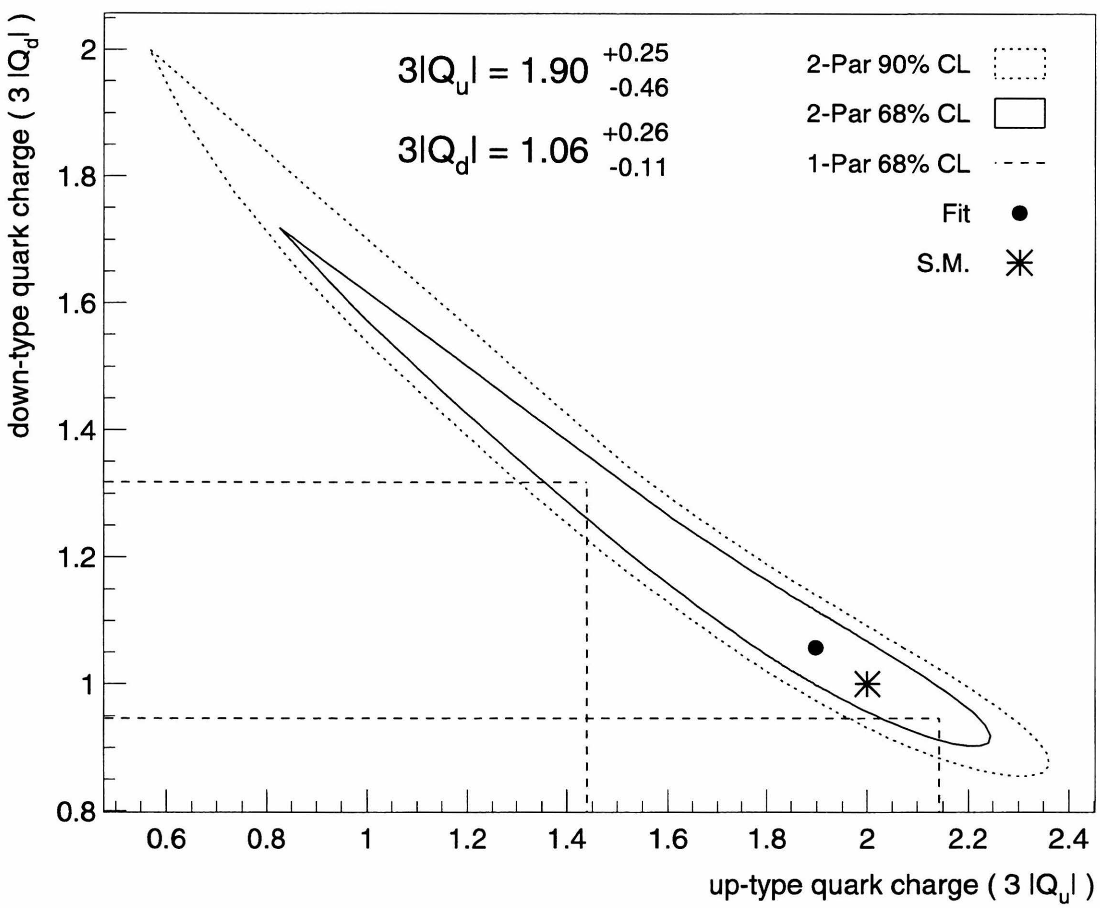

Figure 8.10: One- and two-parameter error regions in $3|Q_u|$ and $3|Q_d|$. The two-parameter regions are defined as the areas contained within contours of constant chi-square, $\chi^2(\bar{c}_u, \bar{c}_d) = \Delta\chi^2$, with $\Delta\chi^2 = 2.28$ (4.61) for the 68% (90%) confidence-level errors. The one-parameter errors are defined by the bounding box of the $\chi^2 = 1$ contour. The fitted values of $3|Q_u|$ and $3|Q_d|$ are shown with a filled circle, and their Standard Model values are shown with an asterisk.

Chapter 9

Summary and Conclusions

In this chapter, I briefly summarize the main results of this thesis and compare them with results from other experiments. I conclude with an outlook on the future potential of isolated hard photon studies.

9.1 Summary of Results

In Chapter 5, I described a selection of events containing isolated and energetic photon candidates using data recorded between 1991 and 1994 by the L3 detector. In Chapter 6, I analyzed these candidates to measure the energy distribution of photons radiated by a primary quark, $Z \to q\bar{q}\gamma$. I found that the main irreducible background is from decays of neutral hadrons (mostly $\pi^0 \to \gamma\gamma$) and that this background is not correctly described by Monte Carlo models. I developed a new method of analyzing electromagnetic shower shapes to study this background directly using data (see Appendix A).

I measured the total rate of isolated final-state radiation (FSR) with energy between 8 GeV and 44 GeV to be

$$\frac{\mathrm{BR}(\mathrm{Z} \to \mathrm{q}\bar{\mathrm{q}}\gamma)}{\mathrm{BR}(\mathrm{Z} \to \mathrm{q}\bar{\mathrm{q}})} = \begin{cases} 5.02 \pm 0.10(\mathrm{stat}) \pm 0.22(\mathrm{syst}) \times 10^{-3} & \alpha_{\mathrm{iso}} = 10^\circ \\ 3.56 \pm 0.08(\mathrm{stat}) \pm 0.15(\mathrm{syst}) \times 10^{-3} & \alpha_{\mathrm{iso}} = 15^\circ \\ 2.85 \pm 0.07(\mathrm{stat}) \pm 0.12(\mathrm{syst}) \times 10^{-3} & \alpha_{\mathrm{iso}} = 20^\circ \\ 2.36 \pm 0.06(\mathrm{stat}) \pm 0.10(\mathrm{syst}) \times 10^{-3} & \alpha_{\mathrm{iso}} = 25^\circ \end{cases},$$

where I define isolation by requiring that the total hadronic energy within a cone of half-angle α_{iso} about the photon direction be less than 100 MeV.

In Chapter 7, I described how I calculate the energy distributions corresponding to those that I measure. In Chapter 8, I compared my experimental results with my theoretical predictions. I found good agreement between them using the Standard Model quark couplings. I performed fits of my prediction to my measured distributions, in order to constrain the values of the quark couplings without assuming the framework of the Standard Model. I combined this constraint with a second constraint that I derived from the Z lineshape in order to solve for the quark couplings.

By assuming the Standard Model quark charges, I determined the values of the quark couplings to the Z boson to be

$$\overline{c}_{\text{u}} = 1.11 \pm 0.17 \quad \text{and} \quad \overline{c}_{\text{d}} = 1.52 \pm 0.11\ .$$

By assuming the Standard Model relationship between the couplings, $\overline{c}_{\text{u}}$ and $\overline{c}_{\text{d}}$, and the electroweak parameters, $\sin^2\overline{\theta}_W$ and ρ_{eff}, I determined the absolute values of the quark charges to be

$$3|Q_{\text{u}}| = 1.90\ ^{+0.25}_{-0.46} \quad \text{and} \quad 3|Q_{\text{d}}| = 1.06\ ^{+0.26}_{-0.11}\ .$$

These results are consistent with the Standard Model.

9.2 Comparison with Other Results

9.2.1 Studies of Final-State Radiation at LEP

The four experiments operating at the LEP accelerator — ALEPH, DELPHI, L3, and OPAL — have all studied isolated FSR and published descriptions of their work. Below, I briefly describe the most recent results of each experiment and compare them with my results. I express errors as combined statistical and systematic experimental uncertainties, respectively. When the quoted errors do not follow this convention, I have calculated them myself based on the information provided in the references. Each of the four experiments uses some form of shower-shape analysis in their studies; however, these methods depend on the details of the different detectors, so I do not discuss them below. In Table 9.1, I summarize the selection cuts and results of the most recent LEP analyses, and compare them with those of this thesis.

	ALEPH	DELPHI	L3	OPAL	Thesis
		Event Sample Analyzed			
Years	1989 – 91	1991 – 93	1990 – 91	1990 – 91	1991 – 94
Hadr Evts	448K	1484K	324K	353K	2760K
		Photon Candidate Selection Cuts			
Energy (E_γ)	> 5 GeV	> 5.5 GeV	> 5 GeV	> 7.5 GeV	> 8 GeV
Fid Vol (θ_γ)	> 18°	> 25°	> 45°	> 44°	> 17.5°
Isol Cone (α_{iso})	20°	20°	15°	15°	20°
Isol Energy (E_{iso})	500 MeV	500 MeV	500 MeV	250 MeV	40 MeV
Jet Isolation	$\alpha_j > 40°$ $y_{\gamma,j} > 0.06$	$y_{\gamma,j} > 0.02$	$\alpha_j > 20°$	$y_{\gamma,j} > 0.06$	—
		Selection Statistics			
Photon Cand	569	3147	3202	541	5224
Cand/10^3 Had Evt	1.3	2.1	9.9	1.5	1.9
		Hadronic Background			
Fraction	11%	17%	33%	6%	8%
DATA/MC	1.5 – 2.5	0.8 – 1.6	1.9	—	1.0 – 2.2
		Errors on Corrected Total Rate			
Statistical	4.9%	3.7%	5.8%	4.9%	2.3%
Systematic	5.9%	6.7%	7.7%	6.8%	4.3%
Combined	7.7%	7.7%	9.6%	8.4%	4.9%

Table 9.1: Summary of the photon candidate event selections and the most recent FSR results of the four LEP experiments, compared with those of this thesis. The information listed under L3 describes our original study. The results listed under OPAL do not include their analysis of 1992 data[102] since they do not quote an FSR rate using this data.

ALEPH[36] have analyzed 448K hadronic Z decays collected between 1989 and 1991[103, 104]. They select photon candidates with energies larger than 5 GeV and polar angles between 18.2° and 161.8°. They also require that candidates have a transverse energy, $E_\gamma \cdot \sin\theta_\gamma$, that is larger than 5 GeV. They use an isolation scheme similar to that which I described in Section 5.2.3, with $\alpha_{\rm iso} = 20°$ and $E_{\rm iso} = 500$ MeV. In addition, they require that the candidate be isolated from the reconstructed jets in the event (the photon is not included in the reconstruction). The angle between each jet and the candidate, α_j, must be larger than 40° and the scaled invariant mass of each jet together with the candidate, $y_{\gamma,j} \equiv m^2_{\gamma,j}/s$, must be larger than some value y_{cut} which they vary between 0.005 and 0.2. ALEPH select 569 photon candidates with $y_{cut} = 0.06$, and estimate that 6% of these are due to hadronic background. They find that the Monte Carlo prediction of this hadronic background underestimates the actual rate by a factor of 2.5 (1.5) for energies between 5 GeV and 10 GeV (10 GeV and 15 GeV). After applying acceptance and detector corrections, ALEPH measure the rate of isolated FSR using their cuts to be[104]

$$\frac{\mathrm{BR}(\mathrm{Z} \rightarrow \mathrm{q\bar{q}}\gamma)}{\mathrm{BR}(\mathrm{Z} \rightarrow \mathrm{q\bar{q}})} = 1.56 \pm 0.08(\mathrm{stat}) \pm 0.09(\mathrm{syst}) \times 10^{-3} \; .$$

ALEPH have not quoted results on the quark couplings.

The DELPHI[37] collaboration have analyzed 1484K hadronic Z decays collected between 1991 and 1993[105, 106]. They select photon candidates with energies larger than 5.5 GeV and within the fiducial volume, $25° < \theta_\gamma < 155°$. They require that the total hadronic energy within a 20° cone about the candidate be less than 500 MeV. DELPHI select 3147 candidates and estimate that 17% of these are due to hadronic background. They also apply a jet isolation requirement, similar to that used by ALEPH, of $y_{\gamma,j} > y_{cut}$ with y_{cut} between 0.01 and 0.2. They find that the Monte Carlo predictions of this background underestimate the actual rate by a factor that varies from 1.6 at 5.5 GeV to 0.75 at 45.5 GeV. After applying acceptance and detector corrections, DELPHI determine a constraint on the quark couplings that is proportional to the rate of isolated FSR that they measure using $y_{cut} = 0.02$[106]

$$8c_{\rm u} + 3c_{\rm d} = 11.71 \pm 0.43(\mathrm{stat}) \pm 0.78(\mathrm{syst}) \pm 0.56(\mathrm{theor}) \; .$$

They combine this constraint with a lineshape constraint, obtaining[106]

$$c_{\mathrm{u}} = 0.91 \,{}^{+0.25}_{-0.36} \quad \text{and} \quad c_{\mathrm{d}} = 1.62 \,{}^{+0.24}_{-0.17} \,.$$

In the first L3 study of FSR, we analyzed 320K hadronic Z decays collected between 1990 and 1991[86, 107]. (I was involved in this earlier analysis, particularly the original determination of the quark couplings[86], but I do not describe it in this thesis.) We selected photon candidates with energies larger than 5 GeV and within the fiducial volume, $45° < \theta_\gamma < 135°$. We required that the hadronic energy within a 15° cone about the candidate be less than 500 MeV and that candidates be isolated from the nearest jet by $\alpha_j > 20°$. We selected 3202 candidates and estimated that 33% of these were from hadronic background. We found that Monte Carlo predictions underestimate this background by a factor of 1.9. After applying acceptance and detector corrections, we determined the rate of isolated FSR using our cuts to be[107]

$$\frac{\mathrm{BR}(\mathrm{Z} \to \mathrm{q\bar{q}}\gamma)}{\mathrm{BR}(\mathrm{Z} \to \mathrm{q\bar{q}})} = 5.2 \pm 0.3(\mathrm{stat}) \pm 0.4(\mathrm{syst}) \times 10^{-3} \,.$$

We also determined the quark couplings to the Z boson to be[86]

$$\bar{c}_{\mathrm{u}} = 0.92 \pm 0.22 \quad \text{and} \quad \bar{c}_{\mathrm{d}} = 1.63 \pm 0.15 \,.$$

OPAL[39] have analyzed 353K hadronic Z decays collected between 1990 and 1991[80, 81, 108, 109]. In Reference [102], they extend this analysis to include data collected in 1992; however, the results that they give there are in terms of normalized distributions and so do not contain information about the rate of isolated FSR or the quark couplings. OPAL select photon candidates with energies larger than 8 GeV and polar angles between 44° and 136°. They require that a 15° cone about the candidate contain no electromagnetic cluster with energy greater than 250 MeV or track with transverse momentum greater than 250 MeV. They also require isolation from jets by $y_{\gamma,j} > y_{cut}$ with y_{cut} between 0.005 and 0.2. They select 541 candidates from the data they collected between 1990 and 1991 and estimate that 6% of these are due to hadronic background. After applying acceptance and detector corrections, OPAL determine a constraint on the quark couplings that is proportional to the rate of isolated FSR that they measure using $y_{cut} = 0.06$[109]

$$8c_{\mathrm{u}} + 3c_{\mathrm{d}} = 12.36 \pm 0.61(\mathrm{stat}) \pm 0.84(\mathrm{syst}) \pm 0.29(\mathrm{theor}) \; .$$

They combine this constraint with a lineshape constraint, obtaining[109]

$$c_{\mathrm{u}} = 0.94 \pm 0.18 \quad \text{and} \quad c_{\mathrm{d}} = 1.62 \pm 0.12 \; .$$

The main differences between the event selections used by earlier studies and the selection that I described in Chapter 5 are in the choice of the photon candidate isolation scheme. In particular, I have chosen a value of the maximum calorimeter energy allowed within the isolation cone, $E_{\mathrm{iso}} = 40$ MeV, that is lower than was used in previous studies, and I do not require isolation with respect to jets. The reason that I use a lower value of E_{iso} is that such a low value can be reliably measured using the L3 electromagnetic calorimeter and significantly reduces the hadronic background. In our original study, we chose a larger value, $E_{\mathrm{iso}} = 500$ MeV, because the L3 detector simulation did not correctly simulate the calorimeter response to low-energy secondary particles in hadron showers. This simulation problem has now been corrected. After applying my tighter isolation cut, using $E_{\mathrm{iso}} = 40$ MeV, I find that an additional cut on the angle to the nearest jet does not improve the purity of my sample. For this reason, and also because jet isolation would require more complicated theoretical calculations, I do not require that my photon candidates be isolated with respect to jets.

The measurements of the rate of isolated FSR obtained by different experiments and in this thesis cannot be directly compared since they reflect different choices of energy and isolation cuts. However, the relative errors on these measurements can be compared (see the bottom of Table 9.1). Both the statistical and systematic experimental errors of my measurement are smaller than those of previous measurements.

My statistical error is smaller because I have analyzed a larger sample of hadronic Z decays. It is difficult to make direct comparisons of the systematic errors reported by different experiments. However, the improvement in the systematic error that I obtain compared with the original L3 analysis (4.3% instead of 7.7%) is mostly due to the new method of shower-shape analysis that I have developed (see Appendix A). In Figure 9.1, I show a comparison of the different measurements of $\bar{c}_{\mathrm{u}}$ and $\bar{c}_{\mathrm{d}}$ reported by DELPHI[106], L3[86], and OPAL[109] with the results that I obtain in this thesis. The errors on these couplings include large theoretical uncertainties in addition to the experimental uncertainties on the measured FSR rate. The previous measurements of $\bar{c}_{\mathrm{u}}$ and $\bar{c}_{\mathrm{d}}$ are individually consistent with the Standard Model. However, there is some evidence that they have a common systematic offset that is not present in my results. None of the previous studies of final-state radiation at LEP have determined the values of the quark charges.

9.2.2 Measurement of the $\mathrm{b\bar{b}}$ Partial Width

L3 have measured[110] the ratio, R_{b}, of the partial decay widths of a Z into b hadrons, $\Gamma(\mathrm{Z} \to \mathrm{b\bar{b}})$, and into all hadrons, $\Gamma(\mathrm{Z} \to \mathrm{q\bar{q}})$,

$$R_{\mathrm{b}} \equiv \frac{\Gamma(\mathrm{Z} \to \mathrm{b\bar{b}})}{\Gamma(\mathrm{Z} \to \mathrm{q\bar{q}})} .$$

We select $\mathrm{b\bar{b}}$ events using a multidimensional analysis that relies on the general properties of these events and therefore does not require a high-momentum lepton tag. We have analyzed 238K events recorded during 1991, and obtain[110]

$$R_{\mathrm{b}} = 0.222 \pm 0.003(\mathrm{stat}) \pm 0.007(\mathrm{syst}) .$$

The value of R_{b} can be expressed in terms of the quark couplings to the Z boson, using my notation of Section 7.1, as

$$R_{\mathrm{b}} = \frac{(1 - \Delta\rho_{\mathrm{b}}) \cdot \bar{c}_{\mathrm{d}}}{2 \cdot \bar{c}_{\mathrm{u}} + (3 - \Delta\rho_{\mathrm{b}}) \cdot \bar{c}_{\mathrm{d}}} .$$

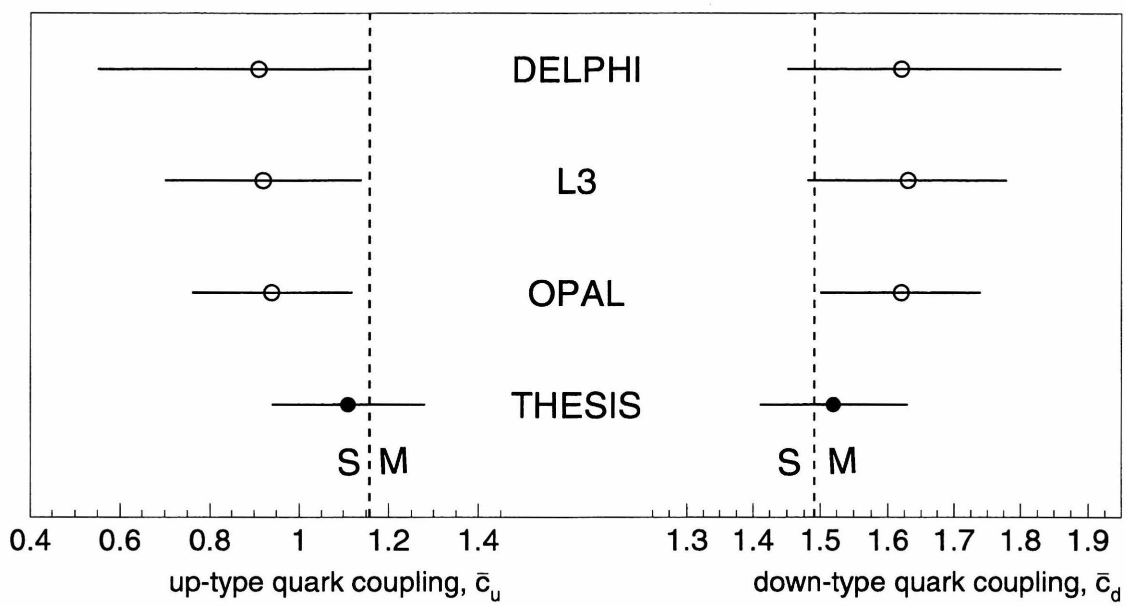

Figure 9.1: Comparison of the different measurements of the effective quark couplings to the Z boson, $\bar{c}_{\mathrm{u}}$ and $\bar{c}_{\mathrm{d}}$, obtained by the LEP experiments and in this thesis. The error bars show combined experimental and theoretical uncertainties. The vertical dashed lines show the Standard Model values.

In Figure 9.2, I superimpose this constraint on $\bar{c}_{\mathrm{u}}$ and $\bar{c}_{\mathrm{d}}$ over the 68% confidence level contours in $\bar{c}_{\mathrm{d}}$ and $\bar{c}_{\mathrm{d}}$ that I calculated in Section 8.3.1. There is good agreement between my results and the L3 measurement of R_{b}.

9.2.3 Measurements of Quark Charges

Many measurements have been performed that constrain the values of the quark charges. They are generally in agreement with the Standard Model values. For example, the ratio

$$R \equiv \frac{\sigma(\mathrm{e}^+\mathrm{e}^- \longrightarrow \text{hadrons})}{\sigma(\mathrm{e}^+\mathrm{e}^- \longrightarrow \gamma \longrightarrow \mu^+\mu^-)}$$

has been measured as a function of the $\mathrm{e}^+\mathrm{e}^-$ center-of-mass energy, $\sqrt{s}$ (for a review, see Reference [73]). Although resonance effects are important at a quark threshold, $\sqrt{s} \simeq 4m_{\mathrm{q}}^2$, the value of R in the continuum regions between thresholds is approxi-

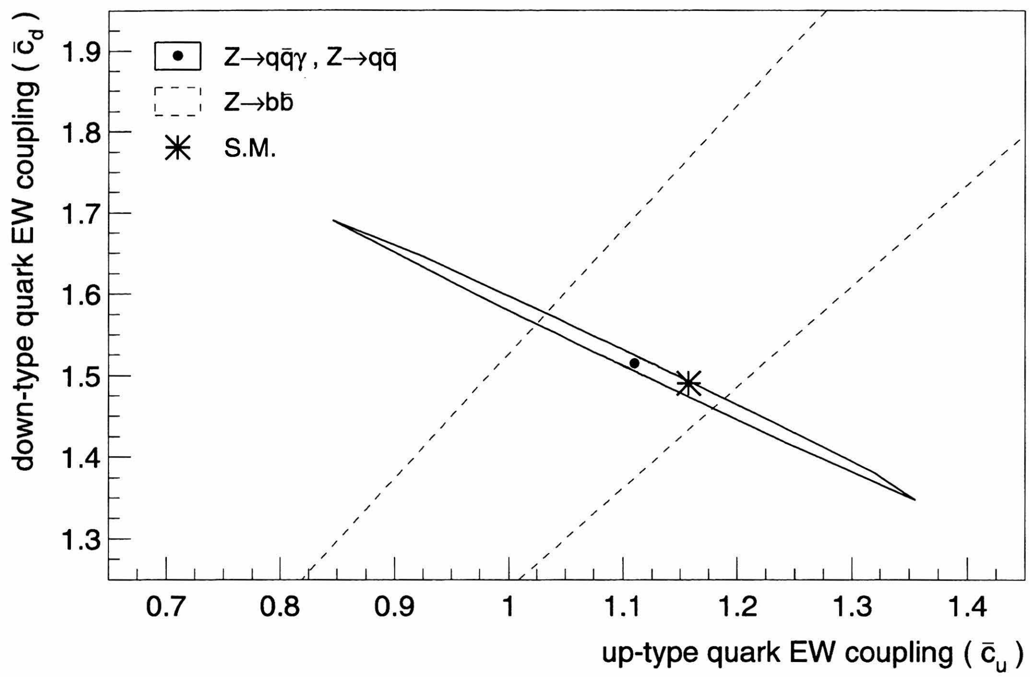

Figure 9.2: Comparison between the 68% confidence-level contours of $\bar{c}_{\mathrm{u}}$ and $\bar{c}_{\mathrm{d}}$ that I calculate and the constraint on these parameters from the L3 measurement of R_{b}.

mately given by

$$R(\sqrt{s}) \simeq N_C \sum\nolimits_{\mathrm{q}} Q_{\mathrm{q}}^2 \,,$$

where $N_C = 3$ is the number of colors in QCD and the sum is over the kinematically accessible quarks ($m_{\mathrm{q}} < \sqrt{s}/2$). Therefore, the change in the continuum value of R across a threshold measures the absolute value of the charge of the corresponding quark. Measurements of R above and below the c-quark and b-quark thresholds provide strong experimental evidence that the quark charges are approximately equal to their Standard Model values.

Measurements of inelastic neutrino-nucleon reactions provide another example of a constraint on the quark charges[101, 111–114]. To a good approximation, the jets of hadrons produced in these reactions originate from a single flavor of quark. For example, the dominant process in $\overline{\nu}N$ reactions is W^- exchange which converts a u quark from the nucleon into an outgoing d quark. Therefore, inelastic neutrino-nucleon reactions provide a high-purity sample of hadron jets originating from a single quark flavor. A method for estimating the charge of this quark is to first measure the net charge of the hadrons in each of these jets, and then to compute the average value of these jet charges. An analysis of $\overline{\nu}$n and $\overline{\nu}$p interactions recorded by the BEBC bubble chamber determined the value of the average jet charge for a sample of d-quark enriched jets to be[101]

$$\langle Q \rangle = -0.38 \pm 0.09 \, .$$

This value agrees with the Standard Model d-quark charge, $Q_{\mathrm{d}} = -1/3$.

Although the approximate values of the quark charges are experimentally well established, fractional charges are a fundamental prediction of the Standard Model and thus deserve to be extensively tested. The measurement of the charges that I describe in this thesis is the first such measurement performed at LEP.

9.3 Outlook

The shower-shape analysis techniques that I have developed to discriminate between overlapping $\pi^0 \to \gamma\gamma$ decays and single photons have application to many analyses that involve energetic photons in hadronic events. These techniques have recently been adopted by L3 to search for inclusive charmless radiative b-decays[115] (b $\to$ sγ), to study event-shape variables at reduced center-of-mass energies[116], and to search for the decays of new scalar bosons into photons[107]. A method based on my techniques has also been proposed[117] for the crystal calorimeter of the CMS detector that will operate at the LHC collider.

The current plan for future LEP operations calls for an upgrade of its center-of-mass energy to above the threshold for W^+W^- pair production by the end of

1996. At these energies, the rate of hadronic Z decays will be negligible. Before this upgrade, L3 will record approximately one million additional hadronic events at the Z peak, resulting in a final sample of approximately four million events. The ultimate reduction in the statistical error that could be achieved using my analysis is therefore from the present value of 2.4% to about 2% (assuming a corresponding increase in Monte Carlo statistics). Since the contribution of statistical uncertainties to the errors on my results is already small, this analysis would not benefit greatly from additional data.

The failure I observe of Monte Carlo models to describe isolated and energetic neutral hadron production has implications for the next generation of high-energy experiments at the Large Hadron Collider (LHC). In particular, these hadrons are a potentially large background to Higgs decay into two photons[118]. By extrapolating the discrepancies between data and Monte Carlo predictions in e^+e^- collisions at 91 GeV, I estimate that the hadronic background to a search for $H \rightarrow \gamma\gamma$ decays at the LHC will be a factor of 1.5–2.5 larger than currently available Monte Carlo models predict[119].

Appendix A

Shower-Shape Analysis

In this appendix, I describe the methods that I have developed to analyze the patterns of energy deposited in the ECAL by electromagnetically showering particles. I refer to these patterns as *shower shapes.* A shower-shape analysis consists of examining the local response of the electromagnetic calorimeter, and can yield information about the type of particle (or particles) responsible for the observed energy deposits, as well as about quantities such as the energy and direction of those particle(s). Since this analysis only uses information about the local detector response, it is complementary to other methods based on global event characteristics.

My motivation for developing these methods is the need to discriminate between bumps that are due to single and multiple photons. This shower-shape analysis provides an important tool for selecting single photons in hadronic events, with minimal contamination from neutral hadrons decaying into overlapping multi-photon states; it can also be applied effectively to related problems, such as electron identification. I have optimized the analysis for particle classification since the performance of the standard parameter estimation techniques, such as the corrected sum-of-9 for energy determination and the energy-weighted center-of-gravity for angle determination, is sufficient for most purposes.

In the following sections, I first define the variables that I have chosen to characterize a shower, then I describe the development of an artificial neural-network discriminator which uses those variables, and finally I discuss the performance of the discriminator. In the last section, I summarize the usage of a Fortran package that implements the discriminator.

A.1 Shower-Shape Variables

A *shower-shape variable* is a quantity that is derived from the crystal energies in a bump and that is sensitive to the differences between single and overlapping photon showers. The electromagnetic shower generated by a single photon is approximately axially symmetric about the incident photon's direction, as shown in Figures A.1(a,b). When the showers from two photons overlap, their combined energy deposit is a superposition of the energy deposits of the individual photons, with an offset between them as shown in Figures A.1(c,d). The resulting shower shape is no longer axially symmetric and thus it can, in principle, be distinguished from the shower shape of a single photon. The general strategy for choosing shower-shape variables is therefore to identify quantities that measure the "roundness" of the energy deposits in a bump. However, quantifying this roundness can be technically difficult, because the angular segmentation of the ECAL is coarse with respect to the characteristic transverse size of a shower. As a result, geometric effects can obscure the roundness of the shower from a single photon when it is incident near the edge of a crystal (see Figure A.1(b)). Variables that are sensitive to the presence of other nearby particles are less useful for analyzing hadronic events. I find that requiring variables to be calculated using only the central 5×5 matrix of crystals in a bump minimizes this sensitivity.

A simple and effective class of shower-shape variables consists of ratios of crystal energy sums, $S_{inner}/(S_{inner} + S_{outer})$, which measure how much of the total energy deposited in a region is concentrated in an inner central region. These ratios are typically larger for single-photon showers than for multiple-overlapping-photon showers, and are reasonably insensitive to geometrical effects since they use crystal-energy sums rather than individual crystal energies. I select the following three shower-shape variables based on energy ratios

$$x_1 = \frac{S_1}{S_9} \quad , \quad x_2 = \frac{S_9 - S_1}{S_{25} - S_1} \quad , \quad x_3 = \frac{S_1}{S_4} \, ,$$

where S_1 is the largest crystal energy in a bump, S_9 (S_{25}) is the sum of energies for the surrounding 3×3 (5×5) matrix of crystals, and S_4 is the largest of the four possible 2×2 crystal energy sums that include the most energetic crystal. Figure A.2 shows a comparison of the distributions of these variables for isolated single photons and isolated neutral pions decaying into overlapping photons, at two different incident particle energies.

A second class of shower-shape variables is based on a moment analysis of the crystal energies in a 5×5 matrix, $E_{u,v}$, where u and v are the local crystal coordinates for a bump. I first calculate the energy-weighted means, $\langle E_i \rangle$, and covariances, $\langle E_i^2 \rangle$ and $\langle E_i E_j \rangle$, and then define two variables corresponding to the widths of the crystal energy distributions in the u and v projections

$$x_4 = \sigma_u^2 = \langle E_u^2 \rangle - \langle E_u \rangle^2 \quad , \quad x_5 = \sigma_v^2 = \langle E_v^2 \rangle - \langle E_v \rangle^2 \, .$$

I also calculate the eigenvalues of the covariance matrix

$$\lambda_\pm = \frac{1}{2}\left(\sigma_u^2 + \sigma_v^2\right) \pm \frac{1}{2}\sqrt{\left(\sigma_u^2 - \sigma_v^2\right)^2 + 4\left(\langle E_u E_v \rangle - \langle E_u \rangle \langle E_v \rangle\right)^2} \, ,$$

which are related to the lengths of the principal axes of the crystal energy distribution, and then define

$$x_6 = \lambda_+ / \lambda_- \, ,$$

which measures the eccentricity of the energy distribution. Figure A.3 shows a comparison of the distributions of these variables for isolated photons and neutral pions.

Figures A.2 and A.3 show distributions of shower-shape variables for bumps in the barrel region of the ECAL. The same variables can also be effectively used to analyze bumps in the endcap regions, where the crystal geometry is more irregular. Figure A.4 shows a comparison between the distributions in the barrel and in the endcaps.

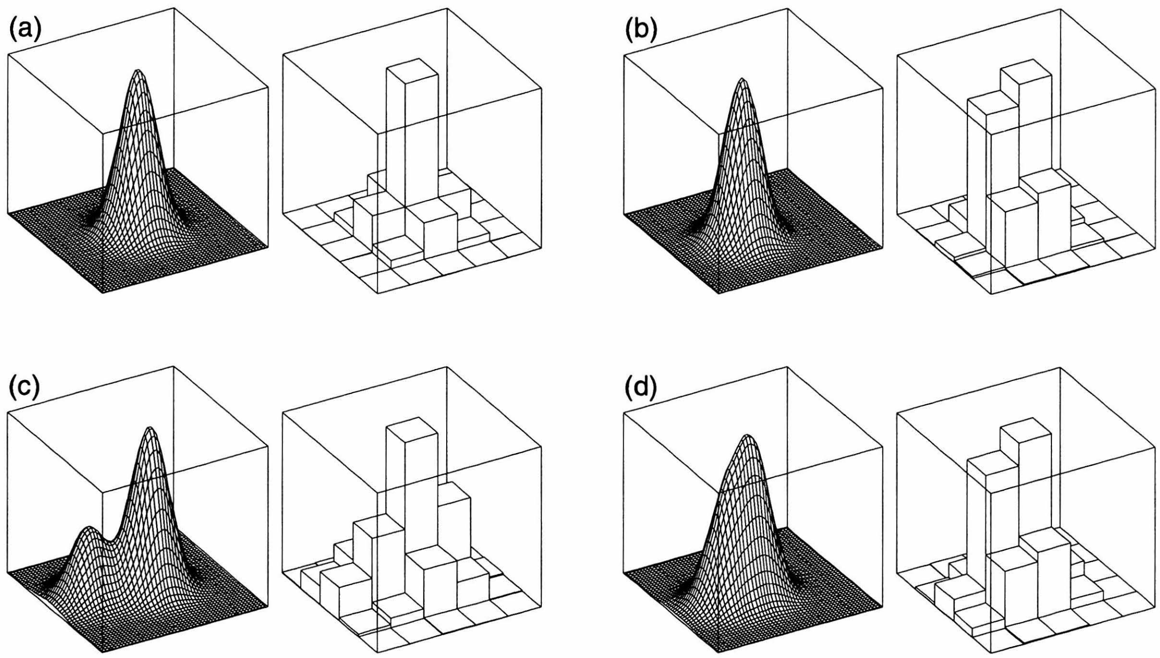

Figure A.1: Examples of the shower shapes generated by single photons (a,b) and by neutral hadrons decaying into pairs of photons (c,d). The left-hand plot of each figure shows the actual distribution of energy deposits while the right-hand figure shows the corresponding crystal energies. In (a), the incident photon is centered on the crystal matrix and the resulting crystal energies have the same axial symmetry as the underlying energy deposits. In (b), the photon is incident near the edge of a crystal and the resulting crystal energies are no longer axially symmetric. In (c), the photons from a hadron decay are easily resolved in the left-hand plot but result in a single reconstructed bump because of the coarse ECAL granularity. In (d), the two photons are almost collinear and the resulting crystal energies are almost indistinguishable from those due to a single photon as shown in (b).

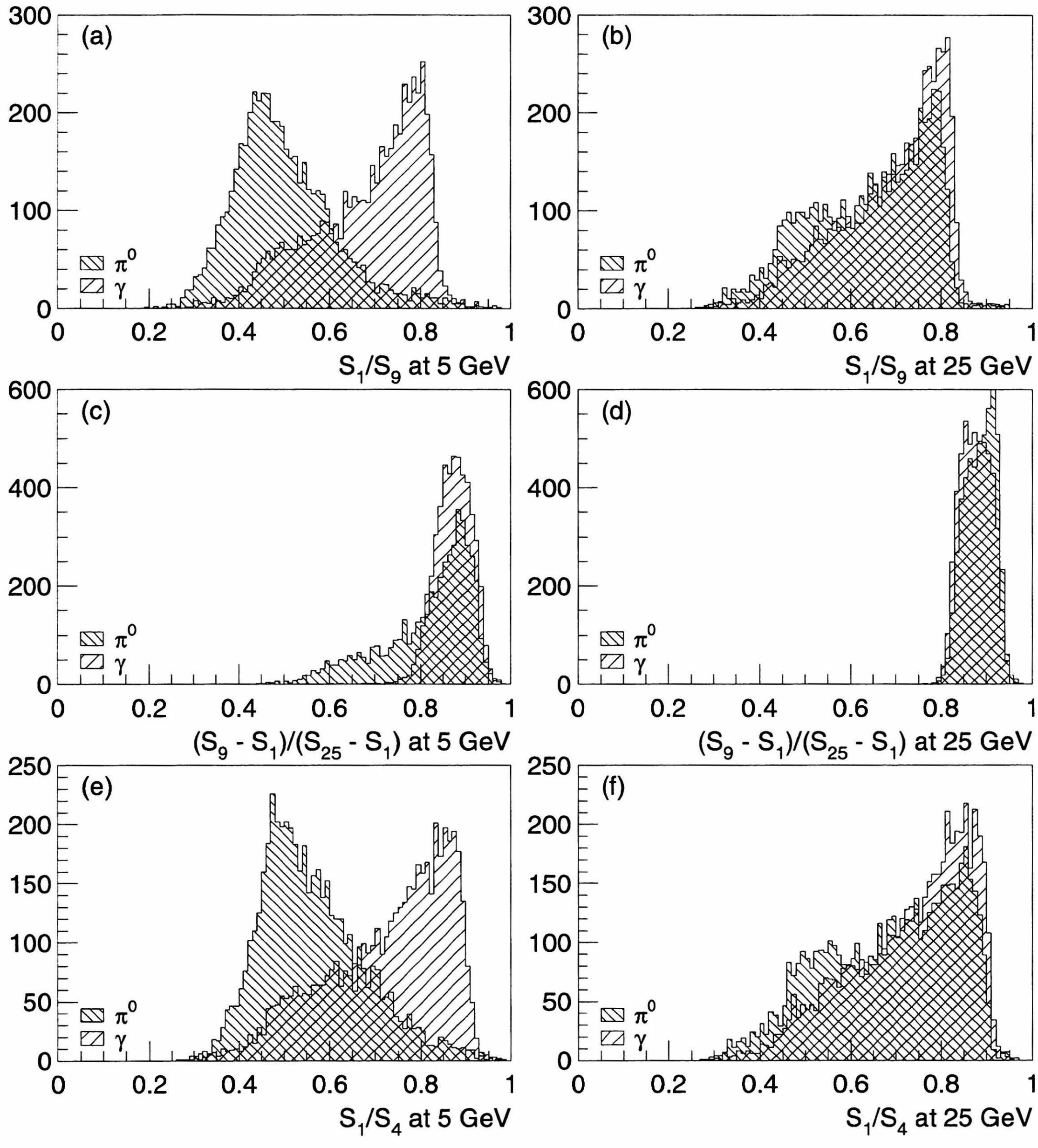

Figure A.2: Distributions of three shower-shape variables based on energy ratios, for isolated photons and isolated neutral pions decaying into overlapping photons at 5 GeV (a,c,e) and 25 GeV (b,d,f). These results were obtained using simulations of single particles incident upon the barrel region of the ECAL.

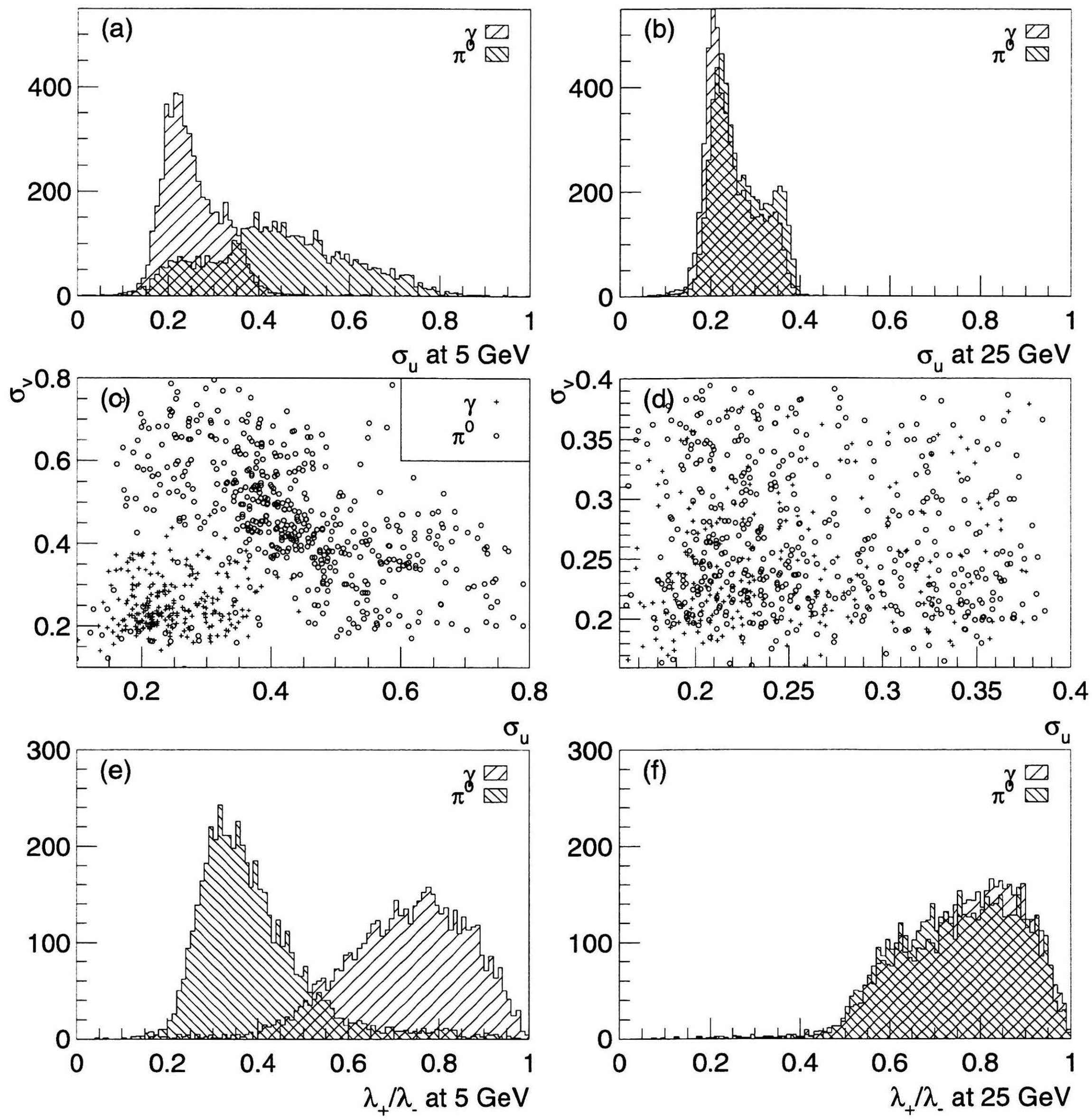

Figure A.3: Distributions of three shower-shape variables based on a moment analysis, for isolated photons and isolated neutral pions decaying into overlapping photons at 5 GeV (a,c,e) and 25 GeV (b,d,f). Plots (a) and (b) show the distributions of σ_u, which are essentially identical to those of σ_v; plots (c) and (d) show the corresponding two-dimensional distributions of σ_u and σ_v. These results were obtained using simulations of single particles incident upon the barrel region of the ECAL.

The good agreement between the two regions, especially at high energies, confirms that the chosen variables are not sensitive to effects associated with any particular crystal geometry.

A.2 Development of a Shower-Shape Discriminator

Although several of the variables introduced in the previous section provide adequate separation between single- and multiple-photon bumps at low energies, no single variable is effective at high energies. Therefore, in order to exploit correlations between variables, and to improve upon the performance of a one-dimensional cut, I seek a multidimensional discriminator function, $F(\vec{x})$ with $\vec{x} \equiv x_i$, whose value is near one (zero) for single- (multiple-) photon bumps.

Simulated events, for which both the shower-shape variables and the target discriminator value (zero or one depending on the particle type) are known, provide suitable input with which to build a discriminator function. A general approach is to assume some parametric form $F(\vec{x};\vec{p})$ for the function, and then find a set of parameters $\vec{p}$ that minimizes the classification error

$$\mathcal{E}^2 = \sum_{\mu} |F(\vec{x}_\mu;\vec{p}) - F_\mu|^2 ,$$

where the sum is taken over the simulated events, which I refer to as the *training sample.* There are many ways to solve this generalized fitting problem; I have chosen to use an artificial neural-network (ANN) approach[120]. This method has the advantage of making minimal assumptions about the functional form of F; however, the large number of parameters it introduces necessitates large training samples.

A.2.1 Artificial Neural-Network Approach

The ANN approach to developing effective discriminator functions is loosely based on an analogy with the learning process in biological neurons, and borrows some of the terminology of this field. Although there are many variations on the ANN approach, I have restricted my attention to the most straightforward implementation, based on a *feed-forward* network using *back-propagation learning*[121].

A feed-forward ANN consists of N_L layers of n_l nodes each, with links connecting each node in a layer to every node in the adjacent layers (see Figure A.5). I refer to the first and last layers as the input and output layers, respectively, and to the intermediate layers as hidden layers. The parameters of an ANN are the weights ω_{ij} associated with each link; there are a total of

$$N_\omega = \sum_{l=2}^{N_L} n_l \cdot n_{l-1}$$

such parameters. For the shower-shape discriminator, I have chosen a network consisting of three layers, with 10 nodes in the input layer, 20 nodes in the hidden layer, and one node in the output layer, which gives a total of 220 parameters. Adding extra hidden layers or extra nodes within a hidden layer, slows down the learning process because of the additional parameters to be determined, and does not improve the discriminator's performance.

In order to evaluate the discriminator function associated with a network, nodes in the input layer are first assigned values corresponding to an input pattern, $y_i = x_i$, and then these values are propagated to nodes in the inner layers according to

$$y_i = f\left(\sum_j \omega_{ij} y_j\right) ,$$

where the summation for each node is taken over the nodes in the previous layer. After iterating this procedure for each layer of the network, the discriminator function value is given by the value of the single node in the output layer. I use the standard choice for the *activation function*[120]

$$f(t) = \frac{1 + \tanh(t)}{2} = \frac{1}{1 + e^{-2t}} \; ,$$

which is responsible for the non-linearity of the network response (see Figure A.6). Learning in the network is achieved by using the back-propagation algorithm, in which the weights are periodically updated to reduce the classification error according to

$$\vec{\omega} \to \vec{\omega} - \eta \frac{\partial \mathcal{E}^2}{\partial \vec{\omega}} \; ,$$

where η is the *learning parameter*[120] and controls the rate at which parameters are adjusted.

A.2.2 Network Training

To generate training samples, I simulate single photons and neutral pions using the standard L3 detector simulation package, SIL3, which is based on GEANT[66, 67] Version 3.16, and takes account of the effects of material in front of the ECAL, the L3 magnetic field, and readout noise. I generate single particles with a vertex position that is smeared according to realistic LEP beam spot dimensions ($\sigma_x = 160\mu$m, $\sigma_y = 10\mu$m, and $\sigma_z = 6.5$mm), and with a random direction uniformly distributed in ϕ and $\cos\theta$. I only record events in which exactly one ECAL bump is reconstructed and for which at least half of the particle's energy is contained within a 3×3 matrix of crystals. I randomly select the type of particle for each event (photon or neutral pion) to obtain an even mix after event selection. I generate samples of approximately ten-thousand events each, at three different energies (5, 15, and 25 GeV), for both the barrel and endcap regions of the ECAL; this provides a total of six training samples.

For each event, I use the six shower-shape variables $(x_1, \ldots, x_6)$ that I defined in Section A.1 as the first six of the ten network inputs. For the seventh input, I use the scaled polar angle of the bump in the event

$$x_7 = (\theta_i - \theta_{min})/(\theta_{max} - \theta_{min}) \; ,$$

where θ_i is the theta index ($1 \leq \theta_i \leq 41$) of the central crystal of the bump, and θ_{min} and θ_{max} are the limits for this index in the barrel or endcap region. Finally, I define the remaining three inputs to be

$$x_{7+k} = E_{1+k}/E_1 \quad (k = 1, 2, 3) ,$$

where E_i are the sorted energies in the central 5×5 matrix of crystals

$$E_1 \geq E_2 \geq E_3 \geq \ldots \geq E_{25} .$$

Inputs of this last type are not genuine shower-shape variables since they have essentially no discrimination power on their own; however, I find empirically that using three such variables optimizes the network's performance.

For network training, I use the JETNET 3.0 package[120]. I use the default values of all of the parameters, except for the learning rate, η, for which I use the value 0.05. I perform training separately for each of the six simulated samples, which yields six independent sets of parameters for the same network architecture. I divide each sample into (two thirds) training patterns and (one third) test patterns, and I perform 1000 (barrel) or 2000 (endcap) iterations through the training patterns in each sample in order to obtain the final network parameters. An important aspect of a network's performance is its ability to generalize to independent samples drawn from the same population as the training sample. In order to ensure that the network training does not focus on accidental features of the training patterns, I apply Gaussian smearing to each crystal's nominal energy, using an RMS width of

$$\sigma(E) = 10\% \cdot E + 10 \text{ MeV} .$$

Note that this amount of smearing is much larger than the typical readout noise, which is 1–2 MeV per crystal, and so does not represent a realistic effect. However, I find that applying a large smearing has a small effect on the ultimate learning ability of the network, since after many training cycles the network effectively averages out the smearing, but more importantly, slows down the initial rate of learning and improves the generalization performance. During training, I periodically monitor the network's generalization ability by comparing the network's discrimination performance on the independent training and test samples. Figure A.7 shows the evolution of these performances during the training of the three barrel networks, and demonstrates good generalization ability.

As shown in Figure A.7, the networks' ability to reject π^0's in simulated events increases rapidly at first and then more slowly. However, during the phase of slow learning, the network eventually learns to recognize features of the simulated events that are not present in real events, and as a result, its performance for data deteriorates with further training cycles. I have chosen the number of training cycles for determining each of the six final network parameter sets in order to balance these two effects.

A.3 Performance of the Shower-Shape Discriminator

Figure A.8 shows a comparison of the performance of the three different network parameter sets in the two regions of the ECAL, for simulated single-particle events of different energies. Each parameter set performs best for events whose energy is near to the energy of the training sample on which it is based. Therefore, I define the discriminator function value for a bump as the network output value obtained with a parameter set that best matches the bump's energy and the region in which it was recorded. For the energy matching, I assume that the bump is due to a single photon, in which case the bump's corrected sum-of-9 energy, S_9^c, is a good estimate of the photon energy. I use the 5 GeV parameter set if $S_9^c \leq 5$ GeV, the 15 GeV set if 5 GeV $< S_9^c \leq 17$ GeV, and otherwise the 25 GeV set. The results in Figure A.8 suggest that using an additional set of parameters trained at 35 GeV would improve the discriminator's performance at high energies; however, I have tested this approach but find no improvement. Figure A.9 shows a comparison of the performance of the final discriminator with other methods that have been used for shower-shape analyses of L3 data. The new discriminator has better π^0 rejection than other methods in the barrel region, and is the only method that can be applied in the endcap region.

Figure A.10 shows a comparison of the final discriminator output distributions for simulated photons and neutral pions of 5 GeV, 15 GeV, and 25 GeV. Since the discriminator chooses network parameters for each bump based on an estimated photon energy, the output distribution near an energy threshold is a superposition of the distributions from the two networks. This effect is particularly evident in the distributions for 5 GeV pions shown in Figure A.10(a,b), where correlations between the discriminator output value and the estimated photon energy generate a complex structure.

A.3.1 Discriminator Output Processing

While the procedure outlined above effectively combines the advantages of the different network parameter sets obtained from training at different energies, it also introduces discontinuities in the network response across energy thresholds. As a result, a cut applied at a fixed value on the discriminator output has an efficiency versus energy that changes abruptly at 5 GeV and 17 GeV. To overcome this problem, I convert the raw discriminator output value into the probability, which I denote p_γ, of obtaining an output value less than the actual output value, given the set of network parameters that were used and assuming that the bump is due to a single photon. More precisely, if $dP(y, E_\gamma)/dy$ is the normalized probability distribution of network output values y for an isolated photon of energy E_γ; then the value of p_γ for a bump whose estimated equivalent photon energy is E_γ and whose discriminator

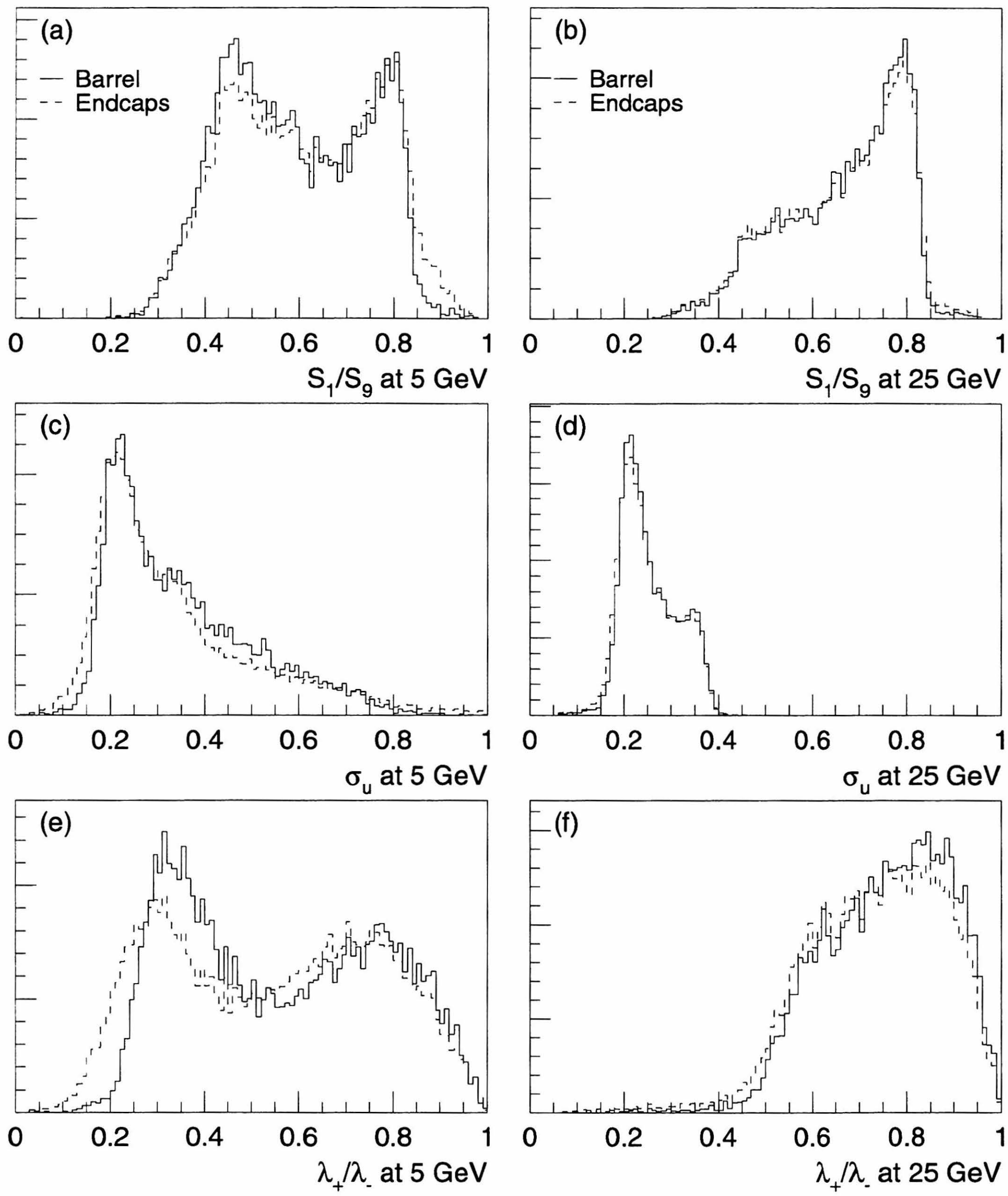

Figure A.4: Comparison of the distributions of the shower-shape variables $x_1 = S_1/S_9$ (a,b), $x_4 = \sigma_u$ (c,d), and $x_6 = \lambda_+/\lambda_-$ in the barrel and endcap regions of the ECAL. Plots (a), (c), and (e) represent an even mix of 5 GeV single photons and overlapping neutral pion decays, and plots (b), (d), and (f) are the same comparisons at 25 GeV.

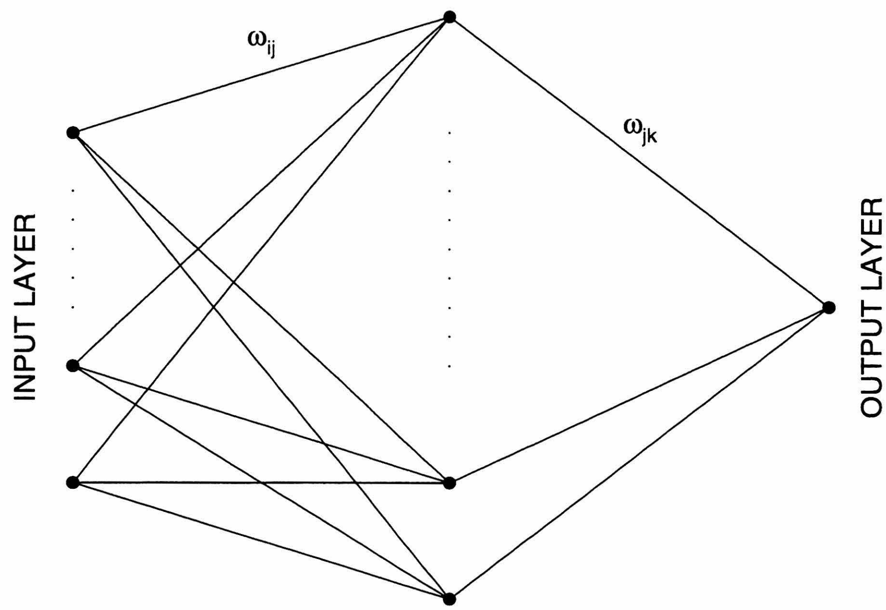

Figure A.5: Schematic diagram of a three-layer ANN, with nodes represented as filled circles, and links as lines between them.

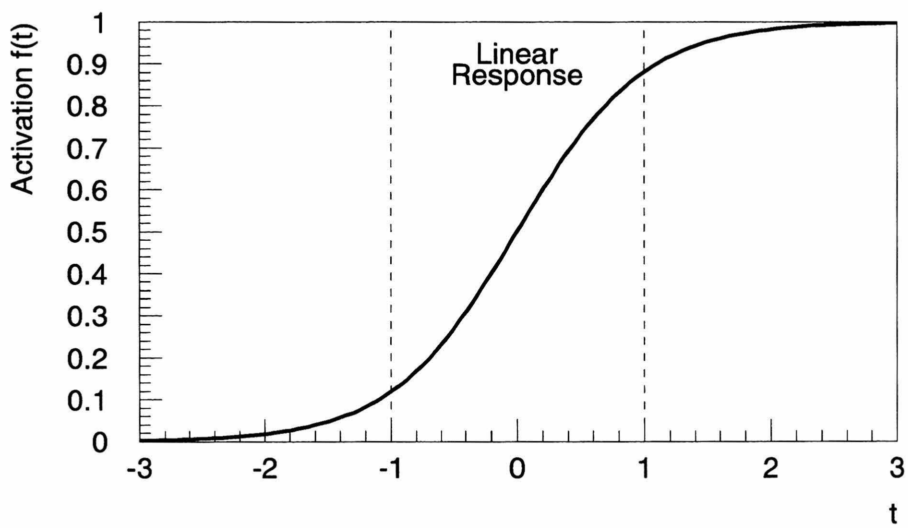

Figure A.6: Graph of a typical ANN activation function, with characteristic *sigmoid* shape. Note that the response is approximately linear in the range $|t| \lesssim 1$, and saturates at zero or one for values beyond this range.

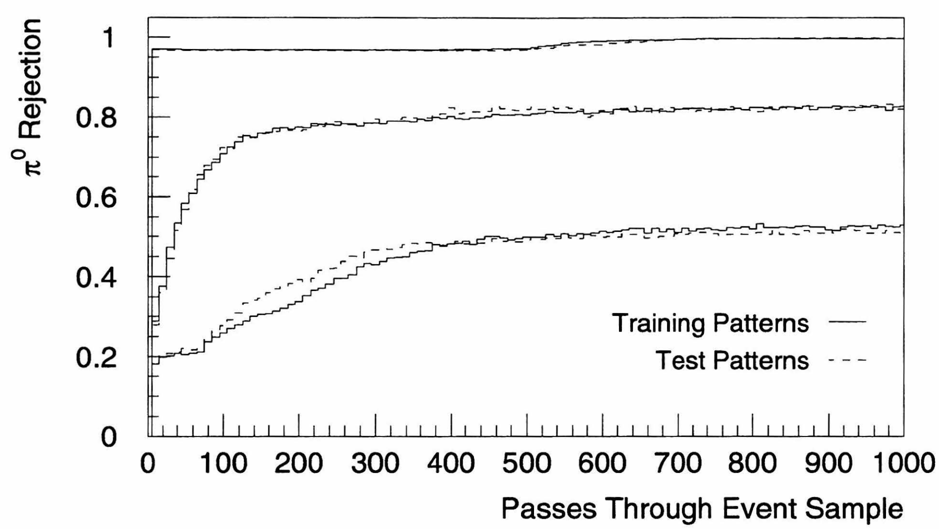

Figure A.7: Plot of the evolution of the network performance for training and test patterns over 1000 iterations through the 5 GeV (upper curves), 15 GeV (middle curves), and 25 GeV (lower curves) barrel event samples. The vertical scale shows the fraction of overlapping $\pi^0 \rightarrow \gamma\gamma$ decays that are rejected with a cut chosen to accept 90% of single photons.

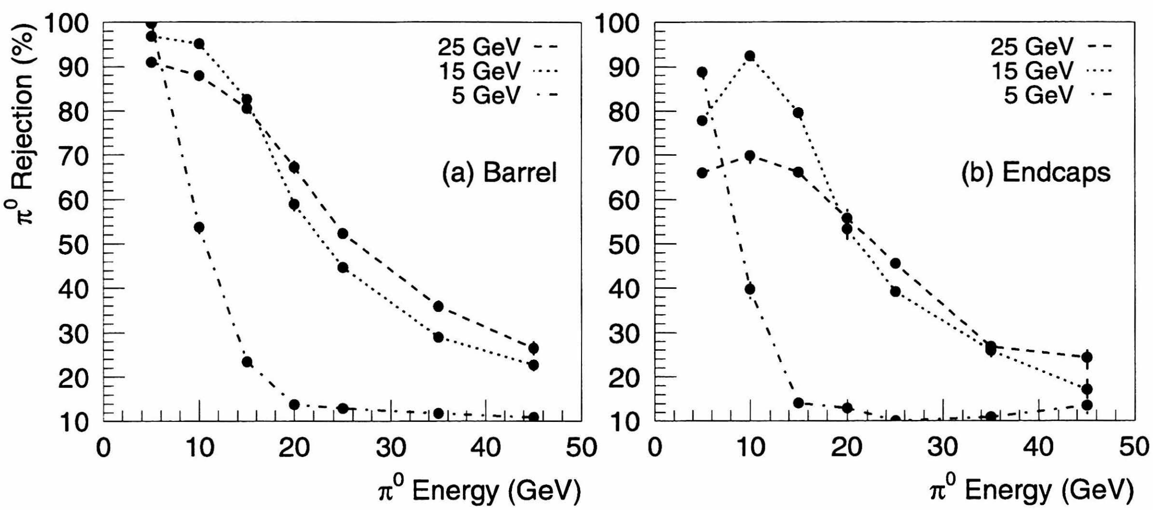

Figure A.8: Comparison of the network performance using parameters obtained from training at different energies (5,15, and 25 GeV) and in different regions (barrel or endcaps), as a function of particle energy. Results are expressed in terms of the fraction of overlapping $\pi^0 \to \gamma\gamma$ decays that are rejected with a cut chosen at each energy to accept 90% of single photons. Plots show the performance in the barrel (a) and endcap (b) regions. Results are determined from single particle (π^0 or γ) events simulated in the detector.

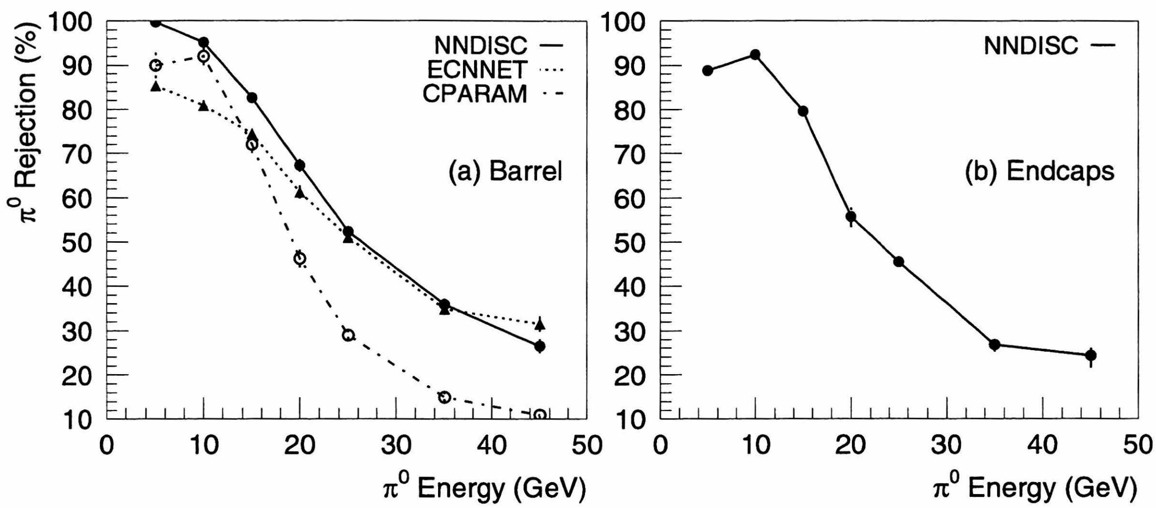

Figure A.9: Performance of the ANN discriminator (NNDISC) as a function of particle energy, expressed in terms of the fraction of overlapping $\pi^0 \rightarrow \gamma\gamma$ decays that are rejected with a cut chosen at each energy to accept 90% of single photons. Plots show the performance in the barrel (a) and endcap (b) regions. In the barrel region, the performance of previous shower-shape analysis methods (ECNNET,CPARAM) are also shown for comparison. Results are determined from single particle (π^0 or γ) events simulated in the detector.

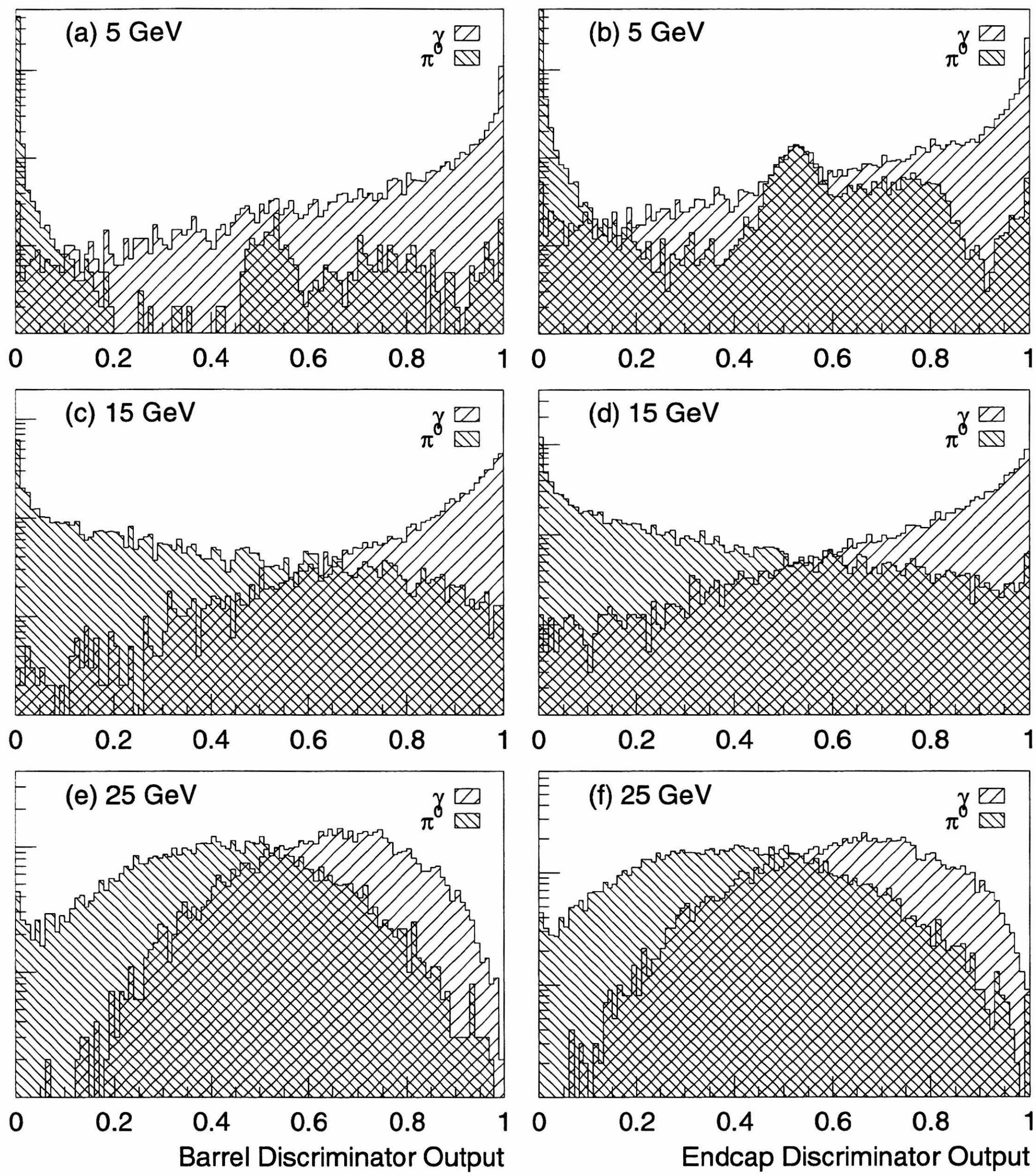

Figure A.10: Distributions of discriminator output values for isolated single particles in the barrel (a,c,e) and endcap (b,d,f) regions, and at 5 GeV (a,b), 15 GeV (c,d), and 25 GeV (e,f). The vertical scale is logarithmic.

output value is y, is given by

$$p_\gamma(y, E_\gamma) = \int_0^y \frac{dP}{dy}(y', E_\gamma)dy' .$$

The resulting distribution of p_γ is then ideally flat for bumps due to isolated single photons, $dP/dp_\gamma = 1$, and peaked near zero for bumps due to multiple overlapping photons. Therefore, applying a fixed cut on the maximum value of p_γ has an efficiency for genuine isolated single photons that is independent of the photon energy, and equal to $1 - p_\gamma$. The efficiency for neutral pions is still energy-dependent, but varies smoothly across energy thresholds.

In order to obtain the conversion between raw discriminator output values and the probability p_γ, I measure the probability distributions dP/dy using radiative Bhabha events from the reaction $e^+e^- \rightarrow e^+e^-\gamma$. These events are independent from the training and test samples described above, and can be selected from both data and Monte Carlo. I select radiative Bhabha events by requiring that they contain at least three reconstructed ECAL bumps that have corrected sum-of-9 energies (S_9^c) greater than 1 GeV and that are isolated from each other by at least 15°. I classify the bumps in an event as either electrons or photons depending on whether they have a matching TEC track in azimuthal angle, using matching criteria that vary with the polar angle. Figure A.11 shows a comparison of the energy distributions of photon and electron bumps in events selected from data and from Monte Carlo simulations based on the BHAGENE3[122] generator. The discrepancies between the data and Monte Carlo distributions reflect differences between the preselections used for data events and the generator-level cuts applied to Monte Carlo events, and do not affect the analysis described below, in which data and Monte Carlo events are only compared within narrow energy intervals.

In order to increase the available statistics for the full energy range, I use both photon and electron bumps. I divide the energy range from 1–47 GeV into 30 intervals of unequal sizes (varying between 1 and 2 GeV), which are chosen to give

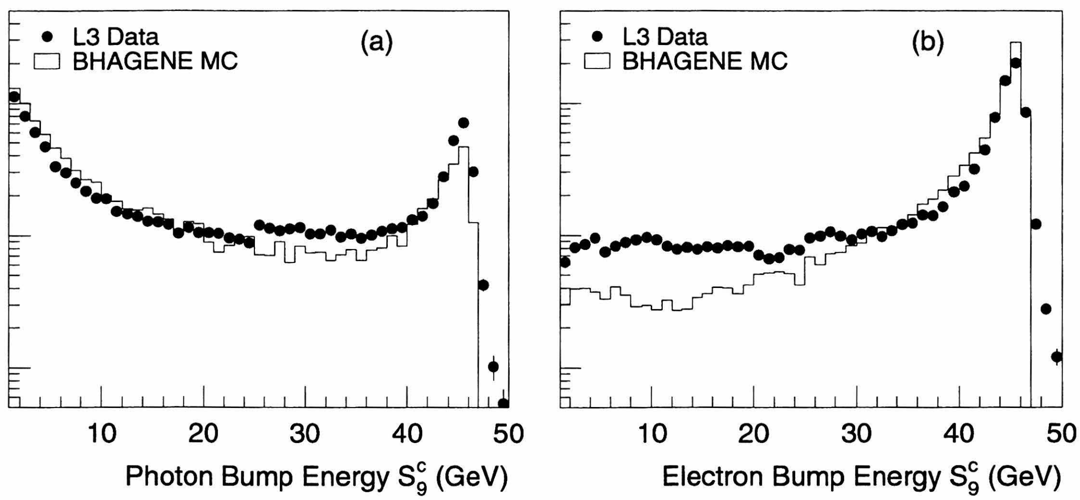

Figure A.11: Energy distributions of photon bumps (a) and electron bumps (b) selected in radiative Bhabha events, comparing results obtained from L3 data (points) and the BHAGENE Monte Carlo (histogram).

approximately the same total number of photon and electron bumps in each interval. In each energy interval and for each ECAL region, I obtain the distributions of the discriminator output values for data and Monte Carlo events. Figure A.12 shows these distributions in three different energy ranges (which combine several intervals in order to improve statistics), and demonstrates that the agreement between data and Monte Carlo is good at low energies but reveals that the agreement becomes worse at higher energies. The discrepancies between data and Monte Carlo are mostly due to inaccuracies in the simulation of the ECAL response, which result in network training bumps that have slightly different characteristics than real bumps. Since these discrepancies are small at low and intermediate energies, which are the most important for π^0/γ separation, I calculate p_γ separately for data and Monte Carlo events, so that by construction, the distributions of p_γ are in agreement.

Figure A.13 shows the distributions of the photon probabilities for simulated single particle (photon or neutral pion) events, in the barrel and endcap regions, and for three different energies. As expected, the distributions for genuine isolated photons are flat at all three energies, and the distributions for overlapping neutral pion decays are peaked near one, and do not display the complicated structure evident in Figure A.10.

A.4 Shower-Shape Discriminator Usage

I have prepared a software package implementing the ANN described in this appendix, which I refer to as NNDISC. The current version of NNDISC, which I have used to prepare the results presented in this appendix, is V1.01. The complete NNDISC package is available within the APL3 package of the standard L3 software distribution for versions after V200. The NNDISC package consists of three Fortran files and provides two levels of interface:

`apdisc.f`	...	an interface using the L3 analysis framework,
`nndisc.f`	...	a low-level interface independent of the L3 framework,
`nndata.f`	...	data describing network parameters and efficiencies.

The usage of the low-level interface to the NNDISC package is

```
CALL NNDISC(ECRY,IDNT,MCFLAG,OUTNN,PROB)
```

with input parameters

```
REAL ECRY(25)
INTEGER IDNT
LOGICAL MCFLAG
```

and output parameters

```
REAL OUTNN,PROB
```

The parameter `MCFLAG` should be set to `.TRUE.` for bumps taken from Monte Carlo events, and otherwise set to `.FALSE.` The parameter `IDNT` should be set to the software identifier of the central crystal of the bump, which is of the form `20RTTPPP` and specifies the region containing the crystal (1 $\leq$`R`$\leq$ 4) and the crystal's polar angle (01 $\leq$`TT`$\leq$ 41) and azimuthal angle (001 $\leq$`PPP`$\leq$ 160) position in that region (the initial 20 is common to all ECAL crystals and is optional). The array `ECRY` should be initialized with the 25 energies (in GeV) of the central 5×5 matrix of crystals for a bump, using the crystal ordering convention of the ECL3 routine `ECNEIG`. The entry in `ECRY` for any crystal for which no energy is available should be zero. Note that missing crystals, especially in the central 3×3 matrix of a bump, significantly degrade the performance of the network. Therefore, `NNDISC` should only be used for bumps in which none of the central 3×3 crystals are either "hot" or "dead". Also, it is important to include the effects of bad crystals in Monte Carlo simulated events. On return, the `NNDISC` subroutine provides the values of the raw discriminator output as `OUTNN` and the probability of obtaining a smaller value for a genuine single photon bump, p_γ, as `PROB`. Both these output values will be between zero and one.

The `APDISC` interface implements a layer above the `NNDISC` interface and is intended to be more convenient to use in the standard L3 analysis framework. The usage is

```
CALL APDISC(LB,OUTNN,PROB,ISTAT)
```

with input parameter

```
INTEGER LB
```

and output parameters

```
REAL OUTNN,PROB
INTEGER ISTAT
```

The output parameters `OUTNN` and `PROB` have the same meaning as given above. The parameter `LB` should be set to the offset of a valid `EBMP` bank in ZEBRA[123] memory. The return value `ISTAT` is used to signal the possible error conditions

`ISTAT=0`	...	no errors detected—normal completion,
`ISTAT=1`	...	missing crystals in the central 3×3 matrix,
`ISTAT=2`	...	invalid ZEBRA links detected,
`ISTAT=3`	...	unable to initialize crystal map.

When `APDISC` returns the status `ISTAT=1`, the values of `OUTNN` and `PROB` are still meaningful; however, the performance of the discriminator is degraded, and the agreement between data and Monte Carlo depends on an accurate simulation of bad crystals.

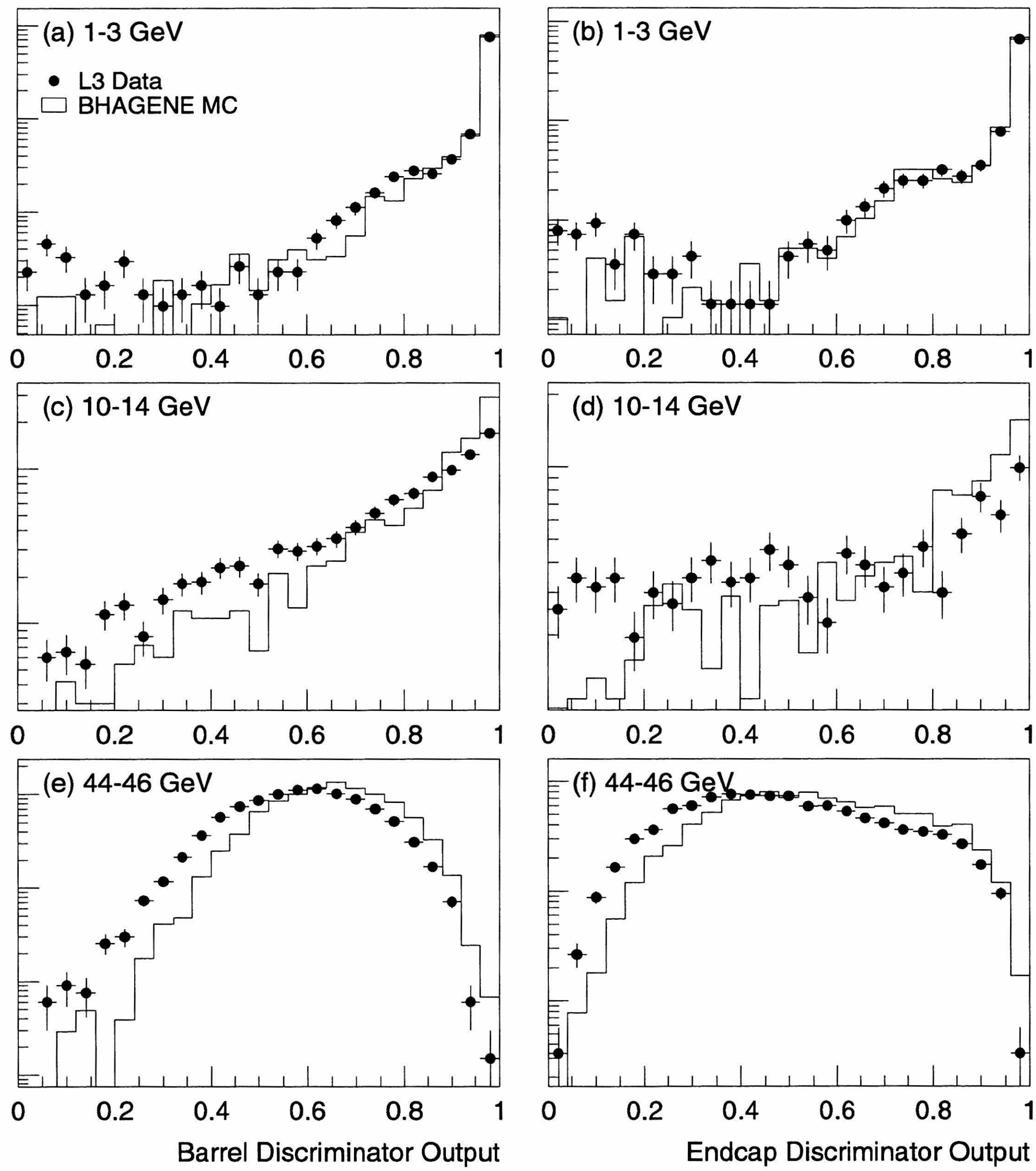

Figure A.12: Comparison of the discriminator output value distributions for photon and electron bumps selected in radiative Bhabha events. Plots correspond to the barrel (a,c,e) and endcap (b,d,f) regions, and to three energy intervals: 1–2 GeV (a,b), 10–12 GeV (c,d), and 44–45 GeV (e,f).

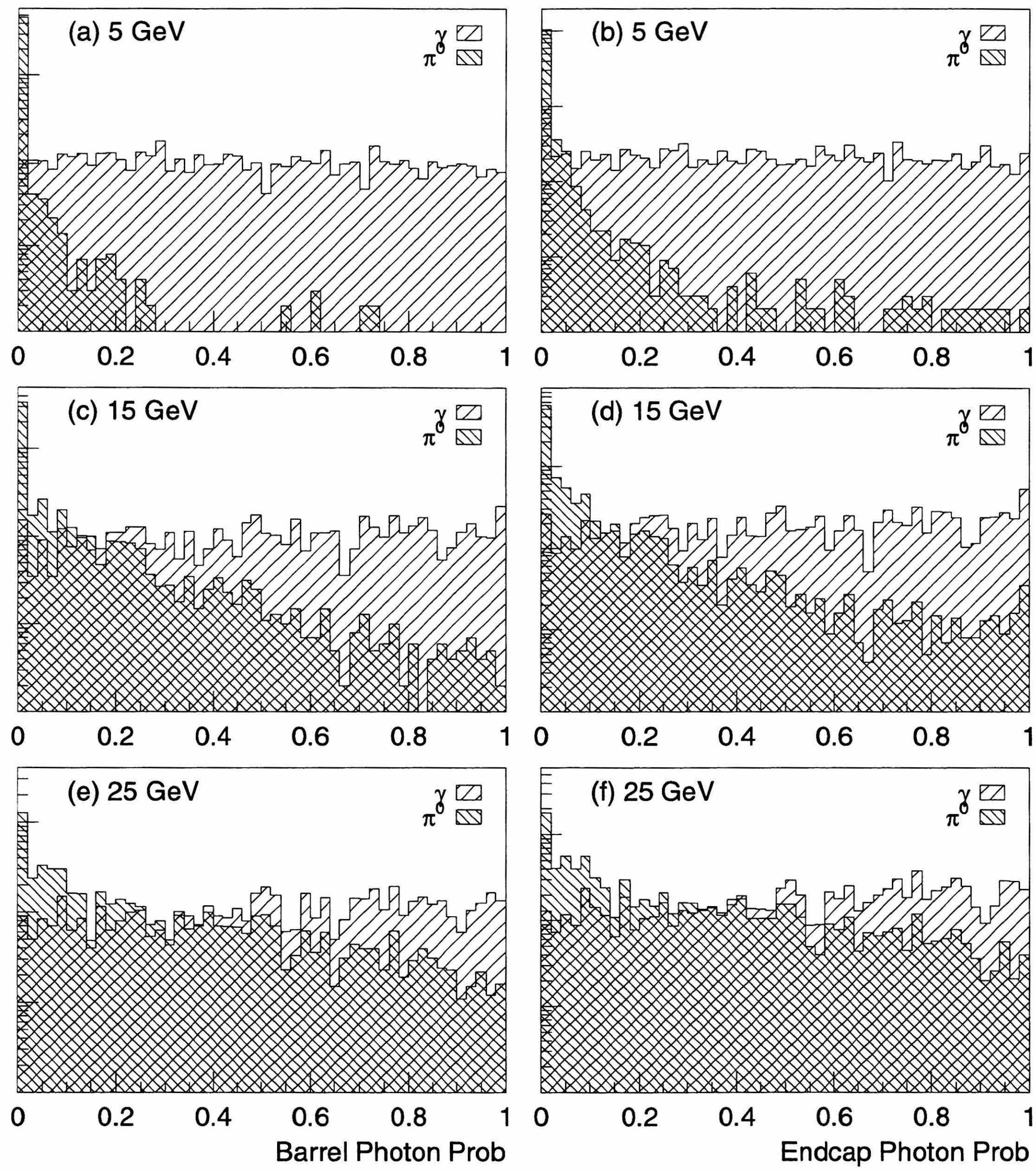

Figure A.13: Distributions of photon probabilities, p_γ, for isolated single particles in the barrel (a,c,e) and endcap (b,d,f) regions, and at 5 GeV (a,b), 15 GeV (c,d), and 25 GeV (e,f). The vertical scale is logarithmic.

References

[1] E. Noether, Nachr. Kgl. Ges. Wiss. Göttingen (1918) 235.

[2] J. Goldstone, Nuovo Cim. **19** (1961) 154.

[3] P. W. Higgs, Phys. Lett. **12** (1964) 132.

[4] S. L. Glashow, Nucl. Phys. B **22** (1961) 579.

[5] S. Weinberg, Phys. Rev. Lett. **19** (1967) 1264.

[6] A. Salam, in Proceedings of the 8th Nobel Symposium, ed. N. Svartholm, (Almquist and Wiksell, Stockholm, 1968).

[7] N. Cabibbo, Phys. Rev. Lett. **10** (1963) 531.

[8] S. L. Glashow and I. Iliopoulos and L. Maiani, Phys. Rev. D **2** (1970) 1285.

[9] M. Kobayashi and K. Maskawa, Prog. Theor. Phys. **49** (1970) 652.

[10] C. Jarlskog, Phys. Rev. Lett. **55** (1985) 1039.

[11] C. Jarlskog, Z. Phys. C **29** (1985) 491.

[12] G. t'Hooft, Nucl. Phys. B **33** (1971) 173.

[13] G. t'Hooft, Nucl. Phys. B **35** (1971) 167.

[14] S. L. Adler, Lectures on Elementary Particles and Quantum Field Theory, in Brandeis Summer Institute, ed. S. Deser, M. Grisaru and H. Pendleton, volume 1, MIT Press, Cambridge, Massachusetts, 1970.

[15] R. Jackiw, Lectures on Current Algebra and Its Applications, Princeton University Press, Princeton, New Jersey, 1972.

[16] G. Burgers and J. Jegerlehner, The Relation between the Electroweak Couplings and the Weak Vector Boson Masses, in Z Physics at LEP 1: Standard Physics, ed. G. Altarelli, R. Kleiss and C. Verzegnassi, CERN, Geneva, 1989.

[17] D. A. Ross and J. C. Taylor, Nucl. Phys. B **51** (1973) 25.

[18] M. Consoli and W. Hollik, in Z Physics at LEP 1: Standard Physics, ed. G. Altarelli, R. Kleiss and C. Verzegnassi, (CERN, Geneva, 1989), volume 1.

[19] D. Bardin et al., ZFITTER: An Analytical Program for Fermion Pair Production in e+e- Annihilation, Preprint CERN-TH 6443/92, CERN, 1992.

[20] M. Y. Han and Y. Nambu, Phys. Rev. B **139** (1965) 1005.

[21] M. Aguilar-Benitez et al., Phys. Lett. B **239** (1990) 1.

[22] G. d'Agostini and W. de Boer and G. Grindhammer, Phys. Lett. B **229** (1989) 160.

[23] R. Marshall, Z. Phys. C **43** (1989) 595.

[24] V. Branchina et al., Phys. Rev. Lett. **65** (1990) 3237.

[25] M. Gell-Mann, Acta Physica Austriaca, Suppl. IX **733** (1972).

[26] H. Fritzsch and M. Gell-Mann, in 16th International Conference on High Energy Physics, ed. J. D. Jackson and A. Roberts, (FERMILAB, Batavia, 1972).

[27] H. Fritzsch and M. Gell-Mann and H. Leytwyler, Phys. Lett. B **47** (1973) 365.

[28] D. J. Gross and F. Wilczek, Phys. Rev. Lett. **30** (1973) 1343.

[29] D. J. Gross and F. Wilczek, Phys. Rev. D **8** (1973) 3633.

[30] H. D. Politzer, Phys. Rev. Lett. **30** (1973) 1346.

[31] W. Caswell, Phys. Rev. Lett. **33** (1974) 244.

[32] D. R. T. Jones, Nucl. Phys. B **75** (1974) 531.

[33] O. V. Tarasov and A. A. Vladimirov and A. Y. Zharkov, Phys. Lett. B **93** (1980) 429.

[34] S. Weinberg, Phys. Rev. Lett. **31** (1973) 494.

[35] S. Weinberg, Phys. Rev. D **8** (1973) 4482.

[36] D. Decamp, Nucl. Instrum. Methods A **294** (1990) 127.

[37] P. Aarnio et al., Nucl. Instrum. Methods A **303** (1991) 233.

[38] B. Adeva et al., Nucl. Instrum. Methods A **289** (1990) 35.

[39] K. Ahmet et al., Nucl. Instrum. Methods A **305** (1991) 275.

[40] A. Hofman, Performance Limitations at LEP, Preprint CERN-SL-94-058, CERN, 1994.

[41] R. Bailey, (World Scientific, Singapore, 1993), volume Int. J. Mod. Phys. A, Proc. Suppl., p. 401.

[42] C. Bovet et al., Final Report of the 1994 Bunch Train Study Group, Preprint CERN-SL-94-95-AP, CERN, 1994.

[43] R. Assmann et al., Energy Calibration with Resonant Depolarization at LEP in 1993, Preprint CERN-SL-94-016, CERN, 1994.

[44] L. Arnaudon et al., Effects of Tidal Forces on the Beam Energy in LEP, Preprint CERN-SL-93-20I-DI, CERN, 1993.

[45] B. Alpat et al., Nucl. Instrum. Methods A **315** (1992) 497.

[46] P. Béné et al., Nucl. Instrum. Methods A **306** (1991) 150.

[47] R. Bizzarri et al., Nucl. Instrum. Methods A **317** (1992) 463.

[48] S. P. Beingessner et al., Nucl. Instrum. Methods A **340** (1994) 322.

[49] Y. Bertsch et al., Nucl. Instrum. Methods A **340** (1994) 309.

[50] X. Cai, Contribution to the Trigger and Data Acquisition System of the L3 Experiment at LEP, Ph.D. thesis, Université de Savoie, Chambéry, France, October 1994.

[51] C. Dionisi et al., Nucl. Instrum. Methods A **336** (1993) 78.

[52] S. Jadach and B. F. L. Ward, Phys. Rev. D **40** (1989) 3582.

[53] S. Jadach et al., Phys. Lett. B **268** (1991) 253.

[54] S. Jadach et al., Comput. Phys. Commun. **70** (1992) 305.

[55] S. Jadach et al., Higher-Order Radiative Corrections to Low-Angle Bhabha Scattering: The YFS Monte Carlo Approach, Preprint CERN-TH/95-38, CERN, 1995, submitted to Physics Letters.

[56] M. Böhm and A. Denner and W. Hollik, Nucl. Phys. B **304** (1988) 687.

[57] F. A. Berends and R. Kleiss and W. Hollik, Nucl. Phys. B **304** (1988) 712.

[58] L3 Collab., S. Dutta et al., Electroweak Update Including Preliminary 1993/94 Data, Preprint L3 Note 1809, CERN, July 1995.

[59] H. Ma et al., Nucl. Instrum. Methods A **274** (1988) 113.

[60] H. Ma and H. Newman and R.Y. Zhu and R. Hamm, Nucl. Instrum. Methods A **281** (1989) 469.

[61] R.Y. Zhu, Nucl. Instrum. Methods A **306** (1991) 145.

[62] T. Sjöstrand, Comput. Phys. Commun. **82** (1994) 74.

[63] T. Sjöstrand, PYTHIA 5.6 and JETSET 7.3: Physics and Manual, Preprint CERN-TH.7112/93, CERN, 1993.

[64] G. Marchesini et al., Comput. Phys. Commun. **67** (1992) 465.

[65] G. Marchesini and B. Webber, Nucl. Phys. B **310** (1988) 461.

[66] R. Brun et al., GEANT 3, CERN, 1984 (revised 1987), CERN DD/EE/84-1.

[67] H. Fesefeldt, GHEISHA, Preprint PITHA 85/02, RWTH Aachen, 1985.

[68] S. Jadach and B. F. L. Ward and Z. Was, Comput. Phys. Commun. **79** (1994) 503.

[69] F. A. Berends and P. H. Daverveldt and R. Kleiss, Nucl. Phys. B **253** (1985) 441.

[70] L3 Collab., M. Acciarri et al., Z. Phys. C **62** (1994) 551.

[71] J. G. Hayes, Numerical Approximations to Functions and Data, chapter Chapter 5: Curve Fitting by Polynomials in One Variable, (University of London, The Athlone Press, 1970).

[72] F. James and M. Roos, MINUIT: Function Minimization and Error Analysis, CERN, 1981, CERN Program Library Long Writeup D506.

[73] Particle Data Group, L. Montanet et al., Phys. Rev. D **50** (1994) 1173.

[74] E. Laermann, T. F. Walsh, I. Schmitt and P. M. Zerwas, Nucl. Phys. B **207** (1982) 205.

[75] MAC Collab., H. R. Band et al., Phys. Rev. Lett. **54** (1985) 95.

[76] TASSO Collab., W. Braunschweig et al., Z. Phys. C **41** (1988) 385.

[77] VENUS Collab., K. Abe et al., Phys. Rev. Lett. **63** (1989) 1776.

[78] JADE Collab., D. D. Pitzl et al., Z. Phys. C **46** (1990) 1.

[79] G. Kramer and B. Lampe, Phys. Lett. B **269** (1991) 401.

[80] OPAL Collab., G. Alexander et al., Phys. Lett. B **264** (1991) 219.

[81] OPAL Collab., P. D. Acton et al., Z. Phys. C **54** (1992) 193.

[82] G. Kramer and H. Spiesberger, in Workshop on Photon Radiation from Quarks, ed. S. Cartwright, (CERN, 1991), p. 26.

[83] D. Kirkby, QCD Corrections to Isolated Hard Photon Production in e^+e^- Annihilation, Preprint CALT-68-1822, Caltech, 1992.

[84] E. W. N. Glover and J. Stirling, Phys. Lett. B **295** (1992) 128.

[85] Z. Kunszt and Z. Trocsanyi, Nucl. Phys. B **394** (1993) 139.

[86] L3 Collab., O. Adriani et al., Phys. Lett. B **301** (1993) 136.

[87] CDF Collab., F. Abe et al., Phys. Rev. Lett. **74** (1995) 2626.

[88] DØ Collab., S. Abachi et al., Phys. Rev. Lett. **74** (1995) 2632.

[89] A. Ali et al., Nucl. Phys. B **167** (1980) 454.

[90] R. K. Ellis and D. A. Ross and A. E. Terrano, Nucl. Phys. B **178** (1981) 421.

[91] G. Kramer and B. Lampe, Fortschr. Phys. **37** (1989) 161.

[92] G. P. Lepage, J. of Comp. Phys. **27** (1978) 192.

[93] S. Banerjee and S. Müller, Determination of α_s from Hadronic Event Shapes Measured on the Z^0 Resonance, Preprint L3 Note 1441, CERN, 1993.

[94] G. Altarelli and G. Parisi, Nucl. Phys. B **126** (1977) 298.

[95] V. V. Sudakov, Sov. Phys. J. E. T. P. **30** (1956) 65.

[96] L. Lönnblad, in Workshop on Photon Radiation from Quarks, ed. S. Cartwright, (CERN, 1991), p. 109.

[97] D. Kirkby, in Workshop on Photon Radiation from Quarks, ed. S. Cartwright, (CERN, 1991), p. 121.

[98] L3 Collab., B. Adeva et al., Z. Phys. C **55** (1992) 39.

[99] P. Mättig and W. Zeuner, Z. Phys. C **52** (1991) 37.

[100] T. Hebbeker et al., Phys. Lett. B **331** (1994) 165.

[101] S. Barlag et al., Z. Phys. C **11** (1982) 283.

[102] OPAL Collab., R. Akers et al., Comparisons of the Properties of Final State Photons in Hadronic Z Decays with Predictions from Matrix Element Calculations, Preprint CERN-PPE/95-13, CERN, 1995.

[103] ALEPH Collab., D. Decamp et al., Phys. Lett. B **264** (1991) 476.

[104] ALEPH Collab., B. Buskulic et al., Z. Phys. C **57** (1993) 17.

[105] DELPHI Collab., P. Abreu et al., Z. Phys. C **53** (1992) 555.

[106] DELPHI Collab., P. Abreu et al., Study of Prompt Photon Production in Hadronic Z Decays, Preprint CERN-PPE/95-101, CERN, 1995.

[107] L3 Collab., O. Adriani et al., Phys. Lett. B **292** (1992) 472.

[108] OPAL Collab., M. Z. Akrawy et al., Phys. Lett. B **246** (1990) 285.

[109] OPAL Collab., P. D. Acton et al., Z. Phys. C **58** (1993) 405.

[110] L3 Collab., O. Adriani et al., Phys. Lett. B **307** (1993) 237.

[111] P. Allen et al., Phys. Lett. B **112** (1982) 88.

[112] J. P. Berge et al., Phys. Lett. B **91** (1980) 311.

[113] P. Allen et al., Nucl. Phys. B **181** (1981) 385.

[114] M. Derrick et al., Phys. Rev. D **24** (1981) 1071.

[115] L3 Collab., O. Adriani et al., Phys. Lett. B **317** (1993) 637.

[116] S. Banerjee, D. Duchesneau and S. Sarkar, Study of Event Shape Variables at Reduced CM Energies from Z Data, Preprint L3 Note 1803, CERN, 1995.

[117] S. Shevchenko, Neutral Pion Rejection in the CMS $PbWO_4$ Crystal Calorimeter, Preprint CMS TN/94-300, CERN, 1994.

[118] C. Seez and T. S. Virdee, The Higgs Two Photon Decay in CMS : an Update, Preprint CMS TN/94-289, CERN, 1994.

[119] D. Kirkby, in Perturbative QCD and Hadronic Interactions, ed. J. Tran Thanh Van, (Editions Frontieres, 1995), volume XXX of *Rencontre de Moriond.*

[120] C. Peterson and T. Rögnvaldsson and L. Lönnblad, Comput. Phys. Commun. **81** (1994) 185.

[121] D. E. Rumelhart and G. E. Hinton and R. J. Williams, Learning Internal Representations by Error Propagation, in Parallel Distributed Processing: Explorations in the Microstructure of Cognition, ed. D. E. Rumelhart and J. L. McClelland, MIT Press, 1986.

[122] J. H. Field, Phys. Lett. B **323** (1994) 432.

[123] J. Shiers et al., ZEBRA, CERN, 1995, CERN Program Library Long Writeups Q100/Q101.